



TECHNICAL UNIVERSITY OF CRETE
SCHOOL OF PRODUCTION ENGINEERING AND MANAGEMENT

Synthesis and Characterization of Ceria-Based Nano-Structured Materials: Structure–Activity Relationships

*Thesis submitted for the partial fulfillment of the requirements for the degree of
Doctor of Philosophy (PhD)*

by

MARIA LYKAKI

Supervisor: Associate Professor Michalis Konsolakis

Chania, Greece, July 2021



TECHNICAL UNIVERSITY OF CRETE
SCHOOL OF PRODUCTION ENGINEERING AND MANAGEMENT

Synthesis and Characterization of Ceria-Based Nano-Structured Materials: Structure–Activity Relationships

by

MARIA LYKAKI

Advisory Committee

Michalis Konsolakis (Supervisor)

Associate Professor, School of Production Engineering and Management
Technical University of Crete (TUC)

Georgios E. Marnellos

Professor, Department of Mechanical Engineering
University of Western Macedonia (UoWM)

Eleni Iliopoulou

Principal Researcher, Chemical Process and Energy Resources Institute (CPERI)
Centre for Research and Technology Hellas (CERTH)

Thesis Examination Committee

Nikolaos Kallithrakas-Kontos

Professor, School of Mineral Resources Engineering
Technical University of Crete (TUC)

Spiros Papaefthimiou

Associate Professor, School of Production Engineering and Management
Technical University of Crete (TUC)

Vassilis N. Stathopoulos

Professor, School of Agricultural Development, Nutrition and Sustainability
National and Kapodistrian University of Athens (NKUA)

Konstantinos Triantafyllidis

Professor, School of Chemistry
Aristotle University of Thessaloniki (AUTH)



Π Ρ Α Κ Τ Ι Κ Ο
ΤΗΣ ΕΠΤΑΜΕΛΟΥΣ ΕΞΕΤΑΣΤΙΚΗΣ ΕΠΙΤΡΟΠΗΣ
ΓΙΑ ΤΗΝ ΚΡΙΣΗ ΤΗΣ ΔΙΔΑΚΤΟΡΙΚΗΣ ΔΙΑΤΡΙΒΗΣ

της **Μαρίας Λυκάκη, του Ιωάννη**

ΔΙΠΛΩΜΑΤΟΥΧΟΥ/ΠΤΥΧΙΟΥΧΟΥ ΤΟΥ ΤΜΗΜΑΤΟΣ

Χημείας του Πανεπιστημίου Κρήτης

Η εξεταστική επιτροπή που διορίστηκε σύμφωνα με τις κείμενες διατάξεις και την απόφαση της Γενικής Συνέλευσης της Σχολής Μηχανικών Παραγωγής και Διοίκησης στη συνεδρίαση 12η Σ.Τμ./25.5.2021 για την κρίση της διδακτορικής διατριβής της **Μαρίας Λυκάκη** συνήλθε σε συνεδρίαση σήμερα την **Πέμπτη 01 Ιουλίου 2021** και παρακολούθησε την υποστήριξη της διατριβής με τίτλο:

«Σύνθεση και χαρακτηρισμός νανο-δομημένων καταλυτικών συστημάτων βασισμένων σε οξείδιο του Διμητηρίου (CeO₂): Σχέσεις δομής – δραστικότητα»

Αγγλικός τίτλος: **«Synthesis and Characterization of Ceria-Based Nano-Structured Materials: Structure – Activity Relationships»**

Μετά την ανάπτυξη της διατριβής, τα μέλη της εξεταστικής επιτροπής, έκαναν ερωτήσεις στην υποψήφια κα Μαρία Λυκάκη τόσο γενικού περιεχομένου, όσο και σχετικές με το θέμα της διατριβής.

Στη συνέχεια, αποχώρησε η υποψήφια και ακολούθησε συζήτηση της επιτροπής.

Η επιτροπή, μετά από ψηφοφορία, έκρινε ότι η διατριβή της Μαρίας Λυκάκη, είναι πρωτότυπη και αποτελεί ουσιαστική συμβολή στην επιστήμη, προτείνει δε προς τη Γενική Συνέλευση με ειδική σύνθεση της Σχολής, ομόφωνα να της απονεμίσει τον τίτλο του Διδάκτορος.

Η ΕΠΙΤΡΟΠΗ

1. Μιχάλης Κονσολάκης, επιβλέπων, ΜΠΔ, Πολυτεχνείο Κρήτης
2. Γεώργιος Ε. Μαρινέλλος, Πανεπιστήμιο Δυτικής Μακεδονίας
3. Ελένη Ηλιοπούλου, ΙΔΕΠ/ΕΚΕΤΑ
4. Νικόλαος Καλλίβρακας-Κόντος, ΜΗΧΟΠ, Πολυτεχνείο Κρήτης
5. Σπύρος Παπαευθυμίου, ΜΠΔ, Πολυτεχνείο Κρήτης
6. Βασίλης Ν. Σταθόπουλος, ΕΚΠΑ
7. Κωνσταντίνος Τριανταφυλλίδης, ΑΠΘ

ΥΠΟΓΡΑΦΗ

The research work was supported by the Hellenic Foundation for Research and Innovation (HFRI) and the General Secretariat for Research and Technology (GSRT), under the HFRI PhD Fellowship grant (GA. no. 34252).



This research has been co-financed by the European Union and Greek national funds through the Operational Program Competitiveness, Entrepreneurship and Innovation, under the call RESEARCH–CREATE–INNOVATE (project code: T1EDK-01894). Research project: LIGBIO-GASOFC.



Co-financed by Greece and the European Union

This research has been co-financed by the European Union and Greek national funds through the Operational Program Competitiveness, Entrepreneurship and Innovation, under the call RESEARCH–CREATE–INNOVATE (project code: T1EDK-00094). Research project: NANOCO2.



Co-financed by Greece and the European Union

During the present thesis, the following laboratories collaborated on the basis of materials synthesis, characterization studies and catalytic evaluation:

- Industrial, Energy and Environmental Systems Lab (IEESL), School of Production Engineering and Management, Technical University of Crete
- Laboratory of Analytical and Environmental Chemistry, School of Mineral Resources Engineering, Technical University of Crete
- Laboratory of Catalysis and Materials (LCM), Associate Laboratory LSRE-LCM, Faculty of Engineering, University of Porto
- Chemical Process & Energy Resources Institute (CPERI), Centre for Research & Technology Hellas (CERTH)
- Institute of Electronic Structure and Laser (IESL), FORTH
- Department of Mechanical Engineering, University of Western Macedonia
- Laboratory of Chemistry and Materials Technology, General (Core) Department, National and Kapodistrian University of Athens.

In the framework of the two research projects mentioned above (LIGBIO-GASOFC and NANOCO₂), the following doctoral theses have been conducted:

1. **"Synthesis and Characterization of Ceria-Based Nano-Structured Materials: Structure–Activity Relationships"** by **Maria Lykaki**.

Supervisor: Associate Professor Michalis Konsolakis

2. **"Rational Design and Development of Nanostructured Non-Precious Metal Oxide Catalysts for Energy and Environmental Applications"** by **Sofia Stefa**.

Supervisor: Associate Professor Michalis Konsolakis

3. **"Design and Evaluation of Advanced CeO₂-Based Transition Metal Catalytic Composites for CO₂ Activation by Renewable H₂ toward Chemicals and Fuels"** by **Georgios Varvoutis**.

Supervisor: Professor Georgios E. Marnellos

In this point, it should be mentioned that the aforementioned doctoral theses are interrelated and complementary to one another due to the collaborative nature and the scientific objectives of the research projects LIGBIO-GASOFC (project code: T1EDK-01894) and NANOCO₂ (project code: T1EDK-00094). In this regard, some characterization results obtained by PhD Candidate Sofia Stefa and some catalytic results obtained by PhD Candidate Georgios Varvoutis are cited in various chapters of the present thesis in a well-defined and distinctive manner.

ΕΥΧΑΡΙΣΤΙΕΣ

Η παρούσα διδακτορική διατριβή δεν θα είχε ολοκληρωθεί χωρίς τη στήριξη και τη σπουδαία συμβολή ορισμένων ανθρώπων, τους οποίους θα ήθελα να ευχαριστήσω μέσα απ' την καρδιά μου.

Πρωτίστως, θα ήθελα να ευχαριστήσω ολόθερμα και να εκφράσω την ευγνωμοσύνη μου στον επιβλέποντα Καθηγητή μου Μιχάλη Κουσολάκη για την εμπιστοσύνη που μου έδειξε, εντάσσοντάς με στην ερευνητική του ομάδα. Η αδιάκοπη καθοδήγησή του και οι πολύτιμες γνώσεις του υπήρξαν καταλυτικοί παράγοντες για την πραγματοποίηση της παρούσας διδακτορικής διατριβής. Ο ζήλος και η ακούραστη διάθεση που επιδεικνύει στους τομείς της έρευνας και της εκπαίδευσης αποτελούν φωτεινά παραδείγματα προς όλους μας. Επίσης, θα ήθελα να ευχαριστήσω τον Καθηγητή Νικόλαο Καλλιθρακα-Κόντο (Πολυτεχνείο Κρήτης) για τη στήριξη του και την άφογη συνεργασία μας όλα αυτά τα χρόνια, εκφράζοντας ταυτόχρονα τη βαθιά μου εκτίμηση και τον σεβασμό μου στο πρόσωπό του.

Επιπλέον, θα ήθελα να ευχαριστήσω τον Καθηγητή Γεώργιο Μαρνέλλο (Πανεπιστήμιο Δυτικής Μακεδονίας, μέλος της τριμελούς επιτροπής) για την επιστημονική καθοδήγηση και τη στήριξη του κατά τη διάρκεια της διδακτορικής διατριβής. Έπειτα, θα ήθελα να ευχαριστήσω την Κύρια Ερευνήτρια Δρ. Ελένη Ηλιοπούλου (Ινστιτούτο Χημικών Διεργασιών και Ενεργειακών Πόρων (ΙΔΕΠ), ΕΚΕΤΑ, μέλος της τριμελούς επιτροπής) για την επιστημονική συμβολή της στην παρούσα διδακτορική διατριβή.

Επίσης, θα ήθελα να ευχαριστήσω τον Καθηγητή Σπύρο Παπαευθυμίου (Πολυτεχνείο Κρήτης) και τον Καθηγητή Κωνσταντίνο Τριανταφυλλίδη (Αριστοτέλειο Πανεπιστήμιο Θεσσαλονίκης) για τη στήριξη και τη συμβολή τους στο πλαίσιο της παρούσας διδακτορικής διατριβής.

Σε αυτό το σημείο, θα ήθελα να ευχαριστήσω τους ανθρώπους με τους οποίους συνεργάστηκα στους τομείς του χαρακτηρισμού υλικών και των καταλυτικών δοκιμών.

Η συμβολή των ανθρώπων αυτών υπήρξε καθοριστική για την πραγματοποίηση της διδακτορικής αυτής διατριβής. Ευχαριστώ θερμά την Καθηγήτρια Sónia A.C. Carabineiro (Nova University of Lisbon), τον Κύριο Ερευνητή Δρ. Παύλο Πανδή (Εθνικό και Καποδιστριακό Πανεπιστήμιο Αθηνών) και τον Καθηγητή Βασίλη Σταθόπουλο (Εθνικό και Καποδιστριακό Πανεπιστήμιο Αθηνών) για την άφογη

συνεργασία μας και τη σημαντική τους συμβολή στην υλοποίηση της παρούσας διδακτορικής διατριβής. Επίσης, θα ήθελα να ευχαριστήσω ολόθερμα την υποψήφια διδάκτορα Σοφία Στέφα (Πολυτεχνείο Κρήτης) για την τεράστια συμβολή της στον τομέα του χαρακτηρισμού υλικών και για την άφορη συνεργασία που έχουμε όλα αυτά τα χρόνια. Επιπλέον, θα ήθελα να ευχαριστήσω τους υποψήφιους διδάκτορες Θανάση Λαμπρόπουλο (Πανεπιστήμιο Αιτικής Μακεδονίας) και Γεώργιο Βαρβούτη (Πανεπιστήμιο Αιτικής Μακεδονίας) για την εξαιρετική συνεργασία και την καίρια συμβολή τους στα καταλυτικά πειράματα.

Εν συνεχεία, θα ήθελα να ευχαριστήσω το σύντροφό μου Φίλιππο για την αμείωτη στήριξη του καθ' όλη την πορεία της διδακτορικής μου διατριβής.

Τέλος, θα ήθελα να ευχαριστήσω ολόψυχα τους γονείς μου Σοφία και Γιάννη και τ' αδέρφια μου Διονύση και Φενάτα για την αδιάκοπη στήριξη και την ενθάρρυνσή τους, όντας πραγματικοί συνοδοιπόροι σε κάθε μου βήμα.

Μαρία Λυκάκη

SHORT ABSTRACT

The rational design and development of highly-active and cost-efficient catalysts for energy and environmental applications constitutes the main research pillar in the area of heterogeneous catalysis. In this perspective, the present thesis aims at the fine-tuning of noble metal (NMs)-free metal oxide catalysts, such as ceria-based transition metal catalysts (M_xO_y/CeO_2 , where M stands for Cu, Co, Fe, Ni) by means of advanced synthetic and/or promotional routes. It was clearly revealed that the adjustment of size, shape and electronic state of ceria-based metal oxides (MOs) can exert a profound influence on the reactivity of metal sites as well as on metal-support interfacial activity, offering extremely active and stable materials for various applications, such as CO oxidation, N_2O decomposition and CO_2 hydrogenation to value-added products.

In the framework of the present thesis, the effect of the preparation method (thermal decomposition, precipitation, hydrothermal) on the solid state properties and the CO oxidation performance of bare ceria nanoparticles was initially investigated. The superiority of the hydrothermal method towards the development of ceria nanoparticles of high specific surface area ($> 90 \text{ m}^2 \text{ g}^{-1}$), well-defined morphology and enhanced redox properties was clearly disclosed. Interestingly, a direct quantitative relationship was established between the catalytic activity and the abundance of weakly bound labile oxygen species.

Driven by the aforementioned results, our research efforts were next focused on the hydrothermal synthesis of ceria nanoparticles of specific morphology, *i.e.*, nanorods (NR), nanopolyhedra (NP), nanocubes (NC). Then, the different ceria nanostructures were at first used as supporting carriers for Cu and Fe active phases in order to gain insight into the effect of ceria shape on the structural defects, the surface chemistry and consequently on the CO oxidation performance. The superiority of the rod-shaped samples, exposing the {100}/{110} crystal facets, was once more revealed, as they exhibited enhanced reducibility and oxygen exchange kinetics, linked to synergistic metal-support interactions. The key role of ceria morphology on the reducibility and oxygen mobility, following the sequence: $NR > NP > NC$, was revealed, without however being affected by the addition of the metal phase, demonstrating the pivotal role of support morphology. A perfect relationship between the catalytic performance and the following parameters was disclosed, on the basis of a Mars-van Krevelen mechanism: i) abundance of weakly bound oxygen species, ii) relative population of Cu^+/Ce^{3+} redox pairs, iii) relative abundance of defects and oxygen vacancies.

Next, the impact of support morphology and alkali promotion was explored towards the development of highly active catalysts for N_2O decomposition. In particular, the effect of

ceria morphology on the physicochemical properties and the N₂O decomposition (deN₂O) performance of cobalt-ceria mixed oxides was explored. Cobalt-ceria nanorods exhibited the best catalytic behaviour (100% N₂O conversion at 500 °C) due to their abundance in Co²⁺ active sites and Ce³⁺ species in conjunction to their improved reducibility, oxygen kinetics and surface area.

Towards the rational design of highly active catalytic composites, the fine-tuning of local surface chemistry of Cu/CeO₂ mixed oxides by means of synthesis procedure and alkali (Cs) promotion was next investigated. It was found that the co-optimization of the synthesis procedure (co-precipitation) and alkali loading (1.0 at Cs per nm²) can boost the deN₂O performance and resistance to O₂ inhibition. The superiority of Cs-doped samples was mainly ascribed to the electronic effect of alkali promoter towards the stabilization of partially reduced Cu⁺/Ce³⁺ pairs, which play a key role in the deN₂O process following a redox-type mechanism.

In the sequence, the combined effect of ceria morphology and active phase nature on the physicochemical properties and the CO₂ hydrogenation performance over ceria-based transition metal catalysts (M/CeO₂, M: Fe, Co, Cu, Ni) was investigated. Independently of the support morphology, the conversion of CO₂ followed the order: Ni/CeO₂ > Co/CeO₂ > Cu/CeO₂ > Fe/CeO₂ > CeO₂. Also, it ought to be mentioned that bare ceria, Cu/CeO₂ and Fe/CeO₂ samples were very active and selective for CO production, whereas Co/CeO₂ and Ni/CeO₂ catalysts were highly active and selective towards methane (CH₄).

Through the present thesis, the pivotal role of support morphology and alkali promotion on the solid state properties, metal-support interactions and in turn, on the catalytic performance of ceria-based mixed oxides was unambiguously revealed.

More importantly, the fine-tuning of size, shape and electronic state can notably affect not only the reactivity of metal sites but also the interfacial activity (*e.g.*, through the formation of oxygen vacancies and the facilitation of redox interplay between the metal and the support) offering a synergistic contribution towards the development of highly active composites. Through the proposed optimization approach extremely active and cost-efficient catalytic materials were obtained for CO oxidation, N₂O decomposition and CO₂ hydrogenation reactions, being among the most active reported so far in open literature. The general optimization framework followed in the present thesis can provide the design principles towards the development of earth-abundant metal oxides for various energy and environmental applications paving also the way for the decrease of noble metals content in NMs-based catalysts.

ΣΥΝΤΟΜΗ ΠΕΡΙΛΗΨΗ

Ο ορθολογικός σχεδιασμός και η ανάπτυξη αποτελεσματικών και συνάμα οικονομικών καταλυτικών συστημάτων για ενεργειακές και περιβαλλοντικές εφαρμογές αποτελεί τον κύριο ερευνητικό πυλώνα στον τομέα της ετερογενούς κατάλυσης. Προς αυτή την κατεύθυνση, στόχο της παρούσας διδακτορικής διατριβής αποτελεί η κατάλληλη τροποποίηση καταλυτών μεταλλοξειδίων απαλλαγμένων ευγενών μετάλλων, όπως μετάλλων μετάπτωσης υποστηριγμένων σε οξείδιο του δημητρίου (M_xO_y/CeO_2 , όπου το M αντιπροσωπεύει τα Cu, Co, Fe, Ni), μέσω προηγμένων μεθόδων σύνθεσης ή/και προώθησης. Ειδικότερα, η τροποποίηση του μεγέθους, του σχήματος και της ηλεκτρονιακής κατάστασης του φορέα ή/και της ενεργούς φάσεως μπορεί να επηρεάσει σημαντικά όχι μόνο τη δραστηριότητα των μεταλλικών κέντρων, αλλά και τη διεπιφανειακή ενεργότητα, οδηγώντας σε εξαιρετικά ενεργά και σταθερά υλικά για ποικίλες εφαρμογές, όπως η οξείδωση του CO, η διάσπαση του N_2O και η υδρογόνωση του CO_2 προς προϊόντα υψηλής προστιθέμενης αξίας.

Επί τη βάση των ανωτέρω, στο πλαίσιο της παρούσας διδακτορικής διατριβής, μελετήθηκε αρχικά η επίδραση της μεθόδου σύνθεσης (θερμική διάσπαση, καταβύθιση, υδροθερμική) στις ιδιότητες στερεάς κατάστασης και στην απόδοση οξείδωσης του CO σε νανο-σωματίδια δημητρίας. Η ανωτερότητα της υδροθερμικής μεθόδου ως προς την ανάπτυξη νανο-σωματιδίων δημητρίας υψηλής ειδικής επιφάνειας ($> 90 \text{ m}^2 \text{ g}^{-1}$), καθορισμένης μορφολογίας και βελτιωμένων αναγωγικών ιδιοτήτων κατέστη εμφανής. Επιπλέον, αναδείχθηκε μια άμεση ποσοτική σχέση ανάμεσα στην καταλυτική ενεργότητα και την αφθονία σε ασθενώς συνδεδεμένα είδη οξυγόνου.

Ορμώμενοι από τα προαναφερθέντα αποτελέσματα, οι ερευνητικές μας προσπάθειες επικεντρώθηκαν στην υδροθερμική σύνθεση νανο-σωματιδίων δημητρίας συγκεκριμένης μορφολογίας, ήτοι νανο-ράβδοι (NR), νανο-πολύεδρα (NP), νανο-κύβοι (NC). Αρχικά, τα διαφορετικά νανο-σωματίδια δημητρίας χρησιμοποιήθηκαν ως υποστρώματα για τις ενεργές φάσεις Cu και Fe προκειμένου να ληφθεί γνώση επί της επίδρασης της μορφολογίας της δημητρίας και των αλληλεπιδράσεων μετάλλου-φορέα στις δομικές ατέλειες, στην επιφανειακή χημεία και κατ' επέκταση, στην καταλυτική απόδοση ως προς την αντίδραση οξείδωσης του CO. Η ανωτερότητα των δειγμάτων νανο-ραβδοειδούς μορφολογίας, στα οποία εκτίθενται τα κρυσταλλογραφικά επίπεδα $\{100\}/\{110\}$, κατέστη εμφανής για άλλη μια φορά, καθώς παρουσίασαν αυξημένη αναγωγική ικανότητα και κινητικότητα οξυγόνου, σχετιζόμενη με τις συνεργιστικές αλληλεπιδράσεις μετάλλου-φορέα. Ο σημαντικός ρόλος της μορφολογίας της δημητρίας στην αναγωγική ικανότητα και

στην κινητικότητα οξυγόνου κατέστη εμφανής, ακολουθώντας τη σειρά: NR > NP > NC, χωρίς, ωστόσο, αυτή να επηρεάζεται από την προσθήκη του μετάλλου. Πιο συγκεκριμένα, επί τη βάση ενός μηχανισμού τύπου Mars-van Krevelen, βρέθηκε μια τέλεια σχέση ανάμεσα στην καταλυτική απόδοση και τις ακόλουθες παραμέτρους: i) αφθονία σε ασθενώς συνδεδεμένα είδη οξυγόνου, ii) σχετικό πληθυσμό σε οξειδοαναγωγικά ζεύγη $\text{Cu}^+/\text{Ce}^{3+}$, iii) σχετική αφθονία σε δομικές ατέλειες και κενές θέσεις οξυγόνου.

Εν συνεχεία, μελετήθηκε η επίδραση της μορφολογίας του φορέα κατά την αντίδραση διάσπασης του N_2O σε μικτά οξείδια κοβαλτίου-δημητρίας. Οι νανο-ράβδοι κοβαλτίου-δημητρίας παρουσίασαν και πάλι τη βέλτιστη καταλυτική συμπεριφορά (100% μετατροπή N_2O στους 500 °C) λόγω της αφθονίας τους σε ενεργά κέντρα Co^{2+} και σε είδη Ce^{3+} σε συνδυασμό με τη βελτιωμένη τους αναγωγική ικανότητα, κινητικότητα οξυγόνου και ειδική επιφάνεια.

Προς την κατεύθυνση του ορθολογικού σχεδιασμού καταλυτικών υλικών υψηλής ενεργότητας, μελετήθηκε, εν συνεχεία, η κατάλληλη τροποποίηση της τοπικής επιφανειακής χημείας των μικτών οξειδίων Cu/CeO_2 μέσω της μεθόδου σύνθεσης και της προώθησης με αλκάλιο (Cs). Ειδικότερα, βρέθηκε ότι η ταυτόχρονη βελτιστοποίηση της μεθόδου σύνθεσης (συγκαταβύθιση) και της φόρτισης σε αλκάλιο (1.0 at Cs/nm^2) μπορεί να ενισχύσει την ενεργότητα διάσπασης του N_2O και την ανθεκτικότητα στο O_2 . Η ανωτερότητα των προωθημένων με Cs δειγμάτων αποδόθηκε, κυρίως, στην ηλεκτρονιακή επίδραση του προωθητή αλκαλίου ως προς τη σταθεροποίηση των μερικώς ανηγμένων ζευγών $\text{Cu}^+/\text{Ce}^{3+}$, τα οποία διαδραματίζουν καίριο ρόλο στη διεργασία διάσπασης του N_2O που ακολουθεί έναν οξειδοαναγωγικού τύπου μηχανισμό.

Στη συνέχεια, μελετήθηκε η συνδυαστική επίδραση της μορφολογίας της δημητρίας και της φύσης της ενεργού φάσης στις φυσικοχημικές ιδιότητες και την καταλυτική συμπεριφορά μετάλλων μετάπτωσης υποστηριγμένων σε δημητρία (M/CeO_2 , M: Fe, Co, Cu, Ni) κατά την αντίδραση υδρογόνωσης του CO_2 . Ανεξαρτήτως της μορφολογίας του υποστρώματος, παρατηρήθηκε η ακόλουθη σειρά ως προς τη μετατροπή του CO_2 : $\text{Ni}/\text{CeO}_2 > \text{Co}/\text{CeO}_2 > \text{Cu}/\text{CeO}_2 > \text{Fe}/\text{CeO}_2 > \text{CeO}_2$. Επίσης, αξίζει να σημειωθεί ότι τα καθαρά υποστρώματα δημητρίας και τα δείγματα Cu/CeO_2 και Fe/CeO_2 ήταν ιδιαίτερα ενεργά και εκλεκτικά ως προς την παραγωγή του CO, ενώ οι καταλύτες Co/CeO_2 και Ni/CeO_2 ήταν ιδιαίτερα ενεργοί και εκλεκτικοί ως προς το μεθάνιο (CH_4).

Εν κατακλείδι, η παρούσα διδακτορική διατριβή ανέδειξε αδιαμφισβήτητα τον καίριο ρόλο της μορφολογίας του φορέα και της επιφανειακής ενίσχυσης στις ιδιότητες στερεάς

κατάστασης, στις αλληλεπιδράσεις μετάλλου-φορέα και κατ' επέκταση στην καταλυτική απόδοση.

Ειδικότερα, η κατάλληλη τροποποίηση του μεγέθους, του σχήματος και της ηλεκτρονιακής κατάστασης βρέθηκε να επηρεάζει σε σημαντικό βαθμό τόσο τη δραστικότητα των μεταλλικών κέντρων όσο και τη διεπιφανειακή ενεργότητα (π.χ. μέσω του σχηματισμού κενών θέσεων οξυγόνου και της υποβοήθησης των οξειδοαναγωγικών αλληλεπιδράσεων ανάμεσα στο μέταλλο και το φορέα) συνεισφέροντας συνεργιστικά προς την ανάπτυξη ιδιαίτερα ενεργών υλικών. Η προτεινόμενη προσέγγιση βελτιστοποίησης οδήγησε σε εξαιρετικά ενεργά καταλυτικά υλικά χαμηλού κόστους για τις αντιδράσεις οξείδωσης του CO, διάσπασης του N₂O και υδρογόνωσης του CO₂, κατατάσσοντάς τα μεταξύ των πιο ενεργών υλικών αναφορικά με τη βιβλιογραφία. Το γενικό πλαίσιο βελτιστοποίησης που ακολουθείται στην παρούσα διδακτορική διατριβή μπορεί να παρέχει τις σχεδιαστικές αρχές προς την ανάπτυξη μεταλλοξειδίων χαμηλού κόστους για ποικίλες ενεργειακές και περιβαλλοντικές εφαρμογές, ανοίγοντας παράλληλα το δρόμο προς τη μείωση της φόρτισης σε ευγενή μέταλλα καταλυτικών συστημάτων βασισμένων σε αυτά.

EXTENDED SYNOPSIS & THESIS STRUCTURE

Ceria or cerium oxide (CeO_2) constitutes a broadly studied material in the field of heterogeneous catalysis due to its unique redox properties which mainly arise from its ability to store or release oxygen depending on the reaction environment (oxidizing or reducing). During the '80s, ceria's successful utilization in three-way catalytic converters paved the way for its subsequent use in various energy and environmental applications, involving, among others, the fuel cell technology, the catalytic abatement of volatile organic compounds (VOCs), the catalytic decomposition of nitrogen oxides (NO_x) or nitrous oxide (N_2O), *etc.*

Moreover, metal oxides, composed of earth-abundant transition metals have gained particular attention towards replacing the rare and highly expensive noble metals. In this context, by combining ceria with earth-abundant and cost-effective transition metals, such as Cu, Co, Ni, Fe, the physicochemical properties of the as-prepared materials can be significantly modified, through the synergistic metal-support interactions, with great implications in the catalytic performance. However, various interrelated factors, including shape, size, composition, chemical state, electronic environment can considerably affect the local surface chemistry of the metal oxides as well as the metal-support interactions with great consequences on the macroscopic catalytic behaviour of these multifunctional materials. Furthermore, it is worth mentioning that the materials in the nanoscale exhibit distinct features originated from the electronic interactions developed among the nanoparticles, thus modifying their surface properties and catalytic performance.

Towards the development of nanostructured catalytic systems with predefined surface chemistry, research efforts have focused lately on two diverse approaches which can be applied independently or synergistically: (i) the advanced synthetic methods towards the development of nanomaterials with predefined morphology, (ii) the appropriate adjustment (fine-tuning) of the catalysts' inherent properties through surface and/or structural promotion.

In light of the above aspects, the objective of the present thesis is the development of noble metal-free nanostructured ceria-based transition metal catalysts, in the form of $\text{M}_x\text{O}_y/\text{CeO}_2$ (hereafter denoted as M/CeO_2 for clarity's sake, where M stands for Cu, Co, Fe, Ni), through advanced synthesis methods which are nonetheless characterized by low cost and simple preparation procedures. In particular, several preparation methods, *i.e.*, thermal decomposition, precipitation, hydrothermal, wet impregnation were employed during synthesis and their impact on the physicochemical properties and consequently, on the

catalytic performance (activity/selectivity/stability) of the as-prepared materials was explored through a thorough characterization study which included various *ex situ* and *in situ* techniques, such as N₂ adsorption at –196 °C (BET method), X-ray diffraction (XRD), X-ray fluorescence (XRF), X-ray photoelectron spectroscopy (XPS), temperature programmed reduction (TPR), scanning/transmission electron microscopy (SEM/TEM) and Raman spectroscopy. The main implications of size/shape/electronic engineering in catalysis are explored on the ground of some of the most pertinent heterogeneous reactions, such as CO oxidation, N₂O decomposition and CO₂ hydrogenation to value-added products. Specifically, the present thesis focuses on the following research objectives:

- (i) Ceria shape effects on the structural defects and surface chemistry,
- (ii) Facet-dependent reactivity of ceria-based transition metal catalytic materials,
- (iii) Fine-tuning of the local surface chemistry towards the development of highly active, selective and stable catalytic materials for various energy/environmental applications,
- (iv) Rational design and fabrication of noble-metal free, cost-efficient catalysts formulations by means of advanced synthetic/promotional routes,
- (v) Establishment of reliable structure-property relationships towards revealing key activity descriptors

In light of the above description, the current thesis is divided into the following chapters:

Chapter 1 describes the recent advances in the field of the rational design of noble metal-free ceria-based catalysts, emphasizing on the effect of size, shape and electronic/chemical environment on the catalytic performance. In specific, on the basis of the Cu/CeO₂ binary system, the main implications of the aforementioned factors in several processes in heterogeneous catalysis, such as CO oxidation, N₂O decomposition, preferential oxidation of CO (CO-PROX), water gas shift reaction (WGSR) and CO₂ hydrogenation to value-added products, are thoroughly discussed.

The following review papers were derived from the above-described research:

1. Michalis Konsolakis and **Maria Lykaki**, "Recent Advances on the Rational Design of Non-Precious Metal Oxide Catalysts Exemplified by CuO_x/CeO₂ Binary System: Implications of Size, Shape and Electronic Effects on Intrinsic Reactivity and Metal-Support Interactions", *Catalysts* 10 (2020) 160. doi: 10.3390/catal10020160

2. Michalis Konsolakis and **Maria Lykaki**, "Facet-Dependent Reactivity of Ceria Nanoparticles Exemplified by CeO₂-Based Transition Metal Catalysts: A Critical Review", *Catalysts* 11 (2021) 452. doi: 10.3390/catal11040452

Chapter 2 describes the synthesis methods followed for the preparation of the materials, the characterization techniques and the catalytic evaluation studies.

In chapters 3–5, the presentation and the discussion of the experimental results is taking place.

Chapter 3 deals with the effect of synthesis parameters on the solid state properties and the CO oxidation performance of bare ceria catalysts. More particularly, three different time- and cost-effective preparation methods (thermal decomposition, precipitation and hydrothermal method of low and high NaOH concentration) were employed for the synthesis of ceria materials. It was found that the hydrothermal method results in the development of ceria nanoparticles of specific morphology (nanorods, nanopolyhedra, nanocubes) and of high surface areas ($> 90 \text{ m}^2 \text{ g}^{-1}$), with the rod-shaped ceria sample exhibiting enhanced reducibility and oxygen kinetics, leading to improved catalytic performance.

Furthermore, **Chapter 3** deals with ceria nanostructures' morphological effects (cubes, polyhedra, rods) on the textural, structural, surface, redox properties and, consequently, on the CO oxidation performance of ceria-based transition metal catalysts M/CeO₂ (M: Cu, Fe). It was found that the support morphology significantly affects the physicochemical properties of the mixed oxides with great implications in their catalytic performance. In particular, ceria's morphology rather than the textural/structural properties profoundly affects the reducibility and oxygen mobility of the mixed oxides, following the order: nanorods > nanopolyhedra > nanocubes, with ceria nanorods exhibiting abundance in structural defects and oxygen vacancies. Also, the addition of the metal oxide phase (copper or iron) into the bare ceria supports boosts the CO oxidation performance, without however altering the order observed for bare ceria samples, *i.e.*, nanorods > nanopolyhedra > nanocubes, with the rod-shaped copper-ceria sample offering complete CO elimination at temperatures as low as 100 °C. Similarly, iron-ceria nanorods exhibit the best catalytic performance, exhibiting, however, complete CO conversion at higher temperatures (~250 °C) in comparison with the equivalent copper catalysts. The latter clearly reveals the pivotal role of active phase nature in conjunction to support morphology. It ought to be mentioned that a perfect relationship between the catalytic performance and the following parameters was disclosed, on the basis of a Mars-van Krevelen mechanism: i) abundance of weakly

bound oxygen species, ii) relative population of $\text{Cu}^+/\text{Ce}^{3+}$ redox pairs, iii) relative abundance of defects and oxygen vacancies.

The following publications resulted from the aforementioned results:

3. **Maria Lykaki**, Eleni Pachatouridou, Eleni Iliopoulou, Sónia A. C. Carabineiro and Michalis Konsolakis, "Impact of the synthesis parameters on the solid state properties and the CO oxidation performance of ceria nanoparticles", *RSC Advances* 7 (2017) 6160–6169. doi: 10.1039/c6ra26712b
4. **Maria Lykaki**, Eleni Pachatouridou, Sónia A. C. Carabineiro, Eleni Iliopoulou, Chrysanthi Andriopoulou, N. Kallithrakas-Kontos, Soghomon Boghosian, Michalis Konsolakis, "Ceria nanoparticles shape effects on the structural defects and surface chemistry: Implications in CO oxidation by Cu/CeO₂ catalysts", *Applied Catalysis B: Environmental* 230 (2018) 18–28. doi: 10.1016/j.apcatb.2018.02.035
5. **Maria Lykaki**, Sofia Stefa, Sónia A. C. Carabineiro, Pavlos K. Pandis, Vassilis N. Stathopoulos and Michalis Konsolakis, "Facet-Dependent Reactivity of Fe₂O₃/CeO₂ Nanocomposites: Effect of Ceria Morphology on CO Oxidation", *Catalysts* 9 (2019) 371. doi:10.3390/catal9040371

Chapter 4 describes ceria's morphological effects on the physicochemical properties and nitrous oxide decomposition (deN₂O) performance of ceria-based cobalt oxide catalysts. In particular, ceria nanoparticles of specific morphology (nanorods, nanopolyhedra, nanocubes) were hydrothermally synthesized and employed as supports for the cobalt oxide phase. The cobalt-ceria catalysts were catalytically evaluated during the deN₂O reaction in the absence and in the presence of oxygen. Once more, the superiority of ceria nanorods, exposing the {100} and {110} crystal facets, was revealed with the addition of cobalt phase greatly enhancing the decomposition of N₂O. Cobalt-ceria nanorods with improved redox and textural properties, along with their abundance in Co²⁺ species, exhibited the best deN₂O performance.

Chapter 4 also focuses on the optimization of the deN₂O performance through the fine-tuning of the local surface chemistry of copper-ceria binary oxides by means of both synthesis procedure and surface promotion. According to the results, highly active and oxygen-tolerant Cu/CeO₂ composites can be obtained through their pre-optimization by co-precipitation and subsequent alkali (Cs) promotion, with the sample of 1.0 at Cs per nm² offering a half-conversion temperature *ca.* 200 °C lower as compared to that of a reference Cu/CeO₂ sample, due mainly to the modifications in the electronic and redox properties induced by the alkali addition. The superior deN₂O performance of the Cs-doped Cu/CeO₂

samples can be attributed to their enhanced reducibility and abundance in partially reduced copper species (Cu^+) stabilized through alkali-aided metal-support interactions.

The following publications were derived from the above-discussed results:

6. **Maria Lykaki**, Eleni Papista, Sónia A. C. Carabineiro, Pedro B. Tavares and Michalis Konsolakis, "Optimization of N_2O decomposition activity of CuO-CeO_2 mixed oxides by means of synthesis procedure and alkali (Cs) promotion", *Catalysis Science & Technology* 8 (2018) 2312–2322. doi: 10.1039/c8cy00316e
7. **Maria Lykaki**, Eleni Papista, Nikolaos Kaklidis, Sónia A. C. Carabineiro and Michalis Konsolakis, "Ceria Nanoparticles' Morphological Effects on the N_2O Decomposition Performance of $\text{Co}_3\text{O}_4/\text{CeO}_2$ Mixed Oxides", *Catalysts* 9 (2019) 233. doi:10.3390/catal9030233

Chapter 5 deals with the impact of ceria's morphology (nanorods and nanocubes) in combination with the effect of active phase nature on the physicochemical properties and the CO_2 hydrogenation performance at atmospheric pressure of ceria-based transition metal catalysts, M/CeO_2 (M: Cu, Co, Fe, Ni). In particular, CO_2 conversion followed the order: $\text{Ni/CeO}_2 > \text{Co/CeO}_2 > \text{Cu/CeO}_2 > \text{Fe/CeO}_2 > \text{CeO}_2$, independently of the support morphology. On the basis of selectivity results, it should be mentioned that bare ceria, Cu/CeO_2 and Fe/CeO_2 samples were very selective for CO production, whereas Co/CeO_2 and Ni/CeO_2 catalysts were highly selective towards methane (CH_4).

The following publications originated from the above results:

8. Michalis Konsolakis, **Maria Lykaki**, Sofia Stefa, Sónia A. C. Carabineiro, Georgios Varvoutis, Eleni Papista and Georgios E. Marnellos, " CO_2 Hydrogenation over Nanoceria-Supported Transition Metal Catalysts: Role of Ceria Morphology (Nanorods versus Nanocubes) and Active Phase Nature (Co versus Cu)", *Nanomaterials* 9 (2019) 1739. doi:10.3390/nano9121739
9. Georgios Varvoutis, **Maria Lykaki**, Sofia Stefa, Eleni Papista, Sónia A. C. Carabineiro, Georgios E. Marnellos and Michalis Konsolakis, "Remarkable efficiency of Ni supported on hydrothermally synthesized CeO_2 nanorods for low-temperature CO_2 hydrogenation to methane", *Catalysis Communications* 142 (2020) 106036. doi: 10.1016/j.catcom.2020.106036

Chapter 6 constitutes the final chapter, summarizing the conclusions derived by the research conducted in the context of the present thesis and offering new perspectives towards the rational design and development of highly active/selective catalytic composites for energy and environmental applications.

ΕΚΤΕΤΑΜΕΝΗ ΣΥΝΟΨΗ & ΔΟΜΗ ΕΡΓΑΣΙΑΣ

Το οξειδίο του δημητρίου ή δημητρία (CeO_2) αποτελεί ένα από τα πλέον χρησιμοποιούμενα υλικά στον τομέα της ετερογενούς κατάλυσης λόγω των μοναδικών οξειδοαναγωγικών του ιδιοτήτων, οι οποίες απορρέουν κυρίως από την ικανότητά του να δεσμεύει/αποδεσμεύει οξυγόνο ανάλογα με το περιβάλλον (οξειδωτικό ή αναγωγικό) της αντίδρασης. Κατά τη διάρκεια της δεκαετίας του '80, η επιτυχής χρήση της δημητρίας στους τριοδικούς καταλυτικούς μετατροπείς οδήγησε στην επακόλουθη εφαρμογή της σε πληθώρα περιβαλλοντικών και ενεργειακών εφαρμογών, οι οποίες συμπεριλαμβάνουν, μεταξύ άλλων, την τεχνολογία των κυψελών καυσίμου, την καταλυτική απομάκρυνση πτητικών οργανικών ενώσεων (VOCs), οξειδίων του αζώτου (NO_x), υποξειδίου του αζώτου (N_2O), κλπ. Επιπλέον, τα οξείδια μετάλλων βασισμένα στα μέταλλα μετάπτωσης, έχουν προσελκύσει ιδιαίτερο ερευνητικό ενδιαφέρον ως προς την αντικατάσταση των σπάνιων και ιδιαίτερα υψηλού κόστους ευγενών μετάλλων. Ιδιαίτερα, ο συνδυασμός της δημητρίας με φθηνά και εν αφθονία μέταλλα μετάπτωσης, όπως Cu, Co, Ni, Fe, μπορεί να οδηγήσει, μέσω κυρίως συνεργιστικών αλληλεπιδράσεων μετάλλου-φορέα, σε σημαντική τροποποίηση των φυσικοχημικών ιδιοτήτων των προς ανάπτυξη υλικών, οι οποίες κατόπιν αντανakλώνται στην καταλυτική συμπεριφορά. Ωστόσο, διάφοροι αλληλοσχετιζόμενοι παράγοντες, όπως η μορφολογία, το μέγεθος, η σύσταση, η χημική κατάσταση, το ηλεκτρονιακό περιβάλλον μπορούν να επηρεάσουν σημαντικά την τοπική επιφανειακή χημεία των μεταλλοξειδίων, καθώς και τις αλληλεπιδράσεις μετάλλου-φορέα επηρεάζοντας σε σημαντικό βαθμό τη μακροσκοπική καταλυτική συμπεριφορά αυτών των πολυ-λειτουργικών υλικών. Επιπρόσθετα, τα υλικά σε επίπεδο νανο-κλίμακας παρουσιάζουν μοναδικά χαρακτηριστικά λόγω του υψηλού λόγου επιφάνειας/όγκου και των ιδιαίτερων ηλεκτρονιακών χαρακτηριστικών των νανο-σωματιδίων, γεγονός που αντανakλάται στις επιφανειακές τους ιδιότητες και την καταλυτική τους απόδοση.

Προς την κατεύθυνση της ανάπτυξης νανο-δομημένων καταλυτικών συστημάτων με προκαθορισμένη επιφανειακή χημεία, οι ερευνητικές προσπάθειες, τα τελευταία χρόνια, έχουν επικεντρωθεί σε δύο κυρίως διαφορετικές προσεγγίσεις, οι οποίες μπορούν να εφαρμοστούν ανεξάρτητα ή εν συνεργεία: (i) εφαρμογή προηγμένων μεθόδων σύνθεσης με σκοπό την ανάπτυξη νανοϋλικών προκαθορισμένης μορφολογίας, (ii) κατάλληλη τροποποίηση των εγγενών χαρακτηριστικών του καταλύτη μέσω της προσθήκης δομικών ή/και επιφανειακών ενισχυτών.

Επί τη βάση της παραπάνω ανάλυσης, στόχος της παρούσας διδακτορικής διατριβής αποτελεί η ανάπτυξη νανο-δομημένων καταλυτικών συστημάτων μετάλλων μετάπτωσης

βασισμένων στη δημητρία, απαλλαγμένων ευγενών μετάλλων, της μορφής M_xO_y/CeO_2 (εφεξής συμβολίζονται ως M/CeO_2 για λόγους σαφήνειας, όπου το M αντιπροσωπεύει τα Cu, Co, Fe, Ni), μέσω προηγμένων μεθόδων σύνθεσης, οι οποίες ωστόσο θα χαρακτηρίζονται από χαμηλό κόστος και απλές διαδικασίες. Συγκεκριμένα, διάφορες μέθοδοι σύνθεσης, όπως θερμική διάσπαση, καταβύθιση, υδροθερμική, υγρός εμποτισμός, χρησιμοποιήθηκαν και μελετήθηκε η επίδρασή τους στα φυσικοχημικά χαρακτηριστικά και την καταλυτική συμπεριφορά (ενεργότητα, εκλεκτικότητα, σταθερότητα) των προς ανάπτυξη υλικών μέσω μιας εκτεταμένης μελέτης χαρακτηρισμού, η οποία περιελάμβανε τόσο *ex situ* όσο και *in situ* τεχνικές, όπως προσρόφηση N_2 στους $-196\text{ }^\circ\text{C}$ (μέθοδος BET), φασματοσκοπία περίθλασης ακτίνων X (XRD), φασματοσκοπία φθορισμού ακτίνων X (XRF), φασματοσκοπία φωτο-ηλεκτρονίων ακτίνων X (XPS), θερμο-προγραμματιζόμενη αναγωγή (TPR), ηλεκτρονική μικροσκοπία σάρωσης/διέλευσης (SEM/TEM) και φασματοσκοπία Raman. Οι κύριες επιδράσεις της κατάλληλης τροποποίησης του μεγέθους, σχήματος και της ηλεκτρονιακής κατάστασης στην κατάλυση διερευνώνται επί τη βάση σημαντικών ετερογενών αντιδράσεων, όπως η οξείδωση του CO , η διάσπαση του υποξειδίου του αζώτου και η υδρογόνωση του CO_2 προς προϊόντα υψηλής προστιθέμενης αξίας. Συγκεκριμένα, η παρούσα διδακτορική διατριβή επικεντρώνεται στους ακόλουθους ερευνητικούς στόχους:

- (i) Επίδραση της μορφολογίας της δημητρίας στις δομικές ατέλειες και την επιφανειακή χημεία,
- (ii) Εξαρτώμενη από τα κρυσταλλογραφικά επίπεδα δραστηριότητα των υποστηριγμένων στη δημητρία καταλυτικών υλικών μετάπτωσης,
- (iii) Κατάλληλη τροποποίηση της τοπικής επιφανειακής χημείας προς την κατεύθυνση της ανάπτυξης καταλυτικών υλικών υψηλής ενεργότητας, εκλεκτικότητας και σταθερότητας για ποικίλες ενεργειακές/περιβαλλοντικές εφαρμογές,
- (iv) Ορθολογικός σχεδιασμός και ανάπτυξη καταλυτικών υλικών χαμηλού κόστους, απαλλαγμένων ευγενών μετάλλων, μέσω προηγμένων μεθόδων σύνθεσης/πρώθησης,
- (v) Εδραίωση αξιόπιστων σχέσεων δομής-δραστηριότητας προς την κατεύθυνση της ανάδειξης σημαντικών δεικτών δραστηριότητας

Επί τη βάση της παραπάνω περιγραφής, η παρούσα διδακτορική διατριβή είναι διαρθρωμένη στα κάτωθι κεφάλαια:

Το **Κεφάλαιο 1** παρουσιάζει τη βιβλιογραφική ανασκόπηση αναφορικά με τις πιο πρόσφατες εξελίξεις στο πεδίο του ορθολογικού σχεδιασμού καταλυτών βασισμένων στη δημητρία, δίνοντας έμφαση στην επίδραση του μεγέθους, του σχήματος και του ηλεκτρονιακού/χημικού περιβάλλοντος στην καταλυτική συμπεριφορά. Συγκεκριμένα, με βάση το καταλυτικό σύστημα Cu/CeO₂, οι κύριες επιδράσεις των προαναφερθέντων παραγόντων σε διάφορες εφαρμογές της ετερογενούς κατάλυσης, όπως η οξείδωση του μονοξειδίου του άνθρακα (CO), η διάσπαση του N₂O, η εκλεκτική οξείδωση του CO (CO-PROX), η αντίδραση μετατόπισης του υδραερίου (WGSR) και η υδρογόνωση του διοξειδίου του άνθρακα (CO₂) προς προϊόντα υψηλής προστιθέμενης αξίας, αναπτύσσονται διεξοδικά. Η παραπάνω έρευνα οδήγησε στη δημοσίευση των ακόλουθων άρθρων ανασκόπησης:

1. Michalis Konsolakis and **Maria Lykaki**, "Recent Advances on the Rational Design of Non-Precious Metal Oxide Catalysts Exemplified by CuO_x/CeO₂ Binary System: Implications of Size, Shape and Electronic Effects on Intrinsic Reactivity and Metal-Support Interactions", *Catalysts* 10 (2020) 160. doi: 10.3390/catal10020160
2. Michalis Konsolakis and **Maria Lykaki**, "Facet-Dependent Reactivity of Ceria Nanoparticles Exemplified by CeO₂-Based Transition Metal Catalysts: A Critical Review", *Catalysts* 11 (2021) 452. doi: 10.3390/catal11040452

Το **Κεφάλαιο 2** αναφέρεται στο πειραματικό μέρος της εργασίας, παρουσιάζοντας τις μεθόδους σύνθεσης που ακολουθήθηκαν για την ανάπτυξη των υλικών, καθώς και τις τεχνικές χαρακτηρισμού και καταλυτικής αποτίμησης.

Στα κεφάλαια 3–5 παρουσιάζονται και αναπτύσσονται τα αποτελέσματα καταλυτικής αξιολόγησης εν παραλλήλω με τις μελέτες χαρακτηρισμού με απώτερο στόχο την εδραίωση ισχυρών σχέσεων δομής-δραστικότητας.

Το **Κεφάλαιο 3** περιγράφει την επίδραση των παραμέτρων σύνθεσης στις ιδιότητες στερεάς κατάστασης και την καταλυτική συμπεριφορά, ως προς την οξείδωση του CO, των καθαρών υποστρωμάτων δημητρίας. Πιο συγκεκριμένα, τρεις διαφορετικές μέθοδοι σύνθεσης (θερμική διάσπαση, καταβύθιση και η υδροθερμική μέθοδος χαμηλής και υψηλής συγκέντρωσης NaOH), οι οποίες χαρακτηρίζονται από χαμηλό κόστος και σύντομους χρόνους σύνθεσης, χρησιμοποιήθηκαν για τη σύνθεση των υλικών δημητρίας. Η υδροθερμική μέθοδος βρέθηκε ότι οδηγεί σε νανο-σωματίδια δημητρίας συγκεκριμένης μορφολογίας (νανο-ράβδοι, νανο-πολύεδρα, νανο-κύβοι) και μεγάλης ειδικής επιφάνειας (> 90 m² g⁻¹), με τις νανο-ράβδους να παρουσιάζουν τη βέλτιστη κινητικότητα

ευμετάβλητου πλεγματικού οξυγόνου, οδηγώντας σε ενισχυμένη αναγωγική ικανότητα και καταλυτική απόδοση.

Επιπλέον, το **Κεφάλαιο 3** παρουσιάζει την επίδραση της μορφολογίας του φορέα δημητριάς (κύβιοι, πολύεδρα, ράβδοι) στα φυσικοχημικά χαρακτηριστικά και στην καταλυτική συμπεριφορά υποστηριγμένων μετάλλων μετάπτωσης, ήτοι M/CeO_2 (M : Cu, Fe). Η μορφολογία του φορέα βρέθηκε να επηρεάζει σημαντικά τις φυσικοχημικές ιδιότητες των μικτών οξειδίων με σημαντική επίδραση στην καταλυτική απόδοση. Αναδείχθηκε ότι η μορφολογία της δημητριάς κι όχι τα χαρακτηριστικά υφής/δομής είναι ο παράγοντας που επηρεάζει σε σημαντικό βαθμό την αναγωγική ικανότητα και την κινητικότητα οξυγόνου των μικτών οξειδίων, ακολουθώντας τη σειρά: νανο-ράβδοι > νανο-πολύεδρα > νανο-κύβιοι, με τις νανο-ράβδους δημητριάς να παρουσιάζουν αφθονία σε δομικές ατέλειες και κενές θέσεις οξυγόνου. Η προσθήκη του μετάλλου (χαλκός ή σίδηρος) στα καθαρά υποστρώματα δημητριάς βελτιώνει θεαματικά την απόδοση οξείδωσης του CO, χωρίς ωστόσο να επηρεάζει τη σειρά δραστηριότητας των καθαρών φορέων, δηλαδή νανο-ράβδοι > νανο-πολύεδρα > νανο-κύβιοι, καταδεικνύοντας το ρόλο κλειδί της μορφολογίας του φορέα. Το δείγμα χαλκού-δημητριάς νανο-ραβδοειδούς μορφολογίας βρέθηκε να επιδεικνύει πλήρη μετατροπή του CO σε πολύ χαμηλή θερμοκρασία (~100 °C), όντας από τις χαμηλότερες που έχουν καταγραφεί για υποστηριγμένους καταλύτες χαλκού. Κατά παρόμοιο τρόπο, οι νανο-ράβδοι σιδήρου-δημητριάς παρουσιάζουν τη βέλτιστη καταλυτική συμπεριφορά, επιδεικνύοντας ωστόσο πλήρη μετατροπή του CO σε υψηλότερες θερμοκρασίες (~250 °C) εν συγκρίσει με τους αντίστοιχους καταλύτες χαλκού. Το τελευταίο αναδεικνύει το σημαντικό ρόλο και της φύσης της ενεργού φάσης σε συνδυασμό με τη μορφολογία του φορέα. Επί τη βάση ενός μηχανισμού τύπου Mars-van Krevelen, αναδείχθηκαν στενές αλληλοσυσχετίσεις ανάμεσα στην καταλυτική συμπεριφορά και τις παρακάτω παραμέτρους: i) την αφθονία σε ασθενώς συνδεδεμένα είδη οξυγόνου, ii) τον σχετικό πληθυσμό σε οξειδοαναγωγικά ζεύγη Cu^+/Ce^{3+} , iii) την σχετική αφθονία σε ατέλειες και κενές θέσεις οξυγόνου.

Τα αποτελέσματα του κεφαλαίου αυτού δημοσιεύτηκαν στα ακόλουθα επιστημονικά περιοδικά:

3. **Maria Lykaki, Eleni Pachatouridou, Eleni Ilioroulou, Sónia A. C. Carabineiro and Michalis Konsolakis, "Impact of the synthesis parameters on the solid state properties and the CO oxidation performance of ceria nanoparticles", RSC Advances 7 (2017) 6160–6169. doi: 10.1039/c6ra26712b**

4. **Maria Lykaki**, Eleni Pachatouridou, Sónia A. C. Carabineiro, Eleni Iliopoulou, Chrysanthi Andriopoulou, N. Kallithrakas-Kontos, Soghomon Boghosian, Michalis Konsolakis, "Ceria nanoparticles shape effects on the structural defects and surface chemistry: Implications in CO oxidation by Cu/CeO₂ catalysts", *Applied Catalysis B: Environmental* 230 (2018) 18–28. doi: 10.1016/j.apcatb.2018.02.035
5. **Maria Lykaki**, Sofia Stefa, Sónia A. C. Carabineiro, Pavlos K. Pandis, Vassilis N. Stathopoulos and Michalis Konsolakis, "Facet-Dependent Reactivity of Fe₂O₃/CeO₂ Nanocomposites: Effect of Ceria Morphology on CO Oxidation", *Catalysts* 9 (2019) 371. doi:10.3390/catal9040371

Το **Κεφάλαιο 4** περιγράφει την επίδραση της μορφολογίας του φορέα δημητριάς στις φυσικοχημικές ιδιότητες και στην καταλυτική συμπεριφορά ως προς τη διάσπαση του N₂O των μικτών οξειδίων κοβαλτίου-δημητριάς. Συγκεκριμένα, νανο-σωματίδια δημητριάς συγκεκριμένης μορφολογίας (νανο-ράβδοι, νανο-πολύεδρα, νανο-κύβοι) παρασκευάστηκαν μέσω της υδροθερμικής μεθόδου και χρησιμοποιήθηκαν ως υποστρώματα για το οξείδιο του κοβαλτίου. Οι καταλύτες κοβαλτίου-δημητριάς αποτιμήθηκαν καταλυτικά κατά την αντίδραση διάσπασης του N₂O, απουσία και παρουσία οξυγόνου. Η ανωτερότητα των νανο-ράβδων δημητριάς στις οποίες εκτίθενται τα κρυσταλλογραφικά επίπεδα {100} και {110}, αναδείχθηκε και κατά την εν λόγω αντίδραση. Οι νανο-ράβδοι κοβαλτίου-δημητριάς με τα βέλτιστα χαρακτηριστικά αναγωγής και υφής, καθώς και με τη μεγαλύτερη συγκέντρωση σε είδη Co²⁺, παρουσιάζουν την υψηλότερη δραστηριότητα ως τη διάσπαση του N₂O.

Το **Κεφάλαιο 4**, επίσης, επικεντρώνεται στη βελτιστοποίηση της διεργασίας διάσπασης του N₂O σε μικτά οξείδια χαλκού-δημητριάς, μέσω της διαδοχικής εφαρμογής προηγμένων μεθόδων σύνθεσης και επιφανειακής προώθησης. Αξιοσημείωτα, η επιφανειακή ενίσχυση με αλκάλια (Cs) σε προ-βελτιστοποιημένα δείγματα Cu/CeO₂ μέσω της μεθόδου σύνθεσης (συγκαταβύθιση) οδήγησε στην περαιτέρω βελτίωση της καταλυτικής δραστηριότητας, αναδεικνύοντας την αποτελεσματικότητα της προτεινόμενης σχεδιαστικής προσέγγισης. Ειδικότερα, τα δείγματα Cu/CeO₂ παρασκευασμένα με συγκαταβύθιση και επακόλουθα ενισχυμένα με 1.0 at Cs/nm² επέδειξαν θερμοκρασία ημίσειας μετατροπής περίπου 200 °C χαμηλότερη συγκριτικά με το δείγμα αναφοράς Cu/CeO₂. Η ανωτερότητα των προωθημένων με Cs δειγμάτων Cu/CeO₂ μπορεί να αποδοθεί στη βελτιωμένη αναγωγική τους ικανότητα και στην αφθονία τους σε μερικώς ανηγμένα είδη χαλκού (Cu⁺), τα οποία σταθεροποιούνται μέσω των υποβοηθούμενων απ' το αλκάλιο αλληλεπιδράσεων μετάλλου-φορέα.

Τα αποτελέσματα του κεφαλαίου αυτού δημοσιεύτηκαν στα ακόλουθα επιστημονικά περιοδικά:

6. **Maria Lykaki**, Eleni Papista, Sónia A. C. Carabineiro, Pedro B. Tavares and Michalis Konsolakis, "Optimization of N_2O decomposition activity of $CuO-CeO_2$ mixed oxides by means of synthesis procedure and alkali (Cs) promotion", *Catalysis Science & Technology* 8 (2018) 2312–2322. doi: 10.1039/c8cy00316e
7. **Maria Lykaki**, Eleni Papista, Nikolaos Kaklidis, Sónia A. C. Carabineiro and Michalis Konsolakis, "Ceria Nanoparticles' Morphological Effects on the N_2O Decomposition Performance of Co_3O_4/CeO_2 Mixed Oxides", *Catalysts* 9 (2019) 233. doi:10.3390/catal9030233

Το **Κεφάλαιο 5** παρουσιάζει την επίδραση της μορφολογίας του φορέα δημητριάς (νανο-ράβδοι και νανο-κύβοι) σε συνδυασμό με τη φύση της ενεργού φάσης στις φυσικοχημικές ιδιότητες και στην καταλυτική συμπεριφορά, ως προς την αντίδραση υδρογόνωσης του CO_2 σε ατμοσφαιρική πίεση, σε καταλύτες μετάλλων μετάπτωσης υποστηριγμένου στη δημητρία, M/CeO_2 (M: Cu, Co, Fe, Ni). Βρέθηκε ότι η μετατροπή του CO_2 ακολουθεί την εξής σειρά: $Ni/CeO_2 > Co/CeO_2 > Cu/CeO_2 > Fe/CeO_2 > CeO_2$, ανεξάρτητα από τη μορφολογία του φορέα. Επί τη βάση των αποτελεσμάτων εκλεκτικότητας, διαπιστώθηκε ότι οι καταλύτες καθαρής δημητριάς, Cu/CeO_2 και Fe/CeO_2 είναι εκλεκτικοί ως προς την παραγωγή CO , ενώ οι καταλύτες Co/CeO_2 και Ni/CeO_2 είναι ιδιαίτερα εκλεκτικοί ως προς το μεθάνιο (CH_4). Ιδιαίτερος, ο συνδυασμός του νικελίου με τις νανο-ράβδους δημητριάς ευνοεί σημαντικά την αντίδραση μεθανίωσης ενώ η αντίδραση της αντίστροφης μετατόπισης υδραερίου (rWGS) ευνοείται στις νανο-ράβδους χαλκού-δημητριάς. Και στις δυο περιπτώσεις επιτεύχθηκαν αποδόσεις πλησίον των θερμοδυναμικών ορίων καταδεικνύοντας την ανωτερότητα των προς ανάπτυξη υλικών.

Τα αποτελέσματα του κεφαλαίου αυτού δημοσιεύτηκαν στα ακόλουθα επιστημονικά περιοδικά:

8. Michalis Konsolakis, **Maria Lykaki**, Sofia Stefa, Sónia A. C. Carabineiro, Georgios Varvoutis, Eleni Papista and Georgios E. Marnellos, " CO_2 Hydrogenation over Nanoceria-Supported Transition Metal Catalysts: Role of Ceria Morphology (Nanorods versus Nanocubes) and Active Phase Nature (Co versus Cu)", *Nanomaterials* 9 (2019) 1739. doi:10.3390/nano9121739
9. Georgios Varvoutis, **Maria Lykaki**, Sofia Stefa, Eleni Papista, Sónia A. C. Carabineiro, Georgios E. Marnellos and Michalis Konsolakis, "Remarkable efficiency of Ni supported on hydrothermally synthesized CeO_2 nanorods for low-temperature CO_2

hydrogenation to methane", Catalysis Communications 142 (2020) 106036. doi: 10.1016/j.catcom.2020.106036

Το **Κεφάλαιο 6** αποτελεί το τελευταίο κεφάλαιο, το οποίο συνοψίζει τα συμπεράσματα της εκπονηθείσας έρευνας, στο πλαίσιο της παρούσας διδακτορικής διατριβής, προτείνοντας συγχρόνως, κατευθύνσεις για μελλοντική έρευνα ως προς τον ορθολογικό σχεδιασμό και την ανάπτυξη καταλυτικών υλικών υψηλής ενεργότητας/εκλεκτικότητας για ενεργειακές και περιβαλλοντικές εφαρμογές.

TABLE OF CONTENTS

SHORT ABSTRACT	i
ΣΥΝΤΟΜΗ ΠΕΡΙΛΗΨΗ	iii
EXTENDED SYNOPSIS & THESIS STRUCTURE	vi
ΕΚΤΕΤΑΜΕΝΗ ΣΥΝΟΨΗ & ΔΟΜΗ ΕΡΓΑΣΙΑΣ	xi
CHAPTER 1	1–76
Rational Design and Optimization Strategies of Non-Precious Metal Oxide Catalysts:	
Literature Review	1
INTRODUCTION	2
1.1. FINE-TUNING OF METAL OXIDES (MOs)	5
1.1.1. Size Effects	6
1.1.2. Shape Effects	8
1.1.3. Electronic Effects	11
1.1.4. Chemical Modifiers	15
1.1.5. Pretreatment Effects	16
1.2. IMPLICATIONS OF MOs FINE-TUNING IN CATALYSIS EXEMPLIFIED BY CuO_x/CeO₂ BINARY SYSTEM	18
1.2.1. CO Oxidation	19
1.2.2. N ₂ O Decomposition	25
1.2.3. Preferential Oxidation of CO (CO-PROX)	28
1.2.4. Water-Gas Shift Reaction (WGSR)	36
1.2.5. CO ₂ Hydrogenation	40
1.3. CONCLUDING REMARKS	45
CHAPTER 2	77–96
Materials Synthesis and Characterization Studies	77
2.1. MATERIALS SYNTHESIS	78
2.1.1. Synthesis of Bare Ceria Nanoparticles by Different Methods	79
2.1.2. Synthesis of Ceria-Based Transition Metal Catalysts through the Wet Impregnation Method	82
2.1.3. Synthesis of Surface (Cs)-Promoted Ceria-Based Copper Catalysts	83
2.2. CHARACTERIZATION TECHNIQUES	87

2.2.1. Elemental Analysis (XRF, ICP)	87
2.2.2. Textural and Structural Characterization (BET and XRD)	88
2.2.3. Morphological Characterization (TEM, SEM-EDS)	88
2.2.4. Redox Characterization (H ₂ -TPR)	89
2.2.5. Surface Characterization (XPS)	89
2.2.6. Structure of anionic sub-lattice and redox properties (Raman)	89
2.3. CATALYTIC EVALUATION STUDIES	91
2.3.1. CO Oxidation	92
2.3.2. N ₂ O Decomposition	93
2.3.3. Hydrogenation of CO ₂ to Methane (CH ₄) or Carbon Monoxide (CO)	94
CHAPTER 3	97–154
Effect of Synthesis Procedure and Ceria's Shape on the Structural Defects and Surface Chemistry of Ceria-Based Transition Metal Catalysts M/CeO₂ (M: Cu, Fe): Implications in CO Oxidation	97
INTRODUCTION	98
3.1. EXPERIMENTAL	101
3.1.1. Materials Synthesis	101
3.1.2. Materials Characterization	101
3.2. CHARACTERIZATION STUDIES OF BARE CERIA OXIDES	103
3.2.1. Textural and Structural Characterization (BET and XRD)	103
3.2.2. Morphological Characterization (SEM/TEM)	106
3.2.3. Redox Properties (H ₂ -TPR)	107
3.2.4. Surface Analysis (XPS)	109
3.2.5. <i>In situ</i> Raman Spectroscopy	111
3.3. CHARACTERIZATION STUDIES OF CERIA-BASED TRANSITION METAL CATALYSTS	116
3.3.1. Textural and Structural Characterization (BET and XRD)	116
3.3.2. Redox Properties (H ₂ -TPR)	119
3.3.3. Surface Analysis (XPS)	122
3.3.4. Morphological Characterization (TEM)	126
3.4. IMPLICATIONS IN CO OXIDATION REACTION	127
3.4.1. CO Oxidation Performance of Bare Ceria Oxides	127
3.4.2. CO Oxidation Performance of Ceria-Based Transition Metal Catalysts	130
3.5. CONCLUDING REMARKS	140

CHAPTER 4	155–202
Effects of Ceria's Morphology or Surface Promotion (Cs) on the Physicochemical Properties of Ceria-Based Transition Metal Catalysts M/CeO₂ (M: Co or Cu): Implications in N₂O Decomposition	155
INTRODUCTION	156
4.1. EXPERIMENTAL	159
4.1.1. Materials Synthesis	159
4.1.2. Materials Characterization	159
4.2. CHARACTERIZATION STUDIES OF Co/CeO ₂ MIXED OXIDES	160
4.2.1. Textural and Structural Characterization (BET and XRD)	160
4.2.2. Morphological Characterization (TEM)	162
4.2.3. Redox Properties (H ₂ -TPR)	163
4.2.4. Surface Analysis (XPS)	165
4.3 CHARACTERIZATION STUDIES OF Cs-PROMOTED Cu/CeO ₂ MIXED OXIDES	168
4.3.1. Textural and Structural Characterization (BET and XRD)	168
4.3.2. Redox Properties (H ₂ -TPR)	170
4.3.3. Surface Analysis (XPS)	173
4.4. IMPLICATIONS IN N ₂ O DECOMPOSITION REACTION	178
4.4.1. N ₂ O Decomposition Performance of Co/CeO ₂ Mixed Oxides	178
4.4.2. N ₂ O Decomposition Performance of Cs-promoted Cu/CeO ₂ Mixed Oxides	182
4.5. CONCLUDING REMARKS	188
CHAPTER 5	203–228
Effects of Ceria's Morphology and Active Phase Nature over Ceria-Based Transition Metal Catalysts M/CeO₂ (M: Fe, Co, Cu, Ni): Implications in CO₂ Hydrogenation	203
INTRODUCTION	204
5.1. EXPERIMENTAL	207
5.1.1. Materials Synthesis	207
5.1.2. Materials Characterization	207
5.2. CHARACTERIZATION STUDIES OF M/CeO ₂ MIXED OXIDES (M: Fe, Co, Cu, Ni)	208
5.2.1. Textural and Structural Characterization (BET and XRD)	208
5.2.2. Morphological Characterization (TEM)	209
5.2.3. Redox Properties (H ₂ -TPR)	210
5.2.4. Surface Analysis (XPS)	212

5.3. IMPLICATIONS IN CO ₂ HYDROGENATION REACTION	213
5.4. CONCLUDING REMARKS	217
CHAPTER 6	229–233
General Conclusions and Future Research Outlook	229
GENERAL CONCLUSIONS	230
FUTURE RESEARCH OUTLOOK	232
Curriculum Vitae	234–238

LIST OF FIGURES

Figure 1.1.	Relative comparison of noble metal and copper metal prices over a five-year period.	3
Figure 1.2.	Schematic illustration of metal oxides' (MOs) fine-tuning by adjusting their size, shape, composition and electronic/chemical state.	5
Figure 1.3.	Turnover frequency (TOF) variation with fraction of atoms exposed and particle size.	8
Figure 1.4.	Model shapes illustrating an anisotropic growth process starting from a truncated cuboctahedron shape. Protecting the {111} facets using a capping agent results in the growth of {100} facets until they disappear and only {111} facets remain on the surface (octahedral shape). The opposite would result in cubic NPs with only {100} facets.	9
Figure 1.5.	(a) Unit cell of the CeO ₂ structure. (b-d) The (100) [or (200)], (110), and (111) planes of the CeO ₂ structure.	10
Figure 1.6.	Correlation of half-conversion temperature (T ₅₀) with the work function of alkali promoted Co ₃ O ₄ . Reaction conditions: 5.0% N ₂ O; m _{cat} = 300 mg; GHSV = 7000 h ⁻¹ ; alkali coverage = ~2 at/nm ² .	12
Figure 1.7.	(a) The half-conversion temperature of N ₂ O (T ₅₀), (b) apparent activation energy (E _a) and (c) work function changes (ΔΦ) as a function of potassium loading (Θ _K) introduced from K ₂ CO ₃ and (c insert) KOH precursor.	13
Figure 1.8.	Surface energy variation versus the surface atomic ratio of K to Fe.	14
Figure 1.9.	Representative nanocarbons used for the preparation of catalytic composites.	15
Figure 1.10.	CO oxidation on annealed 3 nm Cu _{0.1} Ce _{0.9} O _{2-x} , 3 nm CeO ₂ and commercial 5 μm CeO ₂ (Sigma-Aldrich). (A) "Light off" curves and (B) area-normalized Arrhenius plots, measured in 1.0% CO, 2.5% O ₂ balanced in He at a flow rate of 1300 mL min ⁻¹ g _{cat} ⁻¹ for 20 mg catalyst loadings.	21
Figure 1.11.	The activity of nanoshaped CuO _x /CeO ₂ catalysts measured at T = 375 °C.	27
Figure 1.12.	Plots of the number of oxygen vacancies and reduced copper species for the CuO/CeO ₂ catalysts with different support shapes.	32
Figure 1.13.	T ₅₀ vs. (i) shift of the main peak (F _{2g} Raman vibration mode) of fluorite CeO ₂ and (ii) surface concentration of Ce ³⁺ and oxygen vacancies determined via XPS analysis.	35

Figure 1.14.	Low-temperature WGS reaction over the Cu/CeO ₂ catalysts. CO conversion as a function of the copper content in the respect catalysts. Reaction conditions: 1.0 vol.% CO/3.0 vol.% H ₂ O/He, 40,000 h ⁻¹ , 200 °C.	39
Figure 1.15.	Mole ratio of Ce ³⁺ and Cu ⁺ over the reduced Cu/CeO ₂ catalysts as a function of Cu content.	43
Figure 2.1.	Bare ceria nanoparticles prepared by thermal decomposition.	79
Figure 2.2.	Bare ceria nanoparticles prepared by the precipitation method.	80
Figure 2.3.	Hydrothermal synthesis of bare ceria nanoparticles of different morphology (polyhedra, rods, cubes).	81
Figure 2.4.	Synthesis of ceria-based transition metal catalysts M/CeO ₂ -NX (M: Cu, Co, Fe, Ni and NX: NP, NR, NC) through the wet impregnation method.	82
Figure 2.5.	(a) Synthesis of Cu/CeO ₂ mixed oxides through the co-precipitation method, (b) synthesis of Cs-doped Cu/CeO ₂ samples through the wet impregnation method.	84
Figure 3.1.	BET surface area as a function of average grain size (D _{BET}) for ceria samples.	104
Figure 3.2.	(a) BJH desorption pore size distribution and (b) adsorption–desorption isotherms of as-prepared ceria samples.	105
Figure 3.3.	XRD patterns of ceria samples.	106
Figure 3.4.	(a, c, e, g, i) SEM and (b, d, f, h, j) TEM images of ceria samples: (a, b) CeO ₂ -D, (c, d) CeO ₂ -P, (e, f) CeO ₂ -NP, (g, h) CeO ₂ -NR, (i, j) CeO ₂ -NC.	107
Figure 3.5.	H ₂ -TPR profiles of ceria samples.	108
Figure 3.6.	XPS spectra of (a) Ce 3d and (b) O 1s region of ceria samples.	110
Figure 3.7.	(a) <i>In situ</i> Raman spectra obtained for ceria samples prepared by the hydrothermal method (NR, NP and NC as indicated by each spectrum), (b) I _D /I _{F_{2g}} intensity ratio. Laser wavelength, λ ₀ = 491.5 nm; laser power, w = 25 mW; spectral slit width, 6 cm ⁻¹ .	112
Figure 3.8.	<i>In situ</i> sequential Raman spectra obtained for CeO ₂ -NR: (a) under flowing 20% O ₂ /He; (b) under flowing 5 % H ₂ /He. Insets: (A) trace (c) obtained after subtracting trace (b) from trace (a); (B) focus on the spectral region of the F _{2g} band.	114
Figure 3.9.	<i>In situ</i> sequential Raman spectra obtained for CeO ₂ -NP: (a) under flowing 20% O ₂ /He; (b) under flowing 5% H ₂ /He. Insets: (A) trace (c) obtained after subtracting trace (b) from trace (a); (B) focus on the spectral region of the F _{2g} band.	114

Figure 3.10.	<i>In situ</i> sequential Raman spectra obtained for CeO ₂ -NC: (a) under flowing 20% O ₂ /He; (b) under flowing 5% H ₂ /He. Insets: (A) trace (c) obtained after subtracting trace (b) from trace (a); (B) Focus on the spectral region of the F _{2g} band.	115
Figure 3.11.	(a) BJH desorption pore size distribution (PSD) and (b) adsorption-desorption isotherms of Cu/CeO ₂ samples of different morphology (NP-nanopolyhedra, NR-nanorods, NC-nanocubes).	117
Figure 3.12.	XRD patterns of Cu/CeO ₂ samples of different morphology (NP-nanopolyhedra, NR-nanorods, NC-nanocubes).	118
Figure 3.13.	H ₂ -TPR profiles of bare CuO and Cu/CeO ₂ samples.	120
Figure 3.14.	XPS spectra of (a) Ce 3d, (b) O 1s and (c) Cu 2p region of bare CuO and Cu/CeO ₂ samples.	124
Figure 3.15.	TEM images of the samples: (a) Cu/CeO ₂ -NR, (b) Cu/CeO ₂ -NP, (c) Cu/CeO ₂ -NC, (d) Fe/CeO ₂ -NR, (e) Fe/CeO ₂ -NP and (f) Fe/CeO ₂ -NC.	126
Figure 3.16.	(a) CO conversion as a function of temperature and (b) the corresponding Arrhenius plots for ceria samples.	128
Figure 3.17.	CO conversion as a function of temperature for Ceria, Cu/Ceria and Fe/Ceria samples of different morphology (NR, NC and NP, as indicated in each curve). Reaction conditions: 2000 ppm CO, 1 vol.% O ₂ , GHSV = 39,000 h ⁻¹ .	131
Figure 3.18.	Effect of time-on-stream (TOS) on the CO oxidation performance of optimum copper-ceria catalyst of nanorod-shaped morphology. Reaction conditions: 2000 ppm CO, 1 vol.% O ₂ , GHSV = 39,000 h ⁻¹ .	132
Figure 3.19.	Comparison among bare ceria, copper-ceria, iron-ceria and a noble metal catalyst, in terms of half-conversion temperature (T ₅₀) for CO oxidation. Reaction conditions: 2000 ppm CO, 1 vol.% O ₂ , GHSV = 39,000 h ⁻¹ .	133
Figure 3.20.	Schematic illustration of CO oxidation mechanism on Cu/CeO ₂ catalysts.	134
Figure 3.21.	(a) Relationship between the half-conversion temperature (T ₅₀) and the Cu ⁺ percentage derived by XPS for Cu/CeO ₂ samples. (b) Relationship between the half-conversion temperature (T ₅₀) and the surface-to-bulk oxygen ratio (O _s /O _b) derived by TPR analysis for Fe/CeO ₂ samples.	136
Figure 3.22.	Relationship between the CO oxidation performance (r _{CO} , nmol s ⁻¹ g ⁻¹) of Cu/CeO ₂ samples and the oxygen storage capacity (OSC, mmol O ₂ g ⁻¹) as well as the abundance in oxygen vacancies (in terms of $\frac{I_D}{I_{F_{2g}}}$ ratio) of ceria nanorods (NR), nanopolyhedra (NP) and nanocubes (NC).	137

Figure 3.23.	Arrhenius plots for CO conversion as a function of temperature for Ceria and Fe/Ceria samples of different morphology (NR, NC and NP, as indicated). Reaction conditions: 2000 ppm CO, 1 vol.% O ₂ , GHSV = 40,000 h ⁻¹ .	138
Figure 4.1.	(a) The BJH (Barrett–Joyner–Halenda) desorption pore size distribution (PSD) and (b) the adsorption–desorption isotherms of Co/CeO ₂ samples.	161
Figure 4.2.	The XRD patterns of Co/CeO ₂ samples.	162
Figure 4.3.	TEM images of the samples: (a) CeO ₂ -NR, (b) CeO ₂ -NP, (c) CeO ₂ -NC, (d) Co/CeO ₂ -NR, (e) Co/CeO ₂ -NP and (f) Co/CeO ₂ -NC.	163
Figure 4.4.	H ₂ -TPR profiles of pure Co ₃ O ₄ and Co/CeO ₂ samples.	164
Figure 4.5.	XPS spectra of (a) Ce 3d and (b) O 1s of bare CeO ₂ and Co/CeO ₂ samples.	166
Figure 4.6.	(a) Co 2p XPS spectra of Co ₃ O ₄ and Co ₃ O ₄ /CeO ₂ samples, (b) Magnification of the Co 2p _{1/2} peak in the Co/CeO ₂ -NX (NX: NP, NR, NC) samples.	167
Figure 4.7.	Differential pore size distribution (PSD) curves of Cs-doped Cu/CeO ₂ mixed oxides.	169
Figure 4.8.	XRD patterns of Cs-doped Cu/CeO ₂ mixed oxides.	170
Figure 4.9.	H ₂ -TPR profiles of Cs-doped Cu/CeO ₂ mixed oxides.	171
Figure 4.10.	XPS spectra of (a) Ce 3d and (b) O 1s of Cs-doped Cu/CeO ₂ samples.	174
Figure 4.11.	XPS Cu 2p spectra of Cs-doped Cu/CeO ₂ samples.	176
Figure 4.12.	XPS Cs 3d spectra of Cs-doped Cu/CeO ₂ samples.	177
Figure 4.13.	N ₂ O conversion as a function of temperature for bare CeO ₂ and Co/CeO ₂ samples of different morphology (a) in the absence and (b) in the presence of oxygen. Reaction conditions: 1000 ppm N ₂ O, 0 or 2 vol.% O ₂ , GHSV = 40,000 h ⁻¹ .	179
Figure 4.14.	Half-conversion temperature (T ₅₀) as a function of the TPR surface-to-bulk oxygen ratio (O _s /O _b).	180
Figure 4.15.	N ₂ O conversion profiles of Cs-doped Cu/CeO ₂ samples (a) in the absence and (b) in the presence of oxygen. Reaction conditions: 1000 ppmv N ₂ O, 0 or 2.0 v/v% O ₂ balanced with He; GHSV = 40,000 h ⁻¹ .	183
Figure 4.16.	Effect of GHSV on the deN ₂ O performance of optimally promoted Cs-doped Cu/CeO ₂ sample (CsCuCe-1.0). Reaction conditions: 1000 ppmv N ₂ O balanced with He; GHSV = 40,000 h ⁻¹ .	184
Figure 4.17.	Effect of time-on-stream (TOS) on the deN ₂ O performance of optimally promoted Cs-doped Cu/CeO ₂ sample (CsCuCe-1.0) in the presence of	

	oxygen. Reaction conditions: 1000 ppmv N ₂ O, 2.0 v/v% O ₂ balanced with He; GHSV = 40,000 h ⁻¹ .	185
Figure 4.18.	Effect of synthesis procedure and alkali promotion on the deN ₂ O performance of Cu/CeO ₂ mixed oxides. Reaction conditions: 1000 ppmv N ₂ O balanced with He; GHSV = 40,000 h ⁻¹ .	186
Figure 5.1.	XRD patterns of as-prepared samples of nanorod-like (NR) and nanocubic (NC) morphology.	209
Figure 5.2.	TEM images of as-prepared samples of nanorod-like (NR) and nanocubic (NC) morphology: (a) CeO ₂ -NR, (b) CeO ₂ -NC, (c) Co/CeO ₂ -NR, (d) Co/CeO ₂ -NC, (e) Cu/CeO ₂ -NR, (f) Cu/CeO ₂ -NC, (g) Fe/CeO ₂ -NR, (h) Fe/CeO ₂ -NC, (i) Ni/CeO ₂ -NR, (j) Ni/CeO ₂ -NC.	210
Figure 5.3.	H ₂ -TPR profiles of (a) bare ceria and (b) ceria-supported transition metal (Co, Cu, Ni) samples of nanorod-like (NR) and nanocubic (NC) morphology.	212
Figure 5.4.	XPS Ce 3d spectra of as-prepared and reduced bare CeO ₂ and M/CeO ₂ samples of rod-like morphology.	213
Figure 5.5.	Experimental (solid lines) and theoretical (dotted and dashed lines) CO ₂ conversion profiles for commercial CeO ₂ , bare ceria-NX and M/CeO ₂ -NX samples in CO ₂ hydrogenation reaction. Reaction conditions: F = 100 cm ³ /min, GHSV = 20,000 h ⁻¹ , H ₂ :CO ₂ = 9:1, P = 1 atm.	214
Figure 5.6.	Selectivity to CO (a) and CH ₄ (b) as a function of temperature for all samples in the CO ₂ hydrogenation reaction. Reaction conditions: F = 100 cm ³ /min, GHSV = 20,000 h ⁻¹ , H ₂ :CO ₂ = 9:1, P = 1 atm.	215

LIST OF IMAGES

Image 2.1.	From left to right: KERN PNJ precision balance, VELR Scientifica heating magnetic stirrer, WTW pH meter 3110, Rephile Direct–Pure adept ultrapure water system.	78
Image 2.2.	The furnaces used for the aging and calcination of as-prepared materials (Termansys–left, Binder–right).	78
Image 2.3.	The centrifuges used for the recovery of the solid products and the washing of the obtained materials with double deionized water and ethanol (Eppendorf centrifuge 5804–left, MSE Mistral 2000–right).	79
Image 2.4.	Automated system of catalytic experiments: (a) Gas Chromatograph AGILENT 7820A, (b) Mass flow controllers, (c) Flow chart of the catalytic unit system.	91

LIST OF TABLES

Table 1.1.	Indicative studies towards adjusting the CO oxidation performance of CuO _x /CeO ₂ oxides.	23
Table 1.2.	Indicative studies followed to adjust the deN ₂ O performance of CuO _x /CeO ₂ oxides.	26
Table 1.3.	Indicative studies towards adjusting the CO preferential oxidation performance of CuO _x /CeO ₂ oxides.	29
Table 1.4.	Indicative studies towards adjusting the WGSR performance of CuO _x /CeO ₂ oxides.	37
Table 1.5.	Indicative studies towards adjusting the CO ₂ conversion to methanol of CuO _x /CeO ₂ oxides.	42
Table 2.1.	The catalytic materials developed/used in the present thesis.	85
Table 3.1.	Textural and structural characteristics of ceria samples.	103
Table 3.2.	Redox characteristics of ceria samples.	108
Table 3.3.	XPS results for ceria samples.	111
Table 3.4.	Textural and structural characteristics of Cu/CeO ₂ and Fe/CeO ₂ samples.	116
Table 3.5.	Redox characteristics of Cu/CeO ₂ and Fe/CeO ₂ samples.	121
Table 3.6.	XPS results for Cu/CeO ₂ and Fe/CeO ₂ samples.	125
Table 3.7.	Kinetics parameters obtained by Arrhenius equation.	128
Table 3.8.	Conversion performance and specific activity of Cu/Ceria and Fe/Ceria samples.	137
Table 3.9.	Activation Energies (E _a) for the CO oxidation reaction over bare CeO ₂ and Fe/CeO ₂ samples.	139
Table 4.1.	Textural and structural properties of Co/CeO ₂ samples.	160
Table 4.2.	Redox properties of Co/CeO ₂ samples.	164
Table 4.3.	XPS results of bare CeO ₂ and Co/CeO ₂ samples.	166
Table 4.4.	Textural and structural characteristics of Cs-doped Cu/CeO ₂ mixed oxides.	168
Table 4.5.	Redox characteristics of the Cs-doped Cu/CeO ₂ samples.	172
Table 4.6.	Surface characteristics of the Cs-doped Cu/CeO ₂ samples.	175
Table 4.7.	N ₂ O conversion and specific activity of Co/CeO ₂ samples at 420 °C; Reaction conditions: 1000 ppm N ₂ O, 0 or 2 vol.% O ₂ , GHSV = 40,000 h ⁻¹ .	181
Table 4.8.	N ₂ O conversion performance of as-prepared samples in comparison to those reported in the literature.	187
Table 5.1.	Textural, structural and redox properties of as-prepared samples.	208

CHAPTER 1

Rational Design and Optimization Strategies of Non-Precious Metal Oxide Catalysts: Literature Review

Chapter 1 aims at providing the most recent advances on the rational design of MOs, *i.e.*, the general optimization framework followed to fine-tune non-precious metal oxide sites and their surrounding environment by means of appropriate synthetic and promotional/modification routes. Initially, the basic principles of size, shape and



electronic engineering (*e.g.*, through advanced synthetic routes, special pretreatment protocols, alkali promotion, chemical/structural modification by reduced graphene oxide (rGO)) are discussed. It was clearly disclosed that fine-tuning can exert a profound influence not only on the reactivity of metal sites in its own right, but also to metal-support interfacial activity, offering highly active and stable materials for real-life energy and environmental applications. Then, the main implications of size-, shape- and electronic/chemical-adjustment in catalysis are exemplified on the basis of $\text{CuO}_x/\text{CeO}_2$ binary system during some of the most relevant applications in heterogeneous catalysis, such as CO oxidation, N_2O decomposition, preferential oxidation of CO (CO-PROX), water gas shift reaction (WGSR) and CO_2 hydrogenation to value-added products, are thoroughly discussed.

INTRODUCTION

The fast growth rate of population in the last decades has led to an unprecedented increase in energy demands. However, the main energy sources fulfilling global demands originate from fossil fuels, rising significant concerns in relation to sources' availability and environmental degradation. To this end, the development of emerging energy technologies towards the production of environmentally friendly fuels besides the establishment of cost-effective environmental technologies for climate change mitigation has become a main priority in the scientific and industrial community. Clean and reliable energy supply in conjunction with environmental protection by means of highly- and cost-effective technologies is one of the most significant concerns of the 21st century [1–4].

In view of the above aspects, heterogeneous catalysis is expected to have a key role in the near future towards sustainable development. Heterogeneous catalysis has received considerable attention from both the scientific and industrial community, as it is a field of diverse applications, including the petrochemical industry with the production of high quality chemicals and fuels, the fields of energy conversion and storage, as well as the remediation of the environment through the abatement of hazardous substances, signifying its pivotal role in the world economy [1,3,5–7]. Several types of catalysts have been employed for energy and environmental applications, which can be generally classified into: Noble metal (NMs)-based catalysts and NMs-free metal oxides (MOs), such as bare oxides, mixed metal oxides (MMOs), perovskites, zeolites, hexaaluminates, hydrotalcites, spinels, among others. Among these, NMs-based catalysts have been traditionally used in numerous processes, such as CO oxidation [8–11], nitrous oxide (N₂O) decomposition [12–17], water-gas shift reaction [18–20], carbon dioxide (CO₂) hydrogenation [21–25], *etc.*, exhibiting high activity and selectivity. However, their scarcity and extremely high cost render mandatory the development of highly active, stable and selective catalysts that will be of low cost, nonetheless [26,27].

On the other hand, metal oxides (MOs) prepared from earth-abundant and inexpensive transition metals have attracted considerable attention as alternatives to rare and remarkably expensive NMs, due to their particular features, such as enhanced redox properties, thermal stability and catalytic performance in conjunction to their lower cost [2,3,35–43,5,28–34]. The latter is clearly manifested in Figure 1.1, which schematically depicts the cost of noble metals in comparison with copper (a typical transition metal massively involved in MOs) for a five-year period. It is evident that the price of noble metals is larger than that of copper by about four orders of magnitude.

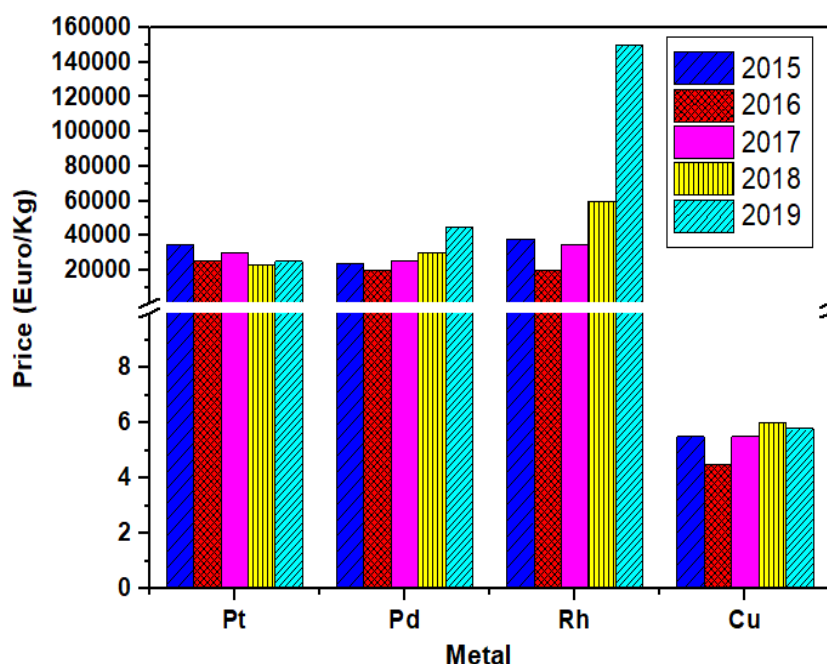


Figure 1.1. Relative comparison of noble metal and copper metal prices over a five-year period. Data taken from <https://www.infomine.com>. Adapted from Reference [44]. Copyright© 2020, MDPI.

Mixed metal oxides (MMOs) appropriately prepared by admixing two or more single metal oxides in a specific proportion, have lately gained particular attention, since they exhibit unique structural and surface properties, which are completely different from that of parent oxides. Amongst the numerous MOs, transition metal-based oxides have gained particular interest, due to their peculiar chemisorption capacity, linked to partially filled d-shells [45,46]. For instance, Cu-based oxides can catalyze a variety of reactions following a redox-type mechanism (*e.g.*, photocatalysis), due to the wide range of Cu oxidation states (mainly Cu^0 , Cu^I , Cu^{II}), which enables reactivity in multi-electron pathways. On the other hand, reducible oxides, such as ceria, not only provide the basis of active phase dispersion, but could have a profound influence on the intrinsic catalytic activity, through metal-support interactions, as will be further discussed in the sequence. In particular, ceria or cerium oxide (CeO_2) has attracted considerable attention, due to its unique properties, including enhanced thermal stability, high oxygen storage capacity (OSC) and oxygen mobility, as well as superior reducibility driven by the formation of surface/structural defects (*e.g.*, oxygen vacancies) through the rapid interplay between the two oxidation states of cerium ($\text{Ce}^{3+}/\text{Ce}^{4+}$) [2,6,29,47–49]. In addition to these physicochemical advantages of cerium oxide, its average 2020 price stands at very low levels (*ca.* 1815 USD/metric ton), with a relative cost trend of $\text{CeO}_2 < \text{TiO}_2 < \text{SiO}_2 < \text{ZnO} < \text{ZrO}_2$, revealing the economic benefits of ceria-based catalytic materials [50]. Moreover, ceria's combination with transition metals leads to improved catalytic

performance, due to the synergy between the metal phase and the support, related to electronic, geometric and bifunctional interactions [31,51–56]. More importantly, the combination of reducible oxides (*e.g.*, CeO₂) with TMs (*e.g.*, Fe, Co, Ni, and Cu) could offer novel catalyst formulations with exceptional properties, arising mainly from the multifaceted electronic and geometric interactions amongst the different counterparts [31,51,61–63,52,54–60]. In this regard, the combination of CuO_x and CeO₂ oxides towards the formation of CuO_x/CeO₂ binary oxides, offers catalytic activities comparable or even better to NMs-based catalysts in various applications, such as CO oxidation, N₂O decomposition, preferential oxidation of CO (CO-PROX), as lately reviewed [31].

The peculiar reactivity of CuO_x/CeO₂ system arises not only from the distinct characteristics of individual CuO_x and CeO₂ phases, but mainly from their synergistic interactions. More specifically, the synergistic effects between the different counterparts of MOs can offer unique characteristics (*e.g.*, improved reducibility, abundant structural defects, *etc.*), reflected then on the catalytic activity [31,58,64–68]. Various interrelated factors are usually considered under the term "synergy", involving among others:

- (i) The superior interfacial reactivity as compared to the reactivity of individual particles;
- (ii) The presence of defects (*e.g.*, oxygen vacancies);
- (iii) The enhanced reducibility of MOs as compared to single ones;
- (iv) The interplay between interfacial redox pairs (*e.g.*, Cu²⁺/Cu⁺ and Ce³⁺/Ce⁴⁺).

In view of the above, very recently, the modulation of metal-support interactions as a tool to enhance the catalytic performance was thoroughly reviewed, disclosing that up to fifteen-fold productivity enhancement can be achieved in reactions related to C1 chemistry by controlling metal-support interactions [63]. However, it is well established today—thanks to the rapid development of sophisticated characterization techniques—that various interrelated factors, such as the composition, the size, the shape, and the electronic state of MOs different counterparts can exert a profound influence on the local surface chemistry and metal-support interactions, and in turn, on the catalytic activity of these multifunctional materials [6,49,73–79,53,54,59,62,69–72]. In view of this fact, size, shape, porous, redox and electronic adjustment by means of appropriate synthetic and promotional/modification routes can provide the vehicle to substantially modifying not only the reactivity of metal sites in its own right, but also the interfacial activity, offering highly active and stable materials for real-life energy and environmental applications (Figure 1.2).

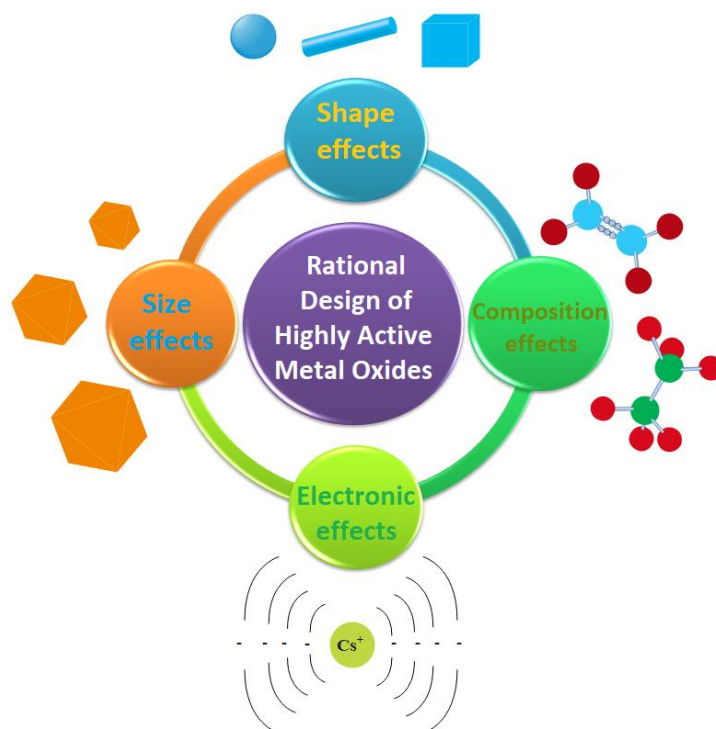


Figure 1.2. Schematic illustration of metal oxides' (MOs) fine-tuning by adjusting their size, shape, composition and electronic/chemical state.

In light of the aforementioned issues, the present chapter aims at exploring the basic principles of MOs fine-tuning by modulating the size, shape and electronic/chemical state by means of appropriate synthetic/promotional routes. The implications of size, shape and electronic/chemical effects in catalysis will be next exemplified on the basis of state-of-the-art catalytic applications of $\text{CuO}_x/\text{CeO}_2$ binary oxide, involving CO oxidation, N_2O decomposition, preferential oxidation of CO (CO-PROX), water gas shift reaction (WGSR), and CO_2 hydrogenation to value-added chemicals/fuels.

1.1. FINE-TUNING OF METAL OXIDES (MOs)

Heterogeneous catalysis traditionally refers to a chemical reaction taking place on the surface of a solid catalyst, involving the adsorption and the activation of reactant(s) on specific active sites, the chemical transformation of adsorbed species and the products' desorption. Thanks to the rapid development of both *in situ* and *ex situ* characterization techniques, it is well acknowledged that the elementary reaction steps are strongly dependent on several parameters involving the size, the shape, the electronic state of individual particles, as well as on their interfacial interactions. Hence, the macroscopic catalytic behaviour can be considered as the outcome of interactions between reactants, intermediates and products with the micro(nano)scopic coordination environment of surface atoms, involving geometric arrangements, electronic confinement, and interfacial effects, among others. In view of this fact, the modulation of the above-mentioned

parameters can profoundly affect the local surface structure and chemistry with great implications in catalysis. It should be mentioned, however, that due to the interplay between structural and chemical factors, it is quite challenging to disclose the fundamental origin of catalytic performance. Thus, it is of vital importance to establish reliable structure-property relationships, unveiling the particular role of each factor at nanoscale.

Moreover, taking into account that the majority of MOs consists of at least two different counterparts, this triggers unique opportunities towards designing various MOs of the same composition, but of different reactivity by adjusting the above-mentioned parameters either in one or both counterparts. In the following, the basic principles of size, shape, and electronic/chemical effects are provided. However, it should be mentioned here that all factors are interrelated; thus, the discrete role of each one in the catalytic activity of MOs cannot be easily disclosed, as further discussed below.

1.1.1. Size Effects

The rapid development of nanotechnology in the last years enables the fabrication of MOs with tunable size and shape at the nanometer scale. Nowadays, it has been both experimentally and theoretically revealed that the surface, structural and electronic properties of nanoparticles (NPs) differ essentially from the corresponding bulk properties. In general, by decreasing the particle size of metal oxide particles down to few nanometers (*e.g.*, <10 nm), a dramatic increase in activity can be generally obtained, attributed to "size effects". This size-dependent reactivity can be ascribed to different contributions, namely: (i) quantum size effects, (ii) presence of low coordinated atoms into nanoparticles' surface, (iii) electronic state of the surface, (iv) strong interparticle interactions. Hereinafter, the particular effect of every contribution is shortly presented for the sake of following discussions in relation to the fine-tuning of MOs. For additional reading, several comprehensive articles in this topical area are recommended [31,54,69,70,72,73,77,80].

In particular, by decreasing the size of a material down to nanometer scale, the surface-to-volume ratio is largely increased, resulting in an increased population of surface sites, being the active sites in catalysis. Besides the modulation of the fraction of atoms on the topmost surface layer, the number of atoms at corners and edges, being considered more active than those at planes, is considerably increased by decreasing the size. More specifically, size decrease leads to a high density of under-coordinated atoms with exceptional adsorption and catalytic properties [54,69,73,81–85]. Typically, surface sites with low coordination number (CN) demonstrate stronger adsorption ability as compared to those of high CN [69,77,86]; linear relationships between the adsorption energy of various adsorbates and the coordination number have been

found for several transition metals, including among others non-precious metals, such as Cu, Ni, and Co [87,88]. Thus, from the geometrical point of view, size decrease has a direct effect on both the number and type of active surface sites reflected then on catalytic activity.

Aside from the "geometric size effects", the electronic state of surface atoms can undergo substantial modifications upon decreasing the particle size down to nanoscale. In particular, when a bulk material with a continuous electron band is subjected to size decrease down to the nanometer scale, the so-called quantum effect or confinement effect is taking place, arising from the presence of discrete electronic states as in the case of molecules [69,72,73,80,89]. For instance, it has been reported that a higher electron density, with a d band close to the Fermi level, can be obtained for Au NPs smaller than *ca.* 2 nm as compared to bigger ones, with great implications in CO oxidation [90–93].

Recently, thanks to the introduction of new generation sophisticated characterization techniques (*e.g.*, high-angle annular dark-field scanning transmission electron microscopy (HAADF-STEM), extended X-ray absorption fine structure (EXAFS)) and computational methods (*e.g.*, Density Functional Theory (DFT) calculations), an indirect size effect linked to the metal-support interactions is clearly revealed. More specifically, even small perturbations between metal nanoparticles and oxide carriers, due to charge transfer between particles, local electric fields, morphological changes, "ligand" effect, *etc.*, can induce a substantial modification in catalytic activity [31,52,58,61,94–96]. To more accurately describe these phenomena, the term Electronic Metal Support Interactions (EMSI) has been recently proposed by Campbell [97] in contrast to classical Strong Metal Support Interactions (SMSI). In view of this concept, tiny metal clusters composed of a few or even single atoms could play a dominant role in catalysis, despite the fact that they do not account for more than a few percent of the total metal content [31,52]. In view of this fact, it has been shown that by controlling the metal (Ni, Pd, Pt) nanocrystal's size, the length of metal-ceria interface is appropriately adjusted with significant implications in CO oxidation; normalized reaction rates were dramatically increased with decreasing the size, due to the increased boundary length.

As an additional implication of size-dependent behaviour, the significant effect of particle size on structural defects of reducible carriers (such as ceria) should be mentioned. In fact, a close relationship between the crystal size of ceria and the concentration of oxygen vacancies has been revealed; the large surface-to-volume ratio in conjunction to the exposure of under-coordinated sites can facilitate the formation of oxygen vacancies and the Ce³⁺ fraction in non-stoichiometric CeO_{2-δ} NPs [70,98–104]. Moreover, an inverse correlation between the lattice parameters of CeO₂ NPs and particle sizes has been established, attributed to the increase of Ce³⁺ and oxygen

vacancies concentration [70]. A similar trend was recorded between the surface-to-bulk oxygen ratio and particle size.

Closing this part concerning the size effects, it should be noted, that although particle size decrease has in general a positive catalytic effect, there is a variation in relation to size-activity relationships depending on catalyst type and reaction environment. For instance, a positive size effect could be obtained if the rate determining step (rds) involves the bond cleavage of a reactant molecule on surface atoms with low coordination number. However, if the same under-coordinated atoms strongly bind dissociated species (*e.g.*, oxygen atoms) this could lead to the poisoning of catalyst surface and thus to the negative size effect. In particular, in reactions with no structure sensitivity, the activity remains unaffected by changes in the particle size (Figure 1.3, line a), while it could decrease with decreasing particle size (Figure 1.3, line b), referred as negative particle size effect or antipathetic structure sensitivity, or increase as the particle size decreases (Figure 1.3, line d), referred as positive particle size effect or sympathetic structure sensitivity [81]. However, the activity may reach a maximum when small particles exhibit a negative effect and larger particles show a positive one (Figure 1.3, line c) [81].

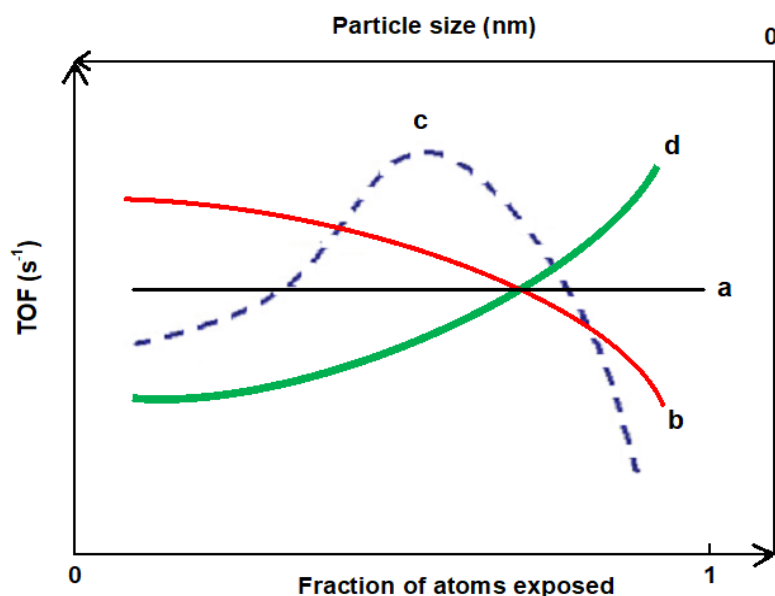


Figure 1.3. Turnover frequency (TOF) variation with fraction of atoms exposed and particle size (see text for a discussion of the curves). Adapted from Ref. [81]. Copyright[©] 1989, Elsevier.

1.1.2. Shape Effects

Nanostructured catalysts possess unique properties originating from nanoscale phenomena linked mainly to size effects, commented above, and shape effects. The latter refers to the modification of catalytic activity through the preferential exposure of specific crystallographic facets on the reaction environment, also termed as morphology-dependent nanocatalysis [53,69,76,77,84,105–

107]. In particular, the catalytic cycle and hence the reaction efficiency, is determined on reactants adsorption/activation and products desorption processes, being strongly influenced by the surface planes of catalysts' particles. In this regard, the simultaneous modulation of size and shape at the nanometer scale can determine the number and the nature of exposed sites, and thus, the catalytic performance. This particular topic is an essential issue within the field of nanocatalysis, aiming at controlling a specific chemical reaction through co-adjusting these parameters at the nanometer scale.

Thanks to the latest advances in materials science, nanostructured catalysts with well-defined crystal facets can be fabricated by precisely controlling nanocrystals' nucleation and growth rate [49,74,77,78,80,106]. The obtained crystal morphology is the result of several synthesis parameters, involving temperature, pressure, concentration, and pH, among others. Several reviews have been devoted to the subject [6,29,78,84,98,106,108,109]. Various structures with similar or different dimensions in all directions, such as nanospheres, nanocubes, nanowires, nanorods, nanosheets, *etc.*, could be obtained.

Ceria's shape control and its implications in catalysis is most probably the most extensively investigated system among metal oxides in heterogeneous catalysis [2,6,105,108,110–113,29,49,53,71,75,76,84,98]. The growth rate mechanism of ceria nanocrystals can be affected by various parameters, such as the basicity or polarity of the solvent [114,115], the aging temperature [116,117], the precursor compound [118,119], and the impregnation medium [120]. Regulation of nanocrystals' nucleation and growth processes results in specific shapes, such as rods and cubes [49,78]. Moreover, by altering the physicochemical conditions during the synthesis procedure (*e.g.*, by the usage of a capping agent), blocking of certain facets or continuous growth of others may occur, as depicted in Figure 1.4.

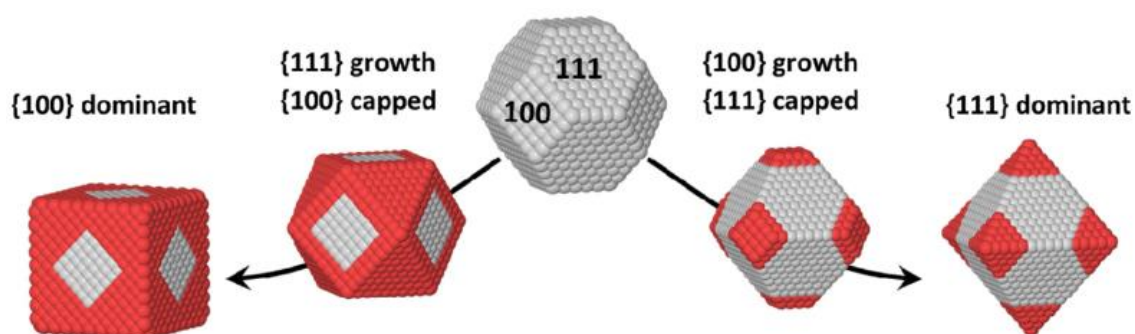


Figure 1.4. Model shapes illustrating an anisotropic growth process starting from a truncated cuboctahedron shape. Protecting the {111} facets using a capping agent results in the growth of {100} facets until they disappear and only {111} facets remain on the surface (octahedral shape). The opposite would result in cubic NPs with only {100} facets. Reproduced with permission from Ref. [121]. Copyright[©] 2015, Elsevier.

There are several synthetic approaches for the preparation of ceria nanoparticles, including precipitation [120,122,123], thermal decomposition [123,124], template or surfactant-assisted method [125–128], microwave-assisted synthesis [129–131], the alcohothermal [126,132] or hydrothermal [123,126,133–137] method, microemulsion [135,138,139], solution combustion [140,141], sol-gel [142–144], sonochemical [145,146], *etc.* However, not all methods lead to particles of well-ordered size and shape with uniform dispersion on the catalyst's surface [121]. Among the different methods, the hydrothermal one has attracted considerable attention, due to the simplicity of the precursor compounds used, the short reaction time, the homogeneity in morphology, as well as the acquisition of various nanostructures, such as rods, polyhedra, cubes, wires [108,118,150–159,123,160,126,133,136,137,147–149]. Ceria nanocrystals have three low-index lattice facets of different activity and stability, namely, {100}, {110}, {111} [49,107,161], as shown in Figure 1.5.

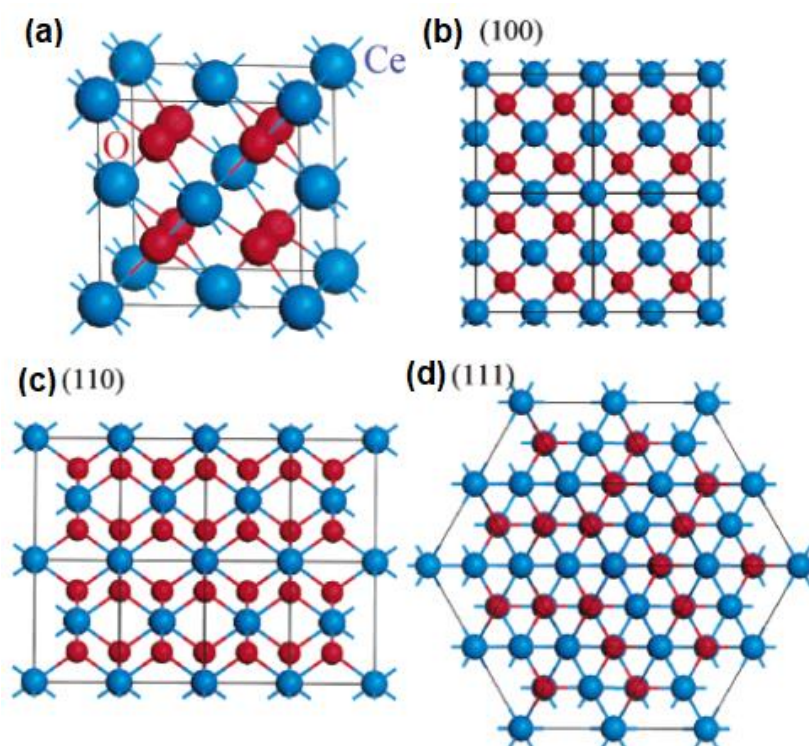


Figure 1.5. (a) Unit cell of the CeO₂ structure. (b-d) The (100) [or (200)], (110), and (111) planes of the CeO₂ structure. Reprinted with permission from Ref. [161]. Copyright[©] 2003, American Chemical Society.

The selective exposure of ceria reactive facets can strongly affect the redox properties of ceria and in turn, its intrinsic characteristics as an active phase or supporting carrier. Popular ceria shapes, mainly, involve nanorods (NR), nanocubes (NC) and nanopolyhedra (NP). Ceria nanorods, mostly, expose the {110} and {100} facets, whereas, nanocubes and nanopolyhedra preferentially expose

the {100} and {111} facets, respectively [49,53,107]. By means of both experimental [84,105,110,150,162,163] and theoretical [113,164–168] studies, it has been shown that the energy formation of anionic vacancies is dependent on the exposed facets, following the order: {111} > {100} > {110}. In this regard, the reactivity of ceria nanorods is, in general, increased upon increasing the fraction of {110} and {100} facets [76].

In view of the above, it has been clearly revealed that the activity and selectivity are strongly affected by the exposed crystal planes. For instance, the formation rate of ammonia on Fe crystals follows the sequence: {111} >> {100} > {110} [169]. Similar morphology-dependent effects have been demonstrated for several noble metal- [106,170] and metal oxide- [53] catalyzed processes. In this point, it should be mentioned that the shape effects with regard to ceria-based transition metal catalysts have been comprehensively reviewed in our most recent paper [171].

1.1.3. Electronic Effects

Besides modulating the local surface structure of MOs by size and shape effects, described above, the fine-tuning of electronic structure by appropriate promoters can be considered as an additional modulating tool. Promoters hold a key role in heterogeneous catalysis towards optimizing the catalytic activity, selectivity and stability by modifying the physicochemical features of MOs, and can be classified into two general categories: structural promoters and electronic promoters. The first category mainly involves the doping of supporting carrier to enhance its structural characteristics and in turn, the stabilization of active phase (*e.g.*, incorporation of rare earth dopants into three-way catalysts [5]). On the other hand, electronic promoters can modify catalysts' surface chemistry either directly or indirectly. The former mainly includes the electrostatic interactions between the reactant molecules and the local electric field of promoters. The latter denotes the promoter-induced modifications on metal Fermi level, which is then reflected on the chemisorptive bond strength of reactants and intermediates with great consequences in catalysis. In particular, the "promoter effect" is related to the changes in the work function (Φ) of the catalysts' surface upon promoter addition, accompanied by substantial modification of its chemisorption properties. The vast majority of electronic promotion over metal oxide catalysts refers to alkali modifiers. It has been well documented that alkali addition can drastically enhance the activity and selectivity of numerous catalytic systems, involving among others Pt-, Pd-, Rh-, Cu-, Fe-based catalysts, in various energy and environmental related reactions (*e.g.*, [169–174]). Various comprehensive studies have been devoted to the role of promoters in heterogeneous catalysis, to which the reader can refer for further reading [178–180].

Figures 1.6 and 1.7 depict the "promoter effect" in the case of alkali-doped Co_3O_4 oxides during the N_2O decomposition [181,182]. A close relationship between the catalytic performance (in

terms of half-conversion temperature, T_{50}) and the work function (Φ) was disclosed revealing the electronic nature of alkali promotion; electropositive modifiers (such as alkalis) can decrease the work function of the catalyst surface, thus, activating the adsorption/decomposition of electron-acceptor molecules (such as N_2O) [181]. However, at high alkali coverages, depolarization occurs, due to the strengthening of the alkali-alkali bond at the expense of the alkali-surface bond, resulting in a work function increase [183].

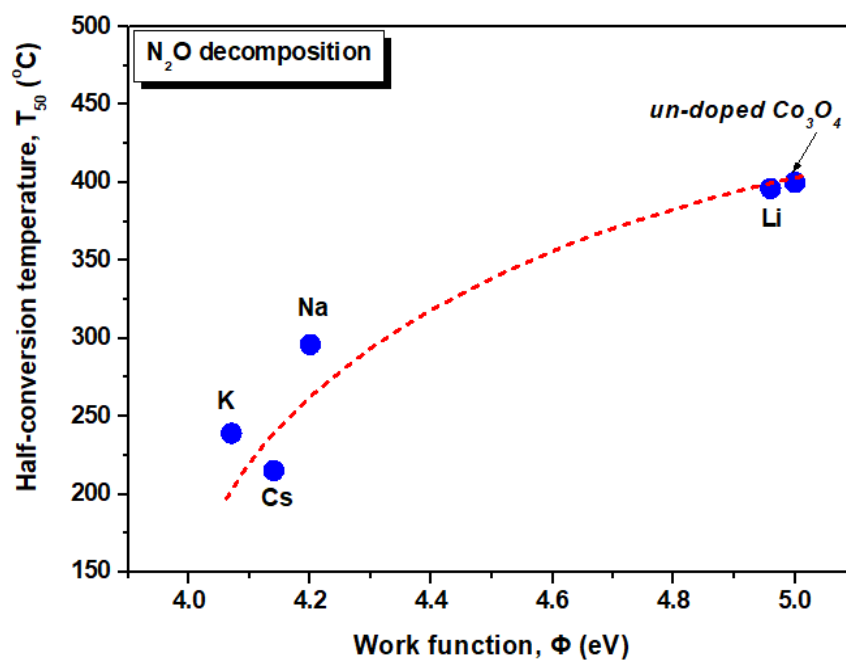


Figure 1.6. Correlation of half-conversion temperature (T_{50}) with the work function of alkali promoted Co_3O_4 . Reaction conditions: 5.0% N_2O ; $m_{cat} = 300$ mg; GHSV = 7000 h^{-1} ; alkali coverage = ~ 2 at/nm^2 . Adapted from Reference [181]. Copyright © 2009, Elsevier.

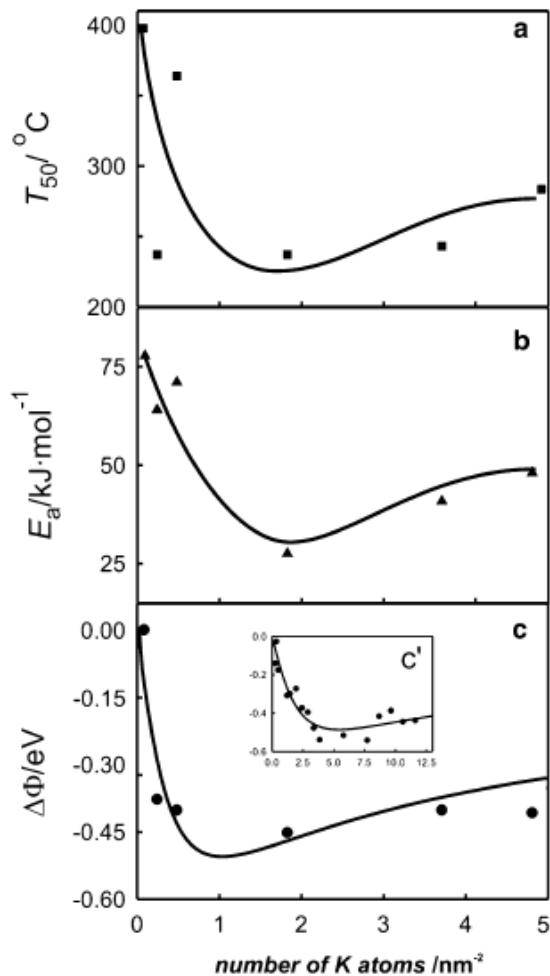


Figure 1.7. (a) The half-conversion temperature of N_2O (T_{50}), (b) apparent activation energy (E_a) and (c) work function changes ($\Delta\Phi$) as a function of potassium loading (Θ_K) introduced from K_2CO_3 and (c insert) KOH precursor. Reproduced with permission from Reference [182]. Copyright © 2008, Springer Nature.

In this point, it should be mentioned that, depending on the support's nature and crystal planes, alkali adsorption may lead to surface reconstruction. This surface reconstruction can be explained by taking into account the structural/electronic perturbations induced by the formation of the alkali-surface bond [184]. As mentioned previously, the crystallographic orientation of the support plays an important role in the diffusion rate of the adsorbed species, as well as in their in-between interaction, resulting in different structural stabilization [184]. For instance, potassium promoter was shown to stabilize certain iron facets in K-promoted iron catalysts, by inducing changes in the crystal growth rate, thus, enabling the formation of small particles with abundance in active facets and affecting the activity and selectivity of the overall system [185]. As shown in Figure 1.8, by increasing the K/Fe surface atomic ratio, the crystal facets become more stable and the surface energy is decreased [185]. This clearly manifests the pivotal role of alkali addition towards co-

adjusting the structural and electronic properties of the catalyst's surface, and in turn, the catalytic performance.

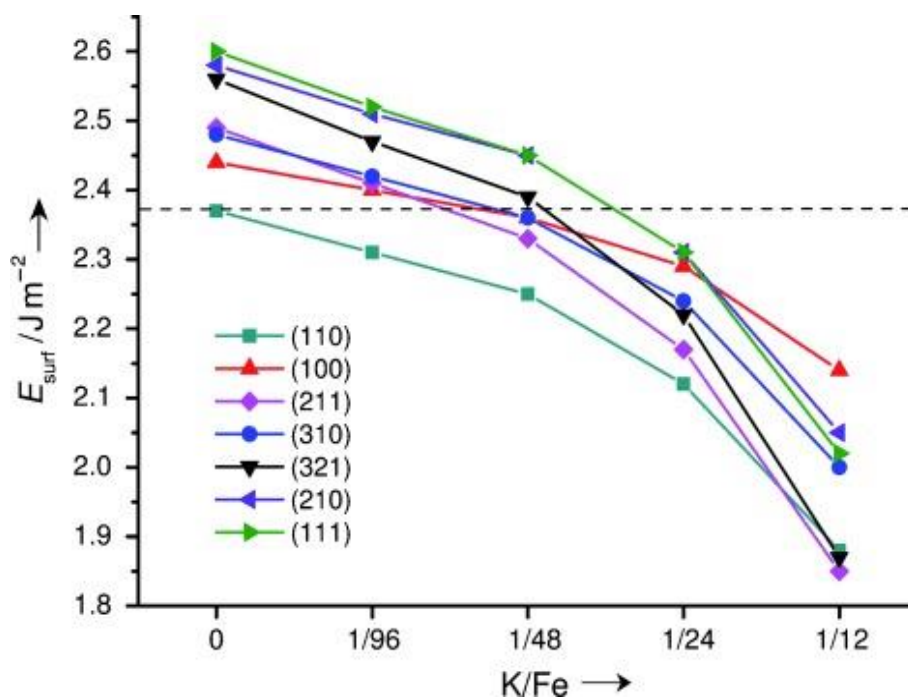


Figure 1.8. Surface energy variation versus the surface atomic ratio of K to Fe. Reproduced with permission from Reference [185]. Copyright © 2011, John Wiley and Sons.

Besides the alkali-induced modifications on the chemisorption properties, significant alterations on the surface oxygen mobility have been demonstrated; alkali addition could facilitate suprafacial recombination of oxygen towards molecular oxygen desorption, thus, liberating active sites [31]. Both the electronic and redox modifications induced by alkali addition can exert remarkable effects on catalytic activity and selectivity, demonstrating the key role of "promoter effect" as an additional adjusting parameter in catalysis.

It should be noted here, as mentioned in the case of size and shape effects, that the promoter effect is not always positive. The latter strongly depends on reactants' type (electron donor or electron acceptor adsorbates) and the work function changes (increase or decrease) induced by the promoter (electropositive or electronegative). Thus, besides the structure-sensitivity, commented above, the electronic sensitivity of a given reaction should always be taken into account, when attempting to co-adjust the size, shape and electronic state.

1.1.4. Chemical Modifiers

Besides the extensive use of alkalis or alkaline earths as promoters, numerous other chemical substances can be employed to modulate the local surface chemistry/structure and in turn, the activity, selectivity and long-term stability of parent catalyst (*e.g.*, [72]). In this regard, metal alloys (*e.g.*, Au-Ni alloys as reforming catalysts [186], Pt-Sn alloys for ethanol oxidation [187]) are extensively employed in catalysis towards obtaining highly active and cost-effective catalytic formulations. Several mechanisms are considered responsible for the enhanced performance of bimetallic systems, involving mainly structural (strain effects) and electronic (charge-transfer effects) modifications that can be induced by the interaction between the different counterparts. The latter substantially modifies the binding energy of adsorbates and the path of chemical reactions with major consequences in catalysis [52,72].

In a similar manner, chemical substances with unique physico-chemical properties, such as carbon-based materials, have lately received considerable attention as chemical modifiers or supporting carriers [73,188]. Various carbon materials, such as carbon nanotubes (CNTs), reduced graphene oxide (rGO), ordered mesoporous carbon (OMC), carbon nanofibers (CNFs), and graphitic carbon nitride (g-C₃N₄), have received particular attention in catalysis after the significant progress in controlled synthesis and the fundamental understanding of their properties. In general, nanocarbons (NCs) (Figure 1.9) possess unique physical (large surface area, specific morphology, appropriate pore structure) and chemical (electronic structure, surface acidity/basicity) properties arising from their nanoscale confined structures [188].

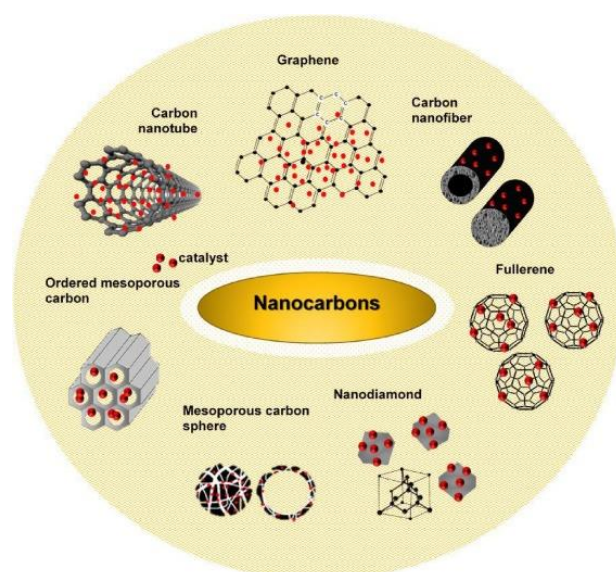


Figure 1.9. Representative nanocarbons used for the preparation of catalytic composites. Reproduced with permission from Ref. [188]. Copyright © 2018, Elsevier.

The combination of metal nanoparticles (NPs) with carbon materials by means of various synthetic approaches can exert significant modifications on the structural and electronic surrounding of NPs with subsequent implications in catalysis [73,188]. For example, confined Fe NPs in CNTs exhibit an almost twice yield to C₅₊ hydrocarbons as compared to Fe particles during the syngas conversion to liquid hydrocarbons [189]. The latter was mainly ascribed to the modified structural and redox properties of confined Fe NPs within CNTs [73]. Moreover, the application of graphene in catalysis allows the fabrication of multifunctional materials with distinct heterostructures, which offer quite different properties as compared to individual materials [188,190,191]. In general, carbon materials with exceptional structural and electronic characteristics can be effectively employed either as supporting materials or chemical modifiers, offering unique opportunities towards modulating the intrinsic reactivity of MOs. For instance, it has been found that the homogeneous distribution of copper atoms on the surface of rGO in combination with the outstanding electronic properties of rGO lead to high electrocatalytic activity, due to the synergy between the two components [192].

Metal-organic frameworks (MOFs) are another type of supporting carriers/chemical modifiers consisting of inorganic metal ions or clusters that are bridged with organic ligands in order for one or more dimensional configurations to be formed [193]. These materials exhibit unique properties, such as high surface area and porosity, while their complex network consisting of various channels allows passage in small molecules [194]. The fabrication of MOF-based MOs composites is of great interest, as it results in the development of materials with tunable properties and functionality. Metal nanoparticles regarded as the active centres can be stabilized by MOFs through confinement effects [195]. For instance, Cu, Ni, and Pd nanoparticles encapsulated by MOFs exhibited high catalytic efficiency, ascribed mainly to the synergistic effects of nanoconfinement and electron-donation offered by MOF framework [196–201]. Furthermore, by changing the MOFs functional groups, products distribution may differ, as a consequence of variations induced in the chemical environment of the catalytically active sites [202].

1.1.5. Pretreatment Effects

Besides the advances that can be induced by adjusting the size, shape and electronic state of MOs, special pretreatment protocols or activation procedures could be applied to further adjust the local surface chemistry of MOs (*e.g.*, [203,204]). In particular, the local surface chemistry of the MOs can be further tailored by appropriate pretreatment protocols, including thermal or chemical pretreatment. According to the pretreatment protocol followed, different properties get affected, resulting in diversified catalytic behaviour. It has been reported that defect engineering by a low-pressure thermal process instead of atmospheric pressure activation, could notably increase the

concentration of oxygen vacancy defects and in turn, the CO oxidation activity of ceria nanoparticles, offering an additional tool towards the fine-tuning of MOs [203]. Moreover, it has been documented that the pretreatment protocol (oxidation or reduction) induces significant effects on the local surface structure of cobalt-ceria oxides affecting the dehydroxylation process in ammonia synthesis [205]. In a similar manner, oxidative pretreatment of cobalt-ceria catalysts resulted in an impoverishment of catalyst surface in cobalt species, due to the preferential existence of cerium species on the outer surface, whereas, cobalt and cerium species were uniformly distributed on the catalyst's surface through the reduction pretreatment, which gave rise to the formation of oxygen vacancies [40]. In addition, a strong interaction between gold and ceria has been observed after O₂ pretreatment, due to the electron transfer from Au⁰ to ceria, giving rise to oxygen vacancy formation, lattice oxygen migration, as well as to the formation of Au^{δ+}-CO and surface bicarbonate species, favouring, thus, the adsorption of CO and the desorption of CO₂ [206]. In terms of T₁₀₀, CO oxidation performance showed the following order: O₂ pretreatment (74 °C) < N₂ pretreatment (142 °C) < 10% CO/Ar pretreatment (169 °C) [206]. In view of the above short discussion, the pretreatment conditions can affect the facilitation with which certain active species are formed on the catalyst's surface, the oxygen mobility or the formation of oxygen defects, with great implications in the catalytic performance.

1.2. IMPLICATIONS OF MOs FINE-TUNING IN CATALYSIS EXEMPLIFIED BY $\text{CuO}_x/\text{CeO}_2$ BINARY SYSTEM

In this section, the implications of metal oxides' fine-tuning by means of the above-described size, shape and electronic/chemical effects are presented, on the basis of the $\text{CuO}_x/\text{CeO}_2$ binary oxide system. This particular catalytic system is selected as representative MOs, taking into account the tremendous fundamental and practical attention lately devoted to the copper-containing cerium oxide materials. More specifically, the abundant availability of copper and ceria and consequently, their lower cost (about four orders of magnitude, Figure 1.1) render the $\text{CuO}_x/\text{CeO}_2$ composites strongly competitive. Moreover, their excellent reactivity –linked to peculiar metal-support interactions– in conjunction to their remarkable resistance to various substances, such as carbon dioxide, water and sulfur is of particular fundamental and practical importance [65,207,208]. Remarkably, copper-containing ceria catalysts appropriately adjusted by the aforementioned routes demonstrated catalytic activity similar or even better than NMs-based catalysts in various applications, such as CO oxidation, the decomposition of N_2O and the water-gas shift reaction, among others [116,126,216–220,149,209–215].

For instance, the inverse $\text{CeO}_x/\text{Cu}(111)$ system exhibits superior CO oxidation performance at a relatively low temperature range (50–100 °C), in which the noble metals do not function well, exhibiting activity values of about one order of magnitude higher than those measured on Pt(100), Pt(111), and Rh(111) [221–223]. The latter has been mainly attributed, on the basis of the most conceptual experimental and theoretical studies, to the existence of Ce^{3+} at the metal-oxide interface which binds O atoms weaker as compared to bulk Ce^{3+} [221,224].

In light of the above aspects, in this section, the main implications of size, shape and electronic/chemical effects on the catalytic performance of $\text{CuO}_x/\text{CeO}_2$ system during some of the most relevant applications in heterogeneous catalysis will be discussed. It should be stressed that it is not the aim of this section to provide an extended overview of $\text{CuO}_x/\text{CeO}_2$ catalytic applications, which can be found in several comprehensive reviews [3,51,65,207,225,226]. It mainly aims to provide a general optimization framework towards the development of highly active and cost-effective MOs, paving also the way for the decrease of precious metal content in NMs-based catalysts.

1.2.1. CO Oxidation

CO oxidation is probably the most studied reaction in heterogeneous catalysis, due to its practical and fundamental significance. The catalytic elimination of CO is of great importance in various applications involving, among others, automotive exhaust emissions control and fuel cell systems. More importantly, CO oxidation can serve as a prototype reaction to gain insight into the structure-property relationships.

Regarding, at first, the CO oxidation activity of individual CuO_x phase, it has been clearly revealed that it is strongly dependent on oxidation state, size and morphology. In particular, the following activity order: $\text{Cu}_2\text{O} > \text{metastable cluster CuO} > \text{CuO}$ has been revealed, closely related to the ability to release lattice oxygen [227,228]. On the other hand, the exposed crystal planes of CuO_x phase drastically affect the CO oxidation; truncated octahedral Cu_2O with {332} facets displayed better activity than low index {111} and {100} planes [229]. Similarly, CuO with exposed {011} planes is more active than close-packed {111} planes [230]. In view of this fact, it has been found that the CO oxidation activity of CuO mesoporous nanosheets with high-index facets is about 35 times higher than that of the commercial sample [231]. In general, surface vacancies, originated from coordinately unsaturated surface Cu atoms, can easily activate oxygen species towards their reaction with the reducing agent [3].

In a similar manner, theoretical and experimental studies have shown that the energy of anionic vacancies formation over bare ceria follows the order: {111} > {100} > {110}, as previously analyzed [84,105,167,168,110,113,150,162–166]. Moreover, a large increase in oxygen vacancies concentration has been found for ceria crystal size lower than *ca.* 10 nm [99], revealing the interrelationship between size and shape effects.

In view of the above aspects, it could be argued that by adjusting the shape and size of individual counterparts of MOs (CuO_x and CeO_2 in the case of $\text{CuO}_x/\text{CeO}_2$ mixed oxides), significant modifications in their redox and catalytic properties can be obtained. The underlying mechanism of this synergistic effect linked to metal-support interactions is the subject of numerous theoretical and experimental studies in catalysis. The latest advances in the field of $\text{CuO}_x\text{-CeO}_2$ interactions and their implications in catalysis have been recently reviewed by Konsolakis [31]. In general, the superiority of binary oxides can be ascribed to various interrelated phenomena, involving among others: (i) electronic perturbations between nanoparticles, (ii) redox interplay between interfacial sites, (iii) facilitation of the formation of structural defects, (iv) improved reducibility and oxygen mobility, (v) unique reactivity of interfacial sites [31]. However, all of these factors are closely related with the intrinsic and extrinsic characteristics of individual oxides, triggering unique opportunities towards the development of highly active MOs by engineering the size and shape of individual oxides and in turn, the interfacial reactivity. Moreover, chemical or

electronic effects induced by aliovalent doping can exert a profound influence on the catalytic performance, offering an additional tool towards the rational design of MOs (Figure 1.2). In the sequence, the optimization of CO oxidation activity of $\text{CuO}_x/\text{CeO}_2$ catalysts by means of the above-mentioned approaches is presented, as an indicative example of MOs rational design.

In this point, it should be mentioned that the pivotal role of ceria morphology in the CO oxidation activity has been reported by several groups [118,136,148,158,209,211,232–234], with most of these revealing the superiority of ceria nanorods.

However, it should be noted that similar or even better catalytic activities can be obtained by different morphologies (*e.g.*, [126,210,211]). In this regard, it was recently shown that sub-nanometer copper oxide clusters (1 wt.% Cu loading) deposited on ceria nanospheres (NS) exhibited superior performance as compared to that deposited on nanorods ($T_{100} = 122$ °C vs. 194 °C) [126]. Extensive characterization investigations revealed that the copper species in nanorods existed in both $\text{Cu}[\text{O}_x]\text{-Ce}$ and CuO_x clusters, while CuO_x clusters dominated in nanospheres. Among these species, only CuO_x clusters could be easily reduced to Cu(I) when they were subjected to interaction with CO, which is considered to be the reason for the enhanced reactivity of $\text{CuO}_x/\text{CeO}_2$ -NS samples [126].

So far, numerous synthesis routes and different precursors have been employed to adjust the structural and morphological characteristics of $\text{CuO}_x/\text{CeO}_2$ composites, mostly summarized by Prasad and Rattan [207]. For instance, it has been found that the use of Ce(III) instead of Ce(IV) precursors can lead to $\text{CuO}_x/\text{CeO}_2$ catalysts with superior reducibility and CO oxidation activity [235]. In particular, it was experimentally shown that Ce(III)-derived samples contained a higher amount of Cu^+ species, through the redox equilibrium $\text{Cu}^{2+} + \text{Ce}^{3+} \leftrightarrow \text{Cu}^+ + \text{Ce}^{4+}$, which are responsible for their enhanced oxidation performance [235]. Moreover, $\text{CuO}_x/\text{CeO}_2$ samples prepared from copper acetate precursor demonstrated better CO oxidation performance as compared to those prepared from nitrate, chloride and sulfate precursors [236]. Avgouropoulos and co-workers [237,238] recently employed a novel hydrothermal method for the synthesis of atomically dispersed $\text{CuO}_x/\text{CeO}_2$ catalysts, offering high CO oxidation performance. By means of various complementary techniques, it was shown that the catalytic activity is mainly related to the nature of highly dispersed copper species rather than the structural/textural characteristics. In a similar manner, Elias et al. [239] reported on the facile synthesis of phase-pure, monodisperse ~ 3 nm $\text{Cu}_{0.1}\text{Ce}_{0.9}\text{O}_{2-x}$ crystallites through solution-based pyrolysis of heterobimetallic Schiff complexes. An increase of CO oxidation activity by one and three orders of magnitude compared to ceria nanoparticles (3 nm) and microparticles (5 μm), respectively, was attained (Figure 1.10).

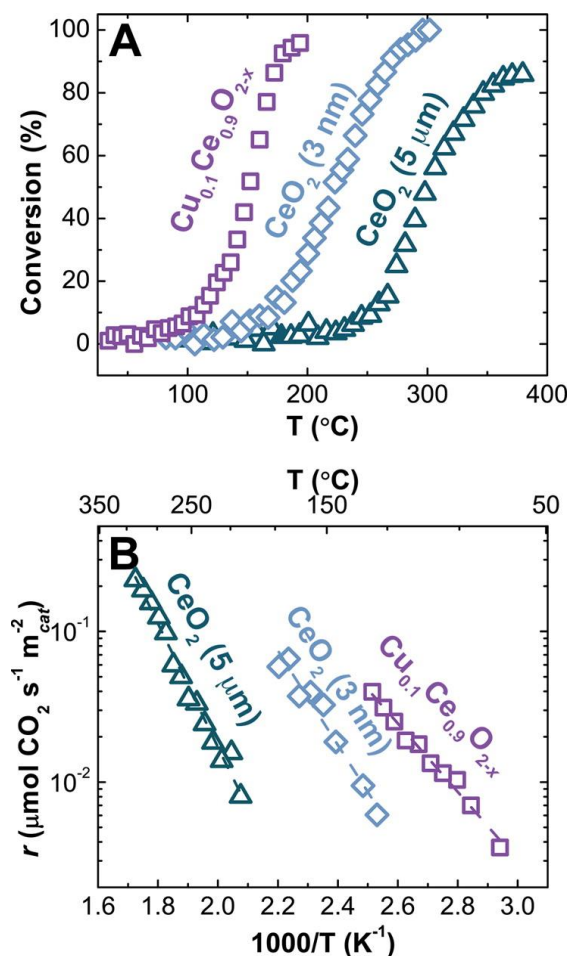


Figure 1.10. CO oxidation on annealed 3 nm $\text{Cu}_{0.1}\text{Ce}_{0.9}\text{O}_{2-x}$, 3 nm CeO_2 and commercial 5 μm CeO_2 (Sigma-Aldrich). (A) "Light off" curves and (B) area-normalized Arrhenius plots, measured in 1.0% CO, 2.5% O_2 balanced in He at a flow rate of $1300 \text{ mL min}^{-1} \text{ g}_{\text{cat}}^{-1}$ for 20 mg catalyst loadings. Reproduced with permission from Reference [239]. Copyright © 2014, American Chemical Society.

Besides the engineering of shape and size, porous structure engineering could exert a significant influence on the CO oxidation activity of $\text{CuO}_x/\text{CeO}_2$ catalysts [125,212]. For example, three-dimensional CuO_x -doped CeO_2 prepared by a hard template method exhibited complete CO conversion at temperatures as low as 50 °C, due to their improved textural and redox properties [212].

Regarding the influence of $\text{CuO}_x/\text{CeO}_2$ composition on the CO oxidation activity, most of the studies revealed an optimum Cu/(Cu+Ce) atomic ratio in the range of 15–30% [211,234,235,240,241]. Within this specific range, the optimum physicochemical characteristics and interfacial interactions can be achieved, reflected then on catalytic activity.

Apart from the above-described approaches that have been put forward to improve the CO oxidation performance of $\text{CuO}_x/\text{CeO}_2$ oxides, the addition of aliovalent elements as structural/surface promoters should be mentioned. In view of this fact, it has been found that the

modification of ceria support by Mn [242] or Sn [243] can drastically modify the dispersion of CuO_x and the redox interplay between Cu species and support, thus, enhancing the CO oxidation performance. Very recently, the tuning of the interfacial properties of $\text{CuO}_x/\text{CeO}_2$ by In_2O_3 doping was also explored [244]. It was found that the CO oxidation performance of $\text{In}_2\text{O}_3\text{-CuO}_x/\text{CeO}_2$ sample greatly exceeds that of parent oxide, offering complete CO conversion at temperatures as low as 100 °C [244]. By means of complementary characterization studies and density functional theory calculations, it was proved that In_2O_3 could modify the geometric structure of CuO_x particles by reducing their size. The latter results in more metal-support interfacial sites and abundant defects. Moreover, the interaction between In and Cu could modify the electronic state of Cu atoms towards the stabilization of partially reduced Cu sites at the interface [244].

Recently, copper-ceria nanosheets were synthesized by using graphene oxide as a sacrificial template, in an attempt to increase the concentration of active interfacial sites [245]. The copper-ceria interaction was further adjusted by appropriate pretreatment, with the catalyst calcined at 600 °C exhibiting complete CO conversion at 90 °C, due to the high concentration in active copper species and oxygen vacancies [245]. Moreover, a sword-like copper-ceria composite derived by a Ce-based MOF with 5 wt.% Cu loading, exhibited superior CO conversion performance ($T_{100} = 100$ °C) in comparison to other irregular-shaped catalysts, due to the good interfacial contact, which resulted in the abundance of Cu^+ active species and oxygen vacancies [194]. Very recently, triple-shelled $\text{CuO}_x/\text{CeO}_2$ hollow nanospheres were synthesized by MOFs, exhibiting high CO conversion performance ($T_{100} = 130$ °C) [246]. This was mainly ascribed to the porous structure of the triple-shelled morphology, offering an enhanced synergistic interaction between copper and ceria [246]. Table 1.1 summarizes, at a glance, indicative attempts followed to adjust the interfacial properties and in turn, the CO oxidation performance of $\text{CuO}_x/\text{CeO}_2$ binary oxides. It is evident that extremely active composites can be obtained by adjusting the shape, size and electronic/chemical state by means of appropriate synthetic and/or promotional routes. It is worth pointing out the superiority of finely-tuned $\text{CuO}_x/\text{CeO}_2$ samples as compared to noble metal-based catalysts, offering unique opportunities towards the rational design of highly active metal oxide catalysts. Moreover, as further guidance, it would be of particular importance to explore the combining effect of different adjusted parameters (*e.g.*, $\text{CuO}_x/\text{CeO}_2$ nanorods co-doped with main-group elements) towards further optimization.

Table 1.1. Indicative studies towards adjusting the CO oxidation performance of CuO_x/CeO₂ oxides.

Reaction Conditions	Adjusted Parameter (Employed Method)	Optimum System	T ₅₀ (°C)	Reference
0.2% CO + 1.0% O ₂ ; WHSV = 75,000 mL g ⁻¹ h ⁻¹ ; GHSV = 39,000 h ⁻¹	shape/size (hydrothermal synthesis)	8.5 wt.% Cu/CeO ₂ -nanorods	72	[116]
1.0% CO + 15.0% O ₂ ; WHSV = 7200 mL g ⁻¹ h ⁻¹	shape/size (hydrothermal synthesis)	15 wt.% Cu/CeO ₂ -nanorods CeO ₂ (15 nm), CuO (6.0 nm)	50	[209]
1.0% CO + 20.0% O ₂ ; WHSV = 80,000 mL g ⁻¹ h ⁻¹	shape/size (alcothermal method)	1.0 wt.% Cu/CeO ₂ -nanospheres (~130–150 nm spheres comprised of 2–5 nm nanoparticles)	85	[126]
1.0% CO + 2.5% O ₂ ; WHSV = 78,000 mL g ⁻¹ h ⁻¹	size/structure (solution-based pyrolysis of heterobimetallic Schiff complexes)	Cu _{0.1} Ce _{0.9} O _{2-x} monodisperse nanoparticles (~3.0 nm)	150	[239]
1.0% CO + 10.0% O ₂ ; WHSV = 60,000 mL g ⁻¹ h ⁻¹	size/structure (thermolytic decomposition in the presence of capping agent)	9.0 at.% Cu/CeO ₂ CeO ₂ (3.3 nm)	85	[210]
1.0% CO, air balance; WHSV = 30,000 mL g ⁻¹ h ⁻¹	size/structure (hydrothermal treatment)	Cu/CeO ₂ -nanospheres (Cu/(Cu+Ce) = 0.33, spherical particles of 300–400 nm diameter composed of nanoparticles of ca. 10 nm)	70	[211]
0.24% CO + 15.0% O ₂ ; WHSV = 60,000 mL g ⁻¹ h ⁻¹	size/structure (hard template method)	10 mol.% Cu/CeO ₂ -microspheres	150	[125]
1.0% CO, air balance; WHSV = 10,000 mL g ⁻¹ h ⁻¹	size/structure (hard template method)	three-dimensional (3D) Cu/CeO ₂ ((Cu/Cu+Ce) = 0.2)	34	[212]
1.0% CO + 21.0% O ₂ ; WHSV = 60,000 mL g ⁻¹ h ⁻¹	shape (thermal annealing of CeMOF precursors)	8.0 wt.% Cu/CeO ₂ -triple-shelled hollow nanospheres	110	[246]
1.0% CO, air balance; WHSV = 52,000 mL g ⁻¹ h ⁻¹	electronic/chemical state (doping by urea combustion method)	5.0 wt.% Cu/Ce _{0.9} Mn _{0.1} O ₂	120	[242]
2.4% CO + 1.2% O ₂ ; WHSV = 32,000 mL g ⁻¹ h ⁻¹	electronic/chemical state (doping by combustion method)	6.0 wt.% Cu/Ce _{0.7} Sn _{0.3} O ₂	80	[243]
1.0% CO + 20.0% O ₂ ; WHSV = 60,000 mL g ⁻¹ h ⁻¹	electronic/chemical state (doping by wetness co-impregnation method)	In ₂ O ₃ -CuO _x /CeO ₂ 1.25 wt.% In, 5.0 wt.% Cu	73	[244]
1.0% CO + 1.0% O ₂ ;	—	1.0 wt.% Pt/CeO ₂	70	[247]

Chapter 1

GHSV = 9600 h ⁻¹				
1.0% CO + 20.0% O ₂ ; WHSV = 60,000 mL g ⁻¹ h ⁻¹	—	3.0 wt.% Pd/CeO ₂	120	[244]
0.95% CO + 1.75% O ₂ ; WHSV = 12,000 mL g ⁻¹ h ⁻¹	—	0.2 wt.% Pd/CeO ₂	180	[248]

WHSV: Weight hourly space velocity [=] mL g⁻¹ h⁻¹; GHSV: Gas hourly space velocity [=] h⁻¹.

1.2.2. N₂O Decomposition

Nitrous oxide (N₂O) has been lately recognized as one of the most potent greenhouse gases and ozone depleting substances [249]. In view of this fact, the catalytic abatement of N₂O has received particular attention as one of the most promising remediation methods. Although noble metals exhibit satisfactory activity, their high cost and sensitivity to various substances (*e.g.*, O₂, H₂O) hinder widespread applications. Hence, as previously stated, noble metal-free composites have gained particular attention as potential candidates. The recent advances in the field of N₂O decomposition over metal oxides have been recently reviewed by Konsolakis [249]. It was clearly revealed that MOs could be effectively applied for N₂O decomposition, demonstrating comparable or even better catalytic performance compared to NMs-based catalysts. More interestingly, it was shown that very active and stable MOs could be obtained by adjusting their size, shape and electronic state through appropriate synthesis and promotional routes [249].

Herein, the main approaches, lately, followed to improve the deN₂O performance of MOs, exemplified by the CuO_x/CeO₂ system, are shortly presented. Table 1.2 presents indicative studies towards this direction. It is worth noticing the comparable or even superior deN₂O performance of finely-tuned CuO_x/CeO₂ samples as compared to noble metal-based catalysts (Table 1.2).

Table 1.2. Indicative studies followed to adjust the deN₂O performance of CuO_x/CeO₂ oxides.

Reaction Conditions	Adjusted Parameter (Employed Method)	Optimum System	T ₅₀ (°C)	Reference
0.26% N ₂ O; GHSV = 19,000 h ⁻¹	composition (citrate acid method)	67 mol.% Cu/CeO ₂	370	[213]
0.25% N ₂ O; GHSV = 45,000 h ⁻¹	composition (hard template replication)	40 mol.% Cu/CeO ₂	440	[250]
0.1% N ₂ O; WHSV = 90,000 mL g ⁻¹ h ⁻¹	size/structure (various synthesis methods)	20 wt.% Cu/CeO ₂ prepared by co-precipitation, CeO ₂ (11.8 nm)	465	[251]
0.1% N ₂ O; WHSV = 90,000 mL g ⁻¹ h ⁻¹	size/structure (co-precipitation method) and electronic state (alkali addition)	Cs-doped (1.0 at/nm ²) Cu/CeO ₂ CeO ₂ (13.5 nm)	420	[214]
0.2% N ₂ O; WHSV = 60,000 mL g ⁻¹ h ⁻¹	size/structure (hydrothermal method)	molar ratio Cu/Ce = 1, CeO ₂ (7.0 nm), CuO (24 nm)	380	[215]
0.25% N ₂ O; WHSV = 120,000 mL g ⁻¹ h ⁻¹	shape (hydrothermal method)	4.0 wt.% Cu/CeO ₂ -nanorods	430	[150]
0.25% N ₂ O; WHSV = 60,000 mL g ⁻¹ h ⁻¹	shape (glycothermal method)	10 wt.% Cu/CeO ₂ -nanospheres	380	[216]
0.1% N ₂ O; WHSV = 60,000 mL g ⁻¹ h ⁻¹	—	0.5 wt.% Rh/Al ₂ O ₃	340	[252]
0.1% N ₂ O; WHSV = 60,000 mL g ⁻¹ h ⁻¹	—	0.5 wt.% Pt/Al ₂ O ₃	500	[252]
0.1% N ₂ O; WHSV = 60,000 mL g ⁻¹ h ⁻¹	—	0.5 wt.% Pd/Al ₂ O ₃	>500	[252]

WHSV: Weight hourly space velocity [=] mL g⁻¹ h⁻¹; GHSV: Gas hourly space velocity [=] h⁻¹.

The effect of ceria morphology (nanorods, nanocubes, nanopolyhedra) on the deN₂O performance of CuO_x/CeO₂ composites was extensively investigated by Pintar and co-workers [150]. Copper clusters located on {100} and {110} planes –preferentially exposed on ceria nanorods– exhibit a normalized activity *ca.* 20% higher compared to {111} planes of polyhedra (Figure 1.11). In terms of conversion performance, the 4.0 wt.% CuO_x/Ceria-nanorods exhibited a half-conversion temperature (T_{50}) of about 430 °C compared to 440 °C and 470 °C of nanopolyhedra and nanocubes, respectively. On the basis of a thorough characterization study, it was disclosed that the oxygen mobility and the regeneration of active Cu phase is easier on ceria nanorods, which in turn, facilitates the deN₂O activity through oxygen desorption and replenishment of active sites [150]. In a similar manner, CuO_x supported on CeO₂ nanospheres exhibited high deN₂O performance (T_{50} = 380 °C, Table 1.2), ascribed mainly to the high population of CuO_x clusters on the high surface area CeO₂ nanospheres [216]. These findings clearly demonstrate the significant advances that can be achieved in the deN₂O process by engineering the size and shape of metal oxide composites.

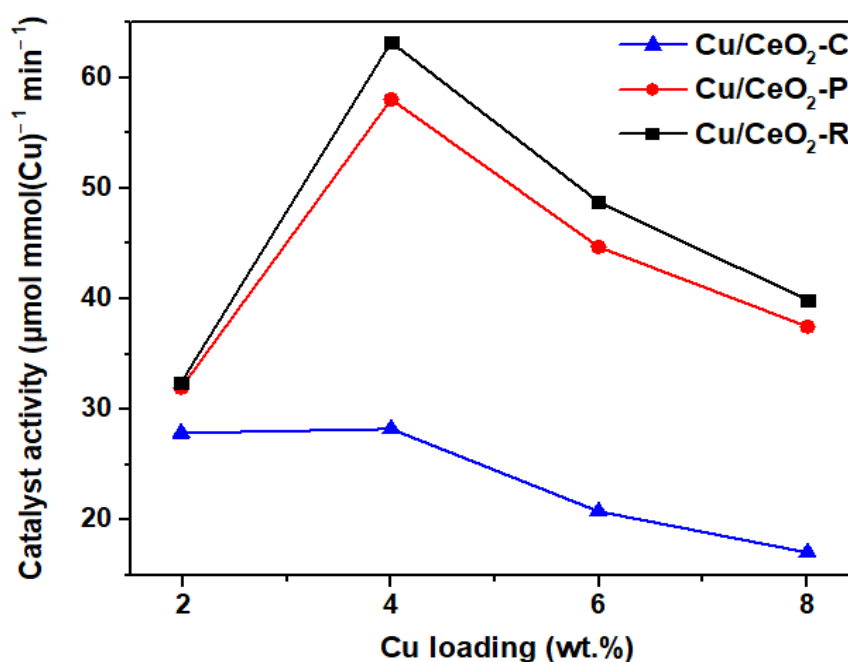


Figure 1.11. The activity of nanoshaped CuO_x/CeO₂ catalysts measured at $T = 375$ °C. Adapted from Reference [150]. Copyright © 2015, American Chemical Society.

1.2.3. Preferential Oxidation of CO (CO-PROX)

The copper-ceria binary oxides are among the most widely investigated catalytic systems in the preferential oxidation of carbon monoxide (CO-PROX), a reaction used for the production of highly purified hydrogen and the removal of CO. $\text{CuO}_x/\text{CeO}_2$ catalysts have gained particular attention in CO-PROX process, due to their superior performance, which is mainly ascribed to the peculiar properties of copper-ceria interface [31].

In light of the above-mentioned size, shape and electronic/chemical effects, numerous efforts have been put forward towards optimizing the CO-PROX performance. Indicative approaches followed to fine-tuning the CO-PROX performance are summarized in Table 1.3, and further discussed below.

Table 1.3. Indicative studies towards adjusting the CO preferential oxidation performance of CuO_x/CeO₂ oxides.

Reaction Conditions	Adjusted Parameter (Employed Method)	Optimum System	Maximum CO Conversion	Reference
1.0% CO + 1.0% O ₂ + 50.0% H ₂ ; WHSV = 60,000 mL g ⁻¹ h ⁻¹	composition (hydrothermal method)	5.0 wt.% Cu/CeO ₂	99.6% at 130 °C	[253]
1.0% CO + 1.0% O ₂ + 50.0% H ₂ ; WHSV = 60,000 mL g ⁻¹ h ⁻¹	composition (co-precipitation method)	30 at.% Cu/CeO ₂	~92% at 143 °C	[254]
1.0% CO + 1.0% O ₂ + 10.0% H ₂ O + 15.0% CO ₂ + 50.0% H ₂ ; WHSV = 30,000 mL g ⁻¹ h ⁻¹	composition (sol-gel precipitation/ chelating-impregnation)	10 wt.% Cu/CeO ₂	~99.5% at 100 °C	[255]
1.0% CO + 1.0% O ₂ + 40.0% H ₂ ; WHSV = 30,000 mL g ⁻¹ h ⁻¹	composition (nanocasting method)	7.0 wt.% Cu/CeO ₂	100% at 110 °C	[256]
1.2% CO + 1.2% O ₂ + 50.0% H ₂ ; WHSV = 20,000 mL g ⁻¹ h ⁻¹	composition/size (freeze-drying method)	6.0 wt.% Cu/CeO ₂ CeO ₂ (9.9 nm), CuO (10.7 nm)	100% at 90 °C	[257]
1.0% CO + 1.0% O ₂ + 50.0% H ₂ ; WHSV = 16,000 mL g ⁻¹ h ⁻¹	composition/size (solvent-free method, cupric nitrate as a copper precursor)	7.5 wt.% Cu/CeO ₂ CeO ₂ (16.3 nm)	100% at 120 °C	[258]
1.0% CO + 1.0% O ₂ + 50.0% H ₂ WHSV = 40,000 mL g ⁻¹ h ⁻¹	chemical state (ultrasound-aided impregnation)	Cu _{0.4} Ce _{0.6} O/CNTs	100% at 120 °C	[259]
1.25% CO + 1.25% O ₂ + 50.0% H ₂ ; WHSV = 20,000 mL g ⁻¹ h ⁻¹	size (Poly(methyl metacrylate) as a template)	6.0 wt.% Cu/CeO ₂ CeO ₂ (5.6 nm)	100% at 115 °C	[260]
1.0% CO + 1.0% O ₂ + 50.0% H ₂ ; WHSV = 36,000 mL g ⁻¹ h ⁻¹	shape (hydrothermal method)	4.0 wt.% Cu/CeO ₂ -octahedra	95% at 140 °C	[261]
1.0% CO + 1.0% O ₂ + 50.0% H ₂ ; WHSV = 60,000 mL g ⁻¹ h ⁻¹	shape (hydrothermal method)	5.0 wt.% Cu/CeO ₂ - rods/polyhedra	>99.0% at 95/90 °C	[147]
1.0% CO + 1.0% O ₂ + 50.0% H ₂ ; WHSV = 40,000 mL g ⁻¹ ·h ⁻¹	shape (hydrothermal method)	Cu/CeO ₂ -spheres CeO ₂ /CuO = 5	100% at 95 °C	[117]
1.0% CO + 1.0% O ₂ + 50.0% H ₂ ; WHSV = 16,000 mL g ⁻¹ ·h ⁻¹	shape (alcothermal method)	5.0 wt.% Cu/CeO ₂ -spheres	100% at 100 °C	[262]
1.0% CO + 1.0% O ₂ + 50.0% H ₂ ; WHSV = 40,000 mL g ⁻¹ ·h ⁻¹	shape (self-templating method)	Cu/CeO ₂ -triple-shelled hollow microspheres	100% at 95 °C	[263]
1.0% CO + 1.0% O ₂ + 50.0% H ₂ ; WHSV = 120,000 mL g ⁻¹ ·h ⁻¹	electronic/chemical state (potassium doping/carbon nanotubes)	Cu/CeO ₂ /CNTs (2.5 wt.% Cu, 20 wt.% CeO ₂ ,	100% at 175 °C	[264]

Chapter 1

		alkali/Cu = 0.68)		
1.0% CO + 1.0% O ₂ + 50.0% H ₂ ; WHSV = 60,000 mL g ⁻¹ h ⁻¹	pretreatment (with hydrogen)	10 wt.% Cu/CeO ₂	72% at 80 °C	[265]
1.0% CO + 1.0% O ₂ + 50.0% H ₂ ; WHSV = 60,000 mL g ⁻¹ h ⁻¹	pretreatment (with 2 M NaOH and etched with an ionic liquid)	10 wt.% Cu/CeO ₂	100% at 150 °C	[266]
1.0% CO + 1.25% O ₂ + 50.0% H ₂ ; WHSV = 25,000 mL g ⁻¹ h ⁻¹	pretreatment (with HNO ₃ , pH < 4)	7.5 wt.% Cu/CeO ₂	100% at 137 °C	[267]

WHSV: Weight hourly space velocity [=] mL g⁻¹ h⁻¹.

Several copper-ceria catalytic systems of various copper loadings have been synthesized by different methods, with the optimum Cu loading varying between 5 and 10 wt.% [253,255–257,268]. A further increase in Cu content from 10 to 15 wt.% has been reported to reduce the catalytic activity, due to the large CuO_x agglomerates on the catalyst surface [255]. It was revealed, by means of both *ex situ* and *in situ* characterization studies, that the desired CO oxidation process is related to partially reduced Cu^+ species, whereas, highly reduced copper species not strongly associated with CeO_2 favour the undesired H_2 oxidation [31,253,268–270]. In view of this fact, extensive research efforts have been put forward to control the two competitive oxidation processes by appropriately adjusting the geometric and electronic interactions between copper and ceria through the above-described fine-tuning approaches.

Regarding the shape effect, different copper-ceria nanostructures (rods, cubes, spheres, octahedra, spindle or multi-shelled morphologies) have been synthesized and studied for the CO–PROX reaction. It was revealed that the shape-controlled synthesis of ceria nanoparticles has a profound influence on the CO–PROX activity and selectivity. In particular, it was found that rod-shaped and polyhedral copper-ceria systems exhibited higher CO conversion performance ($T_{50} = 68$ °C) at low temperatures, as compared to plates ($T_{50} = 71$ °C) and cubes ($T_{50} = 89$ °C) [147]. The latter was mainly attributed to the smaller CuO_x clusters subjected to a strong interaction with the ceria carrier, which, in turn, facilitates the formation of Cu^+ sites and oxygen vacancies [147]. More importantly, a close relationship between measurable physicochemical parameters, such as the amount of Cu^+ species and the A_{584}/A_{454} Raman ratio (related to oxygen vacancies) with the catalytic performance was obtained; rod- and polyhedral-shaped samples exhibited the highest values on Cu^+ species and oxygen vacancies, demonstrating, also, the optimum CO–PROX performance [147].

In this point, it should be mentioned that in relation to which ceria shape is the most active or selective for the CO–PROX process, inconclusive results are acquired, due to the different reaction conditions applied (see Table 1.3) in conjunction to the complexity of CO–PROX process, which is affected to a different extent by the various interrelated parameters (*e.g.*, reducibility, metal dispersion, oxygen vacancies, oxidation state, metal-support interactions). Under this perspective, it was reported that copper-ceria nanocubes exhibited higher CO_2 selectivity than copper-ceria nanorods or nanospheres, due to the difficulty of nanocubes to fully reducing the copper oxide species under CO–PROX conditions [135,271], while, at the same time, exhibiting lower CO conversion than nanorods [271] and nanospheres [135]. In a similar manner, $\text{CuO}_x/\text{CeO}_2$ spheres and spindles, exposing {111} and {002} facets, showed the highest CO conversion ($T_{50} = 69$ and 74 °C, respectively), as well as a wide temperature window for total CO conversion (95–195 °C for spheres and 115–215 °C for spindles), in comparison with octahedrons, cubes and rods [117].

Interestingly, in different shaped ceria nanostructures, a close relationship is found between the concentration of oxygen vacancies and the amount of reduced copper species (Figure 1.12), clearly revealing the key role of exposed facets towards adjusting the catalytic performance. These findings were further substantiated by DFT calculations, showing the high population of oxygen vacancies at the intersection of $\{111\}$ and $\{002\}$ facets in opposition to CeO_2 $\{111\}$ surface [117].

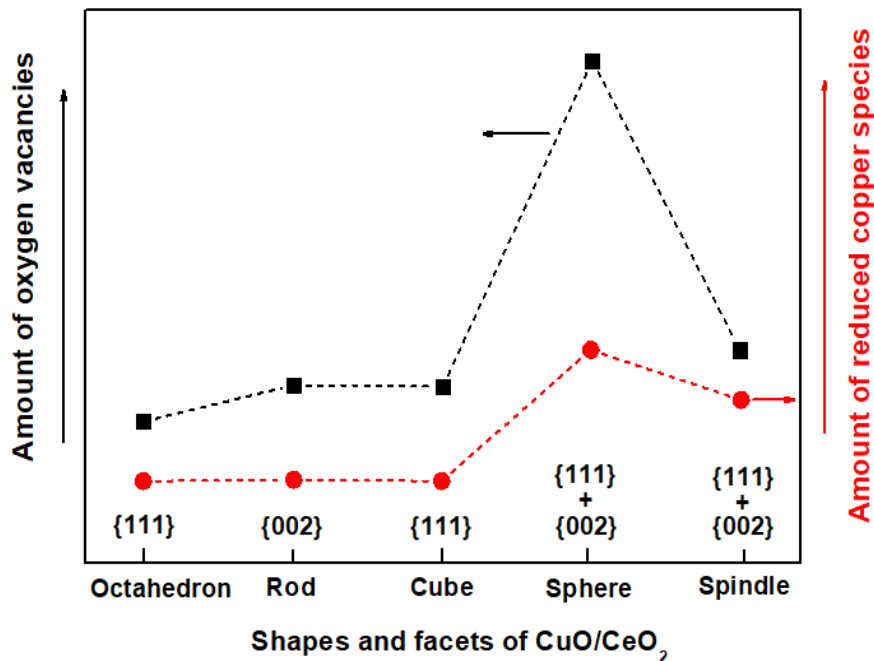


Figure 1.12. Plots of the number of oxygen vacancies and reduced copper species for the CuO/CeO_2 catalysts with different support shapes. Adapted from Reference [117]. Copyright© 2018, Elsevier.

In an attempt to optimize the CO–PROX performance through size and shape engineering single- and multi-shelled copper-ceria hollow microspheres were synthesized [263,272]. By tuning the number of shells, the catalytic activity was notably improved, with the triple-shelled structure exhibiting the highest activity and selectivity (100% CO conversion and 91% CO_2 selectivity at 95 °C), as well as a wide temperature window for complete CO conversion (95–195 °C) [263]. The increase in the number of shells enhances the electronic and geometric interaction between copper and ceria, offering a high population of exposed active sites and an increased space inside the catalyst which facilitates reactants' accessibility [263].

Taking into account the pivotal role of nanoparticles' crystallite size/shape and their consequent effect on metal-support interactions, different preparation routes have been investigated for the synthesis of copper-ceria composites, such as the hydrothermal method, the template-assisted method, the solid-state preparation method, sol-gel, co-precipitation, freeze-drying, deposition-

precipitation, *etc.* [253,254,256–258,260,265,273]. For instance, template-assisted synthesis resulted in small ceria crystallite sizes (*ca.* 5.6 nm), and thus, in a high population of copper-ceria interfacial sites with implications in Cu oxidation state and CO–PROX activity [260]. Moreover, the precursor compounds or the template agent used during synthesis procedure can affect the pore size and volume or the reducibility of the materials [258,274]. Interestingly, ethanol washing during the preparation of CuO_x/CeO₂ oxides leads to decreased particle sizes, as it affects the dehydration process between precursors' particles, resulting in decreased adsorbed water and improved dispersion [275]. Very recently, a novel ultrasound-assisted precipitation method was employed to adjust the defective structure of CeO₂ and in turn, the CO–RPOX activity [276]. By means of characterization techniques and theoretical calculations, it was shown that only two-electron defects on ceria surface (*i.e.*, defects adsorbing oxygen to form peroxides instead of superoxide species which are formed on one-electron defects) were responsible for the formation of Cu⁺ and Ce³⁺ species, which were intimately involved in the CO adsorption and oxygen activation processes [276]. In particular, the adsorption of O₂ on two-electron defects resulted in peroxides formation, followed by Cu ions incorporation towards the development of Cu–O–Ce structure. Meanwhile, the two additional electrons in the two-electron defects facilitate the electronic re-dispersion in Cu–O–Ce structure, leading to the creation of Cu⁺ (CO adsorption sites) and Ce³⁺ (oxygen activation sites).

Another approach in the direction of catalysts functionalization that has attracted considerable attention in recent years is the preparation of inverse catalytic systems. In particular, the co-existence of Cu⁺ and Cu²⁺ ions was observed in star-shaped inverse CeO₂/CuO_x catalysts which exhibited high catalytic activity [277]. Moreover, the alteration of Ce/Cu molar ratio and/or the pH value in the inverse CeO₂/CuO_x catalysts notably affects the morphology and the particle size, which in turn, favours the contact interface between ceria and copper, and thus, the CO oxidation at the expense of H₂ oxidation in PROX process [45]. In addition, a multi-step synthetic approach has been applied for a high concentration of oxygen vacancies to be successfully anchored at the interfaces of the inverse CeO₂/CuO_x system, leading to outstanding CO–PROX activity (~100% CO conversion at a wide temperature window 120–210 °C) and adequate stability [278].

The doping effect on the CO–PROX performance has been also studied in the inverse copper-ceria catalysts [279,280]. It was reported that doping ceria with transition metals (*e.g.*, Fe, Co, Ni) induces changes in the ceria lattice and in the formation of oxygen vacancies [279]. The doping element affects the reducibility of the CeO₂/CuO_x catalysts, while promoting the formation of Ce³⁺ ions and oxygen vacancies, with the NiO-doped CeO₂/CuO_x catalyst exhibiting the highest activity (T₅₀ = 68 °C) and the widest temperature window for total CO conversion (115–155 °C) [279]. In the inverse copper-ceria catalysts, it has also been found that the presence of Zn improves the

CO–PROX performance, as it has the ability to hinder the CuO reduction to highly reduced copper sites which provide the active sites for the H₂ oxidation [280].

By applying appropriate pretreatment protocols, the CO–PROX performance may be also greatly affected. In particular, the pretreatment of copper-ceria catalysts in an oxidative or reductive atmosphere affects the amount and dispersion of the active species, and consequently, the catalytic performance [265]. The pretreatment with hydrogen led to a breakage of the Cu–[O_x]-Ce structure, which resulted in enhanced catalytic performance, indicating the significance of the highly dispersed CuO_x clusters in the CO–PROX process [265]. Furthermore, the pretreatment in an acidic or a basic environment affects the interaction between the two oxide phases. For instance, the pretreatment of ceria spheres in a basic solvent (2M NaOH), followed by etching in an ionic liquid for the acquisition of ceria nanocubes, resulted in the best catalytic activity at temperatures lower than 150 °C, due to the strong interaction between the highly dispersed CuO_x clusters and ceria support [266]. An acidic treatment with nitric acid in nanorod-shaped CuO_x/CeO₂ catalysts has also been performed by Avgouropoulos and co-workers [267]. It was found that a highly acidic environment (pH < 4) led to an enrichment of catalysts' surface in Cu⁺ species and to high concentrations of oxygen vacancies and Ce³⁺ species, while facilitating the formation of surface hydroxyls that are considered responsible for controlling the interfacial interactions in the copper-ceria binary system [267]. All the above-mentioned characteristics in conjunction with the better copper dispersion and the improved reducibility of the highly acidic catalysts resulted in enhanced catalytic performance ($T_{50} \simeq 84$ °C) [267]. The same group has also investigated the pretreatment effect of employing ammonia solutions in copper-ceria nanorods [281]. It was revealed that the textural and structural properties of the modified catalysts remained almost unaffected after treatment, whereas, increasing the Cu:NH₃ ratio to 1:4 resulted in higher reducibility and gave rise to Cu⁺ and surface lattice oxygen species, leading, thus, to improved catalytic performance [281]. As shown in Figure 1.13, close relationships between the half-conversion temperature (T_{50}) and the main Raman peak shift or the concentration of Ce³⁺ and oxygen vacancies were observed [281].

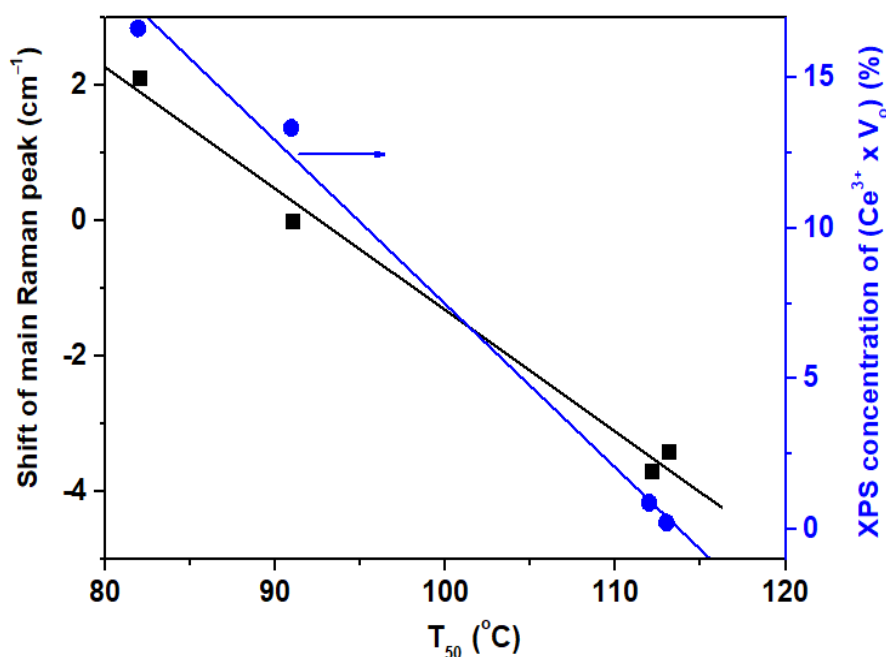


Figure 1.13. T_{50} vs. (i) shift of the main peak (F_{2g} Raman vibration mode) of fluorite CeO_2 and (ii) surface concentration of Ce^{3+} and oxygen vacancies determined via XPS analysis. Adapted from Reference [281]. Copyright© 2018, John Wiley and Sons.

Another adjusted parameter that can exert a profound influence on the catalytic performance is the electronic promotion mainly induced by alkali modifiers, as it may affect the chemisorption ability of active sites, as well as the copper-ceria interactions. In that context, it was found that the presence of K^+ ions in $\text{CuO}_x/\text{CeO}_2$ catalysts has a beneficial effect on CO–PROX process in the presence of both CO_2 and H_2O , since a proper K^+ content was proved to alleviate the CO_2 and H_2O adsorption on the reaction sites and thus, enhancing the catalytic performance [282]. Potassium has also been found to stabilize Cu^+ active species by affecting Cu–Ce interactions [283].

An additional engineering approach towards enhancing the CO–PROX reactivity of $\text{CuO}_x/\text{CeO}_2$ oxides involves the employment of chemical substances of specific architecture and textural properties, such as the carbon-based materials (rGO, CNTs, etc.). These materials favour the dispersion of copper and ceria, while affecting the reducibility and the population of oxygen vacancies, thus, resulting in enhanced catalytic performance at low temperatures [259,284–287]. For instance, the introduction of rGO resulted in abundant Ce^{3+} species and oxygen vacancies, offering high catalytic activity at temperatures below 135°C and good resistance to CO_2 and H_2O [286].

Interestingly, by combining electronic (alkali promotion) and chemical modification (carbon nanotubes), highly active multifunctional composites can be obtained. In copper-ceria catalysts supported on carbon nanotubes (CNTs) with a specific alkali/Cu atomic ratio, *i.e.*, 0.68, the nature

of the alkali metal (Li, Na, K, Cs) has been shown to affect the dispersion of ceria over CNTs and the copper-ceria interaction [264]. K-promoted $\text{CuO}_x/\text{CeO}_2$ oxides combined with CNTs exhibited high catalytic activity ($T_{50} \approx 109^\circ\text{C}$ as compared to 175°C of un-promoted catalyst), attributed to the K-induced modification on redox/electronic properties [264].

1.2.4. Water-Gas Shift Reaction (WGSR)

The water-gas shift reaction (WGSR) plays a key role in the production of pure hydrogen, through the chemical equilibrium: $\text{CO} + \text{H}_2\text{O} \leftrightarrow \text{CO}_2 + \text{H}_2$. Among the different catalytic systems, copper-ceria oxides have gained particular attention, due to their low cost and adequate catalytic performance. Moreover, significant efforts have been put forward towards optimizing the low-temperature WGS activity by means of the above discussed methodologies. Regarding $\text{CuO}_x/\text{CeO}_2$ catalyzed WGSR, two main reaction mechanisms have been proposed, namely, the redox and the associative mechanism. The first one involves the oxidation of adsorbed CO by oxygen originated by H_2O dissociation. The second one involves the reaction of CO with surface hydroxyl groups towards the formation and subsequent decomposition of various intermediate species, such as formates [163,288].

A thorough study concerning the nature of active species and the role of copper-ceria interface for the low-temperature WGSR has been recently performed by Chen *et al.* [288]. It was revealed that the activity of copper-ceria catalysts is intrinsically related with the Cu^+ species present at the interfacial perimeter, with the CO molecule being adsorbed on the Cu^+ sites, while water being dissociatively activated on the oxygen vacancies of ceria [288,289]. In a similar manner, Flytzani-Stephanopoulos and co-workers [290] have earlier shown that strongly bound $\text{Cu}-[\text{O}_x]-\text{Ce}$ species, probably associated with oxygen vacancies of ceria, are the active species for the low-temperature WGSR, whereas, the weakly bound copper oxide clusters and CuO_x nanoparticles act as spectators. Although the distinct role of copper and ceria and their interaction is not well determined, it is generally accepted that the activation of H_2O , linked to copper-ceria interface and oxygen vacancies, is the rate-determining step [288]. Therefore, particular attention has been paid to modulate the interfacial reactivity through the above discussed adjusting approaches. Indicative studies towards modulating the WGSR performance are summarized in Table 1.4, and further discussed below.

Table 1.4. Indicative studies towards adjusting the WGS performance of CuO_x/CeO₂ oxides.

Reaction Conditions	Adjusted Parameter (Employed Method)	Optimum System	Maximum CO Conversion	Reference
10.0% CO + 12.0% CO ₂ + 60.0% H ₂ ; vapor:gas = 1:1; WHSV = 3000 mL g ⁻¹ h ⁻¹	size/structure (precipitation)	20 wt.% Cu/CeO ₂	91.7% at 200 °C	[217,218]
2.0% CO + 10.0% H ₂ O; WHSV = 42,000 mL g ⁻¹ h ⁻¹	size/structure (bulk-nano interfaces by aerosol-spray method)	inverse CeO ₂ /Cu CeO ₂ (2–3 nm)	100% at 350 °C	[291]
1.0% CO + 3.0% H ₂ O; WHSV = 200,000 mL g ⁻¹ h ⁻¹	shape (microemulsion method)	5.0 wt.% Cu/CeO ₂ -nanospheres	64% at 350 °C	[138]
10.0% CO + 5.0% CO ₂ + 10.0% H ₂ O + 7.5% H ₂ ; WHSV = 60,000 mL g ⁻¹ h ⁻¹	shape (precipitation method)	Cu/CeO ₂ -nanoparticles	49% at 400 °C	[120]
3.5% CO + 3.5% CO ₂ + 25.0% H ₂ + 29.0% H ₂ O; GHSV = 6000 h ⁻¹	shape (hydrothermal method)	10 wt.% Cu/CeO ₂ -octahedrons	91.3% at 300 °C	[149]
10.0% CO + 5.0% CO ₂ + 5.0% H ₂ ; vapor:gas = 1:1; GHSV = 6000 h ⁻¹	electronic/chemical state (doping with cobalt by nanocasting)	Cu-Co-CeO ₂ (weight ratio of Cu:Co:Ce = 1:2:7)	95% at 300 °C	[292]
10.0% CO + 12.0% CO ₂ + 60.0% H ₂ ; vapor:gas = 1:1; WHSV = 2337 mL g ⁻¹ h ⁻¹	electronic/chemical state (doping with yttrium by co-precipitation)	Y-doped Cu/CeO ₂ 25 wt.% CuO, 2 wt.% Y ₂ O ₃	93.4% at 250 °C	[220]
15.0% CO + 6.0% CO ₂ + 55.0% H ₂ ; vapor:gas = 1:1; GHSV = 4500 h ⁻¹	pretreatment (with 20 CO ₂ /2H ₂ followed by calcination in O ₂)	10 wt.% Cu/CeO ₂	86% at 350 °C	[293]

WHSV: Weight hourly space velocity [=] mL g⁻¹ h⁻¹. GHSV: Gas hourly space velocity [=] h⁻¹.

The preparation method can affect various characteristics, such as the specific surface area, the total pore volume, the dispersion of the active phase or the crystallite size [217,294]. For instance, copper-ceria catalyst prepared by a hard template method showed higher WGS activity as compared to the one prepared by co-precipitation (62 vs. 54% CO conversion at 450 °C), due to its larger surface area and higher CuO_x dispersion, while they both exhibited a similar amount of acidic surface sites [294]. Among CuO_x/CeO₂ catalysts synthesized by different precipitation methods, the catalysts prepared by stepwise precipitation showed the highest CO conversion, due to their higher reducibility and oxygen defects [219]. Precipitation was also found to give catalysts with higher WGS activity, namely, 91.7% CO conversion at 200 °C, in comparison with the hydrothermal (82%) or sol-gel methods (64.5%), due to their abundance in oxygen vacancies, associated with the small CuO_x crystals and large pore volume [217].

The precipitating agent used could also exert a significant impact on the physicochemical properties of CuO_x/CeO₂ catalysts, with great implications in the catalytic behaviour [218,295]. By employing ammonia water instead of ammonium and potassium carbonate, the WGS activity is notably enhanced (91.7% CO conversion at 200 °C in contrast to 78.3% and 46.2%, respectively), due to the better dispersion of copper species and the stronger copper-ceria interactions [218]. Moreover, the copper precursor compound (nitrate or ammonium ions) and the preparation temperature can notably affect the WGS activity [295].

Recently, it was found that the dispersion of differently formed copper structures (particles, clusters, layers) on ceria of rod-like morphology is dependent on copper loading, with low copper loadings (1–15 mol.%) exhibiting monolayers and/or bilayers of copper, while a further increase in copper loading up to 28 mol.% results in faceted copper particles and multi-layers of copper [289]. At copper loadings up to 15 mol.%, a linear relationship between the CO conversion and the copper content was observed (Figure 1.14), indicating that the number of the active interfacial sites (Cu⁺-V_o-Ce³⁺) is significantly increased along with Cu content up to 15 mol.% [289].

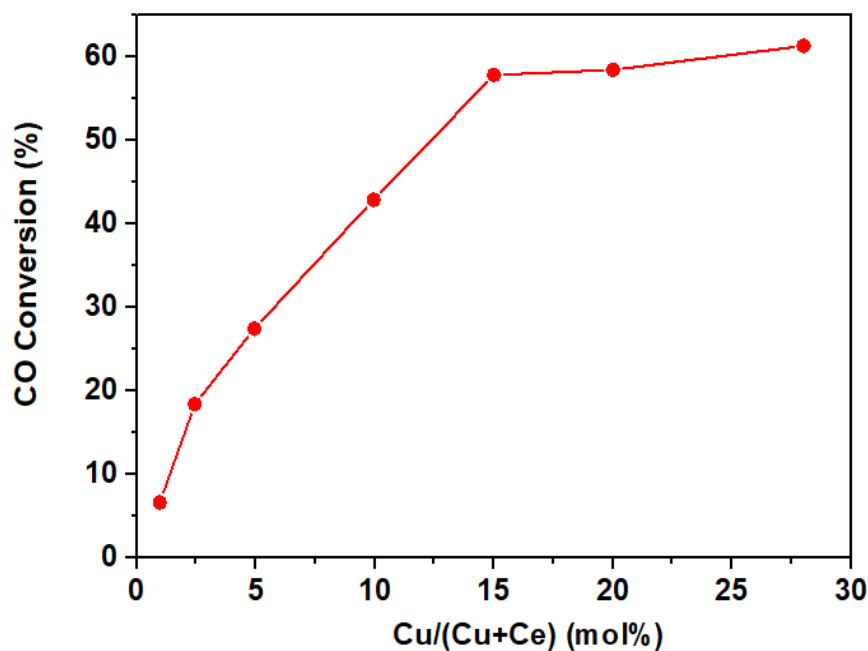


Figure 1.14. Low-temperature WGS reaction over the Cu/CeO₂ catalysts. CO conversion as a function of the copper content in the respect catalysts. Reaction conditions: 1.0 vol.% CO/3.0 vol.% H₂O/He, 40,000 h⁻¹, 200 °C. Adapted from Reference [289]. Copyright© 2019, Elsevier.

The morphological features of both copper and ceria counterparts notably affect the WGS activity. In a comprehensive study by Zhang *et al.* [296], it was reported that Cu cubes exhibit high WGS activity in contrast to Cu octahedra with the Cu–Cu suboxide (Cu_xO, $x \geq 10$) interface of Cu(100) surface being the active sites. In a similar manner, it was shown that ceria nanoshapes (rods, cubes, octahedra) exhibit different behaviour during interaction with CO and H₂O, due to their diverse defect chemistry [297]. Upon CO exposure, ceria nanocubes, exposing {100} planes, favour the formation of oxygen defects at the expense of the existing anti-Frenkel defects, while in nanorods and nanooctahedra (exposing mainly {111} planes) both types of defects are formed [297]. By combining Raman and FTIR results, it was revealed that H₂-reduced ceria rods and octahedra could be further reduced in CO, resulting in the formation of both defects. In contrast, cubes cannot be further reduced by CO; thus, oxygen is available to form carbonates and bicarbonates by converting Frenkel defects to oxygen vacancies [297]. These findings clearly revealed the key role of both copper and ceria nanoshape on the defect chemistry of individual counterparts. It should be noted, however, that in the binary copper-ceria system, where multifaceted interactions are taking place, the relationships between shape effects and catalytic activity can be rather complex, leading to inconsistent conclusions [120,138,149].

Very recently, Yan *et al.* [291] reported on a novel structural design approach towards optimizing the WGS activity of CuO_x/CeO₂ system. In particular, inverse copper-ceria catalysts of high

efficiency were developed through the fabrication of highly stable bulk-nano interfaces under reaction conditions. Nano-sized ceria particles (2–3 nm) were stabilized on bulk copper resulting in abundant ceria-copper interfaces [291]. This inverse catalyst showed outstanding WGS conversion ($T_{100} = 350\text{ }^{\circ}\text{C}$), due to the high amount of interfacial sites and the strong copper-ceria interaction, which facilitated the dissociation of water and the oxidation of CO [291].

The doping approach has also been employed to enhance the WGS activity of $\text{CuO}_x/\text{CeO}_2$ system [220,298]. For instance, copper-ceria catalysts doped with 2 wt.% yttrium have shown excellent WGS activity and high thermal stability, as yttrium favoured the oxygen vacancy formation on ceria [220]. Recently, Wang *et al.* [298] performed DFT calculations in order to theoretically investigate the alkali effect on the WGS activity of Cu(111) and Cu(110) surfaces. It was found that potassium enhances the WGS activity as it favours the dissociation of H_2O and induces stronger promotion on the (111) surface. With regard to other alkali metals (Na, Rb, Cs), the promoting effect on the dissociation of water differentiates with their electronegativities which induce changes in the work function, *i.e.*, the lower the work function, the stronger the promoting effect of the alkali [298].

Finally, the WGS activity and the sintering resistance of the $\text{CuO}_x/\text{CeO}_2$ catalysts can be further enhanced by improving the metal-support interactions through appropriate pretreatment protocols [293,299]. For example, the treatment of $\text{CuO}_x/\text{CeO}_2$ catalyst in a gas mixture of $20\text{CO}_2/2\text{H}_2$ led to highly active catalysts, due to the electron enrichment of copper atoms through the electronic metal-support interactions [293]. Moreover, ceria pretreatment in different atmosphere (air, vacuum or H_2) affected the WGS performance of $\text{CuO}_x/\text{CeO}_2$ catalysts, with the H_2 -pretreated samples exhibiting the highest conversion performance, due to the strong synergism between the two oxide phases, the small CuO_x particle size and the high concentration in oxygen vacancies [299].

1.2.5. CO_2 Hydrogenation

The hydrogenation of carbon dioxide to value-added chemicals, such as methanol, has received considerable attention, in terms of environmental protection and sustainable energy. The significant role of copper-ceria interfacial sites in the CO_2 hydrogenation process has been confirmed by both theoretical and experimental studies [31,300,301]. In particular, metal-oxide interface plays a key role in CO_2 hydrogenation process, as it could provide the active sites for reactants' adsorption, while these interfacial sites may stabilize the key intermediates [302]. In view of this fact, copper-ceria catalysts have shown higher selectivity in methanol than their zirconia-supported counterparts, as the copper-ceria interface favoured the dispersion of copper and the oxygen vacancy formation, while the interaction between copper and ceria led to a

decrease in copper particle size [303]. The interfaces between the defective CeO_{2-x} and the highly dispersed Cu^+/Cu^0 species are considered the active sites for methanol synthesis in the case of $\text{CuO}_x/\text{CeO}_2$ system [304]. Furthermore, the different metal-support interactions between the two catalysts resulted in different reaction intermediates, namely, carbonates for the $\text{CuO}_x/\text{CeO}_2$ catalysts and bicarbonates for the zirconia-supported ones, thus, resulting in different selectivity, with the copper-zirconia composites being highly selective towards CO [303].

In view of the above aspects, the fine-tuning of the metal-support interface could lead to highly active and selective catalysts. Indicative studies towards adjusting the CO_2 conversion to methanol under similar reaction conditions are summarized in Table 1.5, and further discussed below.

Table 1.5. Indicative studies towards adjusting the CO₂ conversion to methanol of CuO_x/CeO₂ oxides.

Reaction Conditions	Adjusted Parameter (Employed Method)	Optimum System	CO ₂ Conversion (Methanol Rate or Selectivity) at 260 °C	Reference
CO ₂ :H ₂ = 1:3; P = 3.0 MPa; GHSV = 1200 h ⁻¹	electronic/chemical state (doping with zinc and dispersion in SBA-15 by incipient wetness impregnation)	Cu _{0.5} Zn _{0.4} Ce _{0.1} /SBA-15	6.5% (33.6 mg g ⁻¹ h ⁻¹)	[305]
CO ₂ :H ₂ = 1:3; P = 3.0 MPa; WHSV = 14,400 mL g ⁻¹ h ⁻¹	electronic/chemical state (doping with alumina by co-precipitation)	60 wt.% Cu/AlCeO	17.0% (11.9 mmol g ⁻¹ h ⁻¹)	[306]
CO ₂ :H ₂ = 1:3; P = 3.0 MPa; GHSV = 6000 h ⁻¹	electronic/chemical state/shape (doping with Ni-Cu by impregnation)	CuNi ₂ /CeO ₂ -nanotubes Ni/(Cu+Ni) = 2/3	17.8% (18.1 mmol g ⁻¹ h ⁻¹)	[307]
CO ₂ :H ₂ = 1:3; P = 3.0 MPa; GHSV = 6000 h ⁻¹	electronic/chemical state/shape (doping with Ni-Cu by impregnation)	CuNi ₂ /CeO ₂ -nanorods 10 wt.% Cu and Ni	18.35% (73.33%)	[308]
CO ₂ :H ₂ = 1:3; P = 2.0 MPa; WHSV = 3000 mL g ⁻¹ h ⁻¹	shape (hydrothermal method)	5.0 wt.% Cu/CeO ₂ -nanorods	2.5% (71.0%)	[133]

WHSV: Weight hourly space velocity [=] mL g⁻¹ h⁻¹; GHSV: Gas hourly space velocity [=] h⁻¹.

The activity and selectivity of the $\text{CuO}_x/\text{CeO}_2$ catalysts for methanol synthesis are greatly affected by the support morphology. Copper-ceria nanorods exposing {100} and {110} crystal planes exhibited the highest methanol yield (Table 1.5) as compared to nanocubes and nanoparticles, due to the strong interaction between the two oxide phases and the high copper dispersion [133]. Copper-ceria nanorods were also found to be more active than nanocubes, while exhibiting similar conversion performance with the nanoparticles, for carbonate (diethyl) hydrogenation [151].

In a similar manner, $\text{CuO}_x/\text{CeO}_2$ catalysts led, mainly, to the production of CO at atmospheric pressures through the RWGS reaction, with the nanorod-shaped catalyst exhibiting higher CO_2 conversion ($\sim 50\%$ at 450°C) as compared to nanospheres ($\sim 40\%$ at 450°C), revealing the structure dependence of the RWGS reaction [139]. The active intermediates are preferably formed on the {110} ceria exposed surface of the rod-like morphology, resulting in high catalytic performance [139].

Copper-ceria nanorods of various copper loadings were also investigated in the hydrogenation of carbonate to methanol, with the catalysts of *ca.* 20 wt.% Cu content exhibiting superior catalytic performance [309]. The copper content can significantly affect the mole fraction of Ce^{3+} and Cu^+ species (Figure 1.15), and in turn, the methanol yield [309].

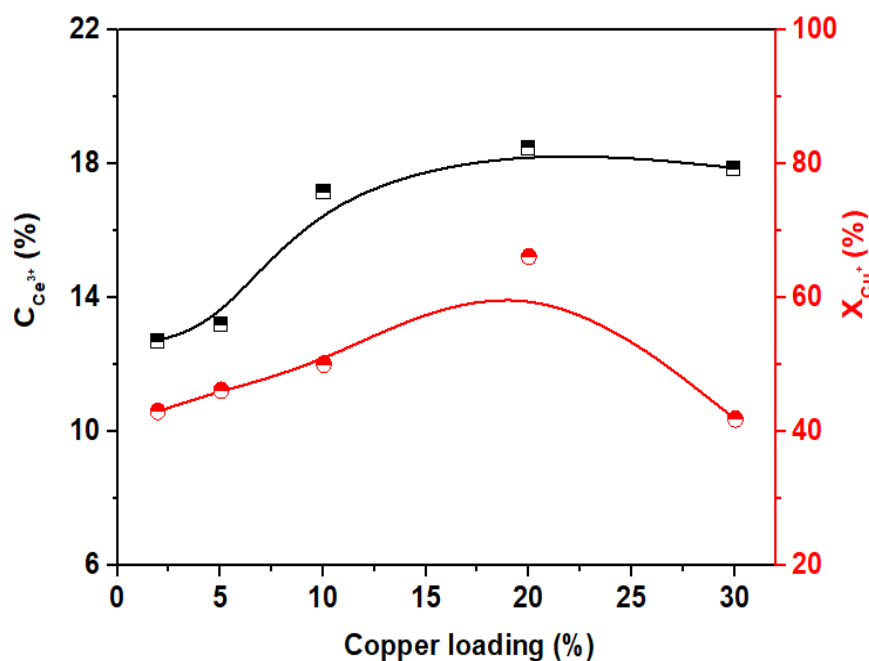


Figure 1.15. Mole ratio of Ce^{3+} and Cu^+ over the reduced Cu/CeO_2 catalysts as a function of Cu content. Adapted from Reference [309]. Copyright © 2018, John Wiley and Sons.

In addition, a space-confined synthetic approach was applied for the synthesis of highly dispersed copper-ceria catalysts for RWGS, offering 100% CO selectivity at 300 °C and ambient pressure [310]. The enhanced catalytic performance was ascribed to the abundance in interfaces formed among the highly dispersed copper nanoparticles and the Ce³⁺ species, thus, favouring H₂ spillover [310].

The controlled synthesis of multicomponent systems could also be an effective approach for highly active and selective hydrogenation catalysts (*e.g.*, [305–308,311]). For instance, the ternary composite consisting of Cu, ZnO, CeO_x, supported on SBA-15 exhibited high catalytic activity for methanol synthesis (Table 1.5), due to the peculiar synergistic effects between the different counterparts [305]. Copper was considered to be the active site for hydrogen activation, while ZnO and CeO_x oxides facilitated the CO₂ adsorption and hydrogen spillover on the interfacial sites [305]. In a similar manner, the introduction of alumina to ceria carrier (Cu/AlCe) led to highly active composites (Table 1.5), mainly ascribed to the high copper dispersion [306]. Interestingly, highly active and selective CO₂ hydrogenation catalysts can be obtained by co-adjusting the composition, structure and shape, in line with the fine-tuning methodology herein proposed (Figure 1.2). In this perspective, bimetallic composites (Cu-Ni) incorporated into ceria nanoparticles of specific morphology (*e.g.*, nanotubes, nanorods) could lead to highly active composites for the CO₂ hydrogenation to methanol (Table 1.5). The enhanced catalytic performance of Cu-Ni/CeO₂ nanoshaped catalysts was mainly interpreted on the basis of the synergistic interaction between Cu and Ni as well as of that between the ceria carrier and Cu-Ni alloy [307,308]. Similarly, the bimetallic Cu-Fe/CeO₂ catalyst has shown enhanced stability in the high-temperature RWGS due mainly to the fact that iron oxide clusters (FeO_x) highly dispersed over ceria act as textural promoters [311]. Finally, copper nanocrystals encapsulated in Zr-based MOFs demonstrated high activity and selectivity for CO₂ hydrogenation to methanol, outperforming the benchmark Cu/ZnO/Al₂O₃ catalyst [200].

1.3. CONCLUDING REMARKS

In the present theoretical chapter (literature review), the copper-ceria binary system has been selected as a reference system to reveal the different approaches that can be followed to modulate the local surface chemistry, and in turn, the catalytic performance of metal oxides (MOs), by means of size, shape and electronic/chemical functionalization. For instance, the employment of appropriate synthetic routes, such as the hydrothermal method, leads to the development of nanoparticles with specific morphologies, exposing distinct crystal facets of different coordination environments, with great implications in catalysis. Moreover, particles' size/shape engineering strongly affects the interfacial reactivity through both geometric and electronic interactions, offering metal oxide systems with the desired properties. In addition, special pretreatment protocols or activation procedures can notably affect the metal dispersion and the population of oxygen defects, with great consequences in the catalytic efficiency. In view of the above, the fine tuning of metal oxides by combining bulk and nano effects or by adjusting the coordination environment could lead to highly efficient catalysts.

Besides the modulation of local surface chemistry by means of size and shape engineering, the electronic/chemical modification (*e.g.*, alkali promotion, incorporation of rGO or g-C₃N₄, employment of MOFs) can be adopted as an additional functionalization tool to regulate the electronic environment and the oxygen exchange kinetics of MOs.

In view of the above aspects, highly active composites, with a comparable or even better performance than that of NMs, have been developed for various processes, such as CO oxidation, N₂O decomposition, preferential oxidation of CO, among others. For instance, the combination of precipitation method with alkali promotion can lead to highly active and oxygen-tolerant CuO_x/CeO₂ catalysts for N₂O decomposition. On the other hand, the modulation of ceria support morphology (nanorods) by the hydrothermal method resulted in CuO_x/CeO₂ composites with superior CO oxidation performance, even better to that of Pt-based catalysts. More importantly, the co-adjustment of different parameters (*e.g.*, the shape of individual counterparts along with the electronic state of metal entities) could lead not only to distinct reactivity of each counterpart, but also to different synergistic interactions, offering mixed metal oxides of unique features. Hence, metal oxides appropriately adjusted by means of suitable synthetic and electronic/chemical modification routes could provide the materials platform for real-life energy and environmental applications.

REFERENCES

1. Yao, X.; Tang, C.; Gao, F.; Dong, L. Research progress on the catalytic elimination of atmospheric molecular contaminants over supported metal-oxide catalysts. *Catal. Sci. Technol.* **2014**, *4*, 2814–2829. doi: 10.1039/c4cy00397g
2. Melchionna, M.; Fornasiero, P. The role of ceria-based nanostructured materials in energy applications. *Mater. Today* **2014**, *17*, 349–357. doi: 10.1016/j.mattod.2014.05.005
3. Fang, Y.; Guo, Y. Copper-based non-precious metal heterogeneous catalysts for environmental remediation. *Chinese J. Catal.* **2018**, *39*, 566–582. doi: 10.1016/S1872-2067(17)62996-6
4. Yuan, C.; Wu, H.B.; Xie, Y.; Lou, X.W. Mixed Transition-Metal Oxides: Design, Synthesis, and Energy-Related Applications. *Angew. Chem. Int. Ed.* **2014**, *53*, 1488–1504. doi: 10.1002/anie.201303971
5. Montini, T.; Melchionna, M.; Monai, M.; Fornasiero, P. Fundamentals and Catalytic Applications of CeO₂-Based Materials. *Chem. Rev.* **2016**, *116*, 5987–6041. doi: 10.1021/acs.chemrev.5b00603
6. Wu, K.; Sun, L.-D.; Yan, C.-H. Recent Progress in Well-Controlled Synthesis of Ceria-Based Nanocatalysts towards Enhanced Catalytic Performance. *Adv. Energy Mater.* **2016**, *6*, 1600501. doi: 10.1002/aenm.201600501
7. Rodriguez, J.A.; Liu, P.; Graciani, J.; Senanayake, S.D.; Grinter, D.C.; Stacchiola, D.; Hrbek, J.; Fernández-Sanz, J. Inverse Oxide/Metal Catalysts in Fundamental Studies and Practical Applications: A Perspective of Recent Developments. *J. Phys. Chem. Lett.* **2016**, *7*, 2627–2639. doi: 10.1021/acs.jpcllett.6b00499
8. Spezzati, G.; Benavidez, A.D.; DeLaRiva, A.T.; Su, Y.; Hofmann, J.P.; Asahina, S.; Olivier, E.J.; Neethling, J.H.; Miller, J.T.; Datye, A.K.; Hensen, E.J.M. CO oxidation by Pd supported on CeO₂(100) and CeO₂(111) facets. *Appl. Catal. B Environ.* **2019**, *243*, 36–46. doi: 10.1016/j.apcatb.2018.10.015
9. Morfin, F.; Nguyen, T.-S.; Rousset, J.-L.; Piccolo, L. Synergy between hydrogen and ceria in Pt-catalyzed CO oxidation: An investigation on Pt–CeO₂ catalysts synthesized by solution combustion. *Appl. Catal. B Environ.* **2016**, *197*, 2–13. doi: 10.1016/j.apcatb.2016.01.056
10. Gatla, S.; Aubert, D.; Flaud, V.; Grosjean, R.; Lunkenbein, T.; Mathon, O.; Pascarelli, S.; Kaper, H. Facile synthesis of high-surface area platinum-doped ceria for low temperature CO oxidation. *Catal. Today* **2019**, *333*, 105–112. doi:

- 10.1016/j.cattod.2018.06.032
11. Gatla, S.; Aubert, D.; Agostini, G.; Mathon, O.; Pascarelli, S.; Lunkenbein, T.; Willinger, M.G.; Kaper, H. Room-Temperature CO Oxidation Catalyst: Low-Temperature Metal-Support Interaction between Platinum Nanoparticles and Nanosized Ceria. *ACS Catal.* **2016**, *6*, 6151–6155. doi: 10.1021/acscatal.6b00677
 12. Parres-Esclapez, S.; Such-Basañez, I.; Illán-Gómez, M.J.; Salinas-Martínez de Lecea, C.; Bueno-López, A. Study by isotopic gases and *in situ* spectroscopies (DRIFTS, XPS and Raman) of the N₂O decomposition mechanism on Rh/CeO₂ and Rh/γ-Al₂O₃ catalysts. *J. Catal.* **2010**, *276*, 390–401. doi: 10.1016/j.jcat.2010.10.001
 13. Zhu, H.; Li, Y.; Zheng, X. In-situ DRIFTS study of CeO₂ supported Rh catalysts for N₂O decomposition. *Appl. Catal. A Gen.* **2019**, *571*, 89–95. doi: 10.1016/j.apcata.2018.12.020
 14. Zheng, J.; Meyer, S.; Köhler, K. Abatement of nitrous oxide by ruthenium catalysts: Influence of the support. *Appl. Catal. A Gen.* **2015**, *505*, 44–51. doi: 10.1016/j.apcata.2015.07.019
 15. Pachatouridou, E.; Papista, E.; Iliopoulou, E.F.; Delimitis, A.; Goula, G.; Yentekakis, I.V.; Marnellos, G.E.; Konsolakis, M. Nitrous oxide decomposition over Al₂O₃ supported noble metals (Pt, Pd, Ir): Effect of metal loading and feed composition. *J. Environ. Chem. Eng.* **2015**, *3*, 815–821. doi: 10.1016/j.jece.2015.03.030
 16. Pachatouridou, E.; Papista, E.; Delimitis, A.; Vasiliades, M.A.; Efstathiou, A.M.; Amiridis, M.D.; Alexeev, O.S.; Bloom, D.; Marnellos, G.E.; Konsolakis, M.; Iliopoulou, E. N₂O decomposition over ceria-promoted Ir/Al₂O₃ catalysts: The role of ceria. *Appl. Catal. B Environ.* **2016**, *187*, 259–268. doi: 10.1016/j.apcatb.2016.01.049
 17. Carabineiro, S.A.C.; Papista, E.; Marnellos, G.E.; Tavares, P.B.; Maldonado-Hódar, F.J.; Konsolakis, M. Catalytic decomposition of N₂O on inorganic oxides: Effect of doping with Au nanoparticles. *Mol. Catal.* **2017**, *436*, 78–89. doi: 10.1016/j.mcat.2017.04.009
 18. Vecchietti, J.; Bonivardi, A.; Xu, W.; Stacchiola, D.; Delgado, J.J.; Calatayud, M.; Collins, S.E. Understanding the Role of Oxygen Vacancies in the Water Gas Shift Reaction on Ceria-Supported Platinum Catalysts. *ACS Catal.* **2014**, *4*, 2088–2096. doi: 10.1021/cs500323u
 19. Pierre, D.; Deng, W.; Flytzani-Stephanopoulos, M. The Importance of Strongly Bound Pt-CeO_x Species for the Water-gas Shift Reaction: Catalyst Activity and Stability Evaluation. *Top. Catal.* **2007**, *46*, 363–373. doi: 10.1007/s11244-007-9013-8
 20. Mei, Z.; Li, Y.; Fan, M.; Zhao, L.; Zhao, J. Effect of the interactions between Pt species

- and ceria on Pt/ceria catalysts for water gas shift: The XPS studies. *Chem. Eng. J.* **2015**, *259*, 293–302. doi: 10.1016/j.cej.2014.07.125
21. Ting, K.W.; Toyao, T.; Siddiki, S.M.A.H.; Shimizu, K. Low-Temperature Hydrogenation of CO₂ to Methanol over Heterogeneous TiO₂-Supported Re Catalysts. *ACS Catal.* **2019**, *9*, 3685–3693. doi: 10.1021/acscatal.8b04821
 22. Wang, F.; He, S.; Chen, H.; Wang, B.; Zheng, L.; Wei, M.; Evans, D.G.; Duan, X. Active Site Dependent Reaction Mechanism over Ru/CeO₂ Catalyst toward CO₂ Methanation. *J. Am. Chem. Soc.* **2016**, *138*, 6298–6305. doi: 10.1021/jacs.6b02762
 23. Sakpal, T.; Lefferts, L. Structure-dependent activity of CeO₂ supported Ru catalysts for CO₂ methanation. *J. Catal.* **2018**, *367*, 171–180. doi: 10.1016/j.jcat.2018.08.027
 24. Vourros, A.; Garagounis, I.; Kyriakou, V.; Carabineiro, S.A.C.; Maldonado-Hódar, F.J.; Marnellos, G.E.; Konsolakis, M. Carbon dioxide hydrogenation over supported Au nanoparticles: Effect of the support. *J. CO₂ Util.* **2017**, *19*, 247–256. doi: 10.1016/j.jcou.2017.04.005
 25. Kyriakou, V.; Vourros, A.; Garagounis, I.; Carabineiro, S.A.C.; Maldonado-Hódar, F.J.; Marnellos, G.E.; Konsolakis, M. Highly active and stable TiO₂-supported Au nanoparticles for CO₂ reduction. *Catal. Commun.* **2017**, *98*, 52–56. doi: 10.1016/j.catcom.2017.05.003
 26. Zhou, Y.; Wang, Z.; Liu, C. Perspective on CO oxidation over Pd-based catalysts. *Catal. Sci. Technol.* **2015**, *5*, 69–81. doi: 10.1039/C4CY00983E
 27. Carter, J.H.; Hutchings, G.J. Recent Advances in the Gold-Catalysed Low-Temperature Water–Gas Shift Reaction. *Catalysts* **2018**, *8*, 627. doi: 10.3390/catal8120627
 28. Aneggi, E.; Boaro, M.; Colussi, S.; De Leitenburg, C.; Trovarelli, A. Chapter 289–Ceria-Based Materials in Catalysis: Historical Perspective and Future Trends. *Handb. Phys. Chem. Rare Earths* **2016**, *50*, 209–242. doi: 10.1016/bs.hpre.2016.05.002
 29. Tang, W.-X.; Gao, P.-X. Nanostructured cerium oxide: preparation, characterization, and application in energy and environmental catalysis. *MRS Commun.* **2016**, *6*, 311–329. doi: 10.1557/mrc.2016.52
 30. Su, X.; Yang, X.; Zhao, B.; Huang, Y. Designing of highly selective and high-temperature durable RWGS heterogeneous catalysts: recent advances and the future directions. *J. Energy Chem.* **2017**, *26*, 854–867. doi: 10.1016/j.jechem.2017.07.006
 31. Konsolakis, M. The role of Copper–Ceria interactions in catalysis science: Recent theoretical and experimental advances. *Appl. Catal. B Environ.* **2016**, *198*, 49–66. doi:

- 10.1016/j.apcatb.2016.05.037
32. Carabineiro, S.A.C.; Chen, X.; Konsolakis, M.; Psarras, A.C.; Tavares, P.B.; Órfão, J.J.M.; Pereira, M.F.R.; Figueiredo, J.L. Catalytic oxidation of toluene on Ce-Co and La-Co mixed oxides synthesized by exotemplating and evaporation methods. *Catal. Today* **2015**, *244*, 161–171. doi: 10.1016/j.cattod.2014.06.018
33. Carabineiro, S.A.C.; Konsolakis, M.; Marnellos, G.E.-N.; Asad, M.F.; Soares, O.S.G.P.; Tavares, P.B.; Pereira, M.F.R.; De Melo Órfão, J.J.; Figueiredo, J.L. Ethyl Acetate Abatement on Copper Catalysts Supported on Ceria Doped with Rare Earth Oxides. *Molecules* **2016**, *21*, 644. doi: 10.3390/molecules21050644
34. Díez-Ramírez, J.; Sánchez, P.; Kyriakou, V.; Zafeiratos, S.; Marnellos, G.E.; Konsolakis, M.; Dorado, F. Effect of support nature on the cobalt-catalyzed CO₂ hydrogenation. *J. CO₂ Util.* **2017**, *21*, 562–571. doi: 10.1016/j.jcou.2017.08.019
35. Konsolakis, M.; Carabineiro, S.A.C.; Marnellos, G.E.; Asad, M.F.; Soares, O.S.G.P.; Pereira, M.F.R.; Órfão, J.J.M.; Figueiredo, J.L. Effect of cobalt loading on the solid state properties and ethyl acetate oxidation performance of cobalt-cerium mixed oxides. *J. Colloid Interface Sci.* **2017**, *496*, 141–149. doi: 10.1016/j.jcis.2017.02.014
36. Konsolakis, M.; Carabineiro, S.A.C.; Marnellos, G.E.; Asad, M.F.; Soares, O.S.G.P.; Pereira, M.F.R.; Órfão, J.J.M.; Figueiredo, J.L. Volatile organic compounds abatement over copper-based catalysts: Effect of support. *Inorganica Chim. Acta* **2017**, *455*, 473–482. doi: 10.1016/j.ica.2016.07.059
37. Konsolakis, M.; Carabineiro, S.A.C.; Tavares, P.B.; Figueiredo, J.L. Redox properties and VOC oxidation activity of Cu catalysts supported on Ce_{1-x}Sm_xO₈ mixed oxides. *J. Hazard. Mater.* **2013**, *261*, 512–521. doi: 10.1016/j.jhazmat.2013.08.016
38. Konsolakis, M.; Ioakeimidis, Z. Surface/structure functionalization of copper-based catalysts by metal-support and/or metal-metal interactions. *Appl. Surf. Sci.* **2014**, *320*, 244–255. doi: 10.1016/j.apsusc.2014.08.114
39. Konsolakis, M.; Ioakimidis, Z.; Kraia, Tz.; Marnellos, G.E. Hydrogen Production by Ethanol Steam Reforming (ESR) over CeO₂ Supported Transition Metal (Fe, Co, Ni, Cu) Catalysts: Insight into the Structure-Activity Relationship. *Catalysts* **2016**, *6*, 39. doi: 10.3390/catal6030039
40. Konsolakis, M.; Sgourakis, M.; Carabineiro, S.A.C. Surface and redox properties of cobalt-ceria binary oxides: On the effect of Co content and pretreatment conditions. *Appl. Surf. Sci.* **2015**, *341*, 48–54. doi: 10.1016/j.apsusc.2015.02.188
41. Kraia, Tz.; Kaklidis, N.; Konsolakis, M.; Marnellos, G.E. Hydrogen production by H₂S

- decomposition over ceria supported transition metal (Co, Ni, Fe and Cu) catalysts. *Int. J. Hydrogen Energy* **2019**, *44*, 9753–9762. doi: 10.1016/j.ijhydene.2018.12.070
42. Lykaki, M.; Papista, E.; Kaklidis, N.; Carabineiro, S.A.C.; Konsolakis, M. Ceria Nanoparticles' Morphological Effects on the N₂O Decomposition Performance of Co₃O₄/CeO₂ Mixed Oxides. *Catalysts* **2019**, *9*, 233. doi: 10.3390/catal9030233
43. Lykaki, M.; Stefa, S.; Carabineiro, S.A.C.; Pandis, P.K.; Stathopoulos, V.N.; Konsolakis, M. Facet-Dependent Reactivity of Fe₂O₃/CeO₂ Nanocomposites: Effect of Ceria Morphology on CO Oxidation. *Catalysts* **2019**, *9*, 371. doi: 10.3390/catal9040371
44. Konsolakis, M.; Lykaki, M. Recent Advances on the Rational Design of Non-Precious Metal Oxide Catalysts Exemplified by CuO_x/CeO₂ Binary System: Implications of Size, Shape and Electronic Effects on Intrinsic Reactivity and Metal-Support Interactions. *Catalysts* **2020**, *10*, 160. doi: 10.3390/catal10020160
45. Zeng, S.; Zhang, W.; Guo, S.; Su, H. Inverse rod-like CeO₂ supported on CuO prepared by hydrothermal method for preferential oxidation of carbon monoxide. *Catal. Commun.* **2012**, *23*, 62–66. doi: 10.1016/j.catcom.2012.02.028
46. Rodriguez, J.A.; Liu, P.; Hrbek, J.; Evans, J.; Pérez, M. Water Gas Shift Reaction on Cu and Au Nanoparticles Supported on CeO₂(111) and ZnO(000 $\bar{1}$): Intrinsic Activity and Importance of Support Interactions. *Angew. Chem. Int. Ed.* **2007**, *46*, 1329–1332. doi: 10.1002/anie.200603931
47. Ranga Rao, G.; Mishra, B.G. Structural, redox and catalytic chemistry of ceria based materials. *Bull. Catal. Soc. India* **2003**, *2*, 122–134.
48. Rodriguez, J.A.; Grinter, D.C.; Liu, Z.; Palomino, R.M.; Senanayake, S.D. Ceria-based model catalysts: Fundamental studies on the importance of the metal-ceria interface in CO oxidation, the water-gas shift, CO₂ hydrogenation, and methane and alcohol reforming. *Chem. Soc. Rev.* **2017**, *46*, 1824–1841. doi: 10.1039/C6CS00863A
49. Zhang, D.; Du, X.; Shi, L.; Gao, R. Shape-controlled synthesis and catalytic application of ceria nanomaterials. *Dalton Trans.* **2012**, *41*, 14455–14475. doi: 10.1039/C2DT31759A
50. Razmgar, K.; Altarawneh, M.; Oluwoye, I.; Senanayake, G. Ceria-Based Catalysts for Selective Hydrogenation Reactions: A Critical Review. *Catal. Surv. from Asia* **2021**, *25*, 27–47. doi: 10.1007/s10563-020-09319-z
51. Dong, L.; Yao, X.; Chen, Y. Interactions among supported copper-based catalyst components and their effects on performance: A review. *Chinese J. Catal.* **2013**, *34*, 851–864. doi: 10.1016/S1872-2067(12)60592-0

52. Pacchioni, G. Electronic interactions and charge transfers of metal atoms and clusters on oxide surfaces. *Phys. Chem. Chem. Phys.* **2013**, *15*, 1737–1757. doi: 10.1039/C2CP43731G
53. Zhou, Y.; Li, Y.; Shen, W. Shape Engineering of Oxide Nanoparticles for Heterogeneous Catalysis. *Chem. Asian J.* **2016**, *11*, 1470–1488. doi: 10.1002/asia.201600115
54. Cargnello, M.; Doan-Nguyen, V.V.T.; Gordon, T.R.; Diaz, R.E.; Stach, E.A.; Gorte, R.J.; Fornasiero, P.; Murray, C.B. Control of Metal Nanocrystal Size Reveals Metal-Support Interface Role for Ceria Catalysts. *Science* **2013**, *341*, 771–773. doi: 10.1126/science.1240148
55. Mistry, H.; Behafarid, F.; Reske, R.; Varela, A.S.; Strasser, P.; Roldan Cuenya, B. Tuning Catalytic Selectivity at the Mesoscale via Interparticle Interactions. *ACS Catal.* **2016**, *6*, 1075–1080. doi: 10.1021/acscatal.5b02202
56. Ahmadi, M.; Mistry, H.; Roldan Cuenya, B. Tailoring the Catalytic Properties of Metal Nanoparticles via Support Interactions. *J. Phys. Chem. Lett.* **2016**, *7*, 3519–3533. doi: 10.1021/acs.jpcclett.6b01198
57. Di Sarli, V.; Landi, G.; Di Benedetto, A.; Lisi, L. Synergy Between Ceria and Metals (Ag or Cu) in Catalytic Diesel Particulate Filters: Effect of the Metal Content and of the Preparation Method on the Regeneration Performance. *Top. Catal.* **2021**, *64*, 256–269. doi: 10.1007/s11244-020-01384-y
58. Hermes, E.D.; Jenness, G.R.; Schmidt, J.R. Decoupling the electronic, geometric and interfacial contributions to support effects in heterogeneous catalysis. *Mol. Simul.* **2015**, *41*, 123–133. doi: 10.1080/08927022.2014.926549
59. Puigdollers, A.R.; Schlexer, P.; Tosoni, S.; Pacchioni, G. Increasing Oxide Reducibility: The Role of Metal/Oxide Interfaces in the Formation of Oxygen Vacancies. *ACS Catal.* **2017**, *7*, 6493–6513. doi: 10.1021/acscatal.7b01913
60. Mitchell, S.; Qin, R.; Zheng, N.; Pérez-Ramírez, J. Nanoscale engineering of catalytic materials for sustainable technologies. *Nat. Nanotechnol.* **2021**, *16*, 129–139. doi: 10.1038/s41565-020-00799-8
61. Senanayake, S.D.; Rodriguez, J.A.; Stacchiola, D. Electronic Metal–Support Interactions and the Production of Hydrogen Through the Water-Gas Shift Reaction and Ethanol Steam Reforming: Fundamental Studies with Well-Defined Model Catalysts. *Top. Catal.* **2013**, *56*, 1488–1498. doi: 10.1007/s11244-013-0148-5
62. Capdevila-Cortada, M.; Vilé, G.; Teschner, D.; Pérez-Ramírez, J.; López, N. Reactivity

- descriptors for ceria in catalysis. *Appl. Catal. B Environ.* **2016**, *197*, 299–312. doi: 10.1016/j.apcatb.2016.02.035
63. Van Deelen, T.W.; Hernández Mejía, C.; De Jong, K.P. Control of metal-support interactions in heterogeneous catalysts to enhance activity and selectivity. *Nat. Catal.* **2019**, *2*, 955–970. doi: 10.1038/s41929-019-0364-x
64. Uzunoglu, A.; Zhang, H.; Andreescu, S.; Stanciu, L.A. CeO₂-MO_x (M: Zr, Ti, Cu) mixed metal oxides with enhanced oxygen storage capacity. *J. Mater. Sci.* **2015**, *50*, 3750–3762. doi: 10.1007/s10853-015-8939-7
65. Tang, X.; Zhang, B.; Li, Y.; Xu, Y.; Xin, Q.; Shen, W. CuO/CeO₂ catalysts: Redox features and catalytic behaviors. *Appl. Catal. A Gen.* **2005**, *288*, 116–125. doi: 10.1016/j.apcata.2005.04.024
66. Lu, Z.; Yang, Z.; He, B.; Castleton, C.; Hermansson, K. Cu-doped ceria: Oxygen vacancy formation made easy. *Chem. Phys. Lett.* **2011**, *510*, 60–66. doi: 10.1016/j.cplett.2011.03.091
67. Wang, X.; Rodriguez, J.A.; Hanson, J.C.; Gamarra, D.; Martínez-Arias, A.; Fernández-García, M. Unusual Physical and Chemical Properties of Cu in Ce_{1-x}Cu_xO₂ Oxides. *J. Phys. Chem. B* **2005**, *109*, 19595–19603. doi: 10.1021/jp051970h
68. Beckers, J.; Rothenberg, G. Redox properties of doped and supported copper-ceria catalysts. *Dalt. Trans.* **2008**, 6573–6578. doi: 10.1039/B809769K
69. Cao, S.; Tao, F.; Tang, Y.; Li, Y.; Yu, J. Size- and shape-dependent catalytic performances of oxidation and reduction reactions on nanocatalysts. *Chem. Soc. Rev.* **2016**, *45*, 4747–4765. doi: 10.1039/C6CS00094K
70. Xu, J.; Harmer, J.; Li, G.; Chapman, T.; Collier, P.; Longworth, S.; Tsang, S.C. Size dependent oxygen buffering capacity of ceria nanocrystals. *Chem. Commun.* **2010**, *46*, 1887–1889. doi: 10.1039/B923780A
71. Sayle, T.X.T.; Caddeo, F.; Zhang, X.; Sakthivel, T.; Das, S.; Seal, S.; Ptasinska, S.; Sayle, D.C. Structure-Activity Map of Ceria Nanoparticles, Nanocubes, and Mesoporous Architectures. *Chem. Mater.* **2016**, *28*, 7287–7295. doi: 10.1021/acs.chemmater.6b02536
72. Roldan Cuenya, B. Synthesis and catalytic properties of metal nanoparticles: Size, shape, support, composition, and oxidation state effects. *Thin Solid Films* **2010**, *518*, 3127–3150. doi: 10.1016/j.tsf.2010.01.018
73. Yang, F.; Deng, D.; Pan, X.; Fu, Q.; Bao, X. Understanding nano effects in catalysis. *Natl. Sci. Rev.* **2015**, *2*, 183–201. doi: 10.1093/nsr/nwv024

74. Dinh, C.T.; Nguyen, T.D.; Kleitz, F.; Do, T.O. Chapter 10—Shape-Controlled Synthesis of Metal Oxide Nanocrystals. In *Book Controlled Nanofabrication: Advances and Applications*, 1st ed.; Lui, R.-S., Ed.; Pan Stanford Publishing Pte. Ltd.: Singapore, 2012; pp. 327–367. ISBN 978-981-4316-87-3.
75. Aneggi, E.; Wiaterski, D.; De Leitenburg, C.; Llorca, J.; Trovarelli, A. Shape-Dependent Activity of Ceria in Soot Combustion. *ACS Catal.* **2014**, *4*, 172–181. doi: 10.1021/cs400850r
76. Ta, N.; Liu, J.; Shen, W. Tuning the shape of ceria nanomaterials for catalytic applications. *Chinese J. Catal.* **2013**, *34*, 838–850. doi: 10.1016/S1872-2067(12)60573-7
77. Li, Y.; Shen, W. Morphology-dependent nanocatalysts: Rod-shaped oxides. *Chem. Soc. Rev.* **2014**, *43*, 1543–1574. doi: 10.1039/C3CS60296F
78. Zhou, K.; Li, Y. Catalysis Based on Nanocrystals with Well-Defined Facets. *Angew. Chem. Int. Ed.* **2012**, *51*, 602–613. doi: 10.1002/anie.201102619
79. Liu, L.; Corma, A. Metal Catalysts for Heterogeneous Catalysis: From Single Atoms to Nanoclusters and Nanoparticles. *Chem. Rev.* **2018**, *118*, 4981–5079. doi: 10.1021/acs.chemrev.7b00776
80. Philippot, K.; Serp, P. Chapter 1—Concepts in Nanocatalysis. In *Book Nanomaterials in Catalysis*, 1st ed.; Serp, P., Philippot, K., Eds.; Wiley-VCH Verlag GmbH & Co. KGaA.: Weinheim, Germany, 2013; pp. 1–54. doi: 10.1002/9783527656875.ch1
81. Che, M.; Bennett, C.O. The Influence of Particle Size on the Catalytic Properties of Supported Metals. *Adv. Catal.* **1989**, *36*, 55–172. doi: 10.1016/S0360-0564(08)60017-6
82. Hvolbæk, B.; Janssens, T.V.W.; Clausen, B.S.; Falsig, H.; Christensen, C.H.; Nørskov, J.K. Catalytic activity of Au nanoparticles. *Nano Today* **2007**, *2*, 14–18. doi: 10.1016/S1748-0132(07)70113-5
83. Tao, F.; Dag, S.; Wang, L.-W.; Liu, Z.; Butcher, D.R.; Bluhm, H.; Salmeron, M.; Somorjai, G.A. Break-Up of Stepped Platinum Catalyst Surfaces by High CO Coverage. *Science* **2010**, *327*, 850–853. doi: 10.1126/science.1182122
84. Qiao, Z.-A.; Wu, Z.; Dai, S. Shape-Controlled Ceria-based Nanostructures for Catalysis Applications. *ChemSusChem* **2013**, *6*, 1821–1833. doi: 10.1002/cssc.201300428
85. Vinod, C.P. Surface science as a tool for probing nanocatalysis phenomena. *Catal. Today* **2010**, *154*, 113–117. doi: 10.1016/j.cattod.2010.03.018
86. Somorjai, G.A.; Li, Y. *Introduction to Surface Chemistry and Catalysis*, 2nd ed.; John

- Wiley & Sons: Hoboken, NJ, USA, 2010; ISBN 978-0-470-50823-7.
87. Calle-Vallejo, F.; Loffreda, D.; Koper, M.T.M.; Sautet, P. Introducing structural sensitivity into adsorption-energy scaling relations by means of coordination numbers. *Nat. Chem.* **2015**, *7*, 403–410. doi: 10.1038/nchem.2226
88. Brodersen, S.H.; Grønbjerg, U.; Hvolbæk, B.; Schiøtz, J. Understanding the catalytic activity of gold nanoparticles through multi-scale simulations. *J. Catal.* **2011**, *284*, 34–41. doi: 10.1016/j.jcat.2011.08.016
89. Hamid, S.B.A.; Schlögl, R. Chapter 20–The Impact of Nanoscience in Heterogeneous Catalysis. In *Book Nano-Micro Interface Bridging Micro Nano Worlds*, 2nd ed.; Van de Voorde, M., Werner, M., Fecht, H.-J., Eds.; Wiley-VCH Verlag GmbH & Co. KGaA.: Hoboken, NJ, USA, 2015; Volume 2, pp. 405–430. doi: 10.1002/9783527679195.ch20
90. Cleveland, C.L.; Landman, U.; Schaaff, T.G.; Shafiqullin, M.N.; Stephens, P.W.; Whetten, R.L. Structural Evolution of Smaller Gold Nanocrystals: The Truncated Decahedral Motif. *Phys. Rev. Lett.* **1997**, *79*, 1873–1876. doi: 10.1103/PhysRevLett.79.1873
91. Chen, M.; Wayne Goodman, D. Catalytically active gold on ordered titania supports. *Chem. Soc. Rev.* **2008**, *37*, 1860–1870. doi: 10.1039/B707318F
92. Van Bokhoven, J.A.; Louis, C.; Miller, J.T.; Tromp, M.; Safonova, O.V.; Glatzel, P. Activation of Oxygen on Gold/Alumina Catalysts: In Situ High-Energy-Resolution Fluorescence and Time-Resolved X-ray Spectroscopy. *Angew. Chem. Int. Ed.* **2006**, *45*, 4651–4654. doi: 10.1002/anie.200601184
93. Walsh, M.J.; Yoshida, K.; Kuwabara, A.; Pay, M.L.; Gai, P.L.; Boyes, E.D. On the Structural Origin of the Catalytic Properties of Inherently Strained Ultrasmall Decahedral Gold Nanoparticles. *Nano Lett.* **2012**, *12*, 2027–2031. doi: 10.1021/nl300067q
94. Hu, P.; Huang, Z.; Amghouz, Z.; Makkee, M.; Xu, F.; Kapteijn, F.; Dikhtiarenko, A.; Chen, Y.; Gu, X.; Tang, X. Electronic Metal–Support Interactions in Single-Atom Catalysts. *Angew. Chem. Int. Ed.* **2014**, *53*, 3418–3421. doi: 10.1002/anie.201309248
95. Han, Z.-K.; Zhang, L.; Liu, M.; Ganduglia-Pirovano, M.V.; Gao, Y. The Structure of Oxygen Vacancies in the Near-Surface of Reduced CeO₂ (111) Under Strain. *Front. Chem.* **2019**, *7*, 436. doi: 10.3389/fchem.2019.00436
96. Murugan, B.; Ramaswamy, A.V. Defect-Site Promoted Surface Reorganization in Nanocrystalline Ceria for the Low-Temperature Activation of Ethylbenzene. *J. Am. Chem. Soc.* **2007**, *129*, 3062–3063. doi: 10.1021/ja066834k

97. Campbell, C.T. Catalyst–support interactions: Electronic perturbations. *Nat. Chem.* **2012**, *4*, 597–598. doi: 10.1038/nchem.1412
98. Sun, C.; Li, H.; Chen, L. Nanostructured ceria-based materials: synthesis, properties, and applications. *Energy Environ. Sci.* **2012**, *5*, 8475–8505. doi: 10.1039/C2EE22310D
99. Zhou, X.-D.; Huebner, W. Size-induced lattice relaxation in CeO₂ nanoparticles. *Appl. Phys. Lett.* **2001**, *79*, 3512. doi: 10.1063/1.1419235
100. Dutta, P.; Pal, S.; Seehra, M.S.; Shi, Y.; Eyring, E.M.; Ernst, R.D. Concentration of Ce³⁺ and Oxygen Vacancies in Cerium Oxide Nanoparticles. *Chem. Mater.* **2006**, *18*, 5144–5146. doi: 10.1021/cm061580n
101. Hailstone, R.K.; DiFrancesco, A.G.; Leong, J.G.; Allston, T.D.; Reed, K.J. A Study of Lattice Expansion in CeO₂ Nanoparticles by Transmission Electron Microscopy. *J. Phys. Chem. C* **2009**, *113*, 15155–15159. doi: 10.1021/jp903468m
102. Migani, A.; Vayssilov, G.N.; Bromley, S.T.; Illas, F.; Neyman, K.M. Dramatic reduction of the oxygen vacancy formation energy in ceria particles: a possible key to their remarkable reactivity at the nanoscale. *J. Mater. Chem.* **2010**, *20*, 10535–10546. doi: 10.1039/C0JM01908A
103. Bruix, A.; Neyman, K.M. Modeling Ceria-Based Nanomaterials for Catalysis and Related Applications. *Catal. Lett.* **2016**, *146*, 2053–2080. doi: 10.1007/s10562-016-1799-1
104. Sk, M.A.; Kozlov, S.M.; Lim, K.H.; Migani, A.; Neyman, K.M. Oxygen vacancies in self-assemblies of ceria nanoparticles. *J. Mater. Chem. A* **2014**, *2*, 18329–18338. doi: 10.1039/C4TA02200A
105. Trovarelli, A.; Llorca, J. Ceria Catalysts at Nanoscale: How Do Crystal Shapes Shape Catalysis? *ACS Catal.* **2017**, *7*, 4716–4735. doi: 10.1021/acscatal.7b01246
106. Li, Y.; Liu, Q.; Shen, W. Morphology-dependent nanocatalysis: metal particles. *Dalt. Trans.* **2011**, *40*, 5811–5826. doi: 10.1039/C0DT01404D
107. Huang, W.; Gao, Y. Morphology-dependent surface chemistry and catalysis of CeO₂ nanocrystals. *Catal. Sci. Technol.* **2014**, *4*, 3772–3784. doi: 10.1039/C4CY00679H
108. Datta, S.; Torrente-Murciano, L. Nanostructured faceted ceria as oxidation catalyst. *Curr. Opin. Chem. Eng.* **2018**, *20*, 99–106. doi: 10.1016/j.coche.2018.03.009
109. Munnik, P.; De Jongh, P.E.; De Jong, K.P. Recent Developments in the Synthesis of Supported Catalysts. *Chem. Rev.* **2015**, *115*, 6687–6718. doi: 10.1021/cr500486u
110. Vilé, G.; Colussi, S.; Krumeich, F.; Trovarelli, A.; Pérez-Ramírez, J. Opposite Face Sensitivity of CeO₂ in Hydrogenation and Oxidation Catalysis. *Angew. Chem. Int. Ed.*

- 2014**, 53, 12069–12072. doi: 10.1002/anie.201406637
111. Yuan, Q.; Duan, H.-H.; Li, L.-L.; Sun, L.-D.; Zhang, Y.-W.; Yan, C.-H. Controlled synthesis and assembly of ceria-based nanomaterials. *J. Colloid Interface Sci.* **2009**, 335, 151–167. doi: 10.1016/j.jcis.2009.04.007
112. Mullins, D.R. The surface chemistry of cerium oxide. *Surf. Sci. Rep.* **2015**, 70, 42–85. doi: 10.1016/j.surfrep.2014.12.001
113. Paier, J.; Penschke, C.; Sauer, J. Oxygen Defects and Surface Chemistry of Ceria: Quantum Chemical Studies Compared to Experiment. *Chem. Rev.* **2013**, 113, 3949–3985. doi: 10.1021/cr3004949
114. Yang, W.; Wang, X.; Song, S.; Zhang, H. Syntheses and Applications of Noble-Metal-free CeO₂-Based Mixed-Oxide Nanocatalysts. *Chem* **2019**, 5, 1743–1774. doi: 10.1016/j.chempr.2019.04.009
115. Castanet, U.; Feral-Martin, C.; Demourgues, A.; Neale, R.L.; Sayle, D.C.; Caddeo, F.; Flitcroft, J.M.; Caygill, R.; Pointon, B.J.; Molinari, M.; Majimel, J. Controlling the {111}/{110} Surface Ratio of Cuboidal Ceria Nanoparticles. *ACS Appl. Mater. Interfaces* **2019**, 11, 11384–11390. doi: 10.1021/acsami.8b21667
116. Lykaki, M.; Pachatouridou, E.; Carabineiro, S.A.C.; Iliopoulou, E.; Andriopoulou, C.; Kallithrakas-Kontos, N.; Boghosian, S.; Konsolakis, M. Ceria nanoparticles shape effects on the structural defects and surface chemistry: Implications in CO oxidation by Cu/CeO₂ catalysts. *Appl. Catal. B Environ.* **2018**, 230, 18–28. doi: 10.1016/j.apcatb.2018.02.035
117. Xie, Y.; Wu, J.; Jing, G.; Zhang, H.; Zeng, S.; Tian, X.; Zou, X.; Wen, J.; Su, H.; Zhong, C.-J.; Cui, P. Structural origin of high catalytic activity for preferential CO oxidation over CuO/CeO₂ nanocatalysts with different shapes. *Appl. Catal. B Environ.* **2018**, 239, 665–676. doi: 10.1016/j.apcatb.2018.08.066
118. He, H.; Yang, P.; Li, J.; Shi, R.; Chen, L.; Zhang, A.; Zhu, Y. Controllable synthesis, characterization, and CO oxidation activity of CeO₂ nanostructures with various morphologies. *Ceram. Int.* **2016**, 42, 7810–7818. doi: 10.1016/j.ceramint.2016.02.005
119. Chang, H.; Ma, L.; Yang, S.; Li, J.; Chen, L.; Wang, W.; Hao, J. Comparison of preparation methods for ceria catalyst and the effect of surface and bulk sulfates on its activity toward NH₃-SCR. *J. Hazard. Mater.* **2013**, 262, 782–788. doi: 10.1016/j.jhazmat.2013.09.043
120. Gawade, P.; Mirkelamoglu, B.; Ozkan, U.S. The Role of Support Morphology and Impregnation Medium on the Water Gas Shift Activity of Ceria-Supported Copper

- Catalysts. *J. Phys. Chem. C* **2010**, *114*, 18173–18181. doi: 10.1021/jp104715w
121. Roldan Cuenya, B.; Behafarid, F. Nanocatalysis: size- and shape-dependent chemisorption and catalytic reactivity. *Surf. Sci. Rep.* **2015**, *70*, 135–187. doi: 10.1016/j.surfrep.2015.01.001
122. Liu, Y.H.; Zuo, J.C.; Ren, X.F.; Yong, L. Synthesis and character of cerium oxide (CeO₂) nanoparticles by the precipitation method. *Metalurgija* **2014**, *53*, 463–465.
123. Lykaki, M.; Pachatouridou, E.; Iliopoulou, E.; Carabineiro, S.A.C.; Konsolakis, M. Impact of the synthesis parameters on the solid state properties and the CO oxidation performance of ceria nanoparticles. *RSC Adv.* **2017**, *7*, 6160–6169. doi: 10.1039/C6RA26712B
124. Shang, H.; Zhang, X.; Xu, J.; Han, Y. Effects of preparation methods on the activity of CuO/CeO₂ catalysts for CO oxidation. *Front. Chem. Sci. Eng.* **2017**, *11*, 603–612. doi: 10.1007/s11705-017-1661-z
125. Zhou, L.; Li, X.; Yao, Z.; Chen, Z.; Hong, M.; Zhu, R.; Liang, Y.; Zhao, J. Transition-Metal Doped Ceria Microspheres with Nanoporous Structures for CO Oxidation. *Sci. Rep.* **2016**, *6*, 23900. doi: 10.1038/srep23900
126. Wang, W.-W.; Yu, W.-Z.; Du, P.-P.; Xu, H.; Jin, Z.; Si, R.; Ma, C.; Shi, S.; Jia, C.-J.; Yan, C.-H. Crystal Plane Effect of Ceria on Supported Copper Oxide Cluster Catalyst for CO Oxidation: Importance of Metal-Support Interaction. *ACS Catal.* **2017**, *7*, 1313–1329. doi: 10.1021/acscatal.6b03234
127. Nakagawa, K.; Ohshima, T.; Tezuka, Y.; Katayama, M.; Katoh, M.; Sugiyama, S. Morphological effects of CeO₂ nanostructures for catalytic soot combustion of CuO/CeO₂. *Catal. Today* **2015**, *246*, 67–71. doi: 10.1016/j.cattod.2014.08.005
128. Chaudhary, S.; Sharma, P.; Kumar, R.; Mehta, S.K. Nanoscale surface designing of Cerium oxide nanoparticles for controlling growth, stability, optical and thermal properties. *Ceram. Int.* **2015**, *41*, 10995–11003. doi: 10.1016/j.ceramint.2015.05.044
129. Miyazaki, H.; Kato, J.I.; Sakamoto, N.; Wakiya, N.; Ota, T.; Suzuki, H. Synthesis of CeO₂ nanoparticles by rapid thermal decomposition using microwave heating. *Adv. Appl. Ceram.* **2010**, *109*, 123–127. doi: 10.1179/174367509X12503626841631
130. Yang, H.; Huang, C.; Tang, A.; Zhang, X.; Yang, W. Microwave-assisted synthesis of ceria nanoparticles. *Mater. Res. Bull.* **2005**, *40*, 1690–1695. doi: 10.1016/j.materresbull.2005.05.014
131. Zawadzki, M. Preparation and characterization of ceria nanoparticles by microwave-assisted solvothermal process. *J. Alloys Compd.* **2008**, *454*, 347–351. doi:

- 10.1016/j.jallcom.2006.12.078
132. Zhang, Y.-W.; Si, R.; Liao, C.-S.; Yan, C.-H.; Xiao, C.-X.; Kou, Y. Facile Alcohothermal Synthesis, Size-Dependent Ultraviolet Absorption, and Enhanced CO Conversion Activity of Ceria Nanocrystals. *J. Phys. Chem. B* **2003**, *107*, 10159–10167. doi: 10.1021/jp034981o
133. Ouyang, B.; Tan, W.; Liu, B. Morphology effect of nanostructure ceria on the Cu/CeO₂ catalysts for synthesis of methanol from CO₂ hydrogenation. *Catal. Commun.* **2017**, *95*, 36–39. doi: 10.1016/j.catcom.2017.03.005
134. Mai, H.-X.; Sun, L.-D.; Zhang, Y.-W.; Si, R.; Feng, W.; Zhang, H.-P.; Liu, H.-C.; Yan, C.-H. Shape-Selective Synthesis and Oxygen Storage Behavior of Ceria Nanopolyhedra, Nanorods, and Nanocubes. *J. Phys. Chem. B* **2005**, *109*, 24380–24385. doi: 10.1021/jp055584b
135. Gamarra, D.; López Cámara, A.; Monte, M.; Rasmussen, S.B.; Chinchilla, L.E.; Hungría, A.B.; Munuera, G.; Gyorffy, N.; Schay, Z.; Cortés Corberán, V.; Conesa, J.C.; Martínez-Arias, A. Preferential oxidation of CO in excess H₂ over CuO/CeO₂ catalysts: Characterization and performance as a function of the exposed face present in the CeO₂ support. *Appl. Catal. B Environ.* **2013**, *130–131*, 224–238. doi: 10.1016/j.apcatb.2012.11.008
136. Piumetti, M.; Bensaid, S.; Andana, T.; Dosa, M.; Novara, C.; Giorgis, F.; Russo, N.; Fino, D. Nanostructured Ceria-Based Materials: Effect of the Hydrothermal Synthesis Conditions on the Structural Properties and Catalytic Activity. *Catalysts* **2017**, *7*, 174. doi: 10.3390/catal7060174
137. Araiza, D.G.; Gómez-Cortés, A.; Díaz, G. Partial oxidation of methanol over copper supported on nanoshaped ceria for hydrogen production. *Catal. Today* **2017**, *282*, 185–194. doi: 10.1016/j.cattod.2016.06.055
138. Yao, S.Y.; Xu, W.Q.; Johnston-Peck, A.C.; Zhao, F.Z.; Liu, Z.Y.; Luo, S.; Senanayake, S.D.; Martínez-Arias, A.; Liu, W.J.; Rodriguez, J.A. Morphological effects of the nanostructured ceria support on the activity and stability of CuO/CeO₂ catalysts for the water-gas shift reaction. *Phys. Chem. Chem. Phys.* **2014**, *16*, 17183–17195. doi: 10.1039/C4CP02276A
139. Lin, L.; Yao, S.; Liu, Z.; Zhang, F.; Li, N.; Vovchok, D.; Martínez-Arias, A.; Castañeda, R.; Lin, J.; Senanayake, S.D.; Su, D.; Ma, D.; Rodriguez, J.A. In Situ Characterization of Cu/CeO₂ Nanocatalysts for CO₂ Hydrogenation: Morphological Effects of Nanostructured Ceria on the Catalytic Activity. *J. Phys. Chem. C* **2018**, *122*, 12934–

12943. doi: 10.1021/acs.jpcc.8b03596
140. Andana, T.; Piumetti, M.; Bensaid, S.; Veyre, L.; Thieuleux, C.; Russo, N.; Fino, D.; Quadrelli, E.A.; Pirone, R. CuO nanoparticles supported by ceria for NO_x-assisted soot oxidation: insight into catalytic activity and sintering. *Appl. Catal. B Environ.* **2017**, *216*, 41–58. doi: 10.1016/j.apcatb.2017.05.061
141. Miceli, P.; Bensaid, S.; Russo, N.; Fino, D. Effect of the morphological and surface properties of CeO₂-based catalysts on the soot oxidation activity. *Chem. Eng. J.* **2015**, *278*, 190–198. doi: 10.1016/j.cej.2014.10.055
142. Liu, J.; Li, Y.; Zhang, J.; He, D. Glycerol carbonylation with CO₂ to glycerol carbonate over CeO₂ catalyst and the influence of CeO₂ preparation methods and reaction parameters. *Appl. Catal. A Gen.* **2016**, *513*, 9–18. doi: 10.1016/j.apcata.2015.12.030
143. He, H.-W.; Wu, X.-Q.; Ren, W.; Shi, P.; Yao, X.; Song, Z.-T. Synthesis of crystalline cerium dioxide hydrosol by a sol-gel method. *Ceram. Int.* **2012**, *38*, S501–S504. doi: 10.1016/j.ceramint.2011.05.063
144. Phonthammachai, N.; Rumruangwong, M.; Gulari, E.; Jamieson, A.M.; Jitkarnka, S.; Wongkasemjit, S. Synthesis and rheological properties of mesoporous nanocrystalline CeO₂ via sol-gel process. *Colloids Surfaces A Physicochem. Eng. Asp.* **2004**, *247*, 61–68. doi: 10.1016/j.colsurfa.2004.08.030
145. Pinjari, D.V.; Pandit, A.B. Room temperature synthesis of crystalline CeO₂ nanopowder: Advantage of sonochemical method over conventional method. *Ultrason. Sonochem.* **2011**, *18*, 1118–1123. doi: 10.1016/j.ultsonch.2011.01.008
146. Yin, L.; Wang, Y.; Pang, G.; Koltypin, Y.; Gedanken, A. Sonochemical Synthesis of Cerium Oxide Nanoparticles–Effect of Additives and Quantum Size Effect. *J. Colloid Interface Sci.* **2002**, *246*, 78–84. doi: 10.1006/jcis.2001.8047
147. Guo, X.; Zhou, R. A new insight into the morphology effect of ceria on CuO/CeO₂ catalysts for CO selective oxidation in hydrogen-rich gas. *Catal. Sci. Technol.* **2016**, *6*, 3862–3871. doi: 10.1039/C5CY01816A
148. Mock, S.A.; Sharp, S.E.; Stoner, T.R.; Radetic, M.J.; Zell, E.T.; Wang, R. CeO₂ nanorods-supported transition metal catalysts for CO oxidation. *J. Colloid Interface Sci.* **2016**, *466*, 261–267. doi: 10.1016/j.jcis.2015.12.026
149. Ren, Z.; Peng, F.; Li, J.; Liang, X.; Chen, B. Morphology-Dependent Properties of Cu/CeO₂ Catalysts for the Water-Gas Shift Reaction. *Catalysts* **2017**, *7*, 48. doi: 10.3390/catal7020048
150. Zabilskiy, M.; Djinović, P.; Tchernychova, E.; Tkachenko, O.P.; Kustov, L.M.; Pintar, A.

- Nanoshaped CuO/CeO₂ Materials: Effect of the Exposed Ceria Surfaces on Catalytic Activity in N₂O Decomposition Reaction. *ACS Catal.* **2015**, *5*, 5357–5365. doi: 10.1021/acscatal.5b01044
151. Cui, Y.; Dai, W.-L. Support morphology and crystal plane effect of Cu/CeO₂ nanomaterial on the physicochemical and catalytic properties for carbonate hydrogenation. *Catal. Sci. Technol.* **2016**, *6*, 7752–7762. doi: 10.1039/C6CY01575A
152. Liu, L.; Yao, Z.; Deng, Y.; Gao, F.; Liu, B.; Dong, L. Morphology and Crystal-Plane Effects of Nanoscale Ceria on the Activity of CuO/CeO₂ for NO Reduction by CO. *ChemCatChem* **2011**, *3*, 978–989. doi: 10.1002/cctc.201000320
153. López, J.M.; Gilbank, A.L.; García, T.; Solsona, B.; Agouram, S.; Torrente-Murciano, L. The prevalence of surface oxygen vacancies over the mobility of bulk oxygen in nanostructured ceria for the total toluene oxidation. *Appl. Catal. B Environ.* **2015**, *174–175*, 403–412. doi: 10.1016/j.apcatb.2015.03.017
154. Araiza, D.G.; Gómez-Cortés, A.; Díaz, G. Reactivity of methanol over copper supported on well-shaped CeO₂: a TPD-DRIFTS study. *Catal. Sci. Technol.* **2017**, *7*, 5224–5235. doi: 10.1039/C7CY00984D
155. Sudarsanam, P.; Hillary, B.; Amin, M.H.; Rockstroh, N.; Bentrup, U.; Brückner, A.; Bhargava, S.K. Heterostructured Copper-Ceria and Iron-Ceria Nanorods: Role of Morphology, Redox, and Acid Properties in Catalytic Diesel Soot Combustion. *Langmuir* **2018**, *34*, 2663–2673. doi: 10.1021/acs.langmuir.7b03998
156. Piumetti, M.; Bensaid, S.; Russo, N.; Fino, D. Nanostructured ceria-based catalysts for soot combustion: Investigations on the surface sensitivity. *Appl. Catal. B Environ.* **2015**, *165*, 742–751. doi: 10.1016/j.apcatb.2014.10.062
157. Wang, S.; Zhao, L.; Wang, W.; Zhao, Y.; Zhang, G.; Ma, X.; Gong, J. Morphology control of ceria nanocrystals for catalytic conversion of CO₂ with methanol. *Nanoscale* **2013**, *5*, 5582–5588. doi: 10.1039/C3NR00831B
158. Wu, Z.; Li, M.; Overbury, S.H. On the structure dependence of CO oxidation over CeO₂ nanocrystals with well-defined surface planes. *J. Catal.* **2012**, *285*, 61–73. doi: 10.1016/j.jcat.2011.09.011
159. Kovacevic, M.; Mojet, B.L.; Van Ommen, J.G.; Lefferts, L. Effects of Morphology of Cerium Oxide Catalysts for Reverse Water Gas Shift Reaction. *Catal. Lett.* **2016**, *146*, 770–777. doi: 10.1007/s10562-016-1697-6
160. Piumetti, M.; Andana, T.; Bensaid, S.; Russo, N.; Fino, D.; Pirone, R. Study on the CO Oxidation over Ceria-Based Nanocatalysts. *Nanoscale Res. Lett.* **2016**, *11*, 165. doi:

- 10.1186/s11671-016-1375-z
161. Wang, Z.L.; Feng, X. Polyhedral Shapes of CeO₂ Nanoparticles. *J. Phys. Chem. B* **2003**, *107*, 13563–13566. doi: 10.1021/jp036815m
162. Li, Y.; Wei, Z.; Gao, F.; Kovarik, L.; Peden, C.H.F.; Wang, Y. Effects of CeO₂ support facets on VO_x/CeO₂ catalysts in oxidative dehydrogenation of methanol. *J. Catal.* **2014**, *315*, 15–24. doi: 10.1016/j.jcat.2014.04.013
163. Mudiyansele, K.; Senanayake, S.D.; Feria, L.; Kundu, S.; Baber, A.E.; Graciani, J.; Vidal, A.B.; Agnoli, S.; Evans, J.; Chang, R.; Axnanda, S.; Liu, Z.; Sanz, J.F.; Liu, P.; Rodriguez, J.A.; Stacchiola, D.J. Importance of the Metal–Oxide Interface in Catalysis: In Situ Studies of the Water–Gas Shift Reaction by Ambient-Pressure X-ray Photoelectron Spectroscopy. *Angew. Chem. Int. Ed.* **2013**, *52*, 5101–5105. doi: 10.1002/anie.201210077
164. Mayernick, A.D.; Janik, M.J. Methane Activation and Oxygen Vacancy Formation over CeO₂ and Zr, Pd Substituted CeO₂ Surfaces. *J. Phys. Chem. C* **2008**, *112*, 14955–14964. doi: 10.1021/jp805134s
165. Nolan, M.; Grigoleit, S.; Sayle, D.C.; Parker, S.C.; Watson, G.W. Density functional theory studies of the structure and electronic structure of pure and defective low index surfaces of ceria. *Surf. Sci.* **2005**, *576*, 217–229. doi: 10.1016/j.susc.2004.12.016
166. Nolan, M.; Parker, S.C.; Watson, G.W. The electronic structure of oxygen vacancy defects at the low index surfaces of ceria. *Surf. Sci.* **2005**, *595*, 223–232. doi: 10.1016/j.susc.2005.08.015
167. Sayle, T.X.T.; Parker, S.C.; Sayle, D.C. Oxidising CO to CO₂ using ceria nanoparticles. *Phys. Chem. Chem. Phys.* **2005**, *7*, 2936–2941. doi: 10.1039/B506359K
168. Sayle, T.X.T.; Cantoni, M.; Bhatta, U.M.; Parker, S.C.; Hall, S.R.; Möbus, G.; Molinari, M.; Reid, D.; Seal, S.; Sayle, D.C. Strain and Architecture-Tuned Reactivity in Ceria Nanostructures; Enhanced Catalytic Oxidation of CO to CO₂. *Chem. Mater.* **2012**, *24*, 1811–1821. doi: 10.1021/cm3003436
169. Spencer, N.D.; Schoonmaker, R.C.; Somorjai, G.A. Iron single crystals as ammonia synthesis catalysts: Effect of surface structure on catalyst activity. *J. Catal.* **1982**, *74*, 129–135. doi: 10.1016/0021-9517(82)90016-1
170. Xie, S.; Choi, S.-H.; Xia, X.; Xia, Y. Catalysis on faceted noble-metal nanocrystals: both shape and size matter. *Curr. Opin. Chem. Eng.* **2013**, *2*, 142–150. doi: 10.1016/j.coche.2013.02.003
171. Konsolakis, M.; Lykaki, M. Facet-Dependent Reactivity of Ceria Nanoparticles

- Exemplified by CeO₂-Based Transition Metal Catalysts: A Critical Review. *Catalysts* **2021**, *11*, 452. doi: 10.3390/catal11040452
172. Zhai, Y.; Pierre, D.; Si, R.; Deng, W.; Ferrin, P.; Nilekar, A.U.; Peng, G.; Herron, J.A.; Bell, D.C.; Saltsburg, H.; Mavrikakis, M.; Flytzani-Stephanopoulos, M. Alkali-Stabilized Pt-OH_x Species Catalyze Low-Temperature Water-Gas Shift Reactions. *Science* **2010**, *329*, 1633–1636. doi: 10.1126/science.1192449
173. Stakheev, A.Y.; Kustov, L.M. Effects of the support on the morphology and electronic properties of supported metal clusters: modern concepts and progress in 1990s. *Appl. Catal. A Gen.* **1999**, *188*, 3–35. doi: 10.1016/S0926-860X(99)00232-X
174. Lee, D.W.; Yoo, B.R. Advanced metal oxide (supported) catalysts: Synthesis and applications. *J. Ind. Eng. Chem.* **2014**, *20*, 3947–3959. doi: 10.1016/j.jiec.2014.08.004
175. Yentekakis, I.V.; Konsolakis, M.; Lambert, R.M.; MacLeod, N.; Nalbantian, L. Extraordinarily effective promotion by sodium in emission control catalysis: NO reduction by propene over Na-promoted Pt/γ-Al₂O₃. *Appl. Catal. B Environ.* **1999**, *22*, 123–133. doi: 10.1016/S0926-3373(99)00042-9
176. Konsolakis, M.; Vrontaki, M.; Avgouropoulos, G.; Ioannides, T.; Yentekakis, I.V. Novel doubly-promoted catalysts for the lean NO_x reduction by H₂ + CO: Pd(K)/Al₂O₃-(TiO₂). *Appl. Catal. B Environ.* **2006**, *68*, 59–67. doi: 10.1016/j.apcatb.2006.07.011
177. Konsolakis, M.; Aligizou, F.; Goula, G.; Yentekakis, I.V. N₂O decomposition over doubly-promoted Pt(K)/Al₂O₃-(CeO₂-La₂O₃) structured catalysts: On the combined effects of promotion and feed composition. *Chem. Eng. J.* **2013**, *230*, 286–295. doi: 10.1016/j.cej.2013.06.083
178. Janek, J. C.G. Vayenas, S. Bebelis, C. Pliangos, S. Brosda, D. Tsiplakides: Electrochemical activation of catalysis: promotion, electrochemical promotion, and metal-support interaction. *J. Solid State Electrochem.* **2002**, *7*, 60–61. doi: 10.1007/s10008-002-0305-4
179. De Lucas-Consuegra, A. New Trends of Alkali Promotion in Heterogeneous Catalysis: Electrochemical Promotion with Alkaline Ionic Conductors. *Catal. Surv. from Asia* **2015**, *19*, 25–37. doi: 10.1007/s10563-014-9179-6
180. Ertl, G.; Knözinger, H.; Weitkamp, J. *Handbook of Heterogeneous Catalysis*; VCH Verlagsgesellschaft mbH: Weinheim, Germany, 1997; ISBN 9783527619474.
181. Stelmachowski, P.; Maniak, G.; Kotarba, A.; Sojka, Z. Strong electronic promotion of Co₃O₄ towards N₂O decomposition by surface alkali dopants. *Catal. Commun.* **2009**, *10*, 1062–1065. doi: 10.1016/j.catcom.2008.12.057

182. Zasada, F.; Stelmachowski, P.; Maniak, G.; Paul, J.-F.; Kotarba, A.; Sojka, Z. Potassium Promotion of Cobalt Spinel Catalyst for N₂O Decomposition—Accounted by Work Function Measurements and DFT Modelling. *Catal. Lett.* **2009**, *127*, 126–131. doi: 10.1007/s10562-008-9655-6
183. Kiskinova, M.P. Chapter 7—Theoretical Approaches to the Description of the Modifier Effects. In *Book Studies in Surface Science and Catalysis—Poisoning and Promotion in Catalysis based on Surface Science Concepts and Experiments*, 1st ed.; Kiskinova, M.P., Delmon, B., Yates, J.T., Eds.; Elsevier Science Publishers B.V.: Amsterdam, The Netherlands, 1991; Volume 70, pp. 285–307. doi: 10.1016/S0167-2991(08)61529-3
184. Kiskinova, M.P. Chapter 4—Interaction of Atomic Adsorbates, Acting As Promoters Or Poisons With Single Crystal Metal Surfaces. In *Book Studies in Surface Science and Catalysis—Poisoning and Promotion in Catalysis Based on Surface Science Concepts and Experiments*, 1st ed.; Kiskinova, M.P., Delmon, B., Yates, J.T., Eds.; Elsevier Science Publishers B.V.: Amsterdam, The Netherlands, 1991; Volume 70, pp. 19–68. doi: 10.1016/S0167-2991(08)61526-8
185. Huo, C.-F.; Wu, B.-S.; Gao, P.; Yang, Y.; Li, Y.-W.; Jiao, H. The Mechanism of Potassium Promoter: Enhancing the Stability of Active Surfaces. *Angew. Chem. Int. Ed.* **2011**, *50*, 7403–7406. doi: 10.1002/anie.201007484
186. Besenbacher, F.; Chorkendorff, I.; Clausen, B.S.; Hammer, B.; Molenbroek, A.M.; Nørskov, J.K.; Stensgaard, I. Design of a Surface Alloy Catalyst for Steam Reforming. *Science* **1998**, *279*, 1913–1915. doi: 10.1126/science.279.5358.1913
187. Lamy, C.; Belgsir, E.M.; Léger, J.-M. Electrocatalytic oxidation of aliphatic alcohols: Application to the direct alcohol fuel cell (DAFC). *J. Appl. Electrochem.* **2001**, *31*, 799–809. doi: 10.1023/A:1017587310150
188. Liang, Y.N.; Oh, W.-D.; Li, Y.; Hu, X. Nanocarbons as platforms for developing novel catalytic composites: overview and prospects. *Appl. Catal. A Gen.* **2018**, *562*, 94–105. doi: 10.1016/j.apcata.2018.05.021
189. Chen, W.; Fan, Z.; Pan, X.; Bao, X. Effect of Confinement in Carbon Nanotubes on the Activity of Fischer–Tropsch Iron Catalyst. *J. Am. Chem. Soc.* **2008**, *130*, 9414–9419. doi: 10.1021/ja8008192
190. Geim, A.K.; Grigorieva, I.V. Van der Waals heterostructures. *Nature* **2013**, *499*, 419–425. doi: 10.1038/nature12385
191. Fu, Q.; Bao, X. Catalysis on a metal surface with a graphitic cover. *Chinese J. Catal.* **2015**, *36*, 517–519. doi: 10.1016/S1872-2067(15)60828-2

192. Ania, C.O.; Seredych, M.; Rodriguez-Castellon, E.; Bandosz, T.J. New copper/GO based material as an efficient oxygen reduction catalyst in an alkaline medium: The role of unique Cu/rGO architecture. *Appl. Catal. B Environ.* **2015**, *163*, 424–435. doi: 10.1016/j.apcatb.2014.08.022
193. Safaei, M.; Foroughi, M.M.; Ebrahimpoor, N.; Jahani, S.; Omid, A.; Khatami, M. A review on metal-organic frameworks: Synthesis and applications. *TrAC - Trends Anal. Chem.* **2019**, *118*, 401–425. doi: 10.1016/j.trac.2019.06.007
194. Wang, Y.; Yang, Y.; Liu, N.; Wang, Y.; Zhang, X. Sword-like CuO/CeO₂ composites derived from a Ce-BTC metal-organic framework with superior CO oxidation performance. *RSC Adv.* **2018**, *8*, 33096–33102. doi: 10.1039/C8RA07531J
195. Yang, Q.; Xu, Q.; Jiang, H.-L. Metal-organic frameworks meet metal nanoparticles: synergistic effect for enhanced catalysis. *Chem. Soc. Rev.* **2017**, *46*, 4774–4808. doi: 10.1039/C6CS00724D
196. Chen, L.; Chen, H.; Luque, R.; Li, Y. Metal-organic framework encapsulated Pd nanoparticles: towards advanced heterogeneous catalysts. *Chem. Sci.* **2014**, *5*, 3708–3714. doi: 10.1039/C4SC01847H
197. Chen, L.; Xu, Q. Metal-Organic Framework Composites for Catalysis. *Matter* **2019**, *1*, 57–89. doi: 10.1016/j.matt.2019.05.018
198. Li, P.-Z.; Aranishi, K.; Xu, Q. ZIF-8 immobilized nickel nanoparticles: highly effective catalysts for hydrogen generation from hydrolysis of ammonia borane. *Chem. Commun.* **2012**, *48*, 3173–3175. doi: 10.1039/C2CC17302F
199. Abdel-Mageed, A.M.; Rungtaweeworanit, B.; Parlinska-Wojtan, M.; Pei, X.; Yaghi, O.M.; Jürgen Behm, R. Highly Active and Stable Single-Atom Cu Catalysts Supported by a Metal-Organic Framework. *J. Am. Chem. Soc.* **2019**, *141*, 5201–5210. doi: 10.1021/jacs.8b11386
200. Rungtaweeworanit, B.; Baek, J.; Araujo, J.R.; Archanjo, B.S.; Choi, K.M.; Yaghi, O.M.; Somorjai, G.A. Copper Nanocrystals Encapsulated in Zr-based Metal-Organic Frameworks for Highly Selective CO₂ Hydrogenation to Methanol. *Nano Lett.* **2016**, *16*, 7645–7649. doi: 10.1021/acs.nanolett.6b03637
201. Ye, J.; Liu, C. Cu₃(BTC)₂: CO oxidation over MOF based catalysts. *Chem. Commun.* **2011**, *47*, 2167–2169. doi: 10.1039/C0CC04944A
202. Li, X.; Goh, T.W.; Li, L.; Xiao, C.; Guo, Z.; Zeng, X.C.; Huang, W. Controlling Catalytic Properties of Pd Nanoclusters through Their Chemical Environment at the Atomic Level Using Isostructural Metal-Organic Frameworks. *ACS Catal.* **2016**, *6*, 3461–3468.

- doi: 10.1021/acscatal.6b00397
203. Lawrence, N.J.; Brewer, J.R.; Wang, L.; Wu, T.-S.; Wells-Kingsbury, J.; Ihrig, M.M.; Wang, G.; Soo, Y.-L.; Mei, W.-N.; Cheung, C.L. Defect Engineering in Cubic Cerium Oxide Nanostructures for Catalytic Oxidation. *Nano Lett.* **2011**, *11*, 2666–2671. doi: 10.1021/nl200722z
204. Mock, S.A.; Zell, E.T.; Hossain, S.T.; Wang, R. Effect of Reduction Treatment on CO Oxidation with CeO₂ Nanorod-Supported CuO_x Catalysts. *ChemCatChem* **2018**, *10*, 311–319. doi: 10.1002/cctc.201700972
205. Lin, B.; Qi, Y.; Wei, K.; Lin, J. Effect of pretreatment on ceria-supported cobalt catalyst for ammonia synthesis. *RSC Adv.* **2014**, *4*, 38093–38102. doi: 10.1039/C4RA06175F
206. Ren, Y.; Tang, K.; Wei, J.; Yang, H.; Wei, H.; Yang, Y. Pretreatment Effect on Ceria-Supported Gold Nanocatalysts for CO Oxidation: Importance of the Gold–Ceria Interaction. *Energy Technol.* **2018**, *6*, 379–390. doi: 10.1002/ente.201700511
207. Prasad, R.; Rattan, G. Preparation Methods and Applications of CuO–CeO₂ Catalysts: A Short Review. *Bull. Chem. React. Eng. Catal.* **2010**, *5*, 7–30. doi: 10.9767/bcrec.5.1.7125.7-30
208. Gawande, M.B.; Goswami, A.; Felpin, F.-X.; Asefa, T.; Huang, X.; Silva, R.; Zou, X.; Zboril, R.; Varma, R.S. Cu and Cu-Based Nanoparticles: Synthesis and Applications in Catalysis. *Chem. Rev.* **2016**, *116*, 3722–3811. doi: 10.1021/acs.chemrev.5b00482
209. Dong, F.; Meng, Y.; Han, W.; Zhao, H.; Tang, Z. Morphology effects on surface chemical properties and lattice defects of Cu/CeO₂ catalysts applied for low-temperature CO oxidation. *Sci. Rep.* **2019**, *9*, 12056. doi: 10.1038/s41598-019-48606-2
210. Fotopoulos, A.; Arvanitidis, J.; Christofilos, D.; Papaggelis, K.; Kalyva, M.; Triantafyllidis, K.; Niarchos, D.; Boukos, N.; Basina, G.; Tzitzios, V. One Pot Synthesis and Characterization of Ultra Fine CeO₂ and Cu/CeO₂ Nanoparticles. Application for Low Temperature CO Oxidation. *J. Nanosci. Nanotechnol.* **2011**, *11*, 8593–8598. doi: 10.1166/jnn.2011.4752
211. Qin, J.; Lu, J.; Cao, M.; Hu, C. Synthesis of porous CuO–CeO₂ nanospheres with an enhanced low-temperature CO oxidation activity. *Nanoscale* **2010**, *2*, 2739–2743. doi: 10.1039/CONR00446D
212. Su, Y.; Dai, L.; Zhang, Q.; Li, Y.; Peng, J.; Wu, R.; Han, W.; Tang, Z.; Wang, Y. Fabrication of Cu-Doped CeO₂ Catalysts with Different Dimension Pore Structures for CO Catalytic Oxidation. *Catal. Surv. from Asia* **2016**, *20*, 231–240. doi:

- 10.1007/s10563-016-9220-z
213. Zhou, H.; Huang, Z.; Sun, C.; Qin, F.; Xiong, D.; Shen, W.; Xu, H. Catalytic decomposition of N₂O over Cu_xCe_{1-x}O_y mixed oxides. *Appl. Catal. B Environ.* **2012**, *125*, 492–498. doi: 10.1016/j.apcatb.2012.06.021
214. Lykaki, M.; Papista, E.; Carabineiro, S.A.C.; Tavares, P.B.; Konsolakis, M. Optimization of N₂O decomposition activity of CuO-CeO₂ mixed oxides by means of synthesis procedure and alkali (Cs) promotion. *Catal. Sci. Technol.* **2018**, *8*, 2312-2322. doi: 10.1039/C8CY00316E
215. Liu, Z.; He, C.; Chen, B.; Liu, H. CuO-CeO₂ mixed oxide catalyst for the catalytic decomposition of N₂O in the presence of oxygen. *Catal. Today* **2017**, *297*, 78–83. doi: 10.1016/j.cattod.2017.05.074
216. Zabilskiy, M.; Djinović, P.; Erjavec, B.; Dražić, G.; Pintar, A. Small CuO clusters on CeO₂ nanospheres as active species for catalytic N₂O decomposition. *Appl. Catal. B Environ.* **2015**, *163*, 113–122. doi: 10.1016/j.apcatb.2014.07.057
217. Li, L.; Zhan, Y.; Zheng, Q.; Zheng, Y.; Chen, C.; She, Y.; Lin, X.; Wei, K. Water–Gas Shift Reaction over CuO/CeO₂ Catalysts: Effect of the Thermal Stability and Oxygen Vacancies of CeO₂ Supports Previously Prepared by Different Methods. *Catal. Lett.* **2009**, *130*, 532–540. doi: 10.1007/s10562-009-9904-3
218. Li, L.; Song, L.; Wang, H.; Chen, C.; She, Y.; Zhan, Y.; Lin, X.; Zheng, Q. Water-gas shift reaction over CuO/CeO₂ catalysts: Effect of CeO₂ supports previously prepared by precipitation with different precipitants. *Int. J. Hydrogen Energy* **2011**, *36*, 8839–8849. doi: 10.1016/j.ijhydene.2011.04.137
219. Li, L.; Song, L.; Chen, C.; Zhang, Y.; Zhan, Y.; Lin, X.; Zheng, Q.; Wang, H.; Ma, H.; Ding, L.; Zhu, W. Modified precipitation processes and optimized copper content of CuO-CeO₂ catalysts for water–gas shift reaction. *Int. J. Hydrogen Energy* **2014**, *39*, 19570–19582. doi: 10.1016/j.ijhydene.2014.09.158
220. She, Y.; Li, L.; Zhan, Y.; Lin, X.; Zheng, Q.; Wei, K. Effect of yttrium addition on water-gas shift reaction over CuO/CeO₂ catalysts. *J. Rare Earths* **2009**, *27*, 411–417. doi: 10.1016/S1002-0721(08)60262-8
221. Yang, F.; Graciani, J.; Evans, J.; Liu, P.; Hrbek, J.; Sanz, J.F.; Rodriguez, J.A. CO Oxidation on Inverse CeO_x/Cu(111) Catalysts: High Catalytic Activity and Ceria-Promoted Dissociation of O₂. *J. Am. Chem. Soc.* **2011**, *133*, 3444–3451. doi: 10.1021/ja1087979
222. Berlowitz, P.J.; Peden, C.H.F.; Wayne Goodman, D. Kinetics of carbon monoxide

- oxidation on single-crystal palladium, platinum, and iridium. *J. Phys. Chem.* **1988**, *92*, 5213–5221. doi: 10.1021/j100329a030
223. Rodriguez, J.A.; Wayne Goodman, D. High-pressure catalytic reactions over single-crystal metal surfaces. *Surf. Sci. Rep.* **1991**, *14*, 1–107. doi: 10.1016/0167-5729(91)90002-F
224. Gamarra, D.; Belver, C.; Fernández-García, M.; Martínez-Arias, A. Selective CO Oxidation in Excess H₂ over Copper–Ceria Catalysts: Identification of Active Entities/Species. *J. Am. Chem. Soc.* **2007**, *129*, 12064–12065. doi: 10.1021/ja073926g
225. Martínez-Arias, A.; Gamarra, D.; Hungría, A.B.; Fernández-García, M.; Munuera, G.; Hornés, A.; Bera, P.; Conesa, J.C.; Cámara, A.L. Characterization of Active Sites/Entities and Redox/Catalytic Correlations in Copper-Ceria-Based Catalysts for Preferential Oxidation of CO in H₂-Rich Streams. *Catalysts* **2013**, *3*, 378–400. doi: 10.3390/catal3020378
226. Senanayake, S.D.; Stacchiola, D.; Rodriguez, J.A. Unique Properties of Ceria Nanoparticles Supported on Metals: Novel Inverse Ceria/Copper Catalysts for CO Oxidation and the Water-Gas Shift Reaction. *Acc. Chem. Res.* **2013**, *46*, 1702–1711. doi: 10.1021/ar300231p
227. Pillai, U.R.; Deevi, S. Room temperature oxidation of carbon monoxide over copper oxide catalyst. *Appl. Catal. B Environ.* **2006**, *64*, 146–151. doi: 10.1016/j.apcatb.2005.11.005
228. Zhao, D.; Tu, C.-M.; Hu, X.-J.; Zhang, N. Notable *in situ* surface transformation of Cu₂O nanomaterials leads to dramatic activity enhancement for CO oxidation. *RSC Adv.* **2017**, *7*, 37596–37603. doi: 10.1039/C7RA05950G
229. Wang, X.; Liu, C.; Zheng, B.; Jiang, Y.; Zhang, L.; Xie, Z.; Zheng, L. Controlled synthesis of concave Cu₂O microcrystals enclosed by {*hhl*} high-index facets and enhanced catalytic activity. *J. Mater. Chem. A* **2013**, *1*, 282–287. doi: 10.1039/C2TA00241H
230. Zhou, K.; Wang, R.; Xu, B.; Li, Y. Synthesis, characterization and catalytic properties of CuO nanocrystals with various shapes. *Nanotechnology* **2006**, *17*, 3939. doi: 10.1088/0957-4484/17/15/055
231. Huang, H.; Zhang, L.; Wu, K.; Yu, Q.; Chen, R.; Yang, H.; Peng, X.; Ye, Z. Hetero-metal cation control of CuO nanostructures and their high catalytic performance for CO oxidation. *Nanoscale* **2012**, *4*, 7832–7841. doi: 10.1039/C2NR32729E
232. Hossain, S.T.; Almesned, Y.; Zhang, K.; Zell, E.T.; Bernard, D.T.; Balaz, S.; Wang, R. Support structure effect on CO oxidation: A comparative study on SiO₂ nanospheres

- and CeO₂ nanorods supported CuO_x catalysts. *Appl. Surf. Sci.* **2018**, *428*, 598–608. doi: 10.1016/j.apsusc.2017.09.199
233. Yao, S.; Mudiyansele, K.; Xu, W.; Johnston-Peck, A.C.; Hanson, J.C.; Wu, T.; Stacchiola, D.; Rodriguez, J.A.; Zhao, H.; Beyer, K.A.; Chapman, K.W.; Chupas, P.J.; Martínez-Arias, A.; Si, R.; Bolin, T.B.; Liu, W.; Senanayake, S.D. Unraveling the Dynamic Nature of a CuO/CeO₂ Catalyst for CO Oxidation in *Operando*: A Combined Study of XANES (Fluorescence) and DRIFTS. *ACS Catal.* **2014**, *4*, 1650–1661. doi: 10.1021/cs500148e
234. Hossain, S.T.; Azeeva, E.; Zhang, K.; Zell, E.T.; Bernard, D.T.; Balaz, S.; Wang, R. A comparative study of CO oxidation over Cu-O-Ce solid solutions and CuO/CeO₂ nanorods catalysts. *Appl. Surf. Sci.* **2018**, *455*, 132–143. doi: 10.1016/j.apsusc.2018.05.101
235. Qi, L.; Yu, Q.; Dai, Y.; Tang, C.; Liu, L.; Zhang, H.; Gao, F.; Dong, L.; Chen, Y. Influence of cerium precursors on the structure and reducibility of mesoporous CuO-CeO₂ catalysts for CO oxidation. *Appl. Catal. B Environ.* **2012**, *119–120*, 308–320. doi: 10.1016/j.apcatb.2012.02.029
236. Sun, S.; Mao, D.; Yu, J.; Yang, Z.; Lu, G.; Ma, Z. Low-temperature CO oxidation on CuO/CeO₂ catalysts: the significant effect of copper precursor and calcination temperature. *Catal. Sci. Technol.* **2015**, *5*, 3166–3181. doi: 10.1039/C5CY00124B
237. Kappis, K.; Papadopoulos, C.; Papavasiliou, J.; Vakros, J.; Georgiou, Y.; Deligiannakis, Y.; Avgouropoulos, G. Tuning the Catalytic Properties of Copper-Promoted Nanoceria via a Hydrothermal Method. *Catalysts* **2019**, *9*, 138. doi: 10.3390/catal9020138
238. Papadopoulos, C.; Kappis, K.; Papavasiliou, J.; Vakros, J.; Kuśmierz, M.; Gac, W.; Georgiou, Y.; Deligiannakis, Y.; Avgouropoulos, G. Copper-promoted ceria catalysts for CO oxidation reaction. *Catal. Today* **2020**, *355*, 647–653. doi: 10.1016/j.cattod.2019.06.078
239. Elias, J.S.; Risch, M.; Giordano, L.; Mansour, A.N.; Shao-Horn, Y. Structure, Bonding, and Catalytic Activity of Monodisperse, Transition-Metal-Substituted CeO₂ Nanoparticles. *J. Am. Chem. Soc.* **2014**, *136*, 17193–17200. doi: 10.1021/ja509214d
240. Li, Y.; Cai, Y.; Xing, X.; Chen, N.; Deng, D.; Wang, Y. Catalytic activity for CO oxidation of Cu-CeO₂ composite nanoparticles synthesized by a hydrothermal method. *Anal. Methods* **2015**, *7*, 3238–3245. doi: 10.1039/C5AY00261C
241. Ma, J.; Jin, G.; Gao, J.; Li, Y.; Dong, L.; Huang, M.; Huang, Q.; Li, B. Catalytic effect of two-phase intergrowth and coexistence CuO-CeO₂. *J. Mater. Chem. A* **2015**, *3*, 24358–

24370. doi: 10.1039/C5TA06435J
242. Zhao, F.; Gong, M.; Zhang, G.; Li, J. Effect of the loading content of CuO on the activity and structure of CuO/Ce-Mn-O catalysts for CO oxidation. *J. Rare Earths* **2015**, *33*, 604–610. doi: 10.1016/S1002-0721(14)60460-9
243. Lin, R.; Luo, M.-F.; Zhong, Y.-J.; Yan, Z.-L.; Liu, G.-Y.; Liu, W.-P. Comparative study of CuO/Ce_{0.7}Sn_{0.3}O₂, CuO/CeO₂ and CuO/SnO₂ catalysts for low-temperature CO oxidation. *Appl. Catal. A Gen.* **2003**, *255*, 331–336. doi: 10.1016/S0926-860X(03)00639-2
244. Zhang, X.; Tian, P.; Tu, W.; Zhang, Z.; Xu, J.; Han, Y.-F. Tuning the Dynamic Interfacial Structure of Copper-Ceria Catalysts by Indium Oxide during CO Oxidation. *ACS Catal.* **2018**, *8*, 5261–5275. doi: 10.1021/acscatal.7b04287
245. Li, W.; Shen, X.; Zeng, R.; Chen, J.; Xiao, W.; Ding, S.; Chen, C.; Zhang, R.; Zhang, N. Constructing copper-ceria nanosheets with high concentration of interfacial active sites for enhanced performance in CO oxidation. *Appl. Surf. Sci.* **2019**, *492*, 818–825. doi: 10.1016/j.apsusc.2019.06.292
246. Song, X.-Z.; Su, Q.-F.; Li, S.-J.; Liu, S.-H.; Zhang, N.; Meng, Y.-L.; Chen, X.; Tan, Z. Triple-shelled CuO/CeO₂ hollow nanospheres derived from metal–organic frameworks as highly efficient catalysts for CO oxidation. *New J. Chem.* **2019**, *43*, 16096–16102. doi: 10.1039/C9NJ04244J
247. Liu, H.-H.; Wang, Y.; Jia, A.-P.; Wang, S.-Y.; Luo, M.-F.; Lu, J.-Q. Oxygen vacancy promoted CO oxidation over Pt/CeO₂ catalysts: A reaction at Pt-CeO₂ interface. *Appl. Surf. Sci.* **2014**, *314*, 725–734. doi: 10.1016/j.apsusc.2014.06.196
248. Meng, L.; Jia, A.-P.; Lu, J.-Q.; Luo, L.-F.; Huang, W.-X.; Luo, M.-F. Synergetic Effects of PdO Species on CO Oxidation over PdO–CeO₂ Catalysts. *J. Phys. Chem. C* **2011**, *115*, 19789–19796. doi: 10.1021/jp2056688
249. Konsolakis, M. Recent Advances on Nitrous Oxide (N₂O) Decomposition over Non-Noble-Metal Oxide Catalysts: Catalytic Performance, Mechanistic Considerations, and Surface Chemistry Aspects. *ACS Catal.* **2015**, *5*, 6397–6421. doi: 10.1021/acscatal.5b01605
250. Zabilskiy, M.; Erjavec, B.; Djinović, P.; Pintar, A. Ordered mesoporous CuO-CeO₂ mixed oxides as an effective catalyst for N₂O decomposition. *Chem. Eng. J.* **2014**, *254*, 153–162. doi: 10.1016/j.cej.2014.05.127
251. Konsolakis, M.; Carabineiro, S.A.C.; Papista, E.; Marnellos, G.E.; Tavares, P.B.; Agostinho Moreira, J.; Romaguera-Barcelay, Y.; Figueiredo, J.L. Effect of preparation

- method on the solid state properties and the deN₂O performance of CuO-CeO₂ oxides. *Catal. Sci. Technol.* **2015**, *5*, 3714–3727. doi: 10.1039/C5CY00343A
252. Parres-Esclapez, S.; Illán-Gómez, M.J.; De Lecea, C.S.M.; Bueno-López, A. On the importance of the catalyst redox properties in the N₂O decomposition over alumina and ceria supported Rh, Pd and Pt. *Appl. Catal. B Environ.* **2010**, *96*, 370–378. doi: 10.1016/j.apcatb.2010.02.034
253. Zhu, P.; Li, J.; Zuo, S.; Zhou, R. Preferential oxidation properties of CO in excess hydrogen over CuO-CeO₂ catalyst prepared by hydrothermal method. *Appl. Surf. Sci.* **2008**, *255*, 2903–2909. doi: 10.1016/j.apsusc.2008.08.033
254. Du, P.-P.; Wang, W.-W.; Jia, C.-J.; Song, Q.-S.; Huang, Y.-Y.; Si, R. Effect of strongly bound copper species in copper-ceria catalyst for preferential oxidation of carbon monoxide. *Appl. Catal. A Gen.* **2016**, *518*, 87–101. doi: 10.1016/j.apcata.2015.10.041
255. Wu, Z.; Zhu, H.; Qin, Z.; Wang, H.; Ding, J.; Huang, L.; Wang, J. CO preferential oxidation in H₂-rich stream over a CuO/CeO₂ catalyst with high H₂O and CO₂ tolerance. *Fuel* **2013**, *104*, 41–45. doi: 10.1016/j.fuel.2010.03.001
256. Jampa, S.; Wangkawe, K.; Tantisriyanurak, S.; Changpradit, J.; Jamieson, A.M.; Chaisuwan, T.; Luengnaruemitchai, A.; Wongkasemjit, S. High performance and stability of copper loading on mesoporous ceria catalyst for preferential oxidation of CO in presence of excess of hydrogen. *Int. J. Hydrogen Energy* **2017**, *42*, 5537–5548. doi: 10.1016/j.ijhydene.2016.08.078
257. Arango-Díaz, A.; Moretti, E.; Talon, A.; Storaro, L.; Lenarda, M.; Núñez, P.; Marrero-Jerez, J.; Jiménez-Jiménez, J.; Jiménez-López, A.; Rodríguez-Castellón, E. Preferential CO oxidation (CO-PROX) catalyzed by CuO supported on nanocrystalline CeO₂ prepared by a freeze-drying method. *Appl. Catal. A Gen.* **2014**, *477*, 54–63. doi: 10.1016/j.apcata.2014.02.033
258. Wang, J.; Pu, H.; Wan, G.; Chen, K.; Lu, J.; Lei, Y.; Zhong, L.; He, S.; Han, C.; Luo, Y. Promoted the reduction of Cu²⁺ to enhance CuO-CeO₂ catalysts for CO preferential oxidation in H₂-rich streams: Effects of preparation methods and copper precursors. *Int. J. Hydrogen Energy* **2017**, *42*, 21955–21968. doi: 10.1016/j.ijhydene.2017.07.122
259. Shi, L.; Zhang, G.; Wang, Y. Tailoring catalytic performance of carbon nanotubes confined CuO-CeO₂ catalysts for CO preferential oxidation. *Int. J. Hydrogen Energy* **2018**, *43*, 18211–18219. doi: 10.1016/j.ijhydene.2018.08.020
260. Cecilia, J.A.; Arango-Díaz, A.; Marrero-Jerez, J.; Núñez, P.; Moretti, E.; Storaro, L.; Rodríguez-Castellón, E. Catalytic Behaviour of CuO-CeO₂ Systems Prepared by

- Different Synthetic Methodologies in the CO-PROX Reaction under CO₂-H₂O Feed Stream. *Catalysts* **2017**, *7*, 160. doi: 10.3390/catal7050160
261. Han, J.; Kim, H.J.; Yoon, S.; Lee, H. Shape effect of ceria in Cu/ceria catalysts for preferential CO oxidation. *J. Mol. Catal. A Chem.* **2011**, *335*, 82–88. doi: 10.1016/j.molcata.2010.11.017
262. Zou, Q.; Zhao, Y.; Jin, X.; Fang, J.; Li, D.; Li, K.; Lu, J.; Luo, Y. Ceria-nano supported copper oxide catalysts for CO preferential oxidation: Importance of oxygen species and metal-support interaction. *Appl. Surf. Sci.* **2019**, *494*, 1166–1176. doi: 10.1016/j.apsusc.2019.07.210
263. Yu, X.; Wu, J.; Zhang, A.; Xue, L.; Wang, Q.; Tian, X.; Shan, S.; Zhong, C.-J.; Zeng, S. Hollow copper-ceria microspheres with single and multiple shells for preferential CO oxidation. *CrystEngComm* **2019**, *21*, 3619–3626. doi: 10.1039/C9CE00272C
264. Dongil, A.B.; Bachiller-Baeza, B.; Castillejos, E.; Escalona, N.; Guerrero-Ruiz, A.; Rodríguez-Ramos, I. Promoter effect of alkalis on CuO/CeO₂/carbon nanotubes systems for the PROx reaction. *Catal. Today* **2018**, *301*, 141–146. doi: 10.1016/j.cattod.2017.03.033
265. Wang, W.-W.; Du, P.-P.; Zou, S.-H.; He, H.-Y.; Wang, R.-X.; Jin, Z.; Shi, S.; Huang, Y.-Y.; Si, R.; Song, Q.-S.; Jia, C.-J.; Yan, C.-H. Highly Dispersed Copper Oxide Clusters as Active Species in Copper-Ceria Catalyst for Preferential Oxidation of Carbon Monoxide. *ACS Catal.* **2015**, *5*, 2088–2099. doi: 10.1021/cs5014909
266. Gong, X.; Liu, B.; Kang, B.; Xu, G.; Wang, Q.; Jia, C.; Zhang, J. Boosting Cu-Ce interaction in Cu_xO/CeO₂ nanocube catalysts for enhanced catalytic performance of preferential oxidation of CO in H₂-rich gases. *Mol. Catal.* **2017**, *436*, 90–99. doi: 10.1016/j.mcat.2017.04.013
267. Papavasiliou, J.; Vakros, J.; Avgouropoulos, G. Impact of acid treatment of CuO-CeO₂ catalysts on the preferential oxidation of CO reaction. *Catal. Commun.* **2018**, *115*, 68–72. doi: 10.1016/j.catcom.2018.07.014
268. Borchers, C.; Martin, M.L.; Vorobjeva, G.A.; Morozova, O.S.; Firsova, A.A.; Leonov, A.V.; Kurmaev, E.Z.; Kukhareno, A.I.; Zhidkov, I.S.; Cholakh, S.O. Cu–CeO₂ nanocomposites: mechanochemical synthesis, physico-chemical properties, CO-PROX activity. *J. Nanoparticle Res.* **2016**, *18*, 344. doi: 10.1007/s11051-016-3640-6
269. Martínez-Arias, A.; Gamarra, D.; Fernández-García, M.; Hornés, A.; Belver, C. Spectroscopic Study on the Nature of Active Entities in Copper–Ceria CO-PROX Catalysts. *Top. Catal.* **2009**, *52*, 1425–1432. doi: 10.1007/s11244-009-9322-1

270. Lu, J.; Wang, J.; Zou, Q.; He, D.; Zhang, L.; Xu, Z.; He, S.; Luo, Y. Unravelling the Nature of the Active Species as well as the Doping Effect over Cu/Ce-Based Catalyst for Carbon Monoxide Preferential Oxidation. *ACS Catal.* **2019**, *9*, 2177–2195. doi: 10.1021/acscatal.8b04035
271. Monte, M.; Gamarra, D.; López Cámara, A.; Rasmussen, S.B.; Gyorffy, N.; Schay, Z.; Martínez-Arias, A.; Conesa, J.C. Preferential oxidation of CO in excess H₂ over CuO/CeO₂ catalysts: Performance as a function of the copper coverage and exposed face present in the CeO₂ support. *Catal. Today* **2014**, *229*, 104–113. doi: 10.1016/j.cattod.2013.10.078
272. Li, W.; Hu, Y.; Jiang, H.; Yang, S.; Li, C. Facile synthesis of multi-shelled hollow Cu–CeO₂ microspheres with promoted catalytic performance for preferential oxidation of CO. *Mater. Chem. Phys.* **2019**, *226*, 158–168. doi: 10.1016/j.matchemphys.2018.12.097
273. Firsova, A.A.; Morozova, O.S.; Vorob'eva, G.A.; Leonov, A.V.; Kukharensko, A.I.; Cholakh, S.O.; Kurmaev, E.Z.; Korchak, V.N. Mechanochemical Activation of Cu–CeO₂ Mixture as a Promising Technique for the Solid-State Synthesis of Catalysts for the Selective Oxidation of CO in the Presence of H₂. *Kinet. Catal.* **2018**, *59*, 160–173. doi: 10.1134/S0023158418020076
274. Yen, H.; Seo, Y.; Kaliaguine, S.; Kleitz, F. Tailored Mesostructured Copper/Ceria Catalysts with Enhanced Performance for Preferential Oxidation of CO at Low Temperature. *Angew. Chem. Int. Ed.* **2012**, *51*, 12032–12035. doi: 10.1002/anie.201206505
275. Liu, Z.; Chen, J.; Zhou, R.; Zheng, X. Influence of Ethanol Washing in Precursor on CuO–CeO₂ Catalysts in Preferential Oxidation of CO in Excess Hydrogen. *Catal. Lett.* **2008**, *123*, 102. doi: 10.1007/s10562-008-9401-0
276. Xia, Y.; Lao, J.; Ye, J.; Cheng, D.; Chen, F.; Zhan, X. Role of Two-Electron Defects on the CeO₂ Surface in CO Preferential Oxidation over CuO/CeO₂ Catalysts. *ACS Sustainable Chem. Eng.* **2019**, *7*, 18421–18433. doi: 10.1021/acssuschemeng.9b04149
277. Xie, Y.; Yin, Y.; Zeng, S.; Gao, M.; Su, H. Coexistence of Cu⁺ and Cu²⁺ in star-shaped CeO₂/Cu_xO catalyst for preferential CO oxidation. *Catal. Commun.* **2017**, *99*, 110–114. doi: 10.1016/j.catcom.2017.06.003
278. Chen, S.; Li, L.; Hu, W.; Huang, X.; Li, Q.; Xu, Y.; Zuo, Y.; Li, G. Anchoring High-Concentration Oxygen Vacancies at Interfaces of CeO_{2-x}/Cu toward Enhanced Activity for Preferential CO Oxidation. *ACS Appl. Mater. Interfaces* **2015**, *7*, 22999–23007. doi:

- 10.1021/acsami.5b06302
279. Zhang, L.; Chen, T.; Zeng, S.; Su, H. Effect of doping elements on oxygen vacancies and lattice oxygen in CeO₂-CuO catalysts. *J. Environ. Chem. Eng.* **2016**, *4*, 2785–2794. doi: 10.1016/j.jece.2016.05.023
280. López Cámara, A.; Cortés Corberán, V.; Barrio, L.; Zhou, G.; Si, R.; Hanson, J.C.; Monte, M.; Conesa, J.C.; Rodriguez, J.A.; Martínez-Arias, A. Improving the CO-PROX Performance of Inverse CeO₂/CuO Catalysts: Doping of the CuO Component with Zn. *J. Phys. Chem. C* **2014**, *118*, 9030–9041. doi: 10.1021/jp5009384
281. Papavasiliou, J.; Rawski, M.; Vakros, J.; Avgouropoulos, G. A Novel Post-Synthesis Modification of CuO-CeO₂ Catalysts: Effect on Their Activity for Selective CO Oxidation. *ChemCatChem* **2018**, *10*, 2096–2106. doi: 10.1002/cctc.201701968
282. Liu, Z.; Zhou, R.; Zheng, X. Influence of residual K⁺ on the catalytic performance of CuO-CeO₂ catalysts in preferential oxidation of CO in excess hydrogen. *Int. J. Hydrogen Energy* **2008**, *33*, 791–796. doi: 10.1016/j.ijhydene.2007.10.011
283. Dongil, A.B.; Bachiller-Baeza, B.; Castillejos, E.; Escalona, N.; Guerrero-Ruiz, A.; Rodríguez-Ramos, I. The promoter effect of potassium in CuO/CeO₂ systems supported on carbon nanotubes and graphene for the CO-PROX reaction. *Catal. Sci. Technol.* **2016**, *6*, 6118–6127. doi: 10.1039/C6CY00304D
284. Ding, J.; Li, L.; Li, H.; Chen, S.; Fang, S.; Feng, T.; Li, G. Optimum Preferential Oxidation Performance of CeO₂-CuO_x-RGO Composites through Interfacial Regulation. *ACS Appl. Mater. Interfaces* **2018**, *10*, 7935–7945. doi: 10.1021/acsami.7b15549
285. Zhang, H.; Xu, C.; Ding, J.; Su, H.; Zeng, S. RGO/MWCNTs/Cu_xO-CeO₂ ternary nanocomposites for preferential CO oxidation in hydrogen-rich streams. *Appl. Surf. Sci.* **2017**, *426*, 50–55. doi: 10.1016/j.apsusc.2017.07.154
286. Xu, C.; Zeng, S.; Zhang, H.; Xie, Y.; Zhang, A.; Jing, G.; Su, H. Facile hydrothermal procedure to synthesize sheet-on-sheet reduced graphene oxide (RGO)/Cu_xO-CeO₂ nanocomposites for preferential oxidation of carbon monoxide. *Int. J. Hydrogen Energy* **2017**, *42*, 14133–14143. doi: 10.1016/j.ijhydene.2017.04.058
287. Wang, Q.; Zhang, H.; Wu, J.; Tuya, N.; Zhao, Y.; Liu, S.; Dong, Y.; Li, P.; Xu, Y.; Zeng, S. Experimental and computational studies on copper-cerium catalysts supported on nitrogen-doped porous carbon for preferential oxidation of CO. *Catal. Sci. Technol.* **2019**, *9*, 3023–3035. doi: 10.1039/C9CY00446G
288. Chen, A.; Yu, X.; Zhou, Y.; Miao, S.; Li, Y.; Kuld, S.; Sehested, J.; Liu, J.; Aoki, T.; Hong, S.; Camellone, M.F.; Fabris, S.; Ning, J.; Jin, C.; Yang, C.; Nefedov, A.; Wöll, C.; Wang,

- Y.; Shen, W. Structure of the catalytically active copper–ceria interfacial perimeter. *Nat. Catal.* **2019**, *2*, 334–341. doi: 10.1038/s41929-019-0226-6
289. Ning, J.; Zhou, Y.; Chen, A.; Li, Y.; Miao, S.; Shen, W. Dispersion of copper on ceria for the low-temperature water-gas shift reaction. *Catal. Today* **2020**, *357*, 460–467. doi: 10.1016/j.cattod.2019.07.048
290. Si, R.; Raitano, J.; Yi, N.; Zhang, L.; Chan, S.-W.; Flytzani-Stephanopoulos, M. Structure sensitivity of the low-temperature water-gas shift reaction on Cu-CeO₂ catalysts. *Catal. Today* **2012**, *180*, 68–80. doi: 10.1016/j.cattod.2011.09.008
291. Yan, H.; Yang, C.; Shao, W.-P.; Cai, L.-H.; Wang, W.-W.; Jin, Z.; Jia, C.-J. Construction of stabilized bulk-nano interfaces for highly promoted inverse CeO₂/Cu catalyst. *Nat. Commun.* **2019**, *10*, 3470. doi: 10.1038/s41467-019-11407-2
292. Wang, X.; Mi, J.; Lin, Z.; Lin, Y.; Jiang, L.; Cao, Y. Efficient fabrication of mesoporous active Cu-Co-CeO₂ catalysts for water-gas shift. *Mater. Lett.* **2016**, *162*, 214–217. doi: 10.1016/j.matlet.2015.09.140
293. Wang, X.; Liu, Y.; Peng, X.; Lin, B.; Cao, Y.; Jiang, L. Sacrificial Adsorbate Strategy Achieved Strong Metal-Support Interaction of Stable Cu Nanocatalysts. *ACS Appl. Energy Mater.* **2018**, *1*, 1408–1414. doi: 10.1021/acsaem.8b00049
294. Djinović, P.; Batista, J.; Levec, J.; Pintar, A. Comparison of water-gas shift reaction activity and long-term stability of nanostructured CuO-CeO₂ catalysts prepared by hard template and co-precipitation methods. *Appl. Catal. A Gen.* **2009**, *364*, 156–165. doi: 10.1016/j.apcata.2009.05.044
295. Chen, C.; Zhan, Y.; Li, D.; Zhang, Y.; Lin, X.; Jiang, L.; Zheng, Q. Preparation of CuO/CeO₂ Catalyst with Enhanced Catalytic Performance for Water-Gas Shift Reaction in Hydrogen Production. *Energy Technol.* **2018**, *6*, 1096–1103. doi: 10.1002/ente.201700750
296. Zhang, Z.; Wang, S.-S.; Song, R.; Cao, T.; Luo, L.; Chen, X.; Gao, Y.; Lu, J.; Li, W.-X.; Huang, W. The most active Cu facet for low-temperature water gas shift reaction. *Nat. Commun.* **2017**, *8*, 488. doi: 10.1038/s41467-017-00620-6
297. Agarwal, S.; Zhu, X.; Hensen, E.J.M.; Mojet, B.L.; Lefferts, L. Surface-Dependence of Defect Chemistry of Nanostructured Ceria. *J. Phys. Chem. C* **2015**, *119*, 12423–12433. doi: 10.1021/acs.jpcc.5b02389
298. Wang, Y.-X.; Wang, G.-C. A Systematic Theoretical Study of Water Gas Shift Reaction on Cu(111) and Cu(110): Potassium Effect. *ACS Catal.* **2019**, *9*, 2261–2274. doi: 10.1021/acscatal.8b04427

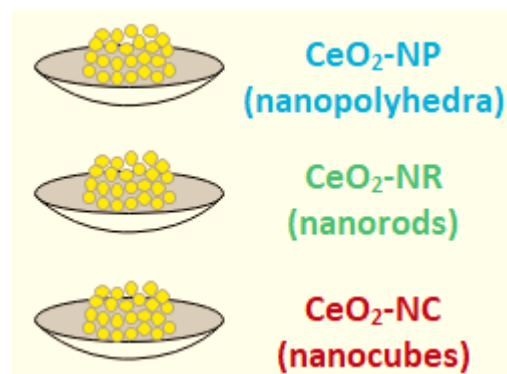
299. Chen, C.; Zhan, Y.; Zhou, J.; Li, D.; Zhang, Y.; Lin, X.; Jiang, L.; Zheng, Q. Cu/CeO₂ Catalyst for Water-Gas Shift Reaction: Effect of CeO₂ Pretreatment. *ChemPhysChem* **2018**, *19*, 1448–1455. doi: 10.1002/cphc.201800122
300. Graciani, J.; Mudiyansele, K.; Xu, F.; Baber, A.E.; Evans, J.; Senanayake, S.D.; Stacchiola, D.J.; Liu, P.; Hrbek, J.; Fernández Sanz, J.; Rodriguez, J.A. Highly active copper-ceria and copper-ceria-titania catalysts for methanol synthesis from CO₂. *Science* **2014**, *345*, 546–550. doi: 10.1126/science.1253057
301. Rodriguez, J.A.; Liu, P.; Stacchiola, D.J.; Senanayake, S.D.; White, M.G.; Chen, J.G. Hydrogenation of CO₂ to Methanol: Importance of Metal-Oxide and Metal-Carbide Interfaces in the Activation of CO₂. *ACS Catal.* **2015**, *5*, 6696–6706. doi: 10.1021/acscatal.5b01755
302. Kattel, S.; Liu, P.; Chen, J.G. Tuning Selectivity of CO₂ Hydrogenation Reactions at the Metal/Oxide Interface. *J. Am. Chem. Soc.* **2017**, *139*, 9739–9754. doi: 10.1021/jacs.7b05362
303. Wang, W.; Qu, Z.; Song, L.; Fu, Q. CO₂ hydrogenation to methanol over Cu/CeO₂ and Cu/ZrO₂ catalysts: Tuning methanol selectivity via metal-support interaction. *J. Energy Chem.* **2020**, *40*, 22–30. doi: 10.1016/j.jechem.2019.03.001
304. Van de Water, L.G.A.; Wilkinson, S.K.; Smith, R.A.P.; Watson, M.J. Understanding methanol synthesis from CO/H₂ feeds over Cu/CeO₂ catalysts. *J. Catal.* **2018**, *364*, 57–68. doi: 10.1016/j.jcat.2018.04.026
305. Hu, X.; Zhao, C.; Guan, Q.; Hu, X.; Li, W.; Chen, J. Selective hydrogenation of CO₂ over a Ce promoted Cu-based catalyst confined by SBA-15. *Inorg. Chem. Front.* **2019**, *6*, 1799–1812. doi: 10.1039/C9QI00397E
306. Li, S.; Guo, L.; Ishihara, T. Hydrogenation of CO₂ to methanol over Cu/AlCeO catalyst. *Catal. Today* **2020**, *339*, 352–361. doi: 10.1016/j.cattod.2019.01.015
307. Tan, Q.; Shi, Z.; Wu, D. CO₂ Hydrogenation to Methanol over a Highly Active Cu-Ni/CeO₂-Nanotube Catalyst. *Ind. Eng. Chem. Res.* **2018**, *57*, 10148–10158. doi: 10.1021/acs.iecr.8b01246
308. Tan, Q.; Shi, Z.; Wu, D. CO₂ hydrogenation over differently morphological CeO₂-supported Cu-Ni catalysts. *Int. J. Energy Res.* **2019**, *43*, 5392–5404. doi: 10.1002/er.4636
309. Li, H.; Cui, Y.; Liu, Q.; Dai, W.-L. Insight into the Synergism between Copper Species and Surface Defects Influenced by Copper Content over Copper/Ceria Catalysts for the Hydrogenation of Carbonate. *ChemCatChem* **2018**, *10*, 619–624. doi:

- 10.1002/cctc.201701384
310. Yang, S.-C.; Pang, S.H.; Sulmonetti, T.P.; Su, W.-N.; Lee, J.-F.; Hwang, B.-J.; Jones, C.W. Synergy between Ceria Oxygen Vacancies and Cu Nanoparticles Facilitates the Catalytic Conversion of CO₂ to CO under Mild Conditions. *ACS Catal.* **2018**, *8*, 12056–12066. doi: 10.1021/acscatal.8b04219
311. Lin, L.; Yao, S.; Rui, N.; Han, L.; Zhang, F.; Gerlak, C.A.; Liu, Z.; Cen, J.; Song, L.; Senanayake, S.D.; Xin, H.L.; Chen, J.G.; Rodriguez, J.A. Conversion of CO₂ on a highly active and stable Cu/FeO_x/CeO₂ catalyst: tuning catalytic performance by oxide-oxide interactions. *Catal. Sci. Technol.* **2019**, *9*, 3735–3742. doi: 10.1039/C9CY00722A

CHAPTER 2

Materials Synthesis and Characterization Studies

Chapter 2 presents in detail the preparation procedures followed during materials synthesis, the characterization techniques applied as well as the conditions used during catalytic evaluation studies. In specific, the preparation methods used for the synthesis of bare ceria nanoparticles as well as of ceria-based transition



metal catalysts are demonstrated in this chapter. The catalytic materials developed in the present thesis were thoroughly characterized by various techniques so as to gain insight into their structural, morphological, surface, redox properties and their catalytic performance was evaluated in different reactions, such as the oxidation of carbon monoxide (CO), the decomposition of nitrous oxide (N₂O) and the hydrogenation of carbon dioxide (CO₂) to methane (CH₄) and carbon monoxide (CO).

2.1. MATERIALS SYNTHESIS

Materials synthesis took place at the Technical University of Crete in the Industrial, Energy and Environmental Systems Lab (IEESL) of the School of Production Engineering and Management in collaboration with the laboratory of Analytical and Environmental Chemistry of the School of Mineral Resources Engineering. The equipment used for nanomaterials' synthesis is presented in the following photographs.

All the catalytic materials developed or used in the present thesis, as well as the catalytic reactions in which they were evaluated, are presented at a glance in Table 2.1.



Image 2.1. From left to right: KERN PNJ precision balance, VELR Scientifica heating magnetic stirrer, WTW pH meter 3110, Rephile Direct–Pure adept ultrapure water system.



Image 2.2. The furnaces used for the aging and calcination of as-prepared materials (Termansys–left, Binder–right).



Image 2.3. The centrifuges used for the recovery of the solid products and the washing of the obtained materials with double deionized water and ethanol (Eppendorf centrifuge 5804–left, MSE Mistral 2000–right).

2.1.1. Synthesis of Bare Ceria Nanoparticles by Different Methods

Bare ceria nanoparticles were synthesized by various methods, such as thermal decomposition, precipitation and the hydrothermal method by modifying the experimental conditions (base concentration, aging temperature). The aforementioned preparation methods are presented in detail below.

Bare Ceria Nanoparticles Prepared by Thermal Decomposition [1]: The $\text{Ce}(\text{NO}_3)_3 \cdot 6\text{H}_2\text{O}$ (purity $\geq 99.0\%$, Fluka) precursor was heated at $500\text{ }^\circ\text{C}$ for 2 h under air flow (heating ramp $5\text{ }^\circ\text{C}/\text{min}$), as shown in Figure 2.1. The sample is denoted as $\text{CeO}_2\text{-D}$.

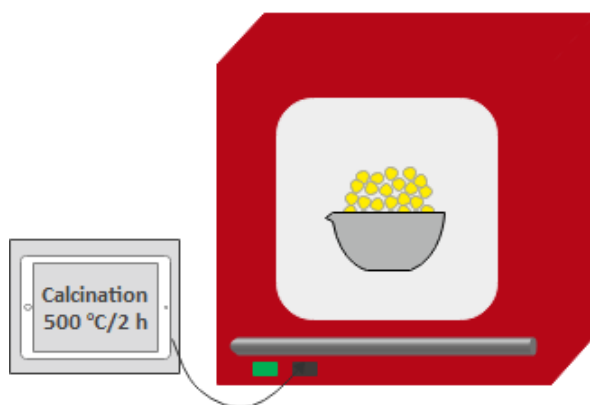


Figure 2.1. Bare ceria nanoparticles prepared by thermal decomposition.

Bare Ceria Nanoparticles Prepared by Precipitation [1]: Initially, the $\text{Ce}(\text{NO}_3)_3 \cdot 6\text{H}_2\text{O}$ (purity $\geq 99.0\%$, Fluka) precursor compound was dissolved in double deionized water (0.50 M) until its complete dissolution. Then, the ammonia solution (25% v/v, EMSURE) was added to the continuously stirred solution at room temperature until pH reached the value of 9–10, and

kept stable for 3 h. The resulting solution was filtered under vacuum and a gel was formed. The precipitate was dried overnight at 110 °C for 12 h and calcined at 500 °C for 2 h under air flow (heating ramp 5 °C/min). The sample is denoted as CeO₂-P. The synthesis procedure is depicted in Figure 2.2.

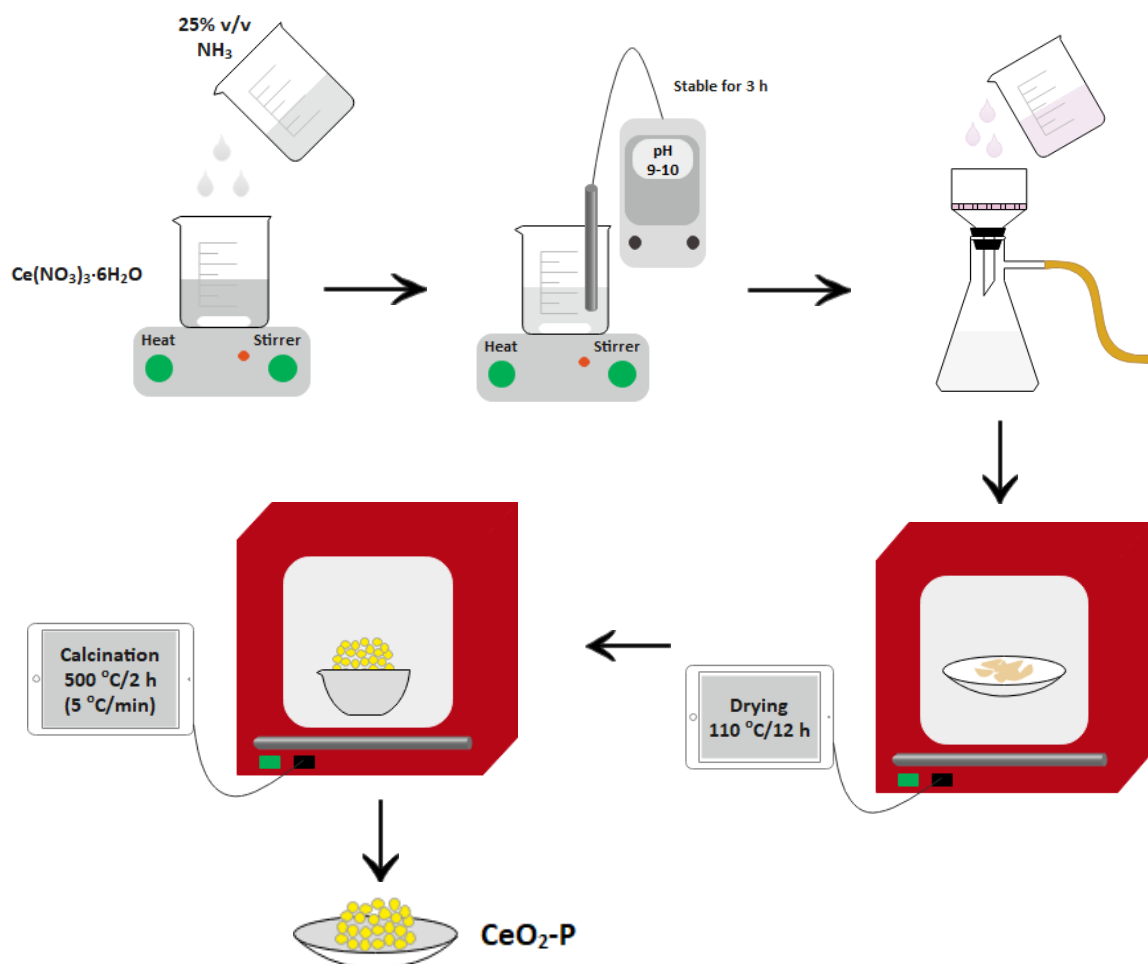


Figure 2.2. Bare ceria nanoparticles prepared by the precipitation method.

Bare Ceria Nanoparticles Prepared by the Hydrothermal Method [2]: During hydrothermal synthesis, the application of diverse experimental conditions, *i.e.*, base concentration (6 or 36.7 M NaOH) and aging temperature (90 or 180 °C), led to the development of different ceria nanostructures, namely nanorods, nanopolyhedra and nanocubes. Specifically, for the synthesis of ceria nanorods, 2.75 mol NaOH (purity \geq 98%, Sigma-Aldrich) was initially dissolved in 75 mL of double deionized water. Then, 175 mL of aqueous solution containing 23 mmol $\text{Ce}(\text{NO}_3)_3 \cdot 6\text{H}_2\text{O}$ (purity \geq 99.0%, Fluka) (0.13 M) was added in the above solution under vigorous stirring until a milky slurry was formed. The mixture was left for additional stirring for 1 h. Then, the final slurry was transferred into a Teflon bottle and aged at 90 °C

for 24 h. In order to obtain ceria nanopolyhedra, the same procedure as above was followed with the only variation of utilizing 0.45 mol NaOH instead of 2.75 mol. For the synthesis of ceria nanocubes, the same procedure as the one followed for the preparation of ceria nanorods was employed, with the only variation being at the final aging temperature, namely 180 °C instead of 90 °C. Subsequently, the solid products were recovered by centrifugation and the obtained materials were washed thoroughly with double deionized water until pH 7, so as to remove any co-precipitated salts and afterwards, they were washed with ethanol (purity 99.8%, ACROS Organics) to avoid nanoparticles' agglomeration. The resulting precipitate was dried at 90 °C for 12 h, followed by calcination at 500 °C for 2 h under air flow (heating ramp 5 °C/min). The samples are designated as CeO₂-NR, CeO₂-NP and CeO₂-NC, representing bare ceria nanorods, nanopolyhedra and nanocubes, respectively. Figure 2.3 depicts the hydrothermal synthesis of the different ceria nanostructures.

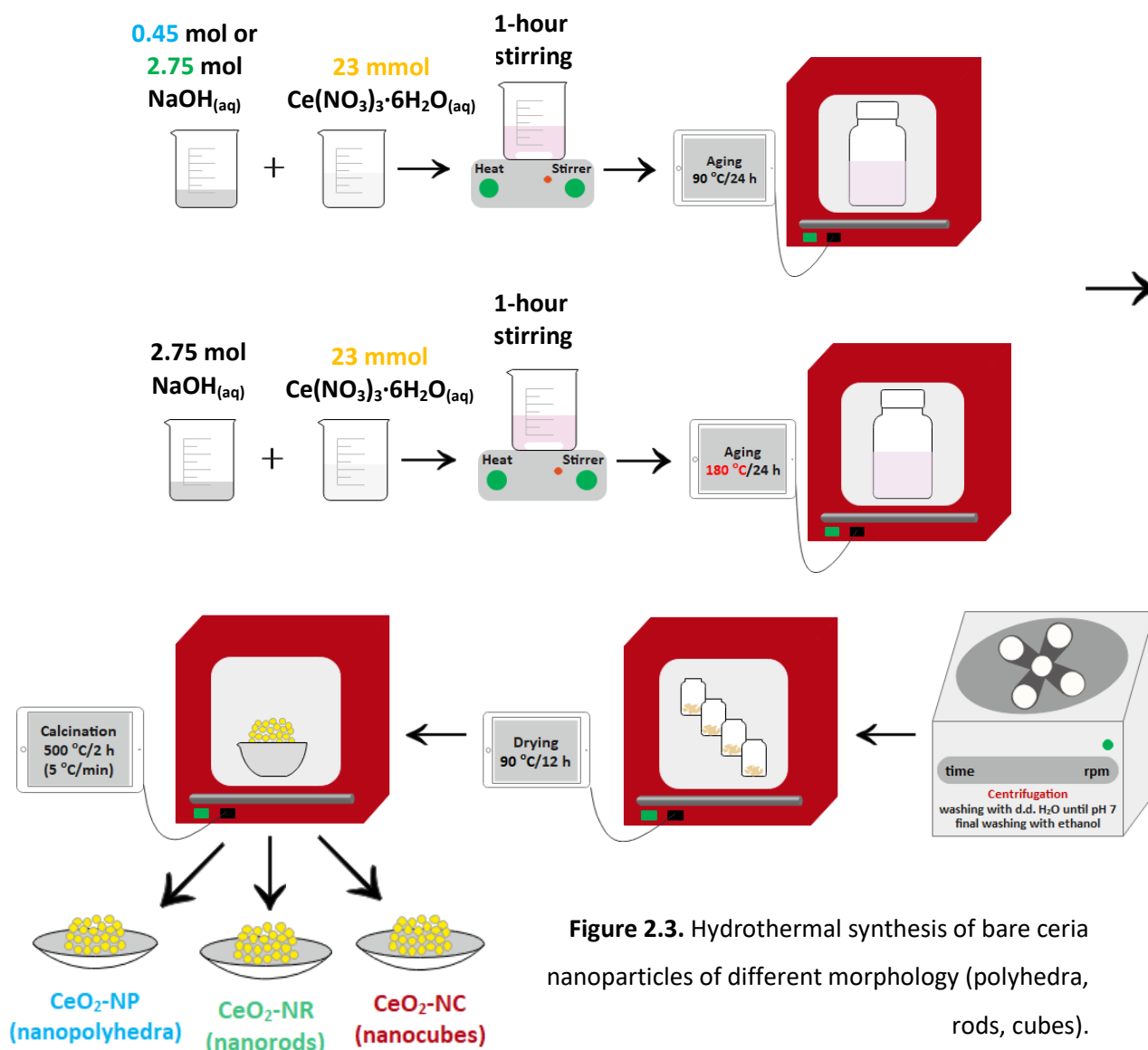


Figure 2.3. Hydrothermal synthesis of bare ceria nanoparticles of different morphology (polyhedra, rods, cubes).

2.1.2. Synthesis of Ceria-Based Transition Metal Catalysts through the Wet Impregnation Method

Different ceria-based transition metal catalysts were prepared by the wet impregnation method. In specific, various transition metals such as copper (Cu), cobalt (Co), iron (Fe) and nickel (Ni) were introduced in the above-mentioned different ceria supports (nanorods, nanopolyhedra, nanocubes) through the wet impregnation method. $M/\text{CeO}_2\text{-NX}$ catalysts (where M: Cu, Co, Fe, Ni and NX: NP–nanopolyhedra, NR–nanorods, NC–nanocubes) were synthesized by the wet impregnation method [2–6]. In particular, aqueous solutions of the metal precursors, *i.e.*, $\text{Cu}(\text{NO}_3)_2 \cdot 2.5\text{H}_2\text{O}$ (Fluka), $\text{Co}(\text{NO}_3)_2 \cdot 6\text{H}_2\text{O}$ (purity $\geq 98\%$, Sigma-Aldrich), $\text{Fe}(\text{NO}_3)_3 \cdot 9\text{H}_2\text{O}$ ($\geq 98\%$, Sigma-Aldrich) and $\text{Ni}(\text{NO}_3)_2 \cdot 6\text{H}_2\text{O}$ (purity $\geq 98\%$, Sigma-Aldrich) were utilized in order to obtain a $M/(M+\text{Ce})$ atomic ratio of 0.2, corresponding to a metal loading of 8.5, 7.8, 7.5 and 8 wt.% for Cu, Co, Fe and Ni, respectively. Afterwards, the obtained suspensions were heated under stirring until water evaporation, dried at $90\text{ }^\circ\text{C}$ for 12 h and finally calcined at $500\text{ }^\circ\text{C}$ for 2 h under air flow (heating ramp $5\text{ }^\circ\text{C}/\text{min}$). The preparation procedure is illustrated in Figure 2.4.

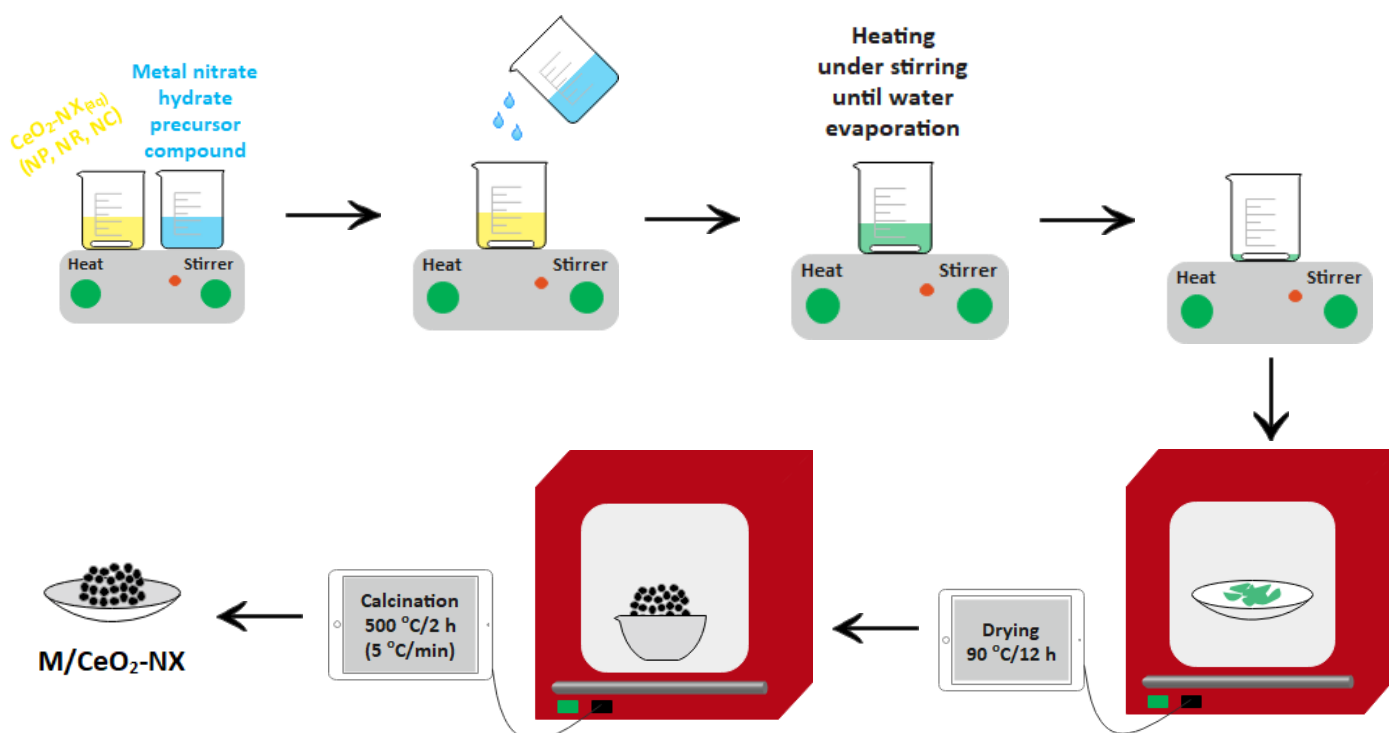


Figure 2.4. Synthesis of ceria-based transition metal catalysts $M/\text{CeO}_2\text{-NX}$ (M: Cu, Co, Fe, Ni and NX: NP, NR, NC) through the wet impregnation method.

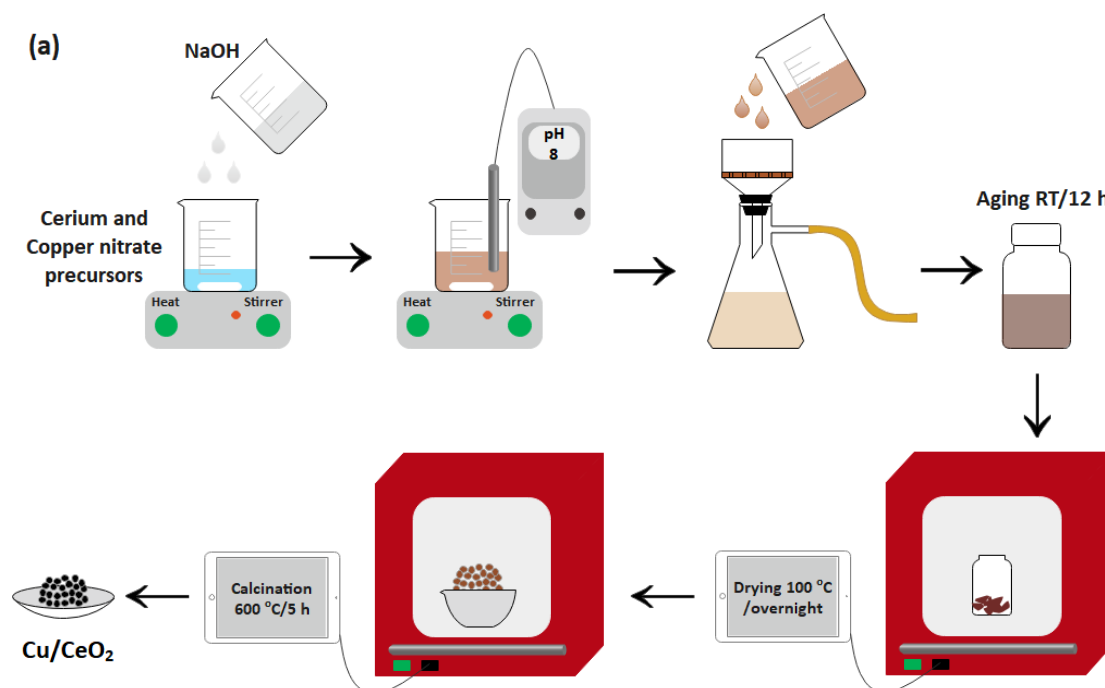
For comparison purposes, two additional samples were synthesized. A bare iron oxide sample denoted as $\text{Fe}_2\text{O}_3\text{-D}$ was prepared by thermal decomposition of $\text{Fe}(\text{NO}_3)_3 \cdot 9\text{H}_2\text{O}$ at

500 °C for 2 h and an iron-ceria mixed oxide was prepared as a physical mixture of 7.5 wt.% Fe₂O₃-D and 92.5 wt.% CeO₂-NR, as it was mixed in agate by hand [4].

2.1.3. Synthesis of Surface (Cs)-Promoted Ceria-Based Copper Catalysts

Initially, the Cu/CeO₂ mixed oxides were prepared by the co-precipitation method [7]. In particular, a base (NaOH) was added, until pH = 8, to an aqueous solution containing the appropriate concentration of cerium and copper nitrate precursor compounds (Sigma-Aldrich) so as to yield a Cu content of 20 wt.%. The obtained precipitate was aged at room temperature for 12 h, followed by filtration and washing. Then, it was dried at 100 °C and calcined at 600 °C for 5 h. The preparation procedure is illustrated in Figure 2.5a.

The prepared Cu/CeO₂ mixed oxides mentioned above were then impregnated with cesium nitrate (CsNO₃, Sigma Aldrich) aqueous solutions of appropriate concentration in order to obtain different Cs contents (0.5–4 atoms per nm² on the basis of the BET surface area of the un-doped sample, *i.e.*, 57 m² g⁻¹) [7]. On a weight basis, the equivalent Cs content corresponds to the range of 0.6–4.8 wt.%. The resulting suspensions were then heated until water evaporation, dried at 100 °C overnight and finally, calcined at 600 °C for 2 h. The preparation procedure is illustrated in Figure 2.5b. The as-prepared samples are denoted as CsCuCe-X, where X stands for the Cs content (0–4 atoms per nm²) of the Cu/CeO₂ mixed oxides (Table 2.1).



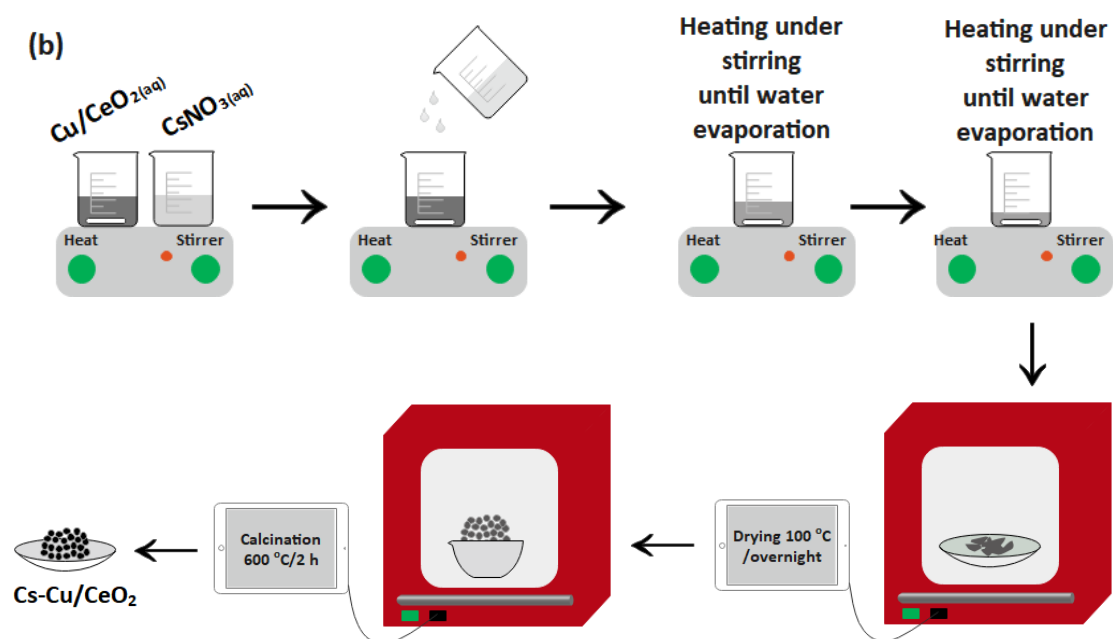


Figure 2.5. (a) Synthesis of Cu/CeO_2 mixed oxides through the co-precipitation method, (b) synthesis of Cs-doped Cu/CeO_2 samples through the wet impregnation method.

Table 2.1. The catalytic materials developed/used in the present thesis.

Material	Preparation method	Precursor compounds	Experimental conditions			Metal loading (wt.%)	Characterization	Catalytic Reaction
			Aging parameters	Drying parameters	Calcination parameters			
Bare ceria nanoparticles								
CeO ₂ -D	Thermal Decomposition	Ce(NO ₃) ₃ ·6H ₂ O	-	-	500 °C/2 h	-	BET, XRD, SEM/EDS, TEM, TPR, XPS	CO+O ₂
CeO ₂ -P	Precipitation			110 °C/12 h				
CeO ₂ -NP	Hydrothermal	Ce(NO ₃) ₃ ·6H ₂ O	90 °C/24 h	90 °C/12 h	500 °C/2 h	-	BET, XRD, TEM, TPR, XPS, RAMAN	CO+O ₂
CeO ₂ -NR								deN ₂ O
CeO ₂ -NC			180 °C/24 h					
Ceria-based transition metal catalysts								
Cu/CeO ₂ -NC	Wet Impregnation	Ce(NO ₃) ₃ ·6H ₂ O		90 °C/12 h	500 °C/2 h	8.5	BET, XRD, XRF, ICP, TEM, TPR, XPS	CO+O ₂
Cu/CeO ₂ -NR		Cu(NO ₃) ₂ ·2.5H ₂ O						CO ₂ +H ₂
Cu/CeO ₂ -NP								
Co/CeO ₂ -NC	Wet Impregnation	Ce(NO ₃) ₃ ·6H ₂ O		90 °C/12 h	500 °C/2 h	7.8	BET, XRD, ICP, TEM, TPR, XPS	deN ₂ O
Co/CeO ₂ -NR		Co(NO ₃) ₂ ·6H ₂ O						CO ₂ +H ₂
Co/CeO ₂ -NP								
Fe/CeO ₂ -NC	Wet Impregnation	Ce(NO ₃) ₃ ·6H ₂ O		90 °C/12 h	500 °C/2 h	7.5	BET, XRD, ICP, SEM/EDS, TEM, TPR, XPS	CO+O ₂
Fe/CeO ₂ -NR		Fe(NO ₃) ₃ ·9H ₂ O						CO ₂ +H ₂
Fe/CeO ₂ -NP								
Fe ₂ O ₃ -D	Thermal Decomposition	Fe(NO ₃) ₃ ·9H ₂ O			500 °C/2 h			CO+O ₂
Fe ₂ O ₃ -D + CeO ₂ -NR	Physical Mixture	Fe ₂ O ₃ -D and CeO ₂ -NR				7.5 wt.% Fe ₂ O ₃ -D and 92.5 wt.% CeO ₂ -NR		CO+O ₂
Ni/CeO ₂ -NC	Wet Impregnation	Ce(NO ₃) ₃ ·6H ₂ O		90 °C/12 h	500 °C/2 h	8.0	BET, XRD, ICP, TEM, TPR, XPS	CO ₂ +H ₂
Ni/CeO ₂ -NR		Ni(NO ₃) ₂ ·6H ₂ O						
Ni/CeO ₂ -NP								

Cs-Promoted Ceria-Based Copper Oxide Catalysts									
CsCuCe-0.0	Co-precipitation	Ce(NO ₃) ₃ ·6H ₂ O Cu(NO ₃) ₂ ·6H ₂ O	RT/12 h	100 °C overnight	600 °C/5 h	Cs 0.0	Cu 20	BET, XRD, TPR, XPS	deN ₂ O
CsCuCe-1.0	Co-precipitation Wet impregnation	Ce(NO ₃) ₃ ·6H ₂ O	RT/12 h	100 °C overnight	600 °C/5 h	1.2	20	BET, XRD, TPR, XPS	deN ₂ O
CsCuCe-2.0		Cu(NO ₃) ₂ ·6H ₂ O				2.4			
CsCuCe-3.0		CsNO ₃				3.6			
CsCuCe-4.0						4.8			

RT: Room Temperature, CO+O₂: CO oxidation reaction, deN₂O: N₂O decomposition reaction, CO₂+H₂: CO₂ hydrogenation reaction

2.2. CHARACTERIZATION TECHNIQUES

The physicochemical properties of as-prepared materials were thoroughly characterized by various techniques, both *ex situ* and *in situ*. In specific, X-ray Fluorescence (XRF) and Inductively Coupled Plasma (ICP) were employed for the determination of the actual metal content, N_2 adsorption-desorption at $-196\text{ }^\circ\text{C}$ (BET method) was performed so as to gain insight into the textural properties, X-ray Diffraction (XRD) for determining the structural properties, Transmission Electron Microscopy (TEM) for providing the morphological features, Scanning Electron Microscopy-Energy Dispersive X-ray Spectroscopy (SEM-EDS) for the elemental mapping, Temperature Programmed Reduction employing H_2 as a reducing agent (H_2 -TPR) for the determination of the redox properties, X-ray Photoelectron Spectroscopy (XPS) for defining the surface characteristics and Raman spectroscopy in order to gain insight into the structural defects of as-prepared samples. In particular, the characterizations of the materials were performed at the Technical University of Crete, the Chemical Process & Energy Resources Institute (CPERI) of the Centre for Research & Technology Hellas (CERTH), the University of Porto and the Institute of Electronic Structure and Laser (IESL-FORTH). The procedure followed for each characterization technique is presented in the following sub-sections.

2.2.1. Elemental Analysis (XRF, ICP)

The metal content of the materials in weight percentage (wt.%) was determined by X-ray Fluorescence (XRF) and Inductively Coupled Plasma Atomic Emission Spectroscopy (ICP-AES) [3,6]. In specific, XRF analyses were performed on an X-ray spectrometer (Amptek X-123) with Si-PIN photodiode. The X-ray spectrometer contains a solid-state detector, a digital pulse processor and a multichannel analyzer, which are interfaced with a computer for data acquisition and analysis. A $25\text{ }\mu\text{m}$ thick silver filter and a $250\text{ }\mu\text{m}$ thick aluminum filter were simultaneously used to reduce background and improve signal-to-noise ratio (SNR) in the energy region (10–30 keV) of the XRF spectrum. The distance between the X-ray tube and the sample as well as between the detector and the sample were 1 cm. A series of Cu/Ceria reference samples with a Cu loading in the range of 1–15 wt.% were employed to obtain a calibration curve. Analysis was performed by the AXIL(RN) software package supplied by the International Atomic Energy Agency [2]. ICP analysis was performed in a Perkin-Elmer Optima 4300DV apparatus [6].

2.2.2. Textural and Structural Characterization (BET and XRD)

The textural characteristics of as-prepared samples were determined by N₂ adsorption-desorption isotherms obtained at -196 °C (Nova 2200e Quantachrome flow apparatus or ASAP 2010 Micromeritics). Specific surface areas (m² g⁻¹) were obtained according to the Brunauer-Emmett-Teller (BET) method at relative pressures in the 0.05–0.30 range. The specific pore volume (cm³ g⁻¹) was calculated based on the highest relative pressure, whereas the average pore size diameter (d_p, nm) was determined by the Barrett-Joyner-Halenda (BJH) method. Prior to measurements, the samples were degassed at 250–300 °C for 5 h under vacuum [2–4,8].

The crystalline structure of bare ceria and copper-ceria samples was determined by powder X-ray diffraction (XRD) on a Siemens D 500 diffractometer operated at 40 kV and 30 mA with Cu Kα radiation (λ = 0.154 nm) [2]. Diffractograms were recorded in the 2–80° 2θ range and at a scanning rate of 0.02° s⁻¹. Scherrer's equation (Eq. 1) was employed to determine the primary particle size of a given crystal phase based on the most intense diffraction peak of CeO₂ (2θ: 28.5° and 47.6°) and CuO (2θ: ~35.3° and 38.2°) patterns [2]:

$$D_{\text{XRD}} = \frac{K \cdot \lambda}{\beta \cdot \cos\theta} \quad (1)$$

where K is the Scherrer constant; λ is the wavelength of the X-ray in nm; β is the line broadening; θ is the Bragg angle [9].

The structural characterization of cobalt-ceria and iron-ceria samples was carried out by means of X-ray diffraction (XRD) in a PAN'alytical X'Pert MPD equipped with a X'Celerator detector and secondary monochromator (Cu Kα λ = 0.154 nm, 50 kV, 40 mA; data recorded at a 0.017° step size, 100 s/step) in the University of Trás-os-Montes e Alto Douro. The collected spectra were analyzed by Rietveld refinement using PowderCell software, allowing the determination of crystallite sizes by means of the Williamson-Hall plot [3,4].

2.2.3. Morphological Characterization (TEM, SEM-EDS)

Bare ceria and ceria-based transition-metal samples (M/CeO₂, M: Cu, Co, Fe, Ni) were analyzed on the basis of their morphological features by Transmission electron microscopy (TEM) and Scanning Electron Microscopy-Energy Dispersive X-ray Spectroscopy (SEM-EDS). TEM analyses were performed on a Leo 906E apparatus, at 120 kV in University of Trás-os-Montes e Alto Douro. Samples were dispersed ultrasonically and a 400 mesh formvar/carbon copper grid was dipped into the solution for the TEM analysis [3,4,6].

In addition, bare ceria samples were characterized by scanning electron microscopy (SEM), using a FEI Quanta 400 FEG ESEM (15 keV) electron microscope. The sample powders were mounted on double sided adhesive tape and observed at different magnifications under two different detection modes: secondary and backscattered electrons. Energy-dispersive X-ray spectroscopy (EDS) confirmed the nature of the components [1].

2.2.4. Redox Characterization (H₂-TPR)

TPR experiments were carried out in an AMI-200 Catalyst Characterization Instrument (Altamira Instruments), employing H₂ as a reducing agent. In a typical H₂-TPR experiment, 50 mg of the sample (grain size 180–355 μm) was heated up to 1100 °C (10 °C/min), under H₂ flow (1.5 cm³) balanced with He (29 cm³). The H₂ consumption was calculated by the integrated area of TPR peaks, calibrated against a known amount of CuO standard sample [1–4,6].

2.2.5. Surface Characterization (XPS)

XPS analysis was performed using a Kratos AXIS Ultra HSA, with VISION software for data acquisition and CASAXPS software for data analysis. The samples were pressed into pellets with ~1 mm thickness and attached to the sample holder with a small cut of double sided carbon tape. The analysis was performed with a monochromatic Al Kα X-ray source (1486.7 eV), operating at 15 kV (90 W), in FAT mode (Fixed Analyser Transmission), with a pass energy of 40 eV for regions (ROI) and 80 eV for survey. Data acquisition was performed with a pressure lower than 1×10^{-6} Pa, employing a charge neutralization system. The effect of the electric charge was corrected by the reference of the carbon peak C 1s (285 eV). The fitting of peak spectra was performed using the CasaXPS software, using Gaussian-Lorentzian peak shape and Shirley (or Linear) type background subtraction [2].

2.2.6. Structure of anionic sub-lattice and redox properties (Raman)

In situ Raman spectroscopic measurements were undertaken in bare ceria samples [2] by using a homemade optical Raman cell, described in detail elsewhere [10]. Approximately 150 mg of powderous sample were pressed into a wafer disc that was mounted on the sample holder of the in situ cell by means of a gold wire. Temperature was controlled and monitored with a thermocouple located very close to the sample. The 491.5 nm line of a Cobolt Calypso diode-pumped solid state laser operated at a power level of less than 20 mW (on the sample) was used for exciting the Raman spectra. The incident laser beam was slightly defocused by means of a cylindrical lens in order to exclude excessive sample

irradiance. The sampling depth of the 491.5 nm laser is several hundred molecular layers, which combined with the area of the irradiation spot result in a considerable sampling volume that is characteristic of the bulk. Changing the irradiation spot did not cause changes in the in situ Raman spectra. The scattered light was collected at right angle (horizontal scattering plane) and analyzed with a 0.85 m Spex 1403 double monochromator with PMT (–20 °C cooled RCA) detection interfaced with a Labspec acquisition software.

For recording the in situ Raman spectra a recently described protocol was followed [11]. Briefly, each sample was first heated in the in situ Raman furnace under flowing 20% O₂/He (30 cm³/min) at a temperature of 440 °C and subjected to the flowing gas for 30 min and the in situ Raman spectrum was recorded under oxidizing conditions at 440 °C. Subsequently, the flowing feed gas was switched to 5% H₂/He (50 cm³/min) at the same temperature (440 °C) and the sample was subjected to flowing reducing atmosphere for 1 h and 45 min in order to attain steady state and the in situ Raman spectrum was recorded at 440 °C. A subsequent reoxidation of the sample was performed to check that the initial features of the Raman spectra obtained under oxidizing conditions could be reinstated. The temperature of 440 °C was chosen, after undertaking the H₂-TPR measurements, in order to achieve an observable spectroscopic effect [11] upon subjecting each sample in oxidation/reduction cycles.

As before [11], for comparison purposes, normalized and so-called "reduced" Raman spectra are used. The normalization procedure eliminates the effect of variations in absorption of incident and scattered light by differently coloured samples, whereas in order to disentangle the effects caused by temperature (depopulation of ground state, *etc.*) and focus on the purely vibrational effects the "reduction" procedure is applied [11]. Briefly, the Stokes reduced intensity is given by:

$$I_R(\tilde{\nu}) = \frac{\tilde{\nu}}{(\tilde{\nu}_0 - \tilde{\nu})^4} \cdot \left[\frac{1}{\exp\left(\frac{hc\tilde{\nu}}{k_B T}\right) - 1} + 1 \right]^{-1} \cdot I_M(\tilde{\nu}) \quad (2)$$

where $I_M(\tilde{\nu})$ is the measured normalized Raman intensity at wavenumber $\tilde{\nu}$, $\tilde{\nu}_0$ is the wavenumber of the laser line used and c , h , k_B are the velocity of light, Planck's constant and Boltzmann's constant, respectively [2].

2.3. CATALYTIC EVALUATION STUDIES

The catalytic materials developed in the present thesis were catalytically evaluated in different reactions, such as CO oxidation, N₂O decomposition and CO₂ hydrogenation to CH₄ and CO. In specific, the catalytic evaluation studies of the materials were performed at the Technical University of Crete in the Industrial, Energy and Environmental Systems Lab (IEESL) of the School of Production Engineering and Management, in collaboration with the Chemical Process & Energy Resources Institute (CPERI) of the Centre for Research & Technology Hellas (CERTH), the University of Porto, the University of Western Macedonia and the National and Kapodistrian University of Athens. The procedures followed for the catalytic studies are presented in the following sub-sections. The following photograph (Image 2.4) depicts the automated system used during catalytic experiments.

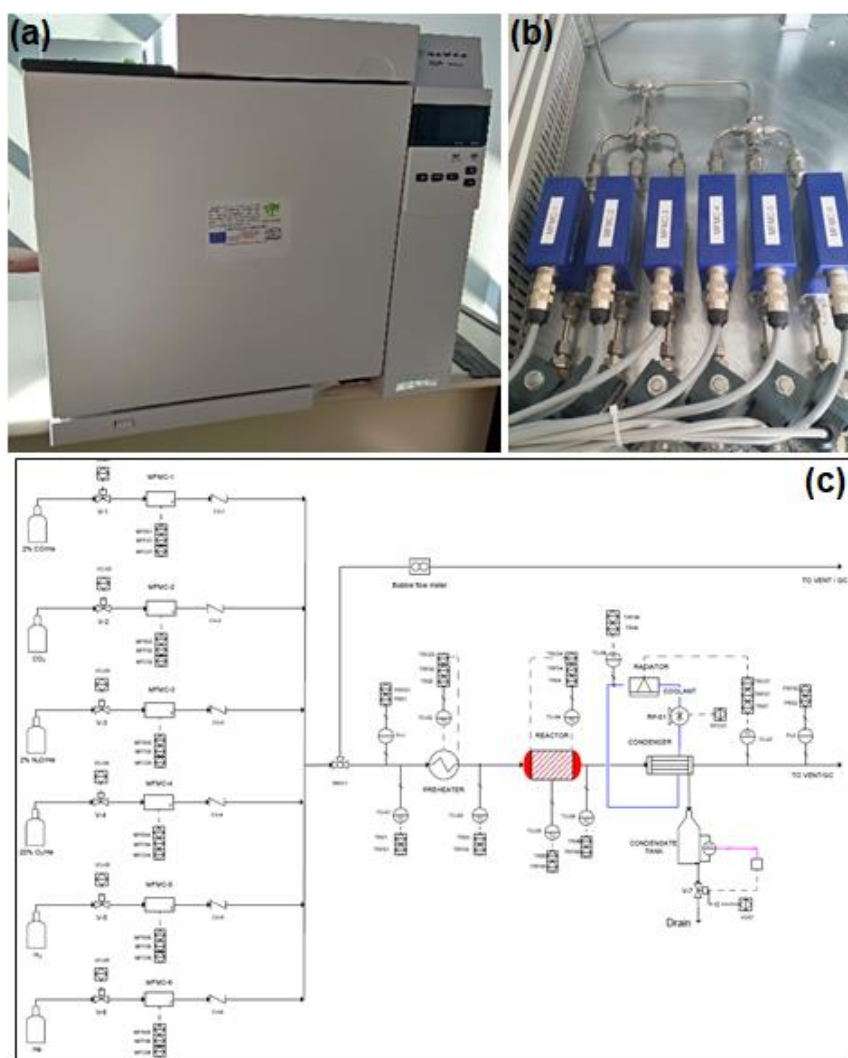


Image 2.4. Automated system of catalytic experiments: (a) Gas Chromatograph AGILENT 7820A, (b) Mass flow controllers, (c) Flow chart of the catalytic unit system.

2.3.1. CO Oxidation

Catalytic tests of bare ceria and copper-ceria samples for CO oxidation were carried out in a quartz fixed-bed reactor (9 mm i.d.). The catalyst (400 mg) and a layer of quartz wool were filled in the reactor. The total flow rate of the feed gas (2000 ppm CO and 1 vol.% O₂ in He) was 500 cm³/min, corresponding to a Gas Hour Space Velocity (GHSV) of 39,000 h⁻¹. Catalytic evaluation measurements were carried out by increasing the temperature by 25-degree steps up to 500 °C. The reactant CO was analyzed by using an online CO analyzer. The CO conversion (X_{CO} , %) was calculated by the following equation (Eq. 3) [2]:

$$X_{CO}(\%) = \frac{[CO]_{in} - [CO]_{out}}{[CO]_{in}} \cdot 100 \quad (3)$$

where $[CO]_{in}$ and $[CO]_{out}$ are the CO concentration (ppm) in the inlet and outlet gas streams, respectively.

Kinetic measurements were also carried out under differential conditions to gain insight into the intrinsic activity of ceria samples. The specific reaction rate of CO consumption (r_{CO} , nmol m⁻² s⁻¹) was calculated using equation (4), whereas the Arrhenius plot was used to determine the activation energy (E_a , kJ/mol) and the pre-exponential factor (A , nmol m⁻² s⁻¹) [1,4].

$$r_{CO}(\text{nmol} \cdot \text{m}^{-2} \cdot \text{s}^{-1}) = \frac{X_{CO} \cdot [CO]_{in} \cdot F \left(\frac{\text{cm}^3}{\text{min}} \right)}{100 \cdot 60 \left(\frac{\text{s}}{\text{min}} \right) \cdot V_m \left(\frac{\text{cm}^3}{\text{mol}} \right) \cdot m_{\text{cat}}(\text{g}) \cdot S_{\text{BET}} \left(\frac{\text{m}^2}{\text{g}} \right)} \cdot 10^9 \quad (4)$$

where F (cm³/min) is the total flow rate, V_m (cm³/mol) is the gas molar volume at STP conditions (298 K and 1 bar), m_{cat} (g) is the mass of catalyst and S_{BET} (m²/g) is the surface area.

Catalytic oxidation of CO over iron-ceria samples was performed in a quartz fixed-bed tubular microreactor (12.95 mm i.d.) at atmospheric pressure, loaded with 0.10 g of catalyst. The reaction stream consisted of 2000 ppm of CO and 1 vol.% O₂ balanced with He in a total feed stream of 80 mL min⁻¹ which was controlled (Mass Flow controllers) and homogenized by a mixing chamber. The catalyst temperature was recorded using a K-Type thermocouple placed in the catalyst bed and the Gas Hour Space Velocity (GHSV) of the feed stream was 40,000 h⁻¹. Prior to catalytic experiments, all samples were treated under a 20 cm³/min flow of 20 vol.% O₂ in He heating up to 480 °C with 10 degrees/min. Samples remained at 480 °C for 30 min and then the temperature was decreased to 25 °C with the same rate. Final purge

with He flow was carried out in order to remove physisorbed species. Catalytic evaluation measurements were carried out every 20 degrees up to 500 °C. CO and CO₂ in the effluent gas were analyzed by gas chromatography (GC), equipped with two fully equipped channels with separated TCD detectors, injectors and capillary columns. The conversion of CO (X_{CO}) was calculated from the difference in CO concentration between the inlet and outlet gas streams, according to equation (3). The specific reaction rate (r , mol m⁻² s⁻¹) of the CO conversion was also estimated under differential reaction conditions ($X_{CO} < 15\%$, $T = 125$ °C, $W/F = 0.075$ g s cm⁻³) using equation (4) [4].

2.3.2. N₂O Decomposition

The catalytic studies for the N₂O decomposition reaction were carried out in a quartz fixed-bed U-shaped reactor (0.8 cm i.d.) with 100 mg of catalyst loading (grain size 180–355 μm), diluted with an equal amount of quartz. The total gas flow rate was 150 cm³ (STP) min⁻¹ corresponding to a gas hourly space velocity (GHSV) of 40,000 h⁻¹. The feed composition during N₂O catalytic decomposition experiments was 1000 ppm N₂O or 1000 ppm N₂O + 2.0 v/v% O₂, balanced with He. The N₂O conversion performance was monitored in the temperature range of 200 to 600 °C. Effluents' composition was analyzed by means of a gas chromatograph (Agilent 7820A or Shimadzu 14B) equipped with a thermal conductivity detector (TCD) and a flame ionization detector (FID). Prior to the catalytic activity measurements, the materials under consideration were subjected to further processing under He flow (100 cm³/min) at 400 °C. In order to minimize the external and internal diffusion limitations, preliminary experiments concerning the influence of particle size and W/F ratio on the deN₂O catalytic performance were carried out. Based on these experiments, a catalyst particle size in the range of 180–355 μm was selected, in addition to a W/F ratio of 0.04 g s cm⁻³ [3]. The conversion of N₂O (X_{N_2O}) was calculated from the difference in N₂O concentration between the inlet and outlet gas streams, according to the following equation (Eq. 5) [3,7]:

$$X_{N_2O}(\%) = \frac{[N_2O]_{in} - [N_2O]_{out}}{[N_2O]_{in}} \cdot 100 \quad (5)$$

The specific reaction rate (r , mol m⁻² s⁻¹) of the N₂O decomposition was also estimated using the equation below (Eq. 6) [3]:

$$r(\text{mol} \cdot \text{m}^{-2} \cdot \text{s}^{-1}) = \frac{X_{\text{N}_2\text{O}} \cdot [\text{N}_2\text{O}]_{\text{in}} \cdot F \left(\frac{\text{cm}^3}{\text{min}} \right)}{100 \cdot 60 \left(\frac{\text{s}}{\text{min}} \right) \cdot V_m \left(\frac{\text{cm}^3}{\text{mol}} \right) \cdot m_{\text{cat}}(\text{g}) \cdot S_{\text{BET}} \left(\frac{\text{m}^2}{\text{g}} \right)} \quad (6)$$

where F and V_m are the total flow rate and gas molar volume, respectively, at standard ambient temperature and pressure conditions (298K and 1 bar), m_{cat} is the catalyst's mass and S_{BET} is the surface area.

2.3.3. Hydrogenation of CO₂ to Methane (CH₄) or Carbon Monoxide (CO)

Catalytic tests for CO₂ hydrogenation were carried out in a quartz fixed-bed U-shaped reactor (i.d. = 1 cm), loaded with 200 mg catalyst diluted with 200 mg of inert SiO₂. Prior to experiments, catalysts were reduced *in situ* at 400 °C for 1 h under pure H₂ flow (50 cm³/min), followed by flushing with He (10 cm³/min). The experiments were conducted at atmospheric pressure and in the temperature range of 200–500 °C at intervals of 20–25 °C and a heating rate of 1 °C/min. The total flow rate of the feed gas mixture was 100 cm³/min, corresponding to a gas hourly space velocity (GHSV) of 20,000 mL g⁻¹ h⁻¹. Gas feed consisted of H₂/CO₂ mixture at a molar ratio of 9 [5,6]. The thermodynamic equilibrium calculations were derived from the mathematical model RGibbs in Aspen Plus software® [5,6].

Carbon dioxide conversion, X_{CO_2} , and product selectivities, S_{CO} and S_{CH_4} , were calculated as follows (Eqs. 7–9) [5,6]:

$$X_{\text{CO}_2} = \frac{([\text{CO}_2]_{\text{in}} \cdot F_{\text{in}}) - ([\text{CO}_2]_{\text{out}} \cdot F_{\text{out}})}{[\text{CO}_2]_{\text{in}} \cdot F_{\text{in}}} \cdot 100 \quad (7)$$

$$S_{\text{CO}} = \frac{[\text{CO}]_{\text{out}}}{[\text{CO}]_{\text{out}} + [\text{CH}_4]_{\text{out}}} \cdot 100 \quad (8)$$

$$S_{\text{CH}_4} = \frac{[\text{CH}_4]_{\text{out}}}{[\text{CO}]_{\text{out}} + [\text{CH}_4]_{\text{out}}} \cdot 100 \quad (9)$$

where $[i]_{\text{in}}$ and $[i]_{\text{out}}$ represent the concentrations of reactants ($i = \text{CO}_2$) or products ($i = \text{CO}$ or CH_4) at the inlet and outlet of the reactor, respectively. F_{in} and F_{out} are the total flow rates (cm³/min) at the inlet and outlet of the reactor, respectively.

REFERENCES

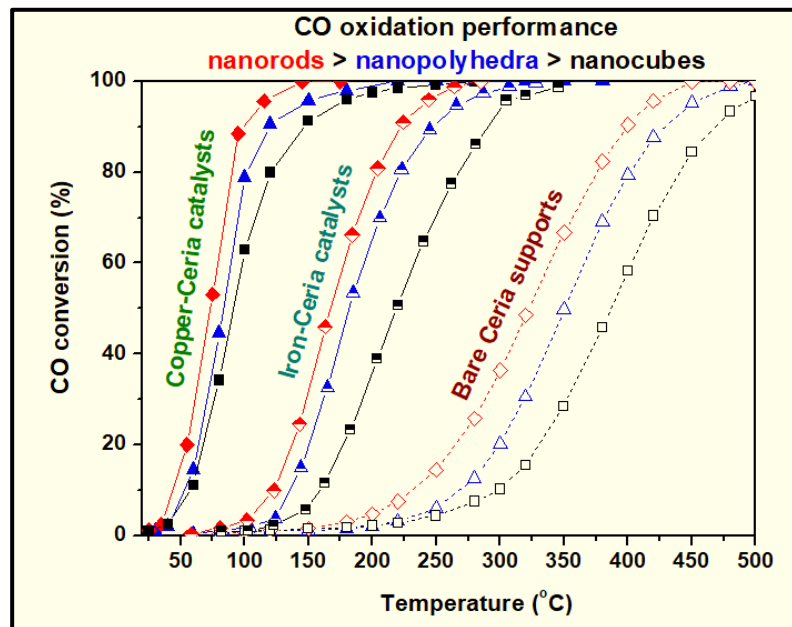
1. Lykaki, M.; Pachatouridou, E.; Iliopoulou, E.; Carabineiro, S.A.C.; Konsolakis, M. Impact of the synthesis parameters on the solid state properties and the CO oxidation performance of ceria nanoparticles. *RSC Adv.* **2017**, *7*, 6160–6169. doi: 10.1039/c6ra26712b
2. Lykaki, M.; Pachatouridou, E.; Carabineiro, S.A.C.; Iliopoulou, E.; Andriopoulou, C.; Kallithrakas-Kontos, N.; Boghosian, S.; Konsolakis, M. Ceria nanoparticles shape effects on the structural defects and surface chemistry: Implications in CO oxidation by Cu/CeO₂ catalysts. *Appl. Catal. B Environ.* **2018**, *230*, 18–28. doi: 10.1016/j.apcatb.2018.02.035
3. Lykaki, M.; Papista, E.; Kaklidis, N.; Carabineiro, S.A.C.; Konsolakis, M. Ceria nanoparticles' morphological effects on the N₂O decomposition performance of Co₃O₄/CeO₂ mixed oxides. *Catalysts* **2019**, *9*, 233. doi: 10.3390/catal9030233
4. Lykaki, M.; Stefa, S.; Carabineiro, S.A.C.; Pandis, P.K.; Stathopoulos, V.N.; Konsolakis, M. Facet-Dependent Reactivity of Fe₂O₃/CeO₂ Nanocomposites: Effect of Ceria Morphology on CO Oxidation. *Catalysts* **2019**, *9*, 371. doi: 10.3390/catal9040371
5. Konsolakis, M.; Lykaki, M.; Stefa, S.; Carabineiro, S.A.C.; Varvoutis, G.; Papista, E.; Marnellos, G.E. CO₂ hydrogenation over nanoceria-supported transition metal catalysts: Role of ceria morphology (nanorods versus nanocubes) and active phase nature (Co versus Cu). *Nanomaterials* **2019**, *9*, 1739. doi: 10.3390/nano9121739
6. Varvoutis, G.; Lykaki, M.; Stefa, S.; Papista, E.; Carabineiro, S.A.C.; Marnellos, G.E.; Konsolakis, M. Remarkable efficiency of Ni supported on hydrothermally synthesized CeO₂ nanorods for low-temperature CO₂ hydrogenation to methane. *Catal. Commun.* **2020**, *142*, 106036. doi: 10.1016/j.catcom.2020.106036
7. Lykaki, M.; Papista, E.; Carabineiro, S.A.C.; Tavares, P.B.; Konsolakis, M. Optimization of N₂O decomposition activity of CuO-CeO₂ mixed oxides by means of synthesis procedure and alkali (Cs) promotion. *Catal. Sci. Technol.* **2018**, *8*, 2312–2322. doi: 10.1039/c8cy00316e
8. Brunauer, S.; Emmett, P.H.; Teller, E. Adsorption of gases in multimolecular layers. *J. Am. Chem. Soc.* **1938**, *60*, 309–319. doi: 10.1021/ja01269a023
9. Saitzek, S.; Blach, J.-F.; Villain, S.; Gavarri, J.-R. Nanostructured ceria: a comparative study from X-ray diffraction, Raman spectroscopy and BET specific surface measurements. *Phys. Stat. Sol.* **2008**, *205*, 1534–1539. doi: 10.1002/pssa.200723419
10. Tsilomelekis, G.; Boghosian, S. On the configuration, molecular structure and

- vibrational properties of MoO_x sites on alumina, zirconia, titania and silica. *Catal. Sci. Technol.* **2013**, *3*, 1869–1888. doi: 10.1039/c3cy00057e
11. Andriopoulou, C.; Trimpalis, A.; Petalidou, K.C.; Sgoura, A.; Efstathiou, A.M.; Boghosian, S. Structural and redox properties of Ce_{1-x}Zr_xO_{2-δ} and Ce_{0.8}Zr_{0.15}RE_{0.05}O_{2-δ} (RE: La, Nd, Pr, Y) solids studied by high temperature *in situ* Raman spectroscopy. *J. Phys. Chem. C* **2017**, *121*, 7931–7943. doi: 10.1021/acs.jpcc.7b00515

CHAPTER 3

Effect of Synthesis Procedure and Ceria's Shape on the Structural Defects and Surface Chemistry of Ceria-Based Transition Metal Catalysts M/CeO₂ (M: Cu, Fe): Implications in CO Oxidation

Chapter 3 deals with the impact of synthesis parameters on the solid state properties and the CO oxidation performance of bare ceria catalysts, is initially investigated. In particular, three different time- and cost-effective preparation methods (thermal



decomposition, precipitation and hydrothermal method of low and high NaOH concentration) were employed for the synthesis of ceria nanomaterials.

In addition, the present chapter deals with the ceria nanoparticles' shape effects, *i.e.*, nanorods (NR), nanopolyhedra (NP) and nanocubes (NC), prepared by the hydrothermal method on the solid state properties and the CO oxidation performance of copper-ceria and iron-ceria mixed oxides. In specific, Chapter 3 reports on ceria nanostructures' morphological effects (cubes, polyhedra, rods) on the textural, structural, surface, redox properties and, consequently, on the CO oxidation performance of bare ceria (CeO₂) and ceria-based transition metal catalysts M/CeO₂ (M: Cu, Fe).

INTRODUCTION

Cerium oxide (CeO_2) or ceria has lately received considerable attention as catalyst or supporting carrier in numerous catalytic processes [1–4], involving, among others, the oxidation of CO, the reduction of NO_x , water-gas shift reaction, reforming reactions, soot combustion, toxic emissions' abatement, wastewater treatment, as well as in further applications like optics [5], biotechnology [6] and so on. The wide application range of ceria-based materials is largely due to the unique properties of ceria, like high thermal stability, high oxygen storage capacity (OSC) and oxygen mobility [2–4,7–11]. In fact, the facile transition between the Ce^{3+} and Ce^{4+} oxidation states, linked to the formation and annihilation of surface/structural defects (*i.e.*, oxygen vacancies), is considered responsible for the superior redox properties of ceria [2–4,11–14].

Moreover, in the nanoscale, materials exhibit important features due to quantum size effects. The surface area is substantially increased by decreasing particle size to the nanometer scale. These nanomaterials show abundance in defect sites such as oxygen vacancies and have more surface atoms than their bulk counterparts [2–4,15–18].

Numerous methods have been employed for the synthesis of nanosized ceria particles, such as hydrothermal [19,20], sonochemical [21], reverse micelles [22] *etc.*, while precipitation method is considered as one of the most widely employed methods due to its simplicity and low cost. The preparation method affects enormously the morphological and surface characteristics of CeO_2 , leading to various geometries, such as nanorods, nanocubes, nanowires, *etc.* [23,24]. In addition, the variation of several parameters during synthesis procedure (*i.e.*, temperature and base concentration) can lead not only to different ceria morphologies with high shape purity, but also to structures with tunable surface areas and defect concentrations [25–28].

For instance, Liu *et al.* [29] synthesized CeO_2 samples by precipitation, hydrothermal and citrate sol-gel methods. CeO_2 prepared with hydrothermal method showed larger surface area, average pore diameter and pore volume. Makinose *et al.* [30] fabricated ceria nanoparticles (NPs) with controlled crystal orientations through an oleate-modified hydrothermal method, which revealed that by altering the molar ratio of the ions in the reaction solution, different ceria facets could be obtained.

Although the majority of ceria-based applications relies on ceria particles of not well-defined morphology, recent theoretical [10,31,32] and experimental [27,33–39] studies have revealed that the redox and, in consequence, the catalytic properties of ceria can be significantly enhanced by tailoring the shape and size of the particles. In fact, ceria

functionalization *via* nanosynthesis routes can exert significant alterations on the structural, surface and redox properties, arising from quantum size effects.

Nano-ceria exhibits abundance of defect sites (*e.g.*, oxygen vacancies) and surface atoms, when compared to the bulk counterpart. Numerous studies [34,40–44] have focused on the fine-tuning of ceria through the development of materials with predefined structural and textural characteristics. On the other hand, it was clearly revealed that the energy formation of anionic vacancies is dependent on the exposed nanocrystals' facets, following the sequence: {111} > {100} > {110}. In this regard, research efforts have been devoted to the synthesis of ceria nanoparticles with abundance of active crystal planes [14,37,41,43–47]. In this regard, Piumetti *et al.* [48] showed that ceria nanocubes exhibited the best catalytic performance for the soot combustion due to the abundance of highly reactive {100} and {110} surfaces. Aneggi *et al.* [49] also showed, by comparing ceria samples of similar surface area, that a higher soot oxidation activity can be obtained for nanocubes and nanorods as compared to polycrystalline samples.

Despite the excellent redox properties of bare ceria that can be further adjusted by engineering its shape and size, the majority of heterogeneous catalysts are based on supported systems rather than on individual counterparts, in view of the fact that "the whole is more than the sum of its parts" [40,50]. Combining ceria with transition metals can improve the catalytic performance due to a peculiar synergistic effect linked to metal-support interactions [40,51,52]. Electronic, geometric and bifunctional interactions between both components are thought to be responsible for the enhanced performance of mixed oxides, when compared to bare oxides [53]. Despite the progress in the field, the fundamental understanding and the experimental verification of the aforementioned "synergistic" phenomena are still under debate [40,50].

Among the different ceria-based catalysts, the copper-ceria system has triggered a substantial interest in heterogeneous catalysis, due to its unique catalytic properties and lower cost compared to noble metal-based catalysts. Nowadays, it is well documented that the complex copper-ceria interactions can be accounted for the enhanced catalytic performance. The advances in relation to the role of copper-ceria interactions in catalysis have been recently comprehensively reviewed [17]. Based on the most constructive experimental and conceptual studies, the superiority of Cu/CeO₂ system can be mainly ascribed to a synergistic effect. In particular, various interrelated phenomena were revealed to affect the interfacial interactions with great consequences on the catalytic performance: (i) electronic perturbations between copper and ceria nanoparticles, (ii) facilitation of the

interplay between $\text{Cu}^{2+}/\text{Cu}^+$ and $\text{Ce}^{3+}/\text{Ce}^{4+}$ redox couples, (iii) facilitation of oxygen vacancies' formation, (iv) enhanced oxygen mobility and reducibility, (v) formation of interfacial sites of unique activity [17].

In addition, it is of great importance to develop cost-effective and highly efficient noble metal-free catalysts based on copper oxide (CuO) or iron oxide (Fe_2O_3), which is considered to be one of the cheapest metal oxides [54]. Among the various catalytic systems, iron-ceria mixed oxides have been studied in several catalytic reactions, such as oxidation processes [54–58], reduction processes [59,60], decomposition reactions [61,62], soot combustion [63,64], *etc.* However, the $\text{Fe}_2\text{O}_3/\text{CeO}_2$ binary system has not been extensively investigated in relation to the support's shape dependence of catalytic activity, which is a high engaging topic.

In light of the above aspects, the adjustment of ceria characteristics, in terms of size and morphology, can exert a profound influence on the aforementioned parameters with great implications in catalysis [17,39,65–68]. For instance, Ouyang *et al.* [46] found that Cu supported on ceria nanorods exhibited the optimum CO_2 hydrogenation activity among different ceria morphologies (nanorods, nanocubes, nanoparticles), ascribed to the strong interaction between copper and ceria nanorods. On the other hand, copper-ceria nanospheres/octahedrons exhibited the optimum water-gas shift activity in comparison with nanorods and nanocubes, which was attributed to the presence of defects and imperfections in the support that favoured strong metal-support interactions, as generally stated [47,67]. In a similar manner, the exposed facets of $\{111\}/\{100\}$ of copper-ceria nanospheres exhibited higher activity than nanorods for CO oxidation, due to the existence of more reducible CuO_x clusters on the nanospheres' surface [69]. In general, the different exposed crystal planes of ceria can alter the geometry and coordination environment of copper ions, affecting the catalytic activity of Cu/Ceria binary system in different ways, depending on the reaction environment [37,45,67,69–71].

CO oxidation reaction has been widely employed as probe reaction to gain insight into the structure-activity correlations [7,13,14,23,28,41,72,73]. It is generally believed that CO oxidation over ceria proceeds through a Mars-van Krevelen mechanism which involves the removal of surface lattice oxygen by CO and the consequent annihilation of oxygen vacancies by gas phase oxygen [73].

Despite the intense interest in the field, the fundamental origin of nanoceria shape effects in catalysis is still a matter of debate. In particular, there is still a lack of atomistic understanding concerning the impact of exposed facets on the solid state properties and, in

turn, on the catalytic performance of ceria-based catalysts. The present chapter aims at comparatively exploring the impact of various widely employed synthesis methods, *i.e.*, precipitation, thermal decomposition and hydrothermal, on the solid state properties of ceria samples. Particular emphasis is given on the synthesis parameters in order for the preparation methods to be cost-effective and not time-consuming. In addition, in the present chapter, the hydrothermally prepared ceria nanostructures (rods, polyhedra, cubes) were employed as supporting carriers for Cu- and Fe-based catalysts. Various *ex situ* (surface area determination, X-ray diffraction, X-ray fluorescence, H₂-temperature programmed reduction, transmission electron microscopy, X-ray photoelectron spectroscopy) and *in situ* (Raman spectroscopy) characterization techniques were employed to gain insight into the impact of ceria exposed facets on the structural defects and surface chemistry of copper-ceria and iron-ceria binary oxides. CO oxidation was employed as probe reaction to reveal the structure-activity relationships.

3.1. EXPERIMENTAL

3.1.1. Materials Synthesis

All of the chemicals used were of analytical reagent grade. Ce(NO₃)₃·6H₂O (purity ≥ 99.0%, Fluka), Cu(NO₃)₂·2.5H₂O (Fluka) and Fe(NO₃)₃·9H₂O (≥ 98%, Sigma-Aldrich) were used as precursors for the preparation of ceria, Cu/Ceria and Fe/Ceria materials. NH₃ (25% v/v, EMSURE), NaOH (purity ≥ 98%, Sigma-Aldrich), ethanol (purity 99.8%, ACROS) and double deionized water were also employed during synthesis procedure.

The catalysts developed in this chapter (CeO₂-D, CeO₂-P, CeO₂-NP, CeO₂-NR, CeO₂-NC, Cu/CeO₂-NP, Cu/CeO₂-NR, Cu/CeO₂-NC, Fe/CeO₂-NP, Fe/CeO₂-NR, Fe/CeO₂-NC) were prepared by the methods described in Chapter 2 in section 2.1 (Materials Synthesis). Also, Table 2.1 in Chapter 2 presents all the materials developed in this study.

3.1.2. Materials Characterization

The textural characteristics of as-prepared catalysts were determined by the N₂ adsorption-desorption isotherms at -196 °C. The crystalline structure of ceria samples was determined by powder X-ray diffraction (XRD). Scherrer's equation (see Eq. 1 in Chapter 2) was employed to determine the particle sizes of bare ceria and copper-ceria samples. The collected spectra of iron-ceria samples were analyzed by Rietveld refinement, allowing the determination of crystallite sizes by means of the Williamson-Hall plot. The redox properties of the samples were assessed by temperature programmed reduction under H₂ atmosphere

(H₂-TPR). Morphological characterization was carried out by scanning/transmission electron microscopy (SEM/TEM) analyses. The surface properties were determined by X-ray photoelectron spectroscopy (XPS). Also, *in situ* Raman spectroscopic measurements were undertaken. The characterization techniques are fully described in Chapter 2 in section 2.2 (Characterization Techniques).

3.2. CHARACTERIZATION STUDIES OF BARE CERIA OXIDES

3.2.1. Textural and Structural Characterization (BET and XRD)

The main textural properties of ceria materials are presented in Table 3.1. By assuming particles' sphericity, the average grain size, D_{BET} , was also calculated using the following equation (Eq. 1).

$$D_{\text{BET}} = \frac{6 \cdot 1000}{S \cdot d} \quad (1)$$

where S is the BET surface area ($\text{m}^2 \text{g}^{-1}$) and d is the density of ceria in the fluorite structure (7.215 g cm^{-3}) [74].

As it can be observed from Table 3.1, the sample prepared by the hydrothermal method of low NaOH concentration ($\text{CeO}_2\text{-NP}$) possesses the highest BET surface area ($109 \text{ m}^2 \text{g}^{-1}$), followed by $\text{CeO}_2\text{-NR}$ ($92 \text{ m}^2 \text{g}^{-1}$), $\text{CeO}_2\text{-D}$ ($87 \text{ m}^2 \text{g}^{-1}$), $\text{CeO}_2\text{-P}$ ($53 \text{ m}^2 \text{g}^{-1}$) and $\text{CeO}_2\text{-NC}$ ($40 \text{ m}^2 \text{g}^{-1}$).

Table 3.1. Textural and structural characteristics of ceria samples.

Sample	BET Analysis			XRD Analysis		
	BET Surface Area ($\text{m}^2 \text{g}^{-1}$)	Pore Volume ($\text{cm}^3 \text{g}^{-1}$)	Average Pore Size (nm)	Average grain size, D_{BET} (nm) ¹	Average crystallite diameter, D_{XRD} (nm) ²	ψ ($D_{\text{BET}}/D_{\text{XRD}}$)
$\text{CeO}_2\text{-NC}$	40	0.12	12.5	21.1	19.2	1.10
$\text{CeO}_2\text{-P}$	53	0.087	6.6	15.6	15.2	1.03
$\text{CeO}_2\text{-D}$	87	0.25	11.6	9.5	9.3	1.02
$\text{CeO}_2\text{-NR}$	92	0.71	30.9	9.1	13.2	0.69
$\text{CeO}_2\text{-NP}$	109	1.04	38.1	7.6	9.5	0.80

¹ Calculated applying eq. (1); ² Calculated applying Scherrer's equation (see Eq. (1) in Chapter 2).

Figure 3.1 depicts the results of BET surface area as a function of average grain size (D_{BET}) for the different ceria samples. Evidently, there is an inverse trend between the BET surface area and the average grain size, implying that the surface area of ceria samples increase with decreasing grain size [75].

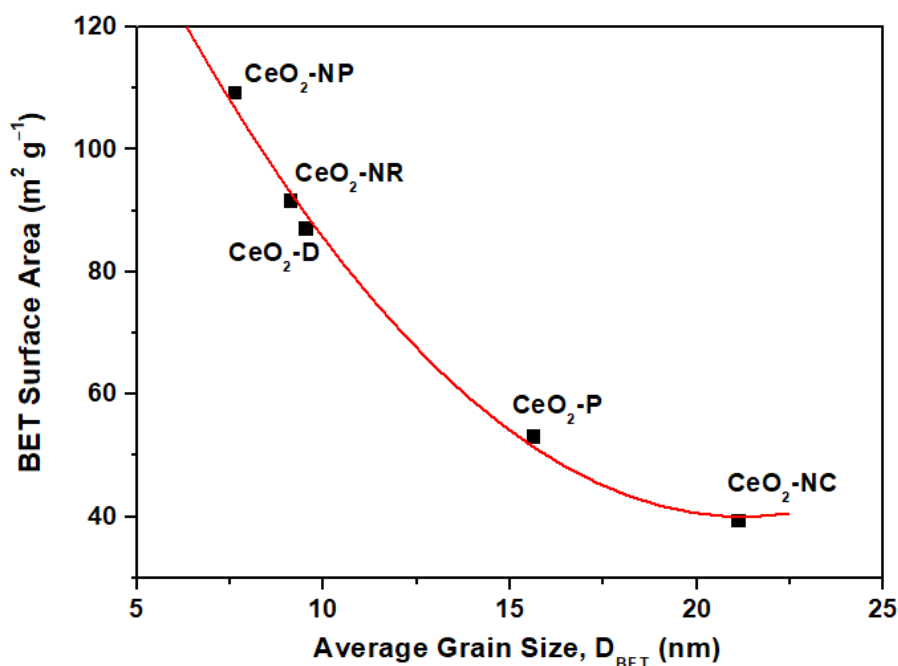


Figure 3.1. BET surface area as a function of average grain size (D_{BET}) for ceria samples. Adapted with permission from Reference [76]. Copyright© 2017, The Royal Society of Chemistry.

To gain insight into the extent of agglomeration of the primary crystallites, the factor $\psi = D_{\text{BET}}/D_{\text{XRD}}$ was also calculated (Table 3.1) [77]. The CeO₂-P and CeO₂-D samples prepared by precipitation and thermal decomposition, respectively, exhibit a similar ψ value of *ca.* 1.0, implying no degree of aggregation. However, the crystallite size is larger than D_{BET} for CeO₂-NR and CeO₂-NP, resulting in ψ values lower than 1.0 (0.69 and 0.80, respectively). The latter indicates non-spherical particles with a small degree of aggregation [78]. Also, the CeO₂-NC sample exhibits a value higher than 1. Therefore, the assumption of the particles' sphericity for the calculation of D_{BET} may not apply to the samples prepared by the hydrothermal method. This finding is in accordance with the TEM analysis (*vide infra*), which indicates the formation of nanoparticles of specific shape (*e.g.*, nanorods, nanocubes, nanopolyhedra) in the hydrothermally prepared ceria samples.

Figure 3.2a shows the Barrett–Joyner–Halenda (BJH) desorption pore size distribution (PSD) of as-prepared samples. In all cases, maxima at pore diameters higher than 3 nm are obtained, implying the mesoporosity of the samples [79]. This can be further corroborated by the existence of adsorption–desorption isotherms of type IV with hysteresis loop at a relative pressure above 0.5 (Figure 3.2b) [57,59,80,81]. The CeO₂-NP sample possesses the highest average pore size (38.1 nm), followed by CeO₂-NR (30.9 nm), CeO₂-NC (12.5 nm), CeO₂-D (11.6 nm) and CeO₂-P (6.6 nm). Moreover, the hydrothermally prepared samples

display a broader PSD as compared to the ones prepared by thermal decomposition and precipitation (Figure 3.2a).

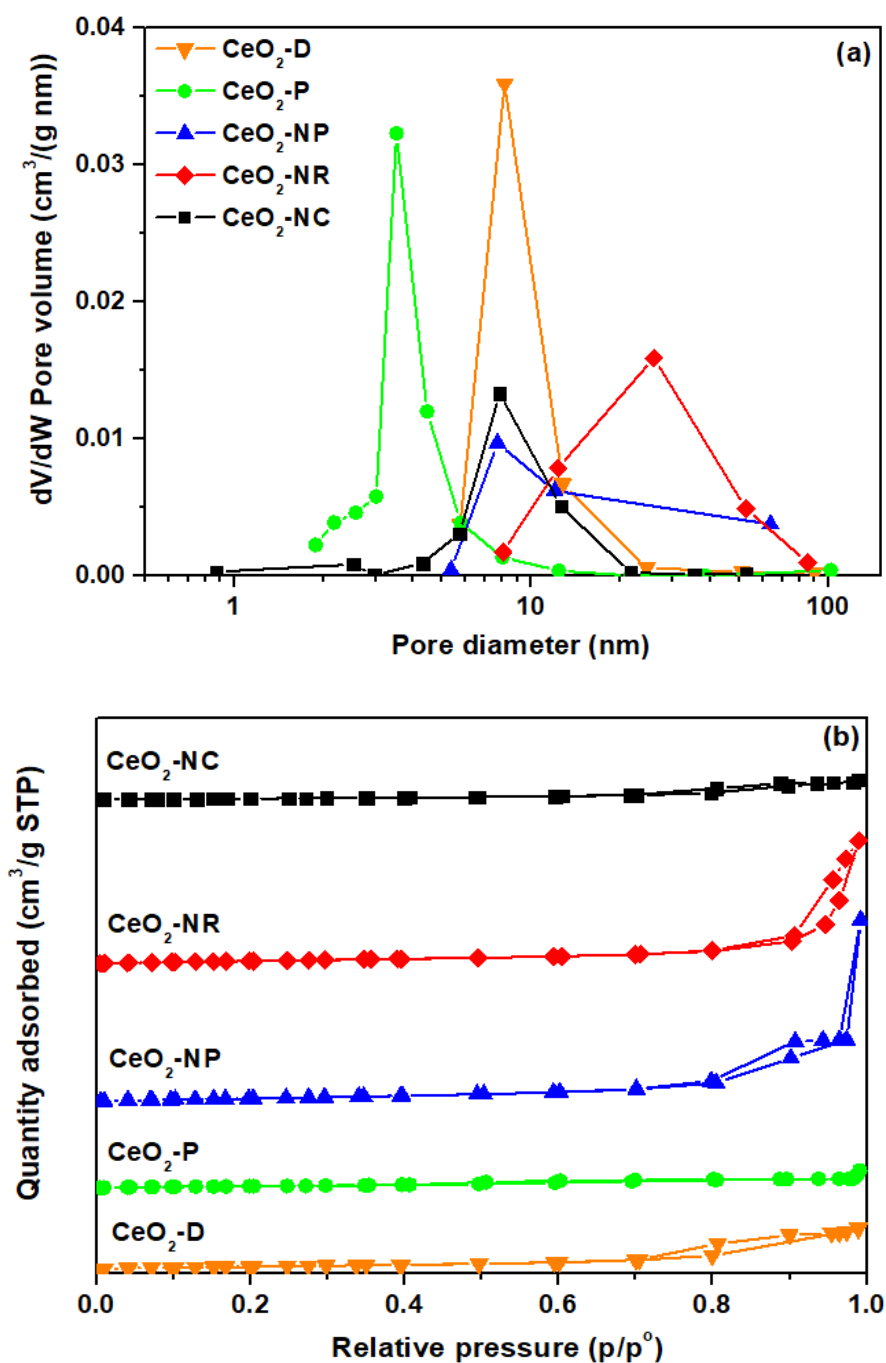


Figure 3.2. (a) BJH desorption pore size distribution and (b) adsorption–desorption isotherms of as-prepared ceria samples. Adapted with permission from Reference [76]. Copyright© 2017, The Royal Society of Chemistry.

The XRD patterns of ceria samples are presented in Figure 3.3. All samples exhibit similar patterns. The main peaks can be indexed to the (111), (200), (220), (311), (222), (400), (331)

and (420) planes of a face-centred cubic fluorite structure of ceria (Fm3m symmetry, no. 225) [82]. It is obvious that the CeO₂-NP and CeO₂-D samples have broader peaks than the other three samples, indicating a smaller crystallite size (D_{XRD} in Table 3.1) [18].

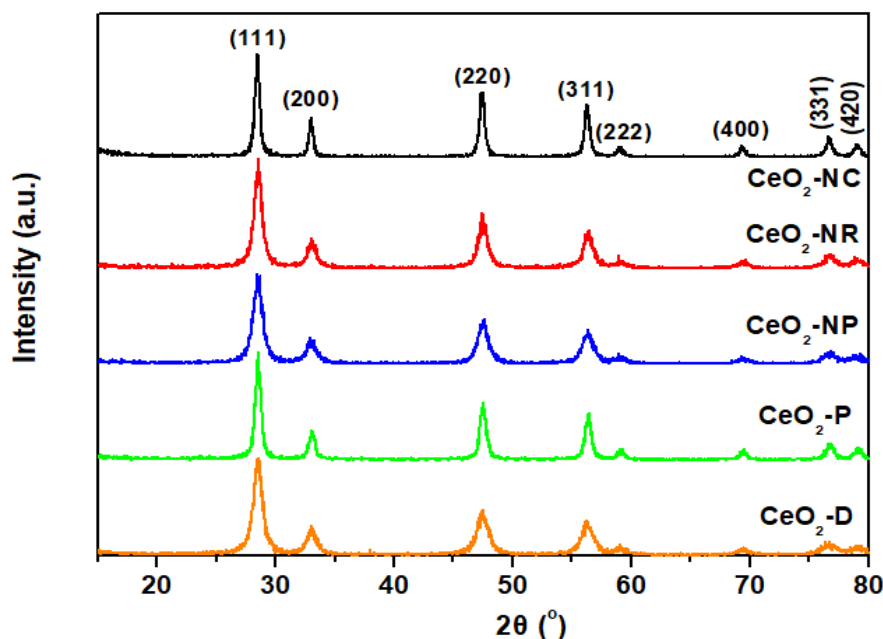


Figure 3.3. XRD patterns of ceria samples. Adapted with permission from Reference [76]. Copyright© 2017, The Royal Society of Chemistry.

3.2.2. Morphological Characterization (SEM/TEM)

The SEM and TEM images of ceria samples prepared by different methods are depicted in Figure 3.4. It is obvious that the samples exhibit different morphologies. According to SEM analyses [76] (Figure 3.4 (a, c, e, g, i)), CeO₂-D (Figure 3.4a) shows flat surfaces with some cracks, which resemble "star" forms. Nevertheless, EDS (not shown) performed in different zones showed that the composition is similar in all regions, that is, cerium oxide. CeO₂-P is shown in Figure 3.4c and different areas are seen again, namely more "solid rocks" together with fragmented material. The hydrothermally prepared sample of low NaOH concentration (Figure 3.4e) exhibits slight agglomeration of the nanoparticles whereas the sample prepared by the hydrothermal method employing high NaOH concentration (Figure 3.6g) implies the existence of a rod-like morphology. Figure 3.4i shows particles of a specific shape that cannot be clearly distinguished by SEM analysis.

In order to clearly gain insight into the impact of preparation procedure on the morphological characteristics of ceria NPs, transmission electron microscopy (TEM) studies were also carried out [76]. Figure 3.4 (b, d, f, h, j) depicts representative images of ceria

samples. CeO₂-D (Figure 3.4b) shows some needle-like features with sizes up to 150 nm, and some smaller particles. CeO₂-P is shown in Figure 3.4d and some spherical/polyhedral forms can be visualized ranging from 10 to 50 nm. The hydrothermally prepared sample of low NaOH concentration (Figure 3.4f) exhibits mostly nanopolyhedra of irregular shapes with their sizes varying between 5 and 11 nm, along with some nanorods. The sample prepared by the hydrothermal method, employing high NaOH concentration (Figure 3.4h) shows the existence of a rod-like morphology, confirming the SEM results. The rods' length varies from 25 to 200 nm and their width ranges from 10 to 18 nm. The hydrothermally prepared sample which was aged at 180 °C for 24 h, clearly exhibits a cubic morphology with the cubes' size varying between 15 and 30 nm.

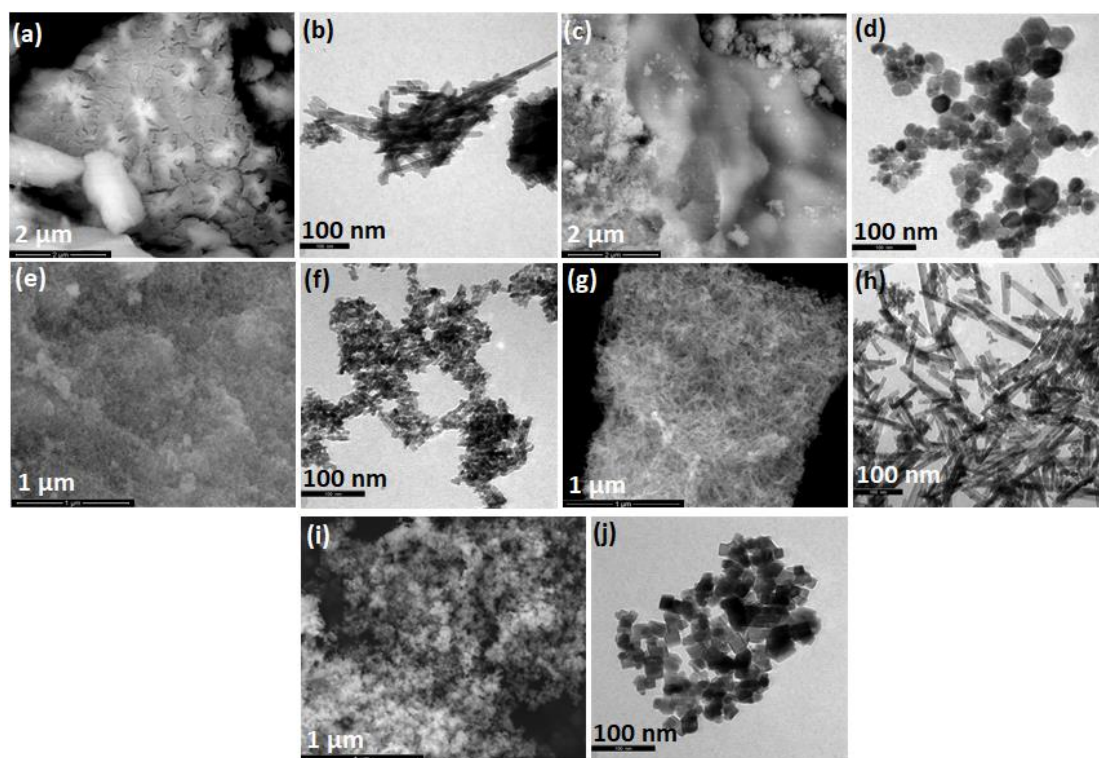


Figure 3.4. (a, c, e, g, i) SEM and (b, d, f, h, j) TEM images of ceria samples: (a, b) CeO₂-D, (c, d) CeO₂-P, (e, f) CeO₂-NP, (g, h) CeO₂-NR, (i, j) CeO₂-NC. Adapted with permission from Reference [76]. Copyright© 2017, The Royal Society of Chemistry.

3.2.3. Redox Properties (H₂-TPR)

TPR experiments were also carried out to investigate the impact of the preparation method on the redox properties of ceria samples. Figure 3.5 presents the reduction profiles of CeO₂ samples, which consist of two broad peaks centred at *ca.* 550 °C and 800 °C. They have been

ascribed to the reduction of surface oxygen (O_s) and bulk oxygen (O_b) of ceria, respectively [18,41,49,83,84].

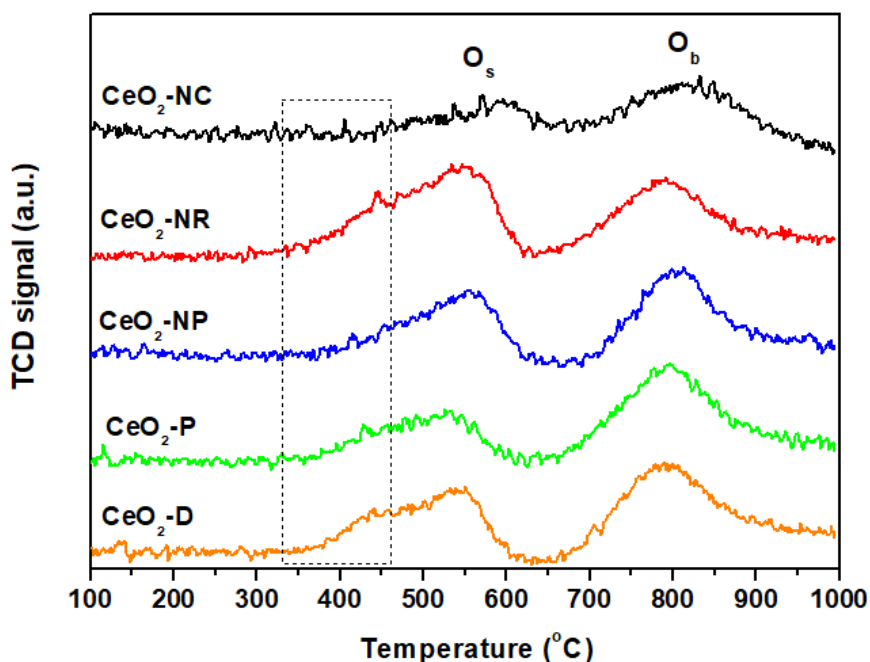


Figure 3.5. H_2 -TPR profiles of ceria samples. Adapted with permission from Reference [76]. Copyright© 2017, The Royal Society of Chemistry.

The H_2 consumption which corresponds to surface oxygen and bulk oxygen reduction is presented in Table 3.2. Notably, the ratio of O_s/O_b is affected by the preparation method, following the order: CeO_2 -P (0.56) < CeO_2 -NC (0.71) < CeO_2 -D (0.72) < CeO_2 -NP (0.94) < CeO_2 -NR (1.13). These results indicate that CeO_2 -NR exhibits the highest population of loosely bound labile oxygen species, resulting in enhanced reducibility and oxygen mobility. In terms of oxygen storage capacity (OSC, Table 3.2), the following trend is obtained: CeO_2 -P (0.20 $mmol O_2 g^{-1}$) < CeO_2 -NC (0.21 $mmol O_2 g^{-1}$) < CeO_2 -NP (0.24 $mmol O_2 g^{-1}$) < CeO_2 -D (0.25 $mmol O_2 g^{-1}$) < CeO_2 -NR (0.29 $mmol O_2 g^{-1}$). This order coincides relatively well with the catalytic activity (*vide infra*), revealing the key role of reducibility.

Table 3.2. Redox characteristics of ceria samples.

Sample	H_2 consumption ($mmol H_2 g^{-1}$)			O_s/O_b ratio	OSC ($mmol O_2 g^{-1}$)	Peak Temperature	
	O_s peak	O_b peak	Total			O_s peak	O_b peak
CeO_2 -P	0.39	0.69	1.08	0.56	0.20	525	795
CeO_2 -D	0.50	0.69	1.19	0.72	0.25	535	790
CeO_2 -NC	0.41	0.58	0.99	0.71	0.21	589	809
CeO_2 -NP	0.48	0.51	0.99	0.94	0.24	555	804
CeO_2 -NR	0.59	0.52	1.11	1.13	0.29	545	788

It is also worth noticing that CeO₂-NR and CeO₂-D, and to a lesser extent CeO₂-NP, exhibit a main O_s peak at 550 °C, accompanied by a shoulder peak at about 450 °C, in contrast to CeO₂-NC which shows one main peak at 589 °C. The latter is in agreement with the lower temperature reduction of {110} and {100} surfaces as compared to {111} [37,45,46]. However, the temperature of maximum H₂ consumption (T_{max}) is strongly dependent on exposed facets, being lower on {100} and {110} surfaces [49,85]; this indicates a higher contribution of these particular facets on CeO₂-NR and CeO₂-D samples. This is in agreement with the TEM analysis (Figure 3.4), which implies the formation of nanorods over Ceria-NR sample and to a lesser extent over CeO₂-D. In a similar manner, a decrease in the T_{max} by more than 100 °C has been observed with nanoshaped (nanocubes/nanorods) compared to polycrystalline conventional ceria [49]. Moreover, it should be noted that the size of CeO₂ NPs strongly affects the surface reduction, being facilitated at smaller sizes [83]. In view of the above aspects, the variation of surface-to-bulk oxygen, both in quantitative and qualitative terms (Figure 3.5, Table 3.2), can be attributed to the different exposed facets as well as to the different ceria NPs size. The present findings unambiguously revealed the pronounced impact of hydrothermal synthesis on the reduction of surface-capping oxygen of ceria. The sample prepared by the hydrothermal method of high NaOH concentration (CeO₂-NR) shows the highest O_s/O_b ratio, which is related to its improved reducibility and high oxygen mobility [86].

3.2.4. Surface Analysis (XPS)

Information about the different elements existing on the surface and their oxidation state are next obtained by X-ray photoelectron spectroscopy. High resolution spectra of Ce 3d and O 1s photoelectrons were obtained (Figures 3.6 a,b). The Ce 3d spectra are analyzed into eight components which correspond to four pairs of spin-orbit doublets (Figure 3.6a). The Ce 3d_{3/2} and Ce 3d_{5/2} spin-orbit components are labelled as u and v, respectively. The peaks labelled as v (882.4 eV), v" (888.9 eV) and v''' (898.3 eV) correspond to 3d_{5/2} level of Ce⁴⁺, while the peaks labelled as u (900.9 eV), u" (907.7 eV) and u''' (916.8 eV) are assigned to 3d_{3/2} level of Ce⁴⁺ [85]. The v and v" peaks are assigned to a mixing of Ce 3d⁹4f² O 2p⁴ and Ce 3d⁹ 4f¹ O 2p⁵ of Ce⁴⁺ states and the v''' peak corresponds to the Ce 3d⁹4f⁰ O 2p⁶ of Ce⁴⁺ final state [87]. The peaks tagged as v' (883.7 eV) and u' (902.2 eV) correspond to one of the two possible electron configurations of the final state of Ce³⁺ species. The ratio of the area for Ce³⁺ peaks to the whole peak area in Ce 3d region can lead to the relative amount of Ce³⁺ [88].

The corresponding O 1s spectra are illustrated in Figure 3.6b. Curve-fitting reveals the presence of two peaks. The low binding energy peaks centred at 529.4 eV (O_I) are assigned to lattice oxygen while the peaks at 531.3 eV (O_{II}) are attributed to surface adsorbed oxygen species, hydroxyl/carbonate groups and oxygen vacancies [88–91]. The relative populations of O_I and O_{II} along with their ratio (O_I/O_{II}) are included in Table 3.3. The CeO_2 -NR sample exhibits the highest ratio (2.13), followed by CeO_2 -NP (2.04), CeO_2 -NC (1.99), CeO_2 -D (1.97) and CeO_2 -P (1.71). Similar results in relation to the abundance of oxygen lattice (O_I) species on hydrothermally prepared ceria polymorphs have been recently reported [92].

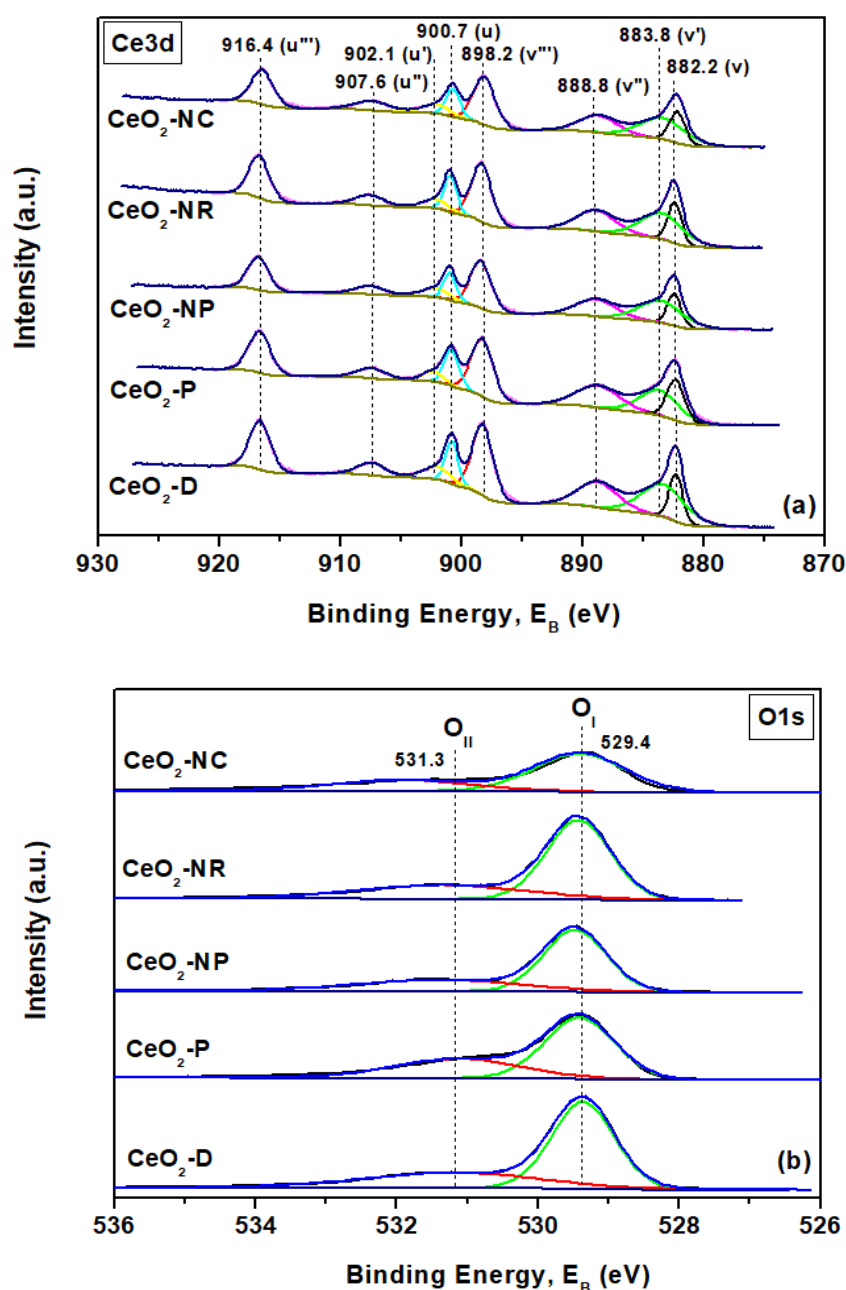


Figure 3.6. XPS spectra of (a) Ce 3d and (b) O 1s region of ceria samples. Adapted with permission from Reference [76]. Copyright© 2017, The Royal Society of Chemistry.

Table 3.3 shows that all samples have a similar amount of Ce^{3+} , which varies between 23.3 and 26.5%. These findings are in accordance with relative literature studies [23,27], where it was found that very similar Ce 3d spectra profiles can be obtained between ceria samples of different morphology, despite the quite different amount of defect sites in the sub-surface/bulk of ceria. In any case, no definitive conclusions in relation to the contribution of Ce^{3+} on the diverse reducibility of the present samples can be revealed. In complete agreement, it was found that the concentration of Ce^{3+} species is almost the same among ceria NPs of different particle size, despite their extremely different redox characteristics [83].

Table 3.3. XPS results for ceria samples.

Sample	O _I (%)	O _{II} (%)	O _I /O _{II}	Ce ³⁺ (%)
CeO ₂ -P	63.1	36.9	1.71	26.5
CeO ₂ -D	66.4	33.6	1.97	26.4
CeO ₂ -NC	66.5	33.5	1.99	23.3
CeO ₂ -NP	67.1	32.9	2.04	25.3
CeO ₂ -NR	68.1	31.9	2.13	24.3

These findings in conjunction to the TPR results (*vide supra*) clearly demonstrated that CeO₂-NR have the highest population of loosely bound oxygen species, offering improved reducibility and oxygen mobility. The latter is expected to notably affect the redox-type mechanism involved in CO oxidation (*vide infra*).

3.2.5. *In situ* Raman Spectroscopy

In situ Raman spectroscopy was employed for the hydrothermally prepared samples, *i.e.*, CeO₂-NP, CeO₂-NR and CeO₂-NC, in order to gain insight into the impact of ceria morphology on the structural defects. Figure 3.7a shows the *in situ* steady-state Raman spectra obtained for the CeO₂-NR, CeO₂-NP and CeO₂-NC samples at 440 °C under flowing 20% O₂/He gas, *i.e.*, under oxidizing conditions. The characteristic F_{2g} mode due to the Fm3m fluorite cubic ceria structure observed at 457 cm⁻¹ prevails in all spectra. Additionally, as reported previously [27,93,94], a weak band at ~260 cm⁻¹ (due to second order transverse acoustic mode) and the so-called defect-induced band (band "D") at ~600 cm⁻¹ "leak" as result of relaxation of symmetry selection rules caused by structural perturbations of the ceria cubic lattice. The intensity of the "D" band is a measure of the deformation of the anionic lattice that leads to punctual defects and O vacancies. Thus, the I_D/I_{F2g} ratio is commensurate to the abundance of structural defects [93]. The anionic lattice of bare ceria is known to be deformed due to O

atoms' relocation from the interior of tetrahedral cationic sub-lattice sites to the interior of ideally empty octahedral cationic sites (Frenkel interstitial sites) [95].

Previously, it was demonstrated that the "D" band is comprised of at least two components, "D1" (above 600 cm^{-1}) and "D2" (below 600 cm^{-1}) [93,94]. Sequential *in situ* steady-state Raman spectra under alternating oxidizing and reducing flowing gas at $450\text{ }^{\circ}\text{C}$ were adequate to demonstrate that band D1 is due to Ce–O modes involving O atoms that are relatively loosely bound (*e.g.*, in Frenkel interstitial sites) and can be detached under the applied reducing conditions at $450\text{ }^{\circ}\text{C}$, whereas band D2 is due to vibrational modes within coordinatively unsaturated sites (*e.g.*, MO_7) and remains unaffected under reducing conditions at $450\text{ }^{\circ}\text{C}$ [93].

Clearly (as seen in Fig. 3.7b), a higher abundance of defects (evidenced by the pertinent relative $I_D/I_{F_{2g}}$ ratios shown in arbitrary scale) is observed for the CeO_2 -NR polymorph and the actual trend, *i.e.*, CeO_2 -NR > CeO_2 -NP > CeO_2 -NC, agrees with the aforementioned redox results as well as with the catalytic activity results discussed below.

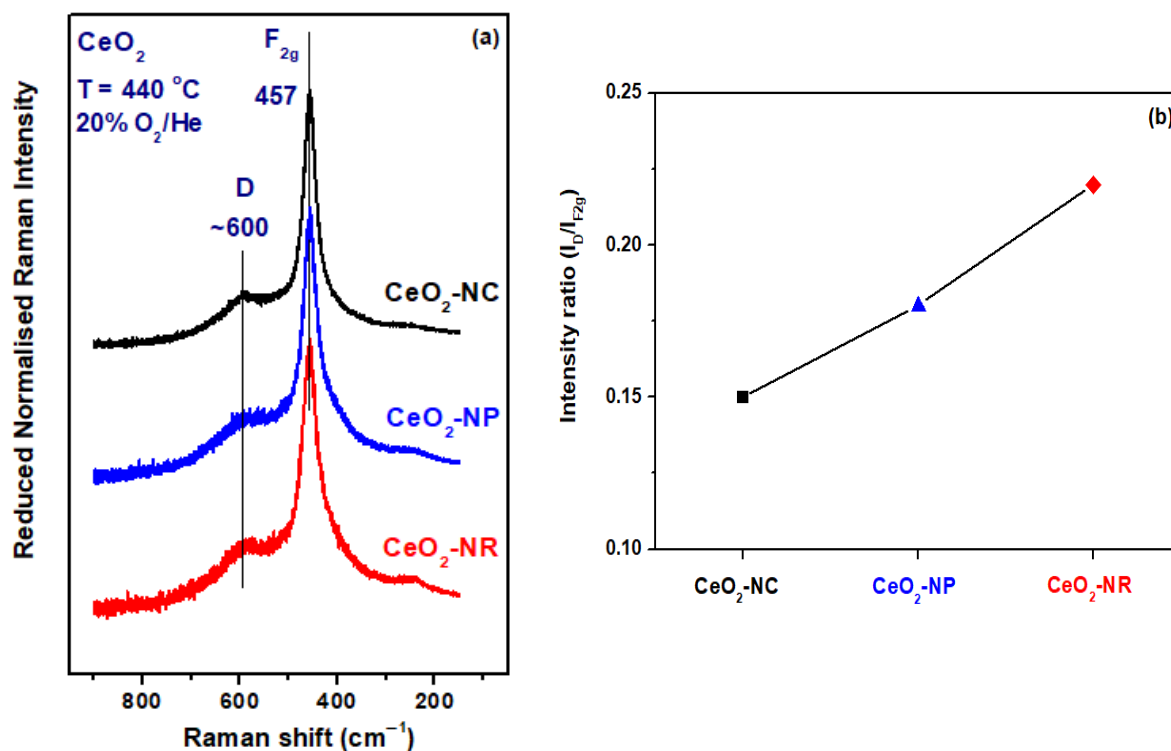


Figure 3.7. (a) *In situ* Raman spectra obtained for ceria samples prepared by the hydrothermal method (NR, NP and NC as indicated by each spectrum), (b) $I_D/I_{F_{2g}}$ intensity ratio. Laser wavelength, $\lambda_0 = 491.5\text{ nm}$; laser power, $w = 25\text{ mW}$; spectral slit width, 6 cm^{-1} . Adapted with permission from Reference [96]. Copyright[©] 2018, Elsevier.

Figures 3.8–3.10 show the *in situ* steady-state sequential Raman spectra obtained at 440 °C for CeO₂-NR (Fig. 3.8), CeO₂-NP (Fig. 3.9) and CeO₂-NC (Fig. 3.10) under oxidizing atmosphere (after treatment for 1 h under flowing 20% O₂/He; spectra marked by (a)) and under reducing atmosphere (after treatment for 1 h and 45 min under flowing 5% H₂/He; spectra marked by (b)). In agreement to our recent detailed report [93], it is evidenced (see insets (A) in Figs. 3.8–3.10 focusing in the region of the "D" band) that under reducing conditions, the "D" band at ~600 cm⁻¹ loses intensity on its high wavenumber side, namely D1, thereby indicating that the Frenkel O interstitials are loosely bound and can be delivered under the applied reducing conditions. By subtracting spectra (b) from their counterpart spectra (a) we obtain the spectroscopic fingerprint of the detached O atoms (traces (c) in insets (A), Figs. 3.8–3.10), as established recently [93,94]. Remarkably, the intensity of the difference band in traces (c) seems to follow the order CeO₂-NR > CeO₂-NP > CeO₂-NC, thereby corroborating the corresponding reducibility sequence evidenced independently by H₂-TPR.

Additionally, the F_{2g} band undergoes a slight red shift under reducing conditions (see insets (B) in Figs. 3.8–3.10 that focus on the spectral region of the F_{2g} band). The observed red shift is justified by a partial Ce⁴⁺ → Ce³⁺ reduction that results in lattice expansion due to the higher ionic radius of Ce³⁺ compared to Ce⁴⁺ (i. r._{Ce³⁺,CN=8} = 1.13 Å > i. r._{Ce⁴⁺,CN=8} = 0.97 Å), along with a probable particle size decrease, with both effects contributing to a slight red shift. Notably, this effect also follows the same trend, *i.e.*, CeO₂-NR > CeO₂-NP > CeO₂-NC, thereby indicating a higher susceptibility for the CeO₂-NR polymorph to reducing conditions.

Previously [93], it was demonstrated by *in situ* Raman spectroscopy that CeO₂ and CeO₂-ZrO₂-based materials undergo a reversible temperature dependence of their anionic sub-lattice structure, which is indicative of a corresponding reversible temperature dependence of their defect topologies. Accordingly, following successive reduction/oxidation cycles, the anionic sub-lattice structure is fully reinstated after treating the CeO₂-NR, CeO₂-NP and CeO₂-NC samples under flowing 20% O₂/He gas at 440 °C for 30 min.

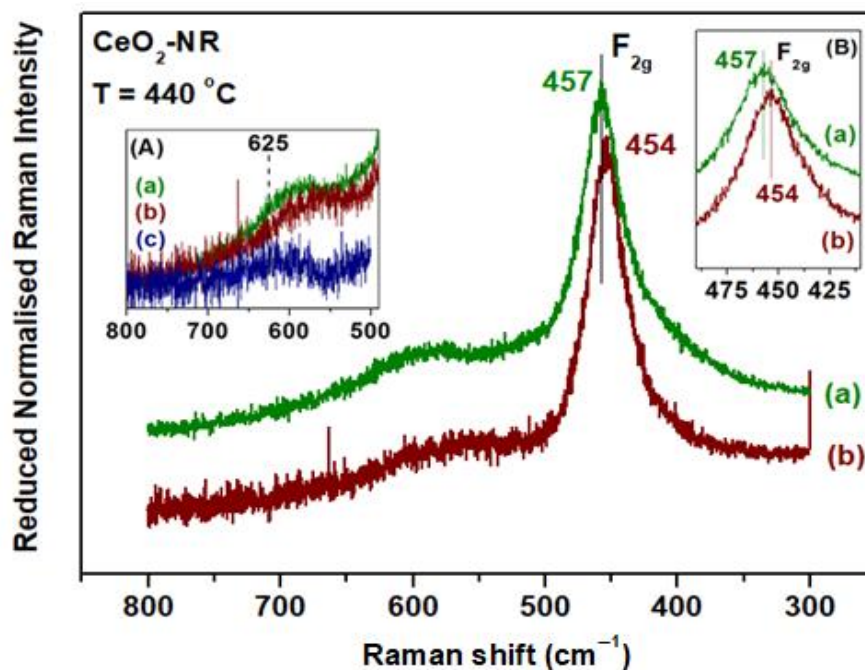


Figure 3.8. *In situ* sequential Raman spectra obtained for CeO₂-NR: (a) under flowing 20% O₂/He; (b) under flowing 5 % H₂/He. Insets: (A) trace (c) obtained after subtracting trace (b) from trace (a); (B) focus on the spectral region of the F_{2g} band. Recording parameters: see Figure 3.7 caption. Adapted with permission from Reference [96]. Copyright© 2018, Elsevier.

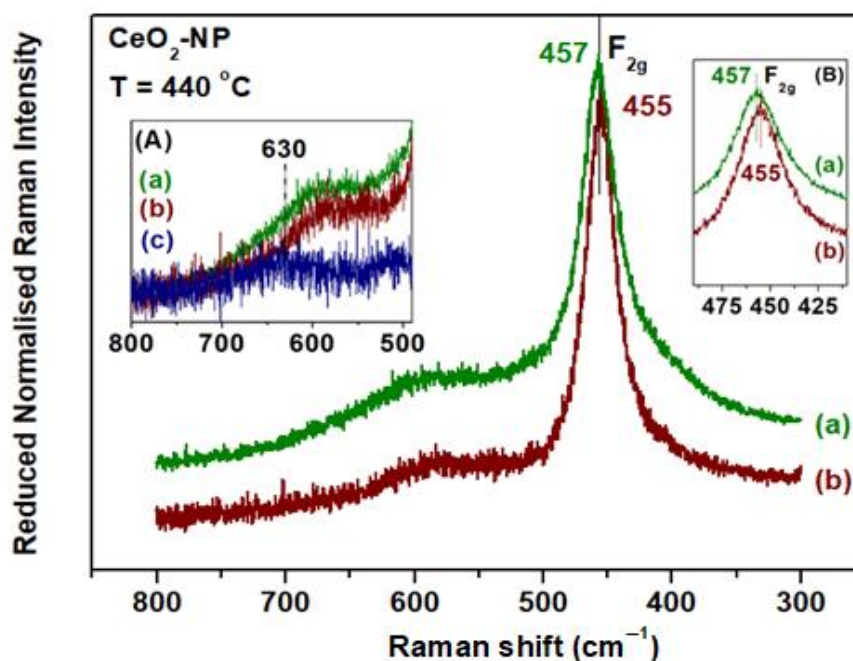


Figure 3.9. *In situ* sequential Raman spectra obtained for CeO₂-NP: (a) under flowing 20% O₂/He; (b) under flowing 5% H₂/He. Insets: (A) trace (c) obtained after subtracting trace (b) from trace (a); (B) focus on the spectral region of the F_{2g} band. Recording parameters: see Figure 3.7 caption. Adapted with permission from Reference [96]. Copyright© 2018, Elsevier.

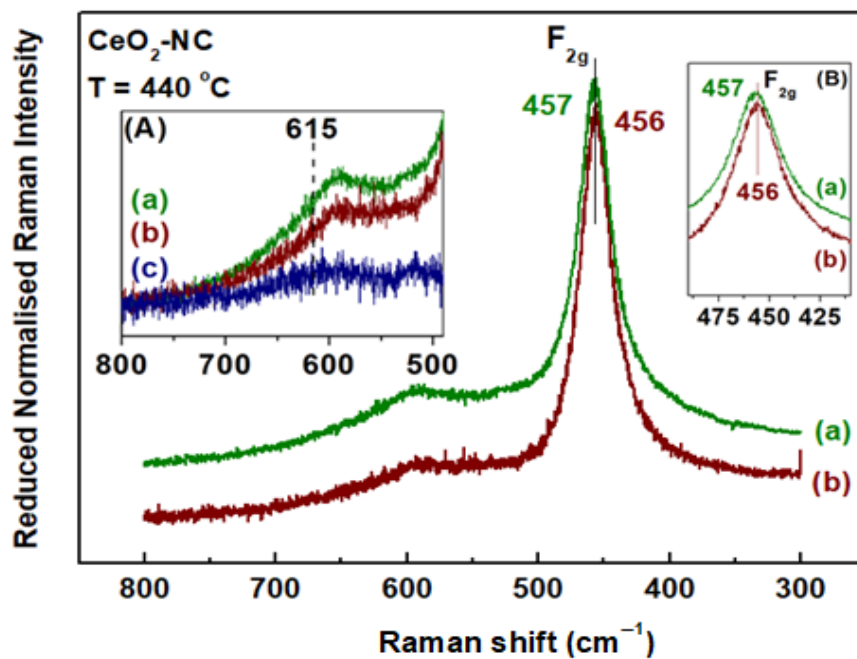


Figure 3.10. *In situ* sequential Raman spectra obtained for CeO₂-NC: (a) under flowing 20% O₂/He; (b) under flowing 5% H₂/He. Insets: (A) trace (c) obtained after subtracting trace (b) from trace (a); (B) Focus on the spectral region of the F_{2g} band. Recording parameters: see Figure 3.7 caption. Adapted with permission from Reference [96]. Copyright © 2018, Elsevier.

3.3. CHARACTERIZATION STUDIES OF CERIA-BASED TRANSITION METAL CATALYSTS

The characterization results of ceria-based transition metal catalysts (M/CeO₂, M: Cu, Fe) are presented in this sub-chapter. It ought to be mentioned, however, that the characterization results of the Fe/CeO₂ samples will be briefly presented in the present thesis for comparison purposes only, as they will be extensively discussed in the PhD thesis of Sofia Stefa [97].

3.3.1. Textural and Structural Characterization (BET and XRD)

The main textural properties of ceria-based samples (BET surface area, total pore volume, average pore size diameter) are presented in Table 3.4. Bare ceria supports exhibit higher BET surface areas (see section 3.2.1) as compared to Cu/CeO₂ and Fe/CeO₂ samples. The incorporation of copper into the ceria carrier leads to a decrease in the BET surface area; a reduction percentage of 13–18% in BET surface area is observed in all cases. The sample with the morphology of nanopolyhedra exhibits the highest BET surface area before and after the incorporation of copper into the ceria support. In particular, the following order regarding the BET surface area of copper-ceria samples is obtained: Cu/CeO₂-NP (91 m² g⁻¹) > Cu/CeO₂-NR (75 m² g⁻¹) > Cu/CeO₂-NC (34 m² g⁻¹). As for the iron-ceria samples, the following order is obtained: Fe/CeO₂-NR (69 m² g⁻¹) > Fe/CeO₂-NP (64 m² g⁻¹) > Fe/CeO₂-NC (32 m² g⁻¹) [97]. The actual Cu content was determined by XRF analysis for all three copper-ceria samples as ~7.5 wt.% (Table 3.4).

Table 3.4. Textural and structural characteristics of Cu/CeO₂ and Fe/CeO₂ samples.

Sample	BET Analysis			XRD Analysis		XRF Analysis
	BET Surface Area (m ² g ⁻¹)	Pore Volume (cm ³ g ⁻¹)	Average Pore Size (nm)	Average crystallite diameter, D _{XRD} (nm) ¹		Cu content (wt.%) ³
				CeO ₂	CuO/Fe ₂ O ₃	
Cu/CeO ₂ -NC	34	0.29	33.4	19.2	52	7.2
Cu/CeO ₂ -NR	75	0.40	21.2	11.6	43	7.4
Cu/CeO ₂ -NP	91	0.29	12.7	9.6	31	7.6
Fe/CeO ₂ -NC	32	0.19	23.3	16.8 ²	52 ²	
Fe/CeO ₂ -NR	69	0.19	11.3	9.7 ²	7 ²	
Fe/CeO ₂ -NP	64	0.12	7.6	8.5 ²	17 ²	

¹ Calculated applying Scherrer's equation (see Eq. (1) in Chapter 2); ² Calculated applying the Williamson–Hall plot after Rietveld refinement of diffractograms; ³ Cu content was determined *via* a linear calibration line with R² > 0.99 obtained by the analysis of reference copper-ceria samples by XRF.

Figures 3.11a and b show the Barrett–Joyner–Halenda (BJH) desorption pore size distribution (PSD) and the adsorption–desorption isotherms of copper-ceria samples,

respectively. Similarly to bare ceria nanoparticles, the mesoporosity of copper-ceria samples is evident.

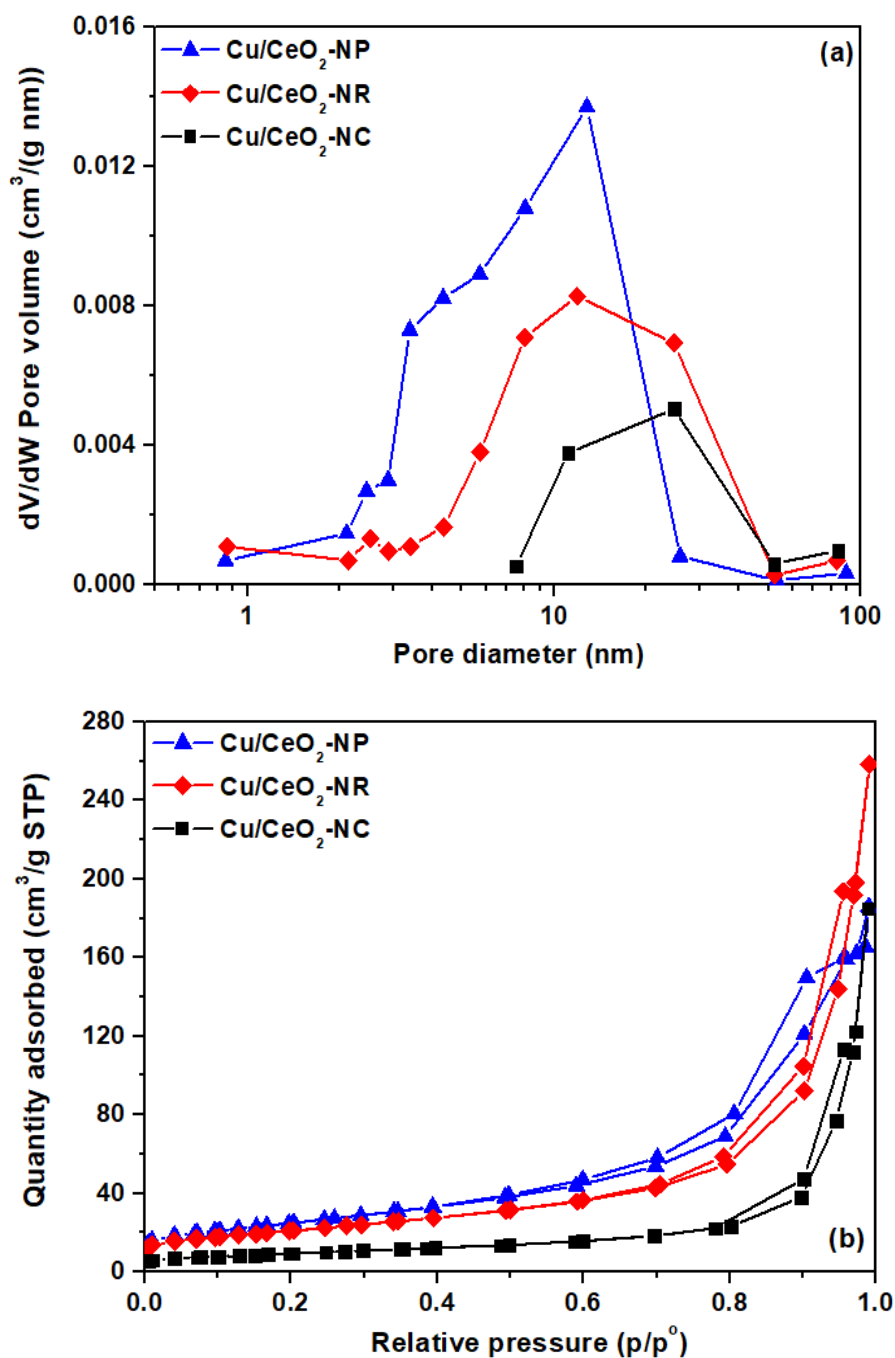


Figure 3.11. (a) BJH desorption pore size distribution (PSD) and (b) adsorption–desorption isotherms of Cu/CeO₂ samples of different morphology (NP-nanopolyhedra, NR-nanorods, NC-nanocubes). Adapted with permission from Reference [96]. Copyright[©] 2018, Elsevier.

The XRD patterns of copper-ceria samples are shown in Figure 3.12. The main peaks can be indexed to (111), (200), (220), (311), (222), (400), (331) and (420) planes of a face-centred

cubic fluorite structure of ceria (Fm3m symmetry, no. 225) [82]. The XRD peaks corresponding to CuO crystal phases at 2θ 35.3°, 38.2° and 62° are observed for all the catalysts, indicating heterodispersion or aggregation of copper species on the surface of cerium oxide [89,98].

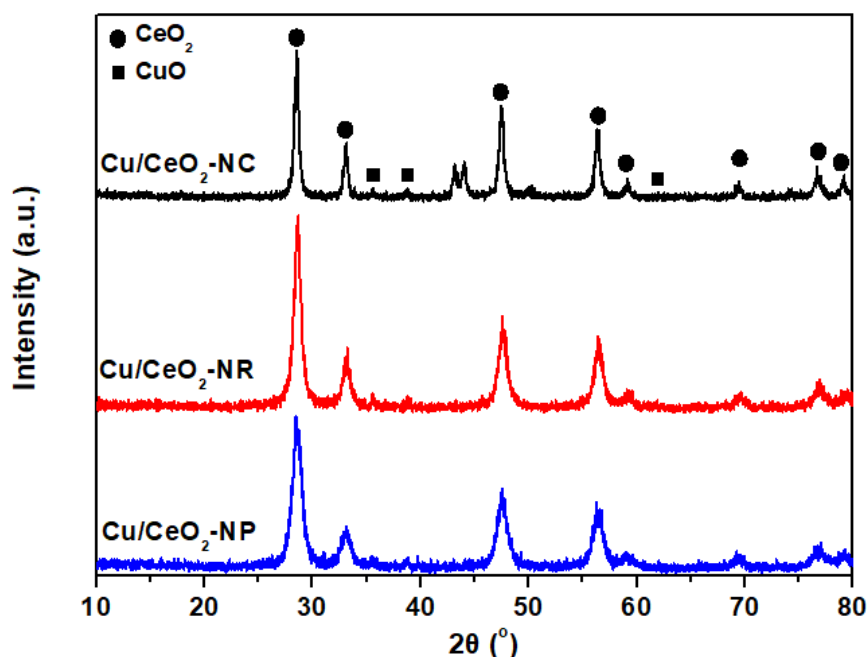


Figure 3.12. XRD patterns of Cu/CeO₂ samples of different morphology (NP-nanopolyhedra, NR-nanorods, NC-nanocubes). Adapted with permission from Reference [96]. Copyright© 2018, Elsevier. The peaks at $2\theta = 42\text{--}44^\circ$ in the Cu/CeO₂-NC sample are attributed to interferences from the stainless steel sample holder.

The average crystallite diameter of CeO₂ and CuO phases were evaluated by XRD diffractions by employing Scherrer's equation (Table 3.4). Measurements of the CeO₂ mean particle size resulted in 19.2, 11.6 and 9.6 nm for the Cu/CeO₂-NC, Cu/CeO₂-NR and Cu/CeO₂-NP, respectively. More or less the same crystallite size was calculated for bare ceria supports, declaring that the addition of copper into ceria does not affect the structural characteristics of ceria supports (see TEM analysis below). Similar crystallite sizes to that obtained here have been recently reported for ceria nanocubes, nanorods and nanopolyhedra prepared by the hydrothermal method [47]. It should be also noted that Cu/CeO₂-NC exhibits the largest ceria crystallite size as well as the smallest BET surface area, leading to the largest CuO particle size and to inferior catalytic performance as will be discussed in the sequence.

Regarding the mean particle size of copper phase the following order was recorded: Cu/CeO₂-NC (52 nm) > Cu/CeO₂-NR (43 nm) > Cu/CeO₂-NP (31 nm), which coincides to that

obtained for CeO₂. In view of this fact, it has been reported that the structural characteristics of ceria can determine the particle size of CuO, with direct implications in catalytic activity [47]. Interestingly, the same trend, in relation to Cu particle size vs. ceria morphology (NC, NR, NP), has been recently found for 20 wt.% Cu/CeO₂ catalysts, verifying the present findings [70]. It is also worth mentioning that the crystallite size of both ceria and CuO particles follows the reverse order of BET area (Table 3.4), implying an agglomeration upon surface area decrease. The same trend was observed by Zabilskiy *et al.* [37] for nanoshaped Cu/CeO₂ catalysts.

The corresponding results regarding the Fe/CeO₂ samples are summarized in Table 3.4 [97]. In particular, the CeO₂ crystallite size is 16.8, 9.7 and 8.5 nm for Fe/CeO₂-NC, Fe/CeO₂-NR and Fe/CeO₂-NP, respectively [97]. Taking into account the crystallite size of iron oxide phase, the following order was obtained: Fe/CeO₂-NC (52 nm) > Fe/CeO₂-NP (17 nm) > Fe/CeO₂-NR (7 nm) [97].

3.3.2. Redox Properties (H₂-TPR)

TPR experiments, employing H₂ as a reducing agent, were carried out to gain insight into the impact of ceria morphology on the redox properties of as-prepared samples. The reduction profiles of Cu/Ceria samples along with that of a CuO reference sample are depicted in Figure 3.13. In Table 3.5 the main reduction peaks along with their corresponding H₂ consumption (mmol H₂ g⁻¹) are summarized. Bare CuO has one reduction peak at 380–392 °C, in accordance with the literature [99]. The reduction profiles of all Cu/CeO₂ samples exhibit two overlapping peaks in the range of 176–228 °C, as well as one peak at *ca.* 793 °C, attributed to the reduction of Ce⁴⁺ into Ce³⁺ [100]. The low-temperature peak (peak α) in the range of 176–194 °C is attributed to the reduction of finely dispersed CuO_x species interacting strongly with the CeO₂ surface [101–103]. The peak at higher temperature (peak β) is related to larger CuO clusters formed on the ceria surface [99]. The reduction of Cu/CeO₂ samples occurs at considerably lower temperature than those of bare CuO and CeO₂ samples (Figs. 3.13 and 3.5, respectively). This is attributed to the "synergetic effect" between the two oxide phases that weakens the metal-oxygen bonds [37,98].

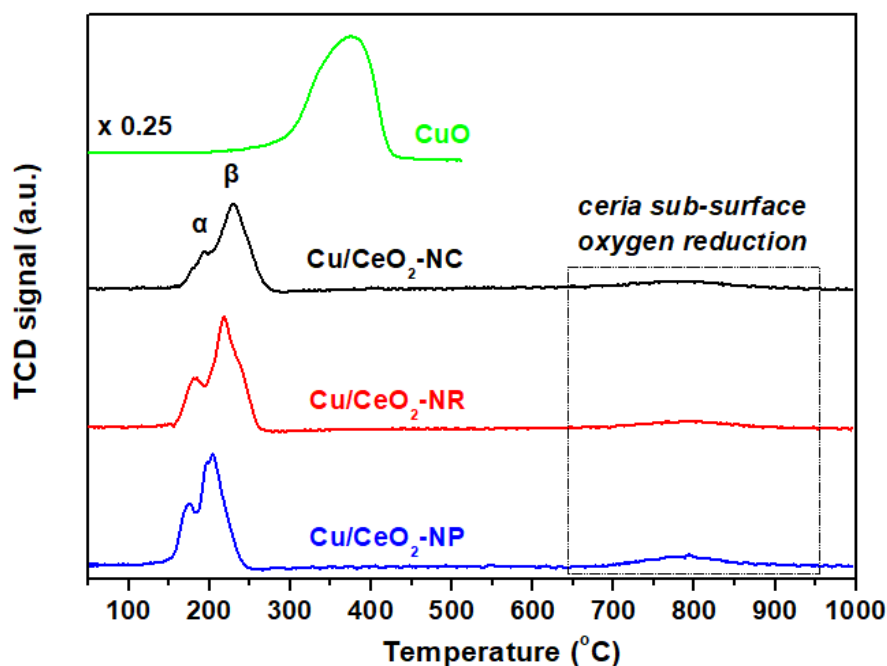


Figure 3.13. H₂-TPR profiles of bare CuO and Cu/CeO₂ samples. Adapted with permission from Reference [96]. Copyright© 2018, Elsevier.

To gain further insight into the impact of support's nature on the reducibility of Cu/CeO₂ samples, the H₂ consumption in the low-temperature range, which is related to the reduction of CuO_x species and surface oxygen of ceria, is estimated (Table 3.5). The following order, in terms of H₂ uptake, is obtained: Cu/CeO₂-NR (1.80 mmol H₂ g⁻¹) > Cu/CeO₂-NP (1.65 mmol H₂ g⁻¹) > Cu/CeO₂-NC (1.50 mmol H₂ g⁻¹). These results indicate the superior reducibility of Cu/CeO₂-NR. Notably, the reduction order of the supported catalysts is perfectly related to that of bare ceria supports (see section 3.2.3) indicating the key role of support morphology on the reducibility of Cu/CeO₂ catalysts. It is also worth noticing that the amount of H₂ required for the reduction of Cu/Ceria samples always surpasses the theoretical amount of H₂ for the complete reduction of CuO to Cu (~1.34 mmol H₂ g⁻¹ on the basis of a Cu nominal loading of 8.5 wt.%).

The present TPR results clearly indicate: (i) the enhanced reducibility of mixed oxides compared to bare ones and (ii) the significant impact of ceria's nanostructure on the redox properties of Cu/CeO₂ binary oxides. These findings can be interpreted in terms of Cu-Ceria interactions, which in turn facilitate the reduction of ceria capping oxygen. In particular, the superior reducibility of mixed oxides can be ascribed to: (i) the hydrogen spillover from Cu sites to ceria carrier, (ii) the electronic metal-support interactions (EMSI) between copper and ceria particles, which directly affect the reducibility of CeO₂ [17]. In view of this fact, a

relationship between the reduction temperature of ceria and the work function of metal dopants has been established [104].

Table 3.5. Redox characteristics of Cu/CeO₂ and Fe/CeO₂ samples.

Sample	H ₂ consumption (mmol H ₂ g ⁻¹) ¹			Peak Temperature (°C)		OSC (mmol O ₂ g ⁻¹)
	Peak (α + β)	CeO ₂ peak	Total	Peak α	Peak β	
Cu/CeO ₂ -NC	1.50	0.65	2.15	194	228	0.75
Cu/CeO ₂ -NP	1.65	0.25	1.90	176	201	0.83
Cu/CeO ₂ -NR	1.80	0.25	2.05	181	217	0.90
	H ₂ consumption (mmol H ₂ g ⁻¹) ¹	H ₂ excess (mmol H ₂ g ⁻¹) ²				
Fe/CeO ₂ -NC	2.47	0.47	0.67			
Fe/CeO ₂ -NP	2.93	0.93	0.70			
Fe/CeO ₂ -NR	3.42	1.42	0.75			

¹ Estimated by the area of the corresponding TPR peaks, which is calibrated against a known amount of CuO standard sample; ² Estimated by the subtraction of H₂ amount required for Fe₂O₃ reduction in 7.5 wt.% Fe/CeO₂ samples (~2 mmol g⁻¹) from the total H₂ consumption [97].

Regarding the corresponding results of Fe/CeO₂ samples (Table 3.5), iron-ceria nanorods exhibit the highest value of H₂ consumption (3.42 mmol H₂ g⁻¹) followed by nanopolyhedra (2.93 mmol H₂ g⁻¹) and nanocubes (2.47 mmol H₂ g⁻¹) perfectly matched to the catalytic conversion order (see below) [97]. It is also worth noticing that the amount of H₂ required for the reduction of Fe/CeO₂ samples always surpasses the theoretical amount of H₂ for the complete reduction of Fe₂O₃ to Fe (~2 mmol H₂ g⁻¹, on the basis of a Fe nominal loading of 7.5 wt.%). The latter reveals the facilitation of ceria capping oxygen reduction in the presence of iron, further corroborating the above findings and the synergistic function of metal and support. The H₂ excess uptake (mmol g⁻¹, Table 3.5), reflecting the extent of ceria oxygen reduction, follows the sequence Fe/CeO₂-NR (1.42) > Fe/CeO₂-NP (0.93) > Fe/CeO₂-NC (0.47), in line with the supports' reducibility [97].

In terms of the oxygen storage capacity (OSC), the following trend is obtained for bare ceria as well as for the ceria-based transition metal samples (Tables 3.2 and 3.5, respectively): nanorods > nanopolyhedra > nanocubes. This order coincides well with the CO oxidation activity (see below), revealing the key role of reducibility.

3.3.3. Surface Analysis (XPS)

XPS analysis was conducted to assess the impact of ceria morphology on elementary oxidation states of Cu/CeO₂ samples. Figure 3.14a shows the Ce 3d XPS spectra of copper-ceria samples, which can be resolved to eight components, as reported in several relevant studies [70,90,102,105–110]. The Ce 3d spectrum consists of two series of spin-orbit lines u and v, as clearly described in section 3.2. 4. Regardless of the number of defect sites in the bulk of ceria, it has been found that ceria samples of various morphologies can exhibit similar Ce 3d spectra profiles [23,27]. The same similarity is observed for copper-ceria samples, as well, in which the amount of Ce³⁺ varies between 21.9 and 23.9% (Table 3.6), with the CeO₂-NR exhibiting the highest population of Ce³⁺ species. With regard to the iron-ceria samples, the population of Ce³⁺ ions is slightly higher than that of bare ceria ones, varying between 25.3 and 28.5% (Table 3.6), without, however, exhibiting significant alterations between the samples of different morphology [97]. Despite the preparation methods and the presence of copper, it has been shown that there are no significant differences in the amount of reduced, non-stoichiometric cerium species, in the external layers of the catalysts [111]. However, the uncertainty in the precise Ce³⁺ determination by XPS, due to high-vacuum conditions and X-ray irradiation, should be mentioned [112].

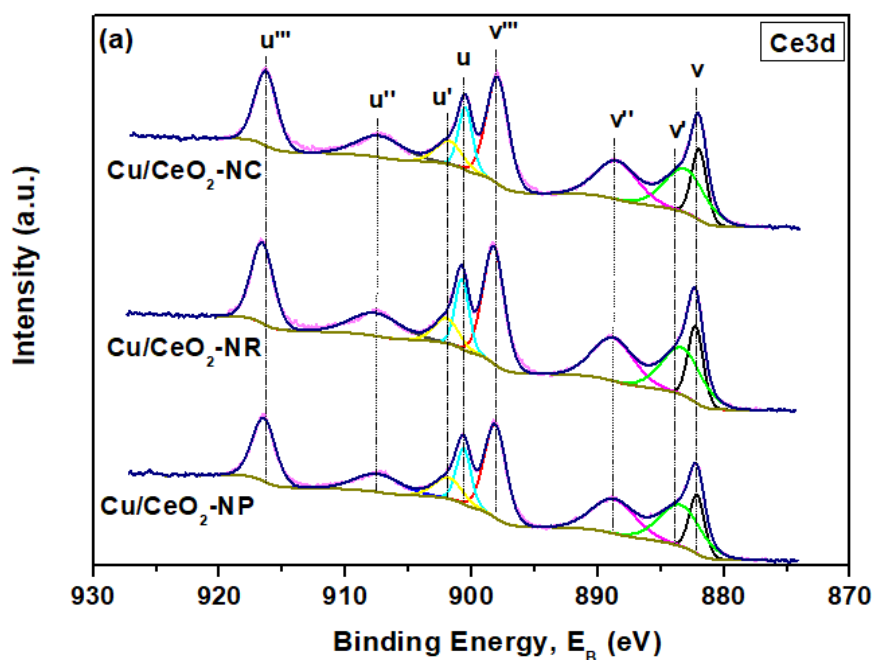
The corresponding O 1s XPS spectra are illustrated in Figure 3.14b. There are two characteristic peaks in the O 1s spectra of all catalysts. The assignment of the peaks has been already performed in section 3.2. 4. In terms of the O_I/O_{II} ratio, ceria-based transition metal samples exhibit the exact same trend as bare ceria supports, namely, nanorods > nanopolyhedra > nanocubes. In specific, for copper-ceria and iron-ceria samples (not shown), the following orders are obtained (Table 3.7): Cu/CeO₂-NR (2.02) > Cu/CeO₂-NP (1.96) > Cu/CeO₂-NC (1.89) and Fe/CeO₂-NR (2.52) > Fe/CeO₂-NP (2.25) > Fe/CeO₂-NC (1.84) [97], implying again the key role of support morphology on oxygen mobility/reducibility. These findings along with the TPR results corroborate that the samples with the rod-like morphology, namely CeO₂-NR, Cu/CeO₂-NR and Fe/CeO₂-NR, demonstrate the highest population of loosely bound labile oxygen species, resulting in improved reducibility and oxygen kinetics.

Figure 3.14c shows the Cu 2p XPS spectra of Cu/CeO₂ samples. For comparison purposes, the spectrum of CuO reference sample is also depicted. All spectra are characterized by two main peaks of Cu 2p_{1/2} (953.7 eV) and Cu2p_{3/2} (933.8 eV), as well as shake-up satellite peaks at 943 eV, which are typical of Cu²⁺ species [52,90,102]. The latter is further confirmed by the XPS spectrum of CuO reference sample.

It should be mentioned here that $\text{Cu}^+/\text{Cu}_2\text{O}$ and $\text{Cu}^{2+}/\text{CuO}$ species cannot be easily resolved because of the proximity in their binding energies [102]. In this regard, the discrimination of Cu oxidation state is usually performed by the comparison of Cu 2p XPS binding energy and Auger parameters in Wagner plots. However, the difficulty in precisely discriminating Cu oxidation states even by means of XPS positions and Auger parameters has been documented [52,113,114]. In light of the above, the determination of the relative population of Cu^+ species is performed here on the basis of a well-established procedure, according to the following equation [90,115,116]:

$$\text{Cu}^+(\%) = \frac{A - \left(\frac{A_{1s}}{B_s}\right) \cdot B}{A + B} \cdot 100 \quad (2)$$

where A is the area of the main Cu $2p_{3/2}$ peak, B is the area of the shake-up peak and A_{1s}/B_s is the ratio of main/shake-up peaks for the reference CuO sample. Analysis of the reference CuO sample (not shown) gives an A_{1s}/B_s value of 1.89, in agreement with the literature [52,115].



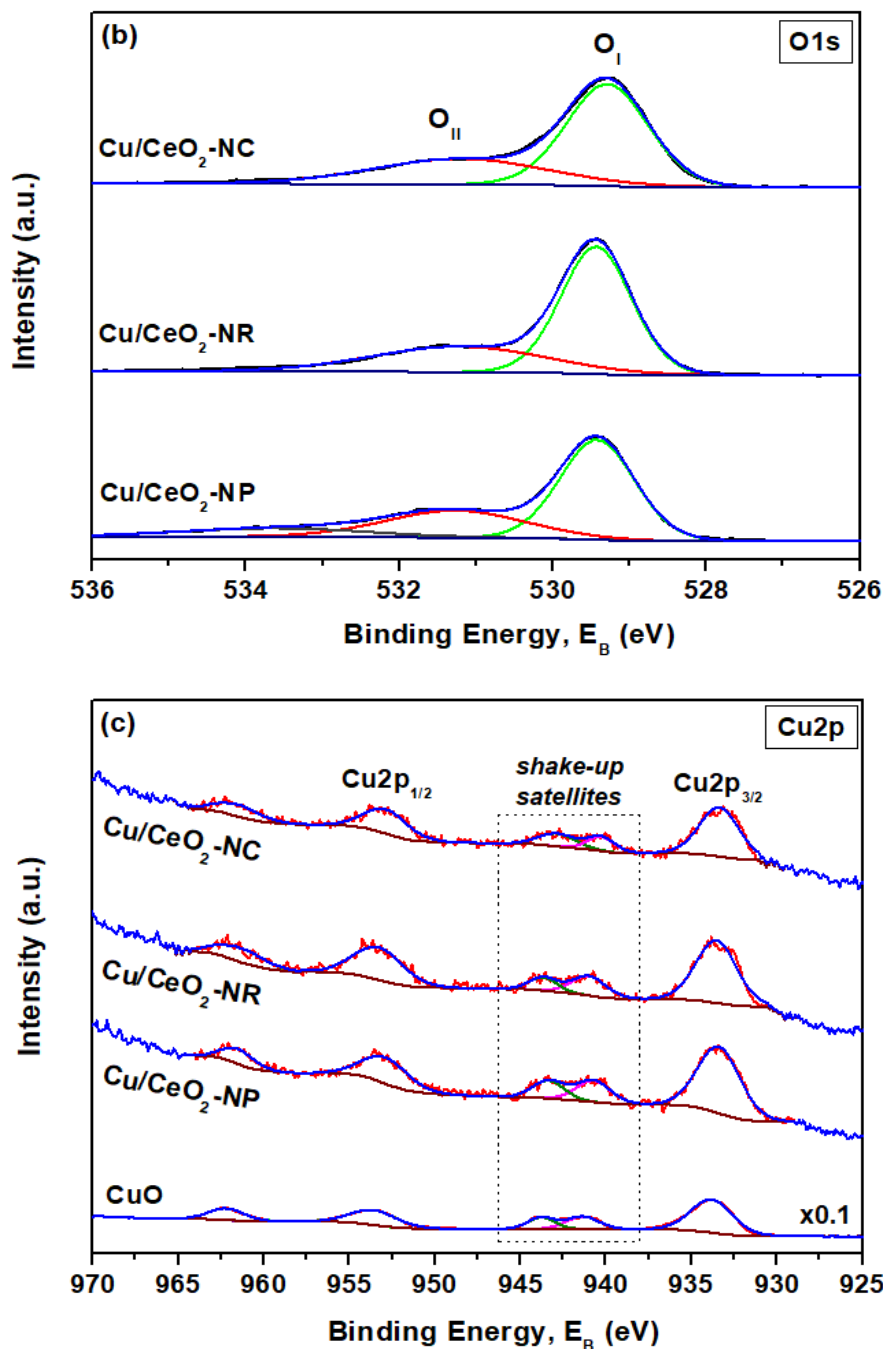


Figure 3.14. XPS spectra of (a) Ce 3d, (b) O 1s and (c) Cu 2p region of bare CuO and Cu/CeO₂ samples. Adapted with permission from Reference [96]. Copyright[©] 2018, Elsevier.

Table 3.6 lists the relative content of Cu⁺ species on Cu/Ceria samples. Cu/CeO₂-NR exhibits the highest concentration (16.1%) followed by Cu/CeO₂-NP (13.0%) and Cu/CeO₂-NC (11.8%). This sequence conforms to the order of O_s/O_b ratio (Table 3.2) and reducibility (Table 3.5), justifying the close relationship between redox and electronic properties established through metal-support interactions. In complete agreement, it has been found that the strong interaction of CuO_x species with rod-like ceria supports can lead to a stable

existence of Cu^+ species in Cu/Ceria samples [102]. Moreover, the same Cu^+ trend, in relation to nanoceria morphology (rods, cubes, polyhedra), was recently revealed for 10 wt.% Cu/ CeO_2 catalysts [47].

Taking into account the Fe^{2+} (%) amount (Table 3.6), calculated by curve-fitting, the following order is obtained for the Fe/ CeO_2 samples of different morphology: Fe/ CeO_2 -NR (14.4) > Fe/ CeO_2 -NP (13.3) > Fe/ CeO_2 -NC (13.1), which again coincides with the catalytic conversion order as described in the sequence and it is indicative of the interfacial interaction between the two oxide phases [97,117]. It should be pointed out that the aforementioned Fe^{2+} (%) amount order is in full compliance with the order of O_s/O_b ratio and the reducibility of the mixed oxides (Tables 3.2 and 3.5, respectively), disclosing the interrelationship between electronic and redox properties induced by iron-ceria interactions.

Table 3.6. XPS results for Cu/ CeO_2 and Fe/ CeO_2 samples.

Sample	O_I (%)	O_{II} (%)	O_I/O_{II}	Ce^{3+} (%)	Cu^+ (%)	Fe^{2+} (%)	Cu/Ce atomic ratio	Fe/(Fe + Ce)
Cu/ CeO_2 -NC	65.4	34.6	1.89	21.9	11.8		0.16	
Cu/ CeO_2 -NR	66.9	33.1	2.02	23.9	16.1		0.18	
Cu/ CeO_2 -NP	66.2	33.8	1.96	23.3	13.0		0.35	
Fe/ CeO_2 -NC ¹	64.8	35.2	1.84	28.5		13.1		0.43
Fe/ CeO_2 -NR ¹	71.6	28.4	2.52	25.3		14.4		0.28
Fe/ CeO_2 -NP ¹	69.2	30.8	2.25	26.5		13.3		0.34

¹ Data taken from [97].

Regarding the Cu distribution to the outer surface, both copper-ceria nanocubes and nanorods exhibit similar values of Cu/Ce surface atomic ratio (0.16 and 0.18, respectively, Table 3.6), which however is slightly lower to the nominal one (0.25), implying an impoverishment of catalyst's surface to copper. On the other hand, in nanopolyhedra the Cu/Ce atomic ratio is almost double (0.35) and higher than the theoretical implying an enrichment of catalyst's surface to copper, in accordance with the literature [70]. The surface atomic ratio Fe/(Fe+Ce) of the Fe/ CeO_2 samples is also presented in Table 3.6 [97]. Apparently, the surface atomic ratio of the rod-shaped sample is near to the nominal one (0.2), indicating a uniform distribution of iron and cerium species over the entire sample. However, nanopolyhedra and nanocubes exhibit higher values of surface atomic ratio than the nominal composition, namely 0.34 and 0.43, respectively, indicating an enrichment of the catalyst's surface in iron species or equally an impoverishment of catalyst's surface to cerium species [97].

3.3.4. Morphological Characterization (TEM)

In order to gain insight into the effect of hydrothermal synthesis on the morphological characteristics of ceria nanoparticles, transmission electron microscopy (TEM) studies were also carried out. Figures 3.15 (a-c) and (d-f) illustrate the TEM images of copper-ceria and iron-ceria [97] samples, respectively. It is evident that the addition of copper or iron into the ceria lattice does not affect the morphology of the support.

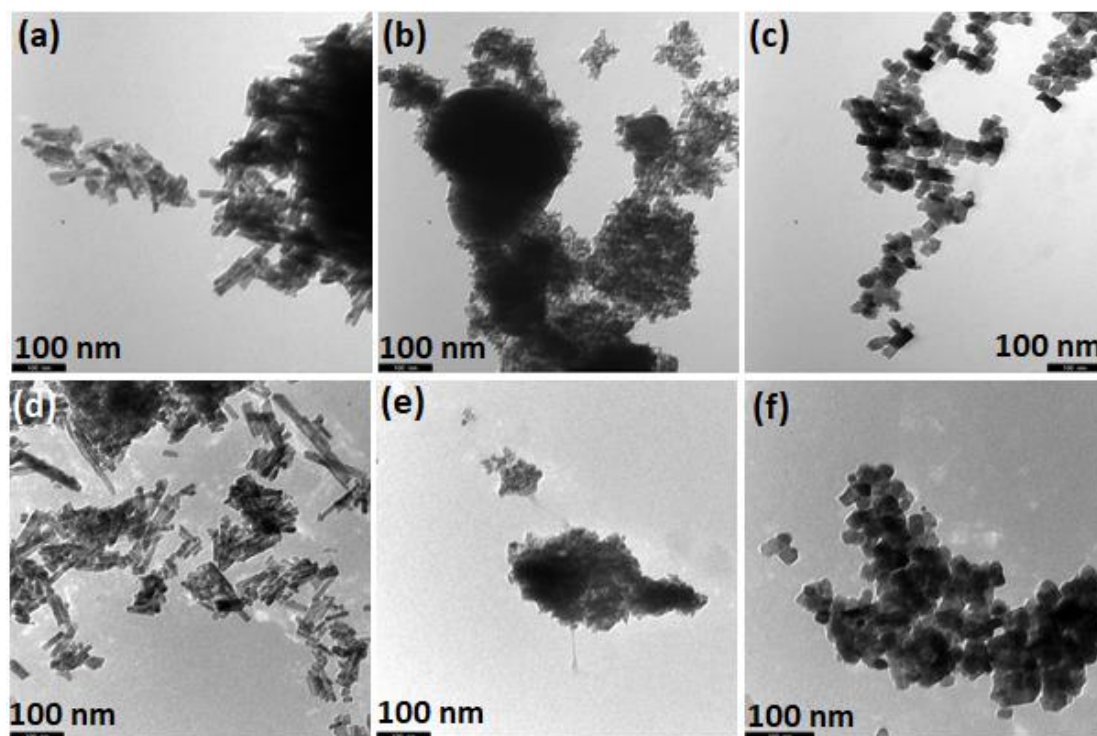


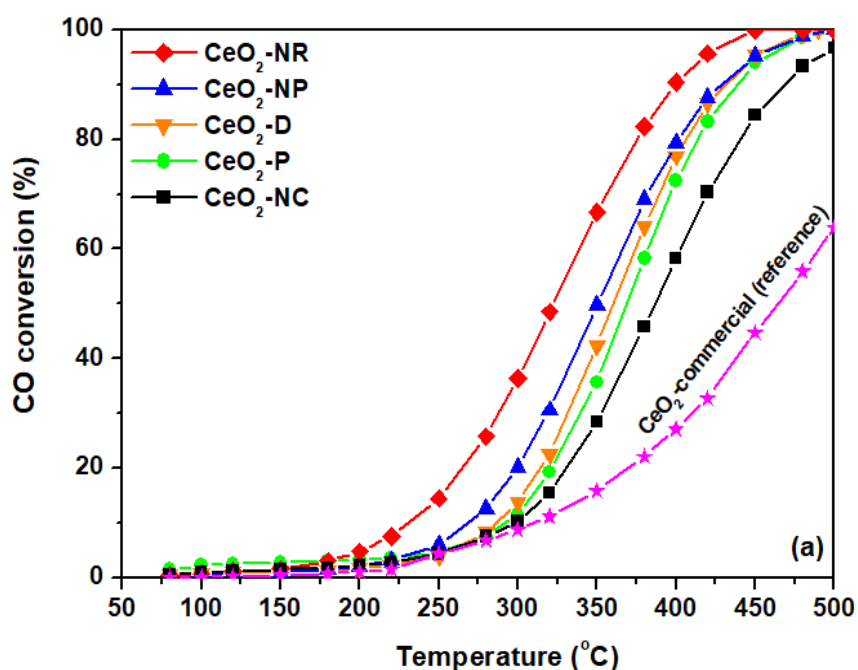
Figure 3.15. TEM images of the samples: (a) Cu/CeO₂-NR, (b) Cu/CeO₂-NP, (c) Cu/CeO₂-NC, (d) Fe/CeO₂-NR, (e) Fe/CeO₂-NP and (f) Fe/CeO₂-NC.

3.4. IMPLICATIONS IN CO OXIDATION REACTION

3.4.1. CO Oxidation Performance of Bare Ceria Oxides

The CO oxidation reaction was employed as a model reaction to gain insight into the extent the different synthesis method, and in turn the different physicochemical characteristics (surface area, crystallite size, reducibility, surface oxygen, exposed facets), can affect the catalytic performance. Figure 3.16a depicts the CO conversion as a function of temperature of the as-synthesized ceria samples. For comparison purposes, a commercial CeO₂ sample (Fluka) was employed as reference material. The superiority of the as-prepared samples as compared to the commercial one is evident. Moreover, the sample prepared by the hydrothermal method of high NaOH concentration and aging at 90 °C for 24 h (CeO₂-NR) demonstrated the optimum performance. In particular, the following oxidation performance, in terms of half-conversion temperature (T_{50}), was obtained: CeO₂-NR (320 °C) > CeO₂-NP (350 °C) > CeO₂-D (360 °C) > CeO₂-P (370 °C) > CeO₂-NC (385 °C) > CeO₂-Comm (460 °C).

The impact of synthesis procedure on the intrinsic reactivity can be more accurately obtained by the Arrhenius plots, in the kinetic regime (Figure 3.16b). To take into account the differences in the BET surface area, the surface-normalized reaction rate ($\text{nmol m}^{-2} \text{s}^{-1}$) instead of CO conversion was employed.



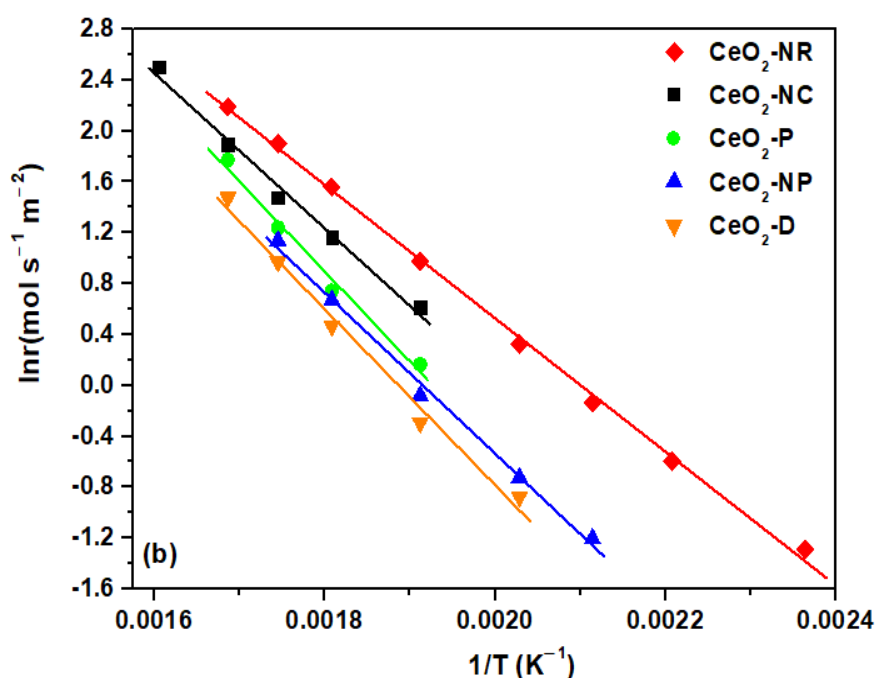


Figure 3.16. (a) CO conversion as a function of temperature and (b) the corresponding Arrhenius plots for ceria samples. Adapted with permission from Reference [76]. Copyright© 2017, The Royal Society of Chemistry.

Table 3.7 summarizes the apparent activation energies (E_a) and the corresponding pre-exponential factors (A) for the ceria samples. The significant effect of synthesis method on the CO oxidation activity on the whole temperature range investigated is evident. The superiority of $\text{CeO}_2\text{-NR}$ is again obvious, showing a specific reaction rate of about one order of magnitude higher, as compared to the other samples. Moreover, the calculated E_a for the $\text{CeO}_2\text{-NR}$ sample is 43.7 kJ/mol, which is the lowest among the samples. In specific, the following order, in terms of E_a , was observed: $\text{CeO}_2\text{-NR}$ (43.7 kJ mol⁻¹) < $\text{CeO}_2\text{-NC}$ (50.7 kJ mol⁻¹) < $\text{CeO}_2\text{-NP}$ (53.8 kJ mol⁻¹) < $\text{CeO}_2\text{-D}$ (57.5 kJ mol⁻¹) < $\text{CeO}_2\text{-P}$ (58.8 kJ mol⁻¹).

Table 3.7. Kinetics parameters obtained by Arrhenius equation.

Sample	Activation Energy, E_a (kJ mol ⁻¹)	Pre-exponential Factor, A (nmol s ⁻¹ m ⁻²)
$\text{CeO}_2\text{-P}$	58.8	8.3×10^5
$\text{CeO}_2\text{-D}$	57.5	4.6×10^5
$\text{CeO}_2\text{-NP}$	53.8	2.5×10^5
$\text{CeO}_2\text{-NC}$	50.7	2.0×10^5
$\text{CeO}_2\text{-NR}$	43.7	6.2×10^4

Based on the above, it can be stated that ceria NPs prepared by the hydrothermal method of high NaOH concentration and aging at 90 °C for 24 h (CeO₂-NR) showed the best catalytic performance for CO oxidation reaction, among all the other samples. These findings can be interpreted on the basis of the well-established Mars-van Krevelen mechanism, in which ceria is reduced by CO and oxidized by gas phase oxygen through a redox cycle. The main steps of this procedure are: i) adsorption of CO on the ceria surface, ii) reaction of the adsorbed CO with the lattice oxygen and formation of reaction intermediates, iii) desorption of these intermediates and production of CO₂ and oxygen vacancies, iv) replenishment of the oxygen vacancies by activating the gas phase oxygen on the catalyst [73,87].

Since the above mechanistic steps exhibit a clear redox character, a strong dependence of CO oxidation performance from the redox properties of catalyst surface is expected. Indeed, CeO₂-NR sample demonstrated the highest population of loosely bound, easily reduced, surface oxygen species, resulting in the highest surface-to-bulk (O_s/O_b) oxygen species abundance (Table 3.2).

It is also worth mentioning that although the CO oxidation performance was in general favoured by the surface area (Table 3.1), it doesn't seem to be the decisive factor governing the CO oxidation activity. For instance, the CeO₂-NP sample possesses the highest surface area (109 m² g⁻¹), without, however, offering the best catalytic performance.

In summary, it can be inferred that the hydrothermal method of high NaOH concentration can result to the formation of CeO₂ nanoparticles with rod-like morphology, with enhanced reducibility and surface oxygen exchange kinetics, and in turn CO oxidation activity [73]. The high concentration of loosely bound oxygen species on ceria nanorods, linked to oxygen mobility and vacancies formation, can be accounted for the superior performance of the Ceria-NR sample.

Hence, this particular parameter can be considered as a reliable descriptor for the CO oxidation performance of Ceria NPs. In view of this fact, in a comprehensive study by Capdevila-Cortada *et al.* [85], exploring the reactivity descriptors for ceria-based materials, the surface reduction (E_{red}) and oxygen basicity (O_{2p}) –linked to vacancy formation energy and the number of adsorption sites– can be considered as the most important reactivity descriptor. Hence, the CO oxidation rate is expected to follow the order $r_{110} > r_{100} > r_{111}$, in agreement with the vacancy formation energy [85].

In light of the above, it has been clearly revealed, both theoretically [118,119] and experimentally [41,49,73] that anionic vacancies' formation is strongly dependent on exposed facets of ceria, being lower on rod-like formations, where the {110} and {100}

planes are prevailing. In a similar manner, the improved low-temperature CO oxidation performance of various transition metals supported on CeO₂-nanorods has been ascribed to the pronounced effect of ceria nanorods towards the formation of oxygen vacancies and CO adsorption sites [13]. The key role of redox properties and in particular of loosely bound oxygen species, on the CO oxidation performance was recently verified by Reddy and co-workers in a series of doped ceria samples [87]. A direct correlation between the lattice oxygen binding energy and the activity was revealed, implying that oxygen species' migration from bulk to surface may determine the overall process. It should be noted, however, that no similar correlation has been observed here; the lattice oxygen binding energy of bare ceria samples is not strongly affected by the preparation method (Figure 3.6). Taking into account the superior reducibility of CeO₂-NR sample, it would be of particular importance to explore the solid state properties and the catalytic performance of binary metal/CeO₂-NR composites. The enhanced redox properties of ceria carrier are expected to notably affect the extent of metal-support interactions [15,50,120] and in turn, the catalytic activity.

3.4.2. CO Oxidation Performance of Ceria-Based Transition Metal Catalysts

The oxidation of CO was also employed as a model reaction in order to reveal the impact of ceria morphology on the catalytic performance of Cu/Ceria and Fe/Ceria samples. Figure 3.17 shows the conversion of CO as a function of temperature for bare CeO₂ as well as for the ceria-based transition metal samples. Obviously, the support morphology affects enormously the catalytic activity. In particular, the following oxidation performance, in terms of half-conversion temperature (T_{50}), was obtained: CeO₂-NR (320 °C) > CeO₂-NP (350 °C) > CeO₂-NC (385 °C). The incorporation of copper into the ceria lattice considerably improves the catalytic performance without, however, affecting the activity order: Cu/CeO₂-NR (72 °C) > Cu/CeO₂-NP (83 °C) > Cu/CeO₂-NC (92 °C). Apparently, the Cu/CeO₂ sample with the rod-like morphology exhibits an excellent catalytic performance, offering almost complete CO elimination at temperatures as low as 100 °C.

The CO oxidation performance was also evaluated in the iron-ceria samples. For comparison purposes, the catalytic performance of bare Fe₂O₃-D prepared by thermal decomposition, as well as of a mechanical mixture of Fe₂O₃-D + CeO₂-NR (see Chapter 2) was investigated in parallel to reveal the individual or synergistic effect of catalyst's counterparts. It should be mentioned that the same trend with the copper-ceria samples is also observed in the iron-ceria ones: Fe/CeO₂-NR (166 °C) > Fe/CeO₂-NP (182 °C) > Fe/CeO₂-NC (219 °C) > Fe₂O₃-D +

$\text{CeO}_2\text{-NR}$ ($272\text{ }^\circ\text{C}$) > $\text{Fe}_2\text{O}_3\text{-D}$ ($277\text{ }^\circ\text{C}$). It is also worth noticing that the preparation method significantly affects the catalytic performance. Specifically, the hydrothermal method, which results in the development of ceria nanoparticles of different morphology, in conjunction to the addition of iron through the wet impregnation method, leads to highly active iron-ceria composites, as compared to the iron-ceria mixed oxide prepared by mechanical mixing ($\text{Fe}_2\text{O}_3\text{-D} + \text{CeO}_2\text{-NR}$, green line in Fig. 3.17). More specifically, the conversion profile of $\text{Fe}/\text{CeO}_2\text{-NR}$ has been shifted by more than $100\text{ }^\circ\text{C}$ to lower temperatures as compared to that of bare $\text{Fe}_2\text{O}_3\text{-D}$, $\text{CeO}_2\text{-NR}$ and $\text{Fe}_2\text{O}_3\text{-D} + \text{CeO}_2\text{-NR}$ mechanical mixture, clearly revealing the synergistic interaction between CeO_2 and Fe_2O_3 induced by the preparation procedure followed.

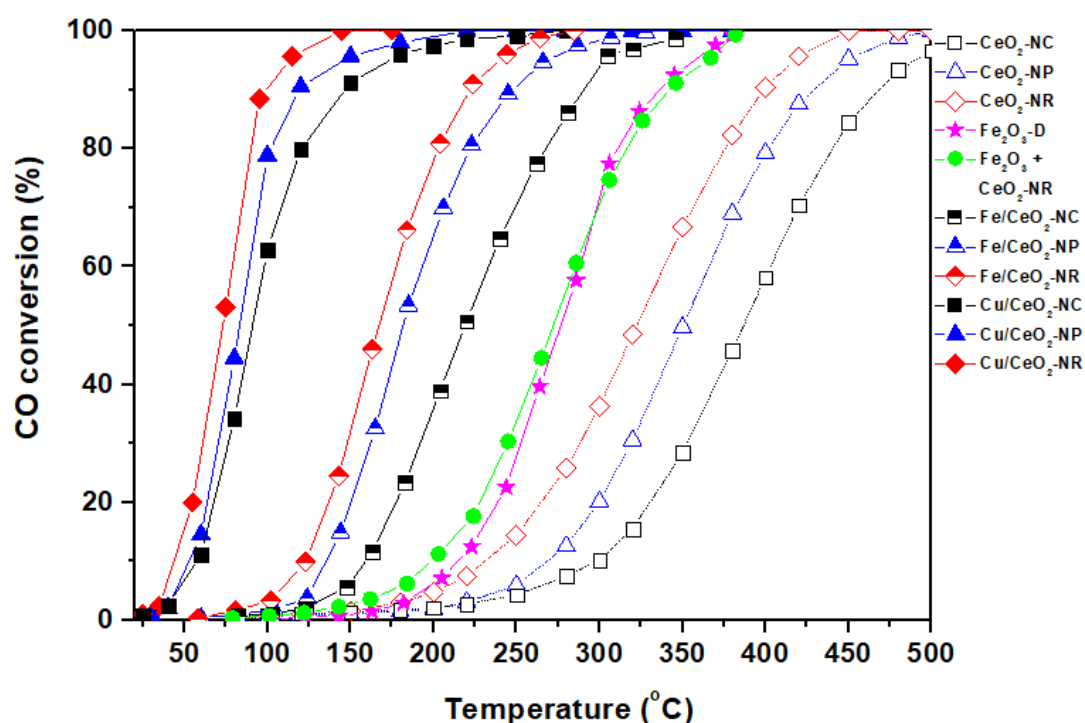


Figure 3.17. CO conversion as a function of temperature for Ceria, Cu/Ceria and Fe/Ceria samples of different morphology (NR, NC and NP, as indicated in each curve). Reaction conditions: 2000 ppm CO, 1 vol.% O_2 , GHSV = $39,000\text{ h}^{-1}$.

In this point, it should be mentioned that stability experiments were undertaken for the optimum rod-shaped catalysts (NR). In particular, a stable conversion performance (100%) was obtained at $150\text{ }^\circ\text{C}$ during a short term (12 h) stability test for the $\text{Cu}/\text{CeO}_2\text{-NR}$ sample (Figure 3.18). Moreover, BET and XRD characterization studies over the spent $\text{Cu}/\text{CeO}_2\text{-NR}$ catalyst (after subjected to activity and stability tests) revealed no textural/structural modifications; the mean crystallite size of ceria is slightly increased to 13 nm as compared to

11.6 nm of fresh sample whereas the BET surface area remained almost unchanged ($73 \text{ m}^2 \text{ g}^{-1}$ as compared to $75 \text{ m}^2 \text{ g}^{-1}$ of fresh sample, Table 3.4). These findings are in agreement with the structural stability of ceria samples upon subsequent oxidation/reduction processes during Raman analysis, further corroborating the reliability of the obtained structure-activity relationships. Similarly, a stable conversion performance ($\sim 80\%$) was attained at $200 \text{ }^\circ\text{C}$ during a short term (24 h) stability experiment over the most active Fe/CeO₂-NR sample.

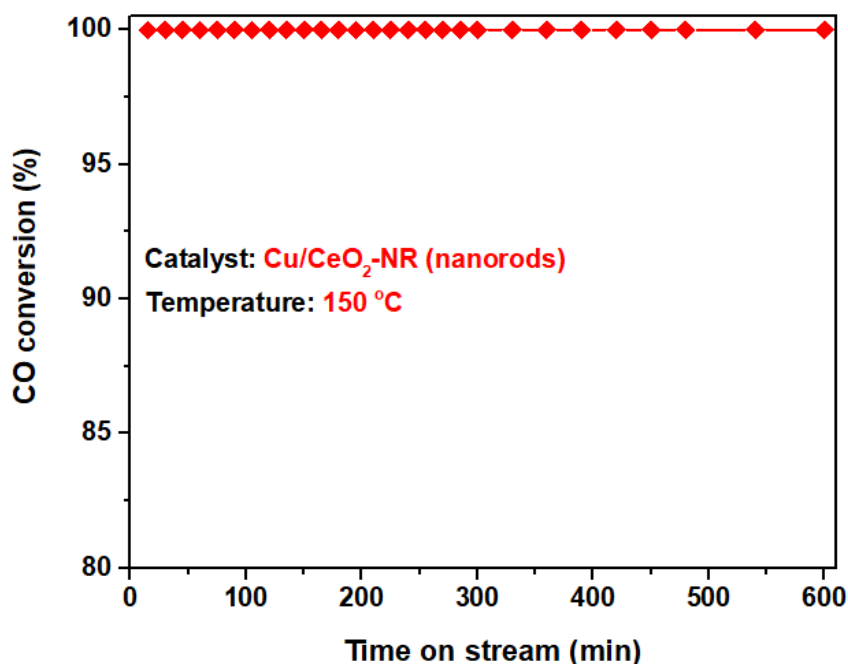


Figure 3.18. Effect of time-on-stream (TOS) on the CO oxidation performance of optimum copper-ceria catalyst of nanorod-shaped morphology. Reaction conditions: 2000 ppm CO, 1 vol.% O₂, GHSV = 39,000 h⁻¹.

Finally, from a practical perspective, the catalytic performance of M/CeO₂-NR samples considerably surpasses the corresponding efficiency of typical precious metal oxidation catalysts, such as Pt/Al₂O₃ (half-conversion temperature of *ca.* 230 °C under similar reaction conditions, Figure 3.19), revealing the effectiveness of shape engineering towards the rational design of cost-efficient noble metal-free catalysts [121].

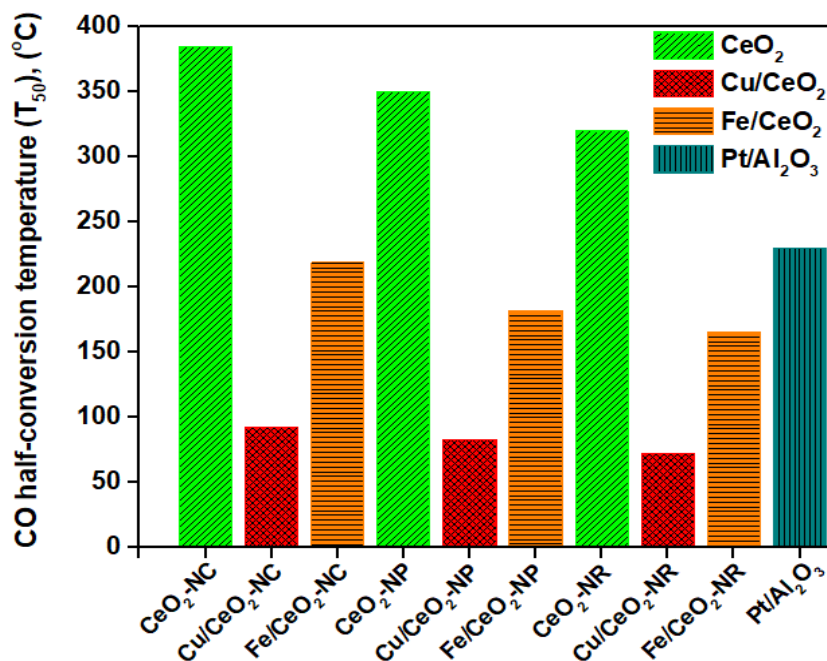


Figure 3.19. Comparison among bare ceria, copper-ceria, iron-ceria and a noble metal catalyst, in terms of half-conversion temperature (T_{50}) for CO oxidation. Reaction conditions: 2000 ppm CO, 1 vol.% O_2 , GHSV = 39,000 h^{-1} .

At this point, the CO oxidation mechanism over ceria-based mixed oxides is thoroughly discussed on the ground of Cu/CeO_2 sample in an attempt to obtain reliable structure-activity relationships. In particular, the present findings can be rationalized on the basis of a Mars-van Krevelen, redox-type mechanism, well-documented in the literature [69,122–126], which mainly involves the following steps, schematically illustrated in Figure 3.20:

- i. chemisorption of CO on Cu^+ active sites towards the formation of $\text{Cu}^+\text{-CO}$ species,
- ii. migration of the chemisorbed CO to the metal-support interface,
- iii. O_2 activation on the oxygen vacancies of CeO_2 and formation of active oxygen (*e.g.*, O_2^-) or lattice oxygen (*e.g.*, O^{2-}) species,
- iv. reaction between the chemisorbed CO at interface and nearby active oxygen and
- v. regeneration of Cu^+ sites and refill of oxygen vacancies by gas phase oxygen involved in consecutive catalytic cycles.

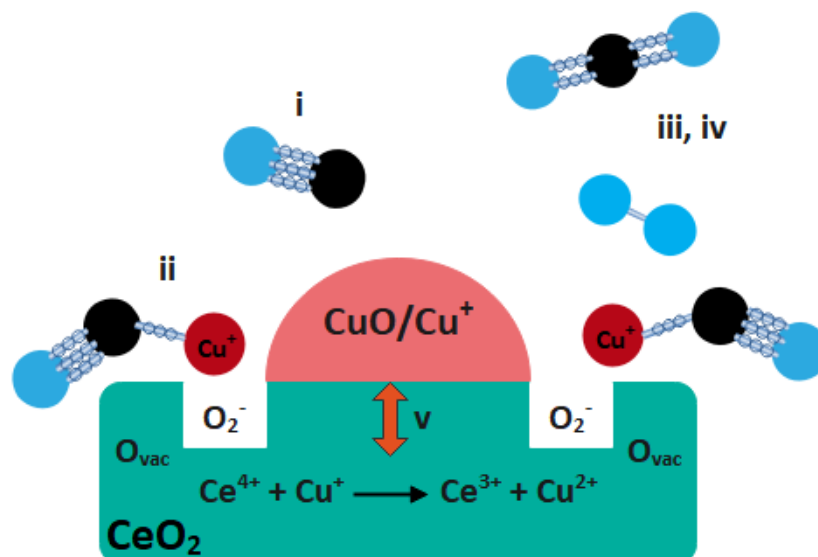


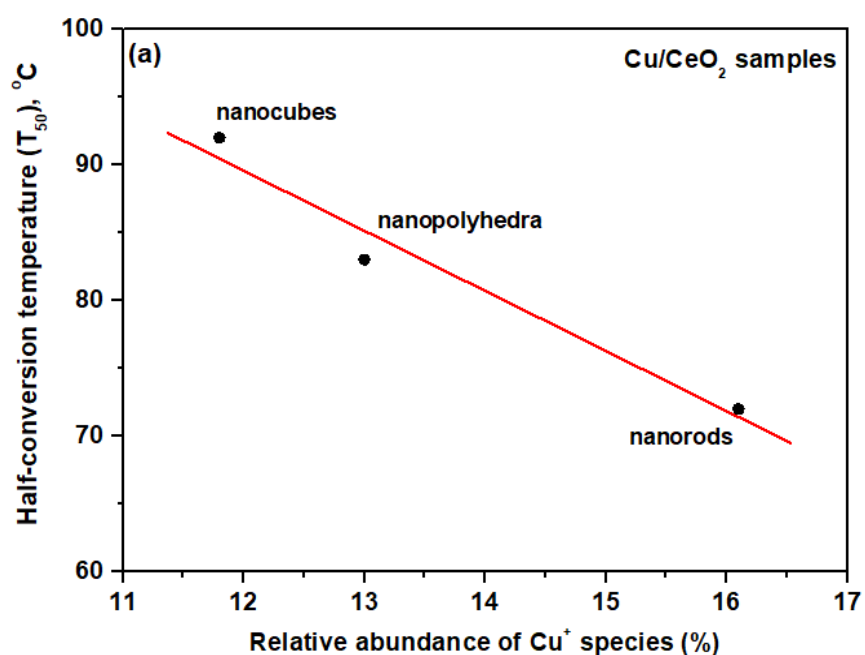
Figure 3.20. Schematic illustration of CO oxidation mechanism on Cu/CeO₂ catalysts. Adapted with permission from Reference [96]. Copyright © 2018, Elsevier.

The above mechanistic scheme clearly reveals the key role played by the redox properties of the support and by its interaction with copper species. In particular, the improved oxygen kinetics/reducibility of ceria carrier facilitates the formation of active oxygen species, whereas the copper-ceria interactions could be considered responsible for the formation of Cu⁺ active species, through the redox equilibrium:



Both factors are crucial towards a high oxidation performance. In view of the above, the superiority of Cu/CeO₂-NR, exposing CeO₂-{100}/{110} facets, can receive a consistent explanation. The improved reducibility and oxygen exchange kinetics of ceria nanorods, linked to their abundance in defects and O vacancies, can be considered as the decisive factors for the enhanced catalytic performance. In a similar manner, the improved CO oxidation performance of Pd supported on ceria nanorods as compared to different ceria morphologies was ascribed to the low oxygen vacancy formation energy, strong reducibility and high surface oxygen mobility [86]. Moreover, the superior carbonate hydrogenation activity of Cu/CeO₂ nanorods as compared to nanocubes and nanoparticles has been attributed to the high reactivity of {110} and {100} planes towards a better balance of defect topology and number of oxygen vacancies followed by Cu⁺ species stabilization, rather than to particle size effects [70].

The establishment of reliable structure-property relationships is crucial towards the way of rational design and fabrication of highly-active composites. In other words, and in relation to the present findings, it is of paramount importance to disclose reliable correlations between key physicochemical parameters and the CO oxidation of M_xO_y/CeO_2 catalysts. In this context, perfect relationships have been obtained between the catalytic performance and the Cu^+ percentage derived by XPS measurements (Figure 3.21a) for Cu/CeO_2 samples, as well as the surface-to-bulk oxygen ratio (O_s/O_b) derived by TPR analysis (Figure 3.21b) for Fe/CeO_2 samples.



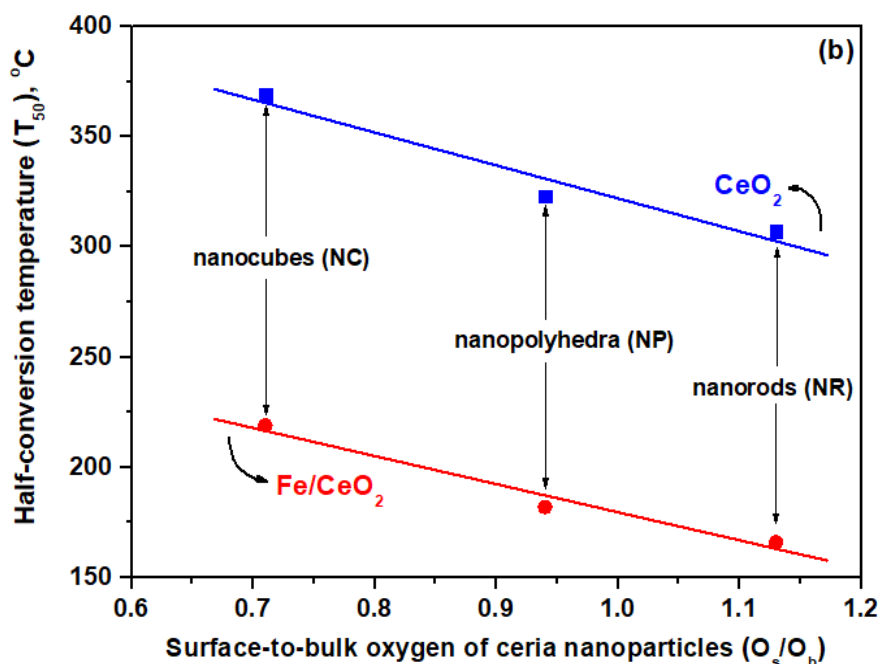


Figure 3.21. (a) Relationship between the half-conversion temperature (T_{50}) and the Cu^+ percentage derived by XPS for Cu/CeO_2 samples. Adapted with permission from Reference [96]. Copyright[©] 2018, Elsevier. (b) Relationship between the half-conversion temperature (T_{50}) and the surface-to-bulk oxygen ratio (O_s/O_b) derived by TPR analysis for Fe/CeO_2 samples. Adapted with permission from Reference [127]. Copyright[©] 2019, MDPI.

Similar structure-property relationships can be obtained by taking into account the CO conversion (%) or CO consumption rate (r_{CO} , $\text{nmol s}^{-1} \text{g}^{-1}$) at differential conditions (GHSV = $39,000 \text{ h}^{-1}$, $X_{\text{CO}} < 25\%$, $T = 60 \text{ }^\circ\text{C}$ for Cu/CeO_2 samples and $X_{\text{CO}} < 15\%$, $T = 125 \text{ }^\circ\text{C}$, GHSV = $40,000 \text{ h}^{-1}$ for Fe/CeO_2 samples), which can rereflect more accurately the impact of reaction conditions and mixed oxides' intrinsic properties on the catalytic performance (Table 3.8). It is evident that the rod-shaped samples exhibit the best catalytic performance (both in terms of conversion and specific activity) as compared to the other two polymorphs, revealing the pivotal role of the exposed crystal planes and the redox characteristics, rather than that of textural characteristics, on the CO oxidation performance.

Table 3.8. Conversion performance and specific activity of Cu/Ceria and Fe/Ceria samples.

Sample	Conversion performance		Specific activity at 60 °C	
	T_{50}^1	X_{CO}^2	r (nmol g ⁻¹ s ⁻¹)	r (nmol m ⁻² s ⁻¹)
Cu/CeO ₂ -NC	92	11	75	188
Cu/CeO ₂ -NP	83	17	116	289
Cu/CeO ₂ -NR	72	25	171	425

Sample	Conversion performance		Specific activity at 125 °C	
	T_{50}	X_{CO}^3	r (nmol g ⁻¹ s ⁻¹)	r (nmol m ⁻² s ⁻¹)
Fe/CeO ₂ -NC	219	2.12	23	0.72
Fe/CeO ₂ -NP	182	3.83	42	0.65
Fe/CeO ₂ -NR	166	11.17	122	1.78

¹ Required temperature for 50% CO conversion; ² CO conversion at 60 °C; ³ CO conversion at 125 °C. Reaction conditions: 2000 ppm CO, 1 vol.% O₂, GHSV = 40,000 h⁻¹.

As a result, perfect relationships between the reaction rate (r_{CO} , mmol s⁻¹ g⁻¹) and the following activity descriptors were disclosed for Cu/CeO₂ samples: (i) population of oxygen vacancies expressed by the $\frac{I_D}{I_{F_{2g}}}$ ratio, and (ii) oxygen storage capacity (OSC), as shown in Figure 3.22. In a similar manner, a relationship between the abundance of structural defects of copper-ceria catalysts and their CO oxidation activity was recently observed [128].

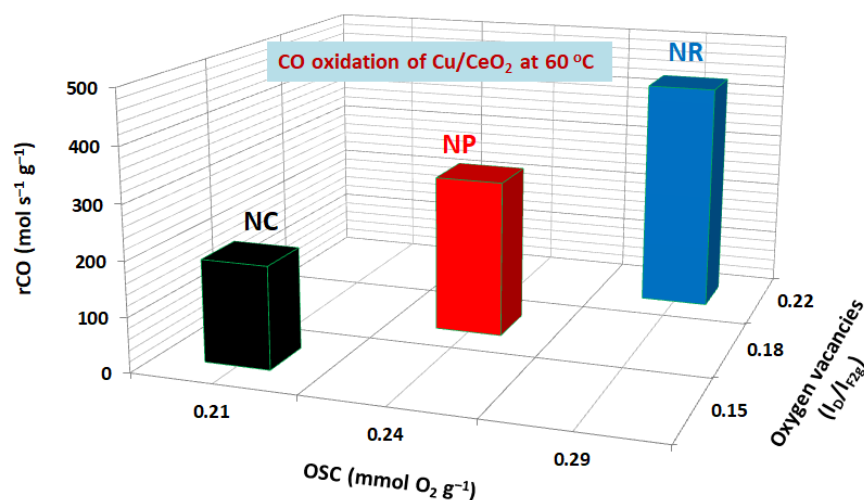


Figure 3.22. Relationship between the CO oxidation performance (r_{CO} , nmol s⁻¹ g⁻¹) of Cu/CeO₂ samples and the oxygen storage capacity (OSC, mmol O₂ g⁻¹) as well as the abundance in oxygen vacancies (in terms of $\frac{I_D}{I_{F_{2g}}}$ ratio) of ceria nanorods (NR), nanopolyhedra (NP) and nanocubes (NC). Adapted with permission from Reference [129]. Copyright© 2021, MDPI.

In order to more closely gain insight into the intrinsic reactivity of iron-ceria samples, the reaction rate under differential conditions was obtained in the form of Arrhenius plots

(Figure 3.23), and the corresponding activation energies (E_a) are summarized in Table 3.9. In relation to the activation energies, the bare nanorod sample ($\text{CeO}_2\text{-NR}$) exhibits the lowest activation energy ($44.2 \text{ kJ}\cdot\text{mol}^{-1}$), followed by nanopolyhedra ($46.7 \text{ kJ}\cdot\text{mol}^{-1}$) and nanocubes ($49.8 \text{ kJ}\cdot\text{mol}^{-1}$), a trend identical to their CO conversion performance. A similar trend is shown for the mixed oxides with $\text{Fe/CeO}_2\text{-NR}$ showing the lowest activation energy among iron-ceria samples, followed by the $\text{Fe/CeO}_2\text{-NP}$ and $\text{Fe/CeO}_2\text{-NC}$ samples. On the other hand, the bare Fe_2O_3 sample exhibits a much higher activation energy (63.3 kJ mol^{-1}), as compared to bare ceria and iron-ceria samples, indicating a higher energy barrier for CO oxidation over Fe_2O_3 . In view of this fact, the higher activation energy of ceria-supported iron samples ($53.5\text{--}58.6 \text{ kJ mol}^{-1}$) as compared to bare ceria ones ($44.2\text{--}49.8 \text{ kJ mol}^{-1}$) can receive a consistent explanation. However, it is worth noticing that iron-ceria catalysts demonstrate the highest activity (Figure 3.23, Table 3.9), despite their higher E_a , implying a more facile reaction path most probably introduced by the iron-ceria interfacial sites. These findings clearly reveal the pivotal role of ceria support morphology in conjunction with iron-ceria interface towards determining the activation energy and in turn the catalytic activity of $\text{Fe}_2\text{O}_3/\text{CeO}_2$ samples.

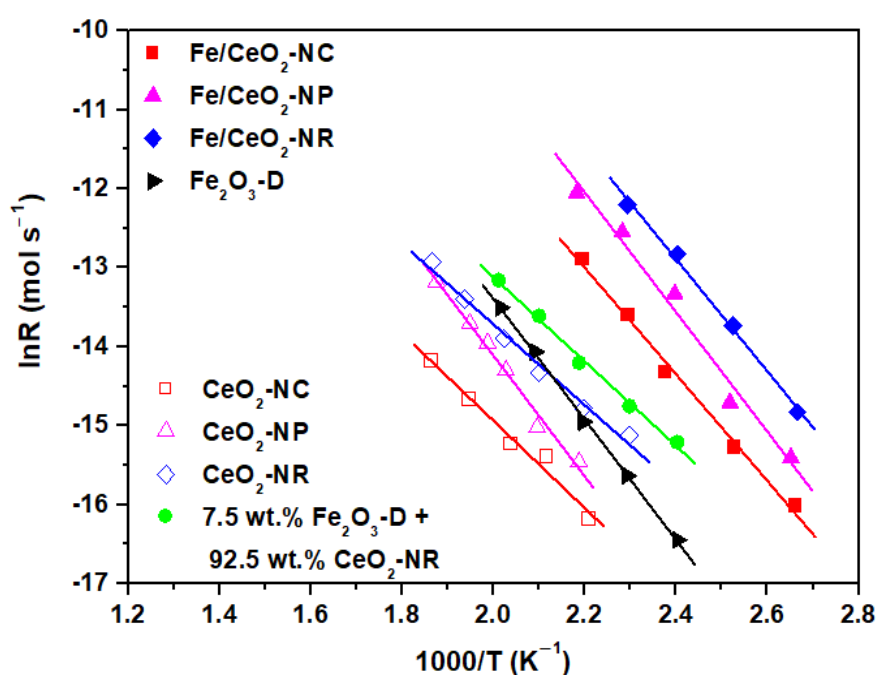


Figure 3.23. Arrhenius plots for CO conversion as a function of temperature for Ceria and Fe/Ceria samples of different morphology (NR, NC and NP, as indicated). Reaction conditions: 2000 ppm CO, 1 vol.% O_2 , GHSV = $40,000 \text{ h}^{-1}$. Adapted with permission from Reference [127]. Copyright © 2019, MDPI.

Table 3.9. Activation Energies (E_a) for the CO oxidation reaction over bare CeO_2 and Fe/CeO_2 samples.

Sample	E_a ($\text{kJ mol}^{-1} \text{K}^{-1}$) (± 0.1)	R^2 (from fitting procedure)
CeO_2 -NR	44.2	0.9943
CeO_2 -NP	46.7	0.9906
CeO_2 -NC	49.8	0.9916
Fe/CeO_2 -NR	53.5	0.9875
Fe/CeO_2 -NP	55.7	0.9853
Fe/CeO_2 -NC	58.6	0.9959
Fe_2O_3 -D	63.3	0.9995
Fe_2O_3 -D + CeO_2 -NR	48.1	0.9983

In summary, the samples with the rod-like morphology exhibit the highest concentration of weakly bound oxygen species which are related to oxygen mobility and the formation of oxygen vacancies. In addition, ceria nanorods seem to facilitate the formation of Cu^+ active species through the $\text{Cu}^{2+}/\text{Cu}^+$ and $\text{Ce}^{4+}/\text{Ce}^{3+}$ redox equilibrium (eq. 3), in agreement with the literature [47].

It is also worth mentioning that the rod-like samples, despite their inferior textural (surface area) and structural (crystallite size) characteristics as compared to polyhedral samples, exhibited the highest catalytic performance. The latter points to the crucial role of exposed facets, rather than structural/textural characteristics, towards the determination of catalytic activity, as previously discussed. However, regarding the iron-ceria samples, the enhanced textural properties (BET surface area and pore volume) of the Fe/CeO_2 -NR sample in comparison with the Fe/CeO_2 -NP and Fe/CeO_2 -NC samples could be further accounted for its enhanced CO conversion performance. Furthermore, it is worth pointing out that the CO oxidation performance follows the same order, namely nanorods > nanopolyhedra > nanocubes, regardless of the active phase used, as the above-mentioned trend was also observed in Cu/CeO_2 nanoparticles of the same morphology, clearly reflecting the key role of support morphology on the catalytic behaviour.

On the other hand, ceria defects and imperfections –linked to its morphology– could affect the particle size and dispersion of active phase, thereby implying the interrelationship between size and shape effects [67]. In addition, the key role of particle size itself on metal-support interactions has been well documented [17]; bonding interactions between metal particles of nanometer size down to single atoms can directly result in strong electronic perturbations (EMSI effect) with great consequences in catalysis. Nevertheless, as the size of the interacting particles increases the role of support is limited to particle's perimeter or interfacial atoms.

In view of the above perspectives, the superior catalytic performance of the rod-shaped samples could be more precisely ascribed to the co-adjustment of interrelated geometric (size) and morphological (shape) characteristics. Nonetheless, the development of model mixed oxides of well-defined morphology and size is a prerequisite in order to gain insight into the distinct role of shape and size.

3.5. CONCLUDING REMARKS

The impact of synthesis parameters on the solid state properties of CeO₂ materials was investigated. CeO₂ prepared by hydrothermal method of high NaOH concentration (CeO₂-NR) demonstrated the optimum CO oxidation performance, with the lowest E_a (43.7 kJ mol⁻¹) among the other ceria samples prepared by precipitation, decomposition and hydrothermal with low NaOH concentration or aging at 180 °C for 24 h. Interestingly, the CO conversion performance of CeO₂-NR sample outperforms notably that of commercial sample, lowering the half-conversion temperature (T₅₀) by ca. 150 °C. The rod-like morphology of CeO₂-NR nanoparticles, with well-defined {100} and {110} reactive planes, favours the enhanced reducibility and lattice oxygen mobility, rendering this material appropriate as catalyst or supporting carrier.

Three nanostructures of ceria with different exposed facets, *i.e.*, nanorods (NR), nanocubes (NC) and nanopolyhedra (NP) were synthesized by the hydrothermal method and employed as supporting carriers for the CuO and Fe₂O₃ phases. Catalytic evaluation studies, employing the CO oxidation as probe reaction, revealed the following activity order: CeO₂-NR > CeO₂-NP > CeO₂-NC. Incorporation of copper or iron to different ceria supports boosts the catalytic performance without, however, affecting the sequence observed for bare ceria. A characterization study by means of complementary *ex situ* and *in situ* characterization techniques was employed to gain insight into the underlying mechanism of observed differences. The results clearly revealed the key role of ceria morphology on the structural defects and oxygen mobility, following the sequence: NR > NP > NC. The superiority of Cu/Ceria samples with the rod-like morphology can be well-rationalized on the basis of a Mars-van Krevelen type of mechanism, involving adsorption of CO on Cu⁺ species and O₂ activation on oxygen vacancies, whereas copper-ceria interactions can facilitate the regeneration of active sites. The Cu/Ceria-NR sample with {100} and {110} reactive planes exhibited the best catalytic performance (T₅₀ = 72 °C) due to its improved surface/redox properties. Notably, a perfect relationship between the catalytic performance and the following parameters was established: i) abundance of loosely bound oxygen species (TPR), ii) relative population of partial reduced Cu⁺/Ce³⁺ redox pairs (XPS/Raman), iii) relative

abundance of defects and O vacancies, as evidenced by the *in situ* Raman results. Despite the inferior textural and structural characteristics of nanorods as compared to polyhedral samples, the former exhibited the highest catalytic performance, revealing the key role of exposed crystal planes.

In a similar manner, iron-ceria nanorods (Fe/CeO₂-NR) exhibited the best catalytic performance ($T_{50} = 166$ °C), attributed mainly to their enhanced reducibility and oxygen kinetics linked to their abundance in loosely bound oxygen species, their highest amount in lattice oxygen and their largest amount of Fe²⁺. Interestingly, significant variations on the reducibility of the binary oxides can be induced by altering ceria's morphology rather than the nature of active phase, implying a different extent of metal-support interactions. The present findings demonstrate that the co-doping of cheap and abundant transition metals (such as iron) on a reducible carrier (such as ceria), along with the rational design of metal/oxides combinations of well-defined size and shape could offer a platform for a wide range of highly active, noble metal-free materials with real life energy and environmental applications.

REFERENCES

1. Paier, J.; Penschke, C.; Sauer, J. Oxygen Defects and Surface Chemistry of Ceria: Quantum Chemical Studies Compared to Experiment. *Chem. Rev.* **2013**, *113*, 3949–3985. doi: 10.1021/cr3004949
2. Montini, T.; Melchionna, M.; Monai, M.; Fornasiero, P. Fundamentals and Catalytic Applications of CeO₂-Based Materials. *Chem. Rev.* **2016**, *116*, 5987–6041. doi: 10.1021/acs.chemrev.5b00603
3. Tang, W.-X.; Gao, P.-X. Nanostructured cerium oxide: preparation, characterization, and application in energy and environmental catalysis. *MRS Commun.* **2016**, *6*, 311–329. doi: 10.1557/mrc.2016.52
4. Zhang, D.; Du, X.; Shi, L.; Gao, R. Shape-controlled synthesis and catalytic application of ceria nanomaterials. *Dalton Trans.* **2012**, *41*, 14455–14475. doi: 10.1039/c2dt31759a
5. Wang, Z.-L.; Li, G.-R.; Ou, Y.-N.; Feng, Z.-P.; Qu, D.-L.; Tong, Y.-X. Electrochemical Deposition of Eu³⁺-Doped CeO₂ Nanobelts with Enhanced Optical Properties. *J. Phys. Chem. C* **2011**, *115*, 351–356. doi: 10.1021/jp1070924
6. Ji, Z.; Wang, X.; Zhang, H.; Lin, S.; Meng, H.; Sun, B.; George, S.; Xia, T.; Nel, A.E.; Zink, J.I. Designed Synthesis of CeO₂ Nanorods and Nanowires for Studying Toxicological Effects of High Aspect Ratio Nanomaterials. *ACS Nano* **2012**, *6*, 5366–5380. doi: 10.1021/nn3012114
7. Kang, Y.; Sun, M.; Li, A. Studies of the Catalytic Oxidation of CO Over Ag/CeO₂ Catalyst. *Catal. Lett.* **2012**, *142*, 1498–1504. doi: 10.1007/s10562-012-0893-2
8. Han, J.; Kim, H.J.; Yoon, S.; Lee, H. Shape effect of ceria in Cu/ceria catalysts for preferential CO oxidation. *J. Mol. Catal. A Chem.* **2011**, *335*, 82–88. doi: 10.1016/j.molcata.2010.11.017
9. Nolan, M. Chapter 6—Surface Effects in the Reactivity of Ceria: A First Principles Perspective. In *Book Catalysis by Materials with Well-Defined Structures*, Wu, Z.; Overbury, S.H., Eds.; Elsevier Inc., 2015; pp. 159–192. ISBN 9780128012178. doi: 10.1016/B978-0-12-801217-8.00006-2
10. Sun, C.; Xue, D. Size-dependent oxygen storage ability of nano-sized ceria. *Phys. Chem. Chem. Phys.* **2013**, *15*, 14414–14419. doi: 10.1039/c3cp51959g
11. Yu, S.-W.; Huang, H.-H.; Tang, C.-W.; Wang, C.-B. The effect of accessible oxygen over Co₃O₄-CeO₂ catalysts on the steam reforming of ethanol. *Int. J. Hydrogen Energy* **2014**, *39*, 20700–20711. doi: 10.1016/j.ijhydene.2014.07.139

12. Melchionna, M.; Fornasiero, P. The role of ceria-based nanostructured materials in energy applications. *Mater. Today* **2014**, *17*, 349–357. doi: 10.1016/j.mattod.2014.05.005
13. Mock, S.A.; Sharp, S.E.; Stoner, T.R.; Radetic, M.J.; Zell, E.T.; Wang, R. CeO₂ nanorods-supported transition metal catalysts for CO oxidation. *J. Colloid Interface Sci.* **2016**, *466*, 261–267. doi: 10.1016/j.jcis.2015.12.026
14. Soler, L.; Casanovas, A.; Urrich, A.; Angurell, I.; Llorca, J. CO oxidation and COPrOx over preformed Au nanoparticles supported over nanoshaped CeO₂. *Appl. Catal. B Environ.* **2016**, *197*, 47–55. doi: 10.1016/j.apcatb.2016.02.025
15. Piumetti, M.; Bensaid, S.; Russo, N.; Fino, D. Nanostructured ceria-based catalysts for soot combustion: Investigations on the surface sensitivity. *Appl. Catal. B Environ.* **2015**, *165*, 742–751. doi: 10.1016/j.apcatb.2014.10.062
16. Vinod, C.P. Surface science as a tool for probing nanocatalysis phenomena. *Catal. Today* **2010**, *154*, 113–117. doi: 10.1016/j.cattod.2010.03.018
17. Konsolakis, M. The role of Copper–Ceria interactions in catalysis science: Recent theoretical and experimental advances. *Appl. Catal. B Environ.* **2016**, *198*, 49–66. doi: 10.1016/j.apcatb.2016.05.037
18. Liu, J.; Zhao, Z.; Wang, J.; Xu, C.; Duan, A.; Jiang, G.; Yang, Q. The highly active catalysts of nanometric CeO₂-supported cobalt oxides for soot combustion. *Appl. Catal. B Environ.* **2008**, *84*, 185–195. doi: 10.1016/j.apcatb.2008.03.017
19. Tok, A.I.Y.; Boey, F.Y.C.; Dong, Z.; Sun, X.L. Hydrothermal synthesis of CeO₂ nanoparticles. *J. Mater. Process. Technol.* **2007**, *190*, 217–222. doi: 10.1016/j.jmatprotec.2007.02.042
20. Ilgaz Soykal, I.; Sohn, H.; Miller, J.T.; Ozkan, U.S. Investigation of the Reduction/Oxidation Behavior of Cobalt Supported on Nano-ceria. *Top. Catal.* **2014**, *57*, 785–795. doi: 10.1007/s11244-013-0235-7
21. Yin, L.; Wang, Y.; Pang, G.; Kolytyn, Y.; Gedanken, A. Sonochemical Synthesis of Cerium Oxide Nanoparticles—Effect of Additives and Quantum Size Effect. *J. Colloid Interface Sci.* **2002**, *246*, 78–84. doi: 10.1006/jcis.2001.8047
22. Gu, F.; Wang, Z.; Han, D.; Shi, C.; Guo, G. Reverse micelles directed synthesis of mesoporous ceria nanostructures. *Mater. Sci. Eng. B* **2007**, *139*, 62–68. doi: 10.1016/j.mseb.2007.01.051
23. Piumetti, M.; Andana, T.; Bensaid, S.; Russo, N.; Fino, D.; Pirone, R. Study on the CO Oxidation over Ceria-Based Nanocatalysts. *Nanoscale Res. Lett.* **2016**, *11*, 165. doi:

- 10.1186/s11671-016-1375-z
24. Lu, X.; Zheng, D.; Gan, J.; Liu, Z.; Liang, C.; Liu, P.; Tong, Y. Porous CeO₂ nanowires/nanowire arrays: electrochemical synthesis and application in water treatment. *J. Mater. Chem.* **2010**, *20*, 7118–7122. doi: 10.1039/c0jm00487a
 25. Kovacevic, M.; Mojet, B.L.; Van Ommen, J.G.; Lefferts, L. Effects of Morphology of Cerium Oxide Catalysts for Reverse Water Gas Shift Reaction. *Catal. Lett.* **2016**, *146*, 770–777. doi: 10.1007/s10562-016-1697-6
 26. López, J.M.; Gilbank, A.L.; García, T.; Solsona, B.; Agouram, S.; Torrente-Murciano, L. The prevalence of surface oxygen vacancies over the mobility of bulk oxygen in nanostructured ceria for the total toluene oxidation. *Appl. Catal. B Environ.* **2015**, *174–175*, 403–412. doi: 10.1016/j.apcatb.2015.03.017
 27. Wu, Z.; Li, M.; Howe, J.; Meyer III, H.M.; Overbury, S.H. Probing Defect Sites on CeO₂ Nanocrystals with Well-Defined Surface Planes by Raman Spectroscopy and O₂ Adsorption. *Langmuir* **2010**, *26*, 16595–16606. doi: 10.1021/la101723w
 28. He, H.; Yang, P.; Li, J.; Shi, R.; Chen, L.; Zhang, A.; Zhu, Y. Controllable synthesis, characterization, and CO oxidation activity of CeO₂ nanostructures with various morphologies. *Ceram. Int.* **2016**, *42*, 7810–7818. doi: 10.1016/j.ceramint.2016.02.005
 29. Liu, J.; Li, Y.; Zhang, J.; He, D. Glycerol carbonylation with CO₂ to glycerol carbonate over CeO₂ catalyst and the influence of CeO₂ preparation methods and reaction parameters. *Appl. Catal. A Gen.* **2016**, *513*, 9–18. doi: 10.1016/j.apcata.2015.12.030
 30. Makinose, Y.; Taniguchi, T.; Katsumata, K.; Okada, K.; Matsushita, N. Facet control of ceria nanocrystals synthesized by an oleate-modified hydrothermal method. *Adv. Powder Technol.* **2016**, *27*, 64–71. doi: 10.1016/j.appt.2015.10.004
 31. Monte, M.; Munuera, G.; Costa, D.; Conesa, J.C.; Martínez-Arias, A. Near-ambient XPS characterization of interfacial copper species in ceria-supported copper catalysts. *Phys. Chem. Chem. Phys.* **2015**, *17*, 29995–30004. doi: 10.1039/c5cp04354a
 32. Sayle, T.X.T.; Caddeo, F.; Zhang, X.; Sakthivel, T.; Das, S.; Seal, S.; Ptasinska, S.; Sayle, D.C. Structure-Activity Map of Ceria Nanoparticles, Nanocubes, and Mesoporous Architectures. *Chem. Mater.* **2016**, *28*, 7287–7295. doi: 10.1021/acs.chemmater.6b02536
 33. Yao, X.; Gao, F.; Yu, Q.; Qi, L.; Tang, C.; Dong, L.; Chen, Y. NO reduction by CO over CuO–CeO₂ catalysts: effect of preparation methods. *Catal. Sci. Technol.* **2013**, *3*, 1355–1366. doi: 10.1039/c3cy20805b
 34. Qiao, Z.-A.; Wu, Z.; Dai, S. Shape-Controlled Ceria-based Nanostructures for Catalysis

- Applications. *ChemSusChem* **2013**, *6*, 1821–1833. doi: 10.1002/cssc.201300428
35. Matte, L.P.; Kilian, A.S.; Luza, L.; Alves, M.C.M.; Morais, J.; Baptista, D.L.; Dupont, J.; Bernardi, F. Influence of the CeO₂ Support on the Reduction Properties of Cu/CeO₂ and Ni/CeO₂ Nanoparticles. *J. Phys. Chem. C* **2015**, *119*, 26459–26470. doi: 10.1021/acs.jpcc.5b07654
36. Zabilskiy, M.; Djinočić, P.; Tchernychova, E.; Pintar, A. N₂O decomposition over CuO/CeO₂ catalyst: New insights into reaction mechanism and inhibiting action of H₂O and NO by operando techniques. *Appl. Catal. B Environ.* **2016**, *197*, 146–158. doi: 10.1016/j.apcatb.2016.02.024
37. Zabilskiy, M.; Djinočić, P.; Tchernychova, E.; Tkachenko, O.P.; Kustov, L.M.; Pintar, A. Nanoshaped CuO/CeO₂ Materials: Effect of the Exposed Ceria Surfaces on Catalytic Activity in N₂O Decomposition Reaction. *ACS Catal.* **2015**, *5*, 5357–5365. doi: 10.1021/acscatal.5b01044
38. Singha, R.K.; Shukla, A.; Yadav, A.; Sivakumar Konathala, L.N.; Bal, R. Effect of metal-support interaction on activity and stability of Ni-CeO₂ catalyst for partial oxidation of methane. *Appl. Catal. B Environ.* **2017**, *202*, 473–488. doi: 10.1016/j.apcatb.2016.09.060
39. Mukherjee, D.; Reddy, B.M. Noble metal-free CeO₂-based mixed oxides for CO and soot oxidation. *Catal. Today* **2018**, *309*, 227–235. doi: 10.1016/j.cattod.2017.06.017
40. Cargnello, M.; Doan-Nguyen, V.V.T.; Gordon, T.R.; Diaz, R.E.; Stach, E.A.; Gorte, R.J.; Fornasiero, P.; Murray, C.B. Control of Metal Nanocrystal Size Reveals Metal-Support Interface Role for Ceria Catalysts. *Science* **2013**, *341*, 771–773. doi: 10.1126/science.1240148
41. Vilé, G.; Colussi, S.; Krumeich, F.; Trovarelli, A.; Pérez-Ramírez, J. Opposite Face Sensitivity of CeO₂ in Hydrogenation and Oxidation Catalysis. *Angew. Chem. Int. Ed.* **2014**, *53*, 12069–12072. doi: 10.1002/anie.201406637
42. Mudiyansele, K.; Senanayake, S.D.; Feria, L.; Kundu, S.; Baber, A.E.; Graciani, J.; Vidal, A.B.; Agnoli, S.; Evans, J.; Chang, R.; Axnanda, S.; Liu, Z.; Sanz, J.F.; Liu, P.; Rodriguez, J.A.; Stacchiola, D.J. Importance of the Metal–Oxide Interface in Catalysis: In Situ Studies of the Water–Gas Shift Reaction by Ambient-Pressure X-ray Photoelectron Spectroscopy. *Angew. Chem. Int. Ed.* **2013**, *52*, 5101–5105. doi: 10.1002/anie.201210077
43. Trovarelli, A.; Llorca, J. Ceria Catalysts at Nanoscale: How Do Crystal Shapes Shape Catalysis? *ACS Catal.* **2017**, *7*, 4716–4735. doi: 10.1021/acscatal.7b01246

44. Wu, K.; Sun, L.-D.; Yan, C.-H. Recent Progress in Well-Controlled Synthesis of Ceria-Based Nanocatalysts towards Enhanced Catalytic Performance. *Adv. Energy Mater.* **2016**, *6*, 1600501. doi: 10.1002/aenm.201600501
45. Liu, L.; Yao, Z.; Deng, Y.; Gao, F.; Liu, B.; Dong, L. Morphology and Crystal-Plane Effects of Nanoscale Ceria on the Activity of CuO/CeO₂ for NO Reduction by CO. *ChemCatChem* **2011**, *3*, 978–989. doi: 10.1002/cctc.201000320
46. Ouyang, B.; Tan, W.; Liu, B. Morphology effect of nanostructure ceria on the Cu/CeO₂ catalysts for synthesis of methanol from CO₂ hydrogenation. *Catal. Commun.* **2017**, *95*, 36–39. doi: 10.1016/j.catcom.2017.03.005
47. Ren, Z.; Peng, F.; Li, J.; Liang, X.; Chen, B. Morphology-Dependent Properties of Cu/CeO₂ Catalysts for the Water-Gas Shift Reaction. *Catalysts* **2017**, *7*, 48. doi: 10.3390/catal7020048
48. Piumetti, M.; Van der Linden, B.; Makkee, M.; Miceli, P.; Fino, D.; Russo, N.; Bensaid, S. Contact dynamics for a solid-solid reaction mediated by gas-phase oxygen: Study on the soot oxidation over ceria-based catalysts. *Appl. Catal. B Environ.* **2016**, *199*, 96–107. doi: 10.1016/j.apcatb.2016.06.006
49. Aneggi, E.; Wiaterski, D.; De Leitenburg, C.; Llorca, J.; Trovarelli, A. Shape-Dependent Activity of Ceria in Soot Combustion. *ACS Catal.* **2014**, *4*, 172–181. doi: 10.1021/cs400850r
50. Vayssilov, G.N.; Lykhach, Y.; Migani, A.; Staudt, T.; Petrova, G.P.; Tsud, N.; Skála, T.; Bruix, A.; Illas, F.; Prince, K.C.; Matolín, V.; Neyman, K.M.; Libuda, J. Support nanostructure boosts oxygen transfer to catalytically active platinum nanoparticles. *Nat. Mater.* **2011**, *10*, 310–315. doi: 10.1038/nmat2976
51. Qiu, N.; Zhang, J.; Wu, Z. Peculiar surface-interface properties of nanocrystalline ceria-cobalt oxides with enhanced oxygen storage capacity. *Phys. Chem. Chem. Phys.* **2014**, *16*, 22659–22664. doi: 10.1039/c4cp03390f
52. Konsolakis, M.; Carabineiro, S.A.C.; Papista, E.; Marnellos, G.E.; Tavares, P.B.; Agostinho Moreira, J.; Romaguera-Barcelay, Y.; Figueiredo, J.L. Effect of preparation method on the solid state properties and the deN₂O performance of CuO-CeO₂ oxides. *Catal. Sci. Technol.* **2015**, *5*, 3714–3727. doi: 10.1039/c5cy00343a
53. Pan, C.-J.; Tsai, M.-C.; Su, W.-N.; Rick, J.; Akalework, N.G.; Agegnehu, A.K.; Cheng, S.-Y.; Hwang, B.-J. Tuning/exploiting Strong Metal-Support Interaction (SMSI) in Heterogeneous Catalysis. *J. Taiwan Inst. Chem. Eng.* **2017**, *74*, 154–186. doi: 10.1016/j.jtice.2017.02.012

54. Zhu, X.; Du, Y.; Wang, H.; Wei, Y.; Li, K.; Sun, L. Chemical interaction of Ce-Fe mixed oxides for methane selective oxidation. *J. Rare Earths* **2014**, *32*, 824–830. doi: 10.1016/S1002-0721(14)60148-4
55. Bao, H.; Chen, X.; Fang, J.; Jiang, Z.; Huang, W. Structure-activity Relation of Fe₂O₃–CeO₂ Composite Catalysts in CO Oxidation. *Catal. Lett.* **2008**, *125*, 160–167. doi: 10.1007/s10562-008-9540-3
56. Wang, W.; Li, W.; Guo, R.; Chen, Q.; Wang, Q.; Pan, W.; Hu, G. A CeFeO_x catalyst for catalytic oxidation of NO to NO₂. *J. Rare Earths* **2016**, *34*, 876–881. doi: 10.1016/S1002-0721(16)60109-6
57. Tan, L.; Tao, Q.; Gao, H.; Li, J.; Jia, D.; Yang, M. Preparation and catalytic performance of mesoporous ceria-base composites CuO/CeO₂, Fe₂O₃/CeO₂ and La₂O₃/CeO₂. *J. Porous Mater.* **2017**, *24*, 795–803. doi: 10.1007/s10934-016-0318-5
58. Massa, P.; Dafinov, A.; Cabello, F.M.; Fenoglio, R. Catalytic wet peroxide oxidation of phenolic solutions over Fe₂O₃/CeO₂ and WO₃/CeO₂ catalyst systems. *Catal. Commun.* **2008**, *9*, 1533–1538. doi: 10.1016/j.catcom.2007.12.025
59. Han, J.; Meeprasert, J.; Maitarad, P.; Nammuangruk, S.; Shi, L.; Zhang, D. Investigation of the Facet-Dependent Catalytic Performance of Fe₂O₃/CeO₂ for the Selective Catalytic Reduction of NO with NH₃. *J. Phys. Chem. C* **2016**, *120*, 1523–1533. doi: 10.1021/acs.jpcc.5b09834
60. Prieto-Centurion, D.; Eaton, T.R.; Roberts, C.A.; Fanson, P.T.; Notestein, J.M. Catalytic reduction of NO with H₂ over redox-cycling Fe on CeO₂. *Appl. Catal. B Environ.* **2015**, *168–169*, 68–76. doi: 10.1016/j.apcatb.2014.11.055
61. Nadar, A.; Banerjee, A.M.; Pai, M.R.; Pai, R.V.; Meena, S.S.; Tewari, R.; Tripathi, A.K. Catalytic properties of dispersed iron oxides Fe₂O₃/MO₂ (M = Zr, Ce, Ti and Si) for sulfuric acid decomposition reaction: Role of support. *Int. J. Hydrogen Energy* **2018**, *43*, 37–52. doi: 10.1016/j.ijhydene.2017.10.163
62. Perez-Alonso, F.J.; Melián-Cabrera, I.; López Granados, M.; Kapteijn, F.; Fierro, J.L.G. Synergy of Fe_xCe_{1-x}O₂ mixed oxides for N₂O decomposition. *J. Catal.* **2006**, *239*, 340–346. doi: 10.1016/j.jcat.2006.02.008
63. Shen, Q.; Lu, G.; Du, C.; Guo, Y.; Wang, Y.; Guo, Y.; Gong, X. Role and reduction of NO_x in the catalytic combustion of soot over iron-ceria mixed oxide catalyst. *Chem. Eng. J.* **2013**, *218*, 164–172. doi: 10.1016/j.cej.2012.12.010
64. Sudarsanam, P.; Hillary, B.; Amin, M.H.; Rockstroh, N.; Bentrup, U.; Brückner, A.; Bhargava, S.K. Heterostructured Copper-Ceria and Iron-Ceria Nanorods: Role of

- Morphology, Redox, and Acid Properties in Catalytic Diesel Soot Combustion. *Langmuir* **2018**, *34*, 2663–2673. doi: 10.1021/acs.langmuir.7b03998
65. Dong, L.; Yao, X.; Chen, Y. Interactions among supported copper-based catalyst components and their effects on performance: A review. *Chinese J. Catal.* **2013**, *34*, 851–864. doi: 10.1016/S1872-2067(12)60592-0
66. Xanthopoulou, G.G.; Novikov, V.A.; Knysh, Yu.A.; Amosov, A.P. Nanocatalysts for Low-Temperature Oxidation of CO: Review. *Eurasian Chem.-Technol. J.* **2015**, *17*, 17–31. doi: 10.18321/ectj190
67. Yao, S.Y.; Xu, W.Q.; Johnston-Peck, A.C.; Zhao, F.Z.; Liu, Z.Y.; Luo, S.; Senanayake, S.D.; Martínez-Arias, A.; Liu, W.J.; Rodriguez, J.A. Morphological effects of the nanostructured ceria support on the activity and stability of CuO/CeO₂ catalysts for the water-gas shift reaction. *Phys. Chem. Chem. Phys.* **2014**, *16*, 17183–17195. doi: 10.1039/c4cp02276a
68. Maciel, C.G.; Silva, T.D.F.; Hirooka, M.I.; Belgacem, M.N.; Assaf, J.M. Effect of nature of ceria support in CuO/CeO₂ catalyst for PROX-CO reaction. *Fuel* **2012**, *97*, 245–252. doi: 10.1016/j.fuel.2012.02.004
69. Wang, W.-W.; Yu, W.-Z.; Du, P.-P.; Xu, H.; Jin, Z.; Si, R.; Ma, C.; Shi, S.; Jia, C.-J.; Yan, C.-H. Crystal Plane Effect of Ceria on Supported Copper Oxide Cluster Catalyst for CO Oxidation: Importance of Metal-Support Interaction. *ACS Catal.* **2017**, *7*, 1313–1329. doi: 10.1021/acscatal.6b03234
70. Cui, Y.; Dai, W.-L. Support morphology and crystal plane effect of Cu/CeO₂ nanomaterial on the physicochemical and catalytic properties for carbonate hydrogenation. *Catal. Sci. Technol.* **2016**, *6*, 7752–7762. doi: 10.1039/c6cy01575a
71. Araiza, D.G.; Gómez-Cortés, A.; Díaz, G. Partial oxidation of methanol over copper supported on nanoshaped ceria for hydrogen production. *Catal. Today* **2017**, *282*, 185–194. doi: 10.1016/j.cattod.2016.06.055
72. Rao, R.; Yang, M.; Li, C.; Dong, H.; Fang, S.; Zhang, A. A facile synthesis for hierarchical porous CeO₂ nanobundles and their superior catalytic performance for CO oxidation. *J. Mater. Chem. A* **2015**, *3*, 782–788. doi: 10.1039/C4TA03875D
73. Wu, Z.; Li, M.; Overbury, S.H. On the structure dependence of CO oxidation over CeO₂ nanocrystals with well-defined surface planes. *J. Catal.* **2012**, *285*, 61–73. doi: 10.1016/j.jcat.2011.09.011
74. Dziembaj, R.; Zaitz, M.M.; Rutkowska, M.; Molenda, M.; Chmielarz, L. Nanostructured Co-Ce-O systems for catalytic decomposition of N₂O. *Catal. Today* **2012**, *191*, 121–

124. doi: 10.1016/j.cattod.2012.02.045
75. Walter, L.M.; Morse, J.W. Reactive surface area of skeletal carbonates during dissolution: effect of grain size. *J. Sediment. Research.* **1984**, *54*, 1081–1090. doi: 10.1306/212F8562-2B24-11D7-8648000102C1865D
76. Lykaki, M.; Pachatouridou, E.; Iliopoulou, E.; Carabineiro, S.A.C.; Konsolakis, M. Impact of the synthesis parameters on the solid state properties and the CO oxidation performance of ceria nanoparticles. *RSC Adv.* **2017**, *7*, 6160–6169. doi: 10.1039/c6ra26712b
77. Fu, Y.-P.; Wen, S.-B.; Lu, C.-H. *Progress in Nanotechnology: Applications*, The American Ceramics Society, John Wiley & Sons, 2010, pp. 197–203. ISBN 978-0-470-40840-7
78. Teleki, A.; Wengeler, R.; Wengeler, L.; Nirschl, H.; Pratsinis, S.E. Distinguishing between aggregates and agglomerates of flame-made TiO₂ by high-pressure dispersion. *Powder Technol.* **2008**, *181*, 292–300. doi: 10.1016/j.powtec.2007.05.016
79. Allwar, A.; Md Noor, A.; Nawil, M. Textural Characteristics of Activated Carbons Prepared from Oil Palm Shells Activated with ZnCl₂ and Pyrolysis Under Nitrogen and Carbon Dioxide. *J. Phys. Sci.* **2008**, *19*, 93–104.
80. Anushree; Kumar, S.; Sharma, C. Synthesis, characterization and catalytic wet air oxidation property of mesoporous Ce_{1-x}Fe_xO₂ mixed oxides. *Mater. Chem. Phys.* **2015**, *155*, 223–231. doi: 10.1016/j.matchemphys.2015.02.034
81. Trens, P.; Stathopoulos, V.; Hudson, M.J.; Pomonis, P. Synthesis and characterization of packed mesoporous tungsteno-silicates: application to the catalytic dehydrogenation of 2-propanol. *Appl. Catal. A Gen.* **2004**, *263*, 103–108. doi: 10.1016/j.apcata.2003.12.004
82. Farahmandjou, M.; Zarinkamar, M. Synthesis of nano-sized ceria (CeO₂) particles via a cerium hydroxy carbonate precursor and the effect of reaction temperature on particle morphology. *J. Ultrafine Grained Nanostructured Mater.* **2015**, *48*, 5–10. doi: 10.7508/JUFGNSM.2015.01.002
83. Xu, J.; Harmer, J.; Li, G.; Chapman, T.; Collier, P.; Longworth, S.; Tsang, S.C. Size dependent oxygen buffering capacity of ceria nanocrystals. *Chem. Commun.* **2010**, *46*, 1887–1889. doi: 10.1039/b923780a
84. Luo, J.-Y.; Meng, M.; Li, X.; Li, X.-G.; Zha, Y.-Q.; Hu, T.-D.; Xie, Y.-N.; Zhang, J. Mesoporous Co₃O₄-CeO₂ and Pd/Co₃O₄-CeO₂ catalysts: Synthesis, characterization and mechanistic study of their catalytic properties for low-temperature CO oxidation. *J. Catal.* **2008**, *254*, 310–324. doi: 10.1016/j.jcat.2008.01.007

85. Capdevila-Cortada, M.; Vilé, G.; Teschner, D.; Pérez-Ramírez, J.; López, N. Reactivity descriptors for ceria in catalysis. *Appl. Catal. B Environ.* **2016**, *197*, 299–312. doi: 10.1016/j.apcatb.2016.02.035
86. Hu, Z.; Liu, X.; Meng, D.; Guo, Y.; Guo, Y.; Lu, G. Effect of Ceria Crystal Plane on the Physicochemical and Catalytic Properties of Pd/Ceria for CO and Propane Oxidation. *ACS Catal.* **2016**, *6*, 2265–2279. doi: 10.1021/acscatal.5b02617
87. Mukherjee, D.; Rao, B.G.; Reddy, B.M. CO and soot oxidation activity of doped ceria: Influence of dopants. *Appl. Catal. B Environ.* **2016**, *197*, 105–115. doi: 10.1016/j.apcatb.2016.03.042
88. Jin, H.; You, R.; Zhou, S.; Ma, K.; Meng, M.; Zheng, L.; Zhang, J.; Hu, T. In-situ DRIFTS and XANES identification of copper species in the ternary composite oxide catalysts CuMnCeO during CO preferential oxidation. *Int. J. Hydrogen Energy* **2015**, *40*, 3919–3931. doi: 10.1016/j.ijhydene.2015.01.086
89. Konsolakis, M.; Ioakimidis, Z.; Kraia, Tz.; Marnellos, G.E. Hydrogen Production by Ethanol Steam Reforming (ESR) over CeO₂ Supported Transition Metal (Fe, Co, Ni, Cu) Catalysts: Insight into the Structure-Activity Relationship. *Catalysts* **2016**, *6*, 39. doi: 10.3390/catal6030039
90. Carabineiro, S.A.C.; Konsolakis, M.; Marnellos, G.E.-N.; Asad, M.F.; Soares, O.S.G.P.; Tavares, P.B.; Pereira, M.F.R.; De Melo Órfão, J.J.; Figueiredo, J.L. Ethyl Acetate Abatement on Copper Catalysts Supported on Ceria Doped with Rare Earth Oxides. *Molecules* **2016**, *21*, 644. doi: 10.3390/molecules21050644
91. Soler, L.; Casanovas, A.; Escudero, C.; Pérez-Dieste, V.; Aneggi, E.; Trovarelli, A.; Llorca, J. Ambient Pressure Photoemission Spectroscopy Reveals the Mechanism of Carbon Soot Oxidation in Ceria-Based Catalysts. *ChemCatChem* **2016**, *8*, 2748–2751. doi: 10.1002/cctc.201600615
92. Li, G.; Wu, B.; Li, L. Surface-structure effect of nano-crystalline CeO₂ support on low temperature CO oxidation. *J. Mol. Catal. A Chem.* **2016**, *424*, 304–310. doi: 10.1016/j.molcata.2016.08.035
93. Andriopoulou, C.; Trimpalis, A.; Petalidou, K.C.; Sgoura, A.; Efstathiou, A.M.; Boghosian, S. Structural and Redox Properties of Ce_{1-x}Zr_xO_{2-δ} and Ce_{0.8}Zr_{0.15}RE_{0.05}O_{2-δ} (RE: La, Nd, Pr, Y) Solids Studied by High Temperature *in Situ* Raman Spectroscopy. *J. Phys. Chem. C* **2017**, *121*, 7931–7943. doi: 10.1021/acs.jpcc.7b00515
94. Ilieva, L.; Petrova, P.; Pantaleo, G.; Zanella, R.; Liotta, L.F.; Georgiev, V.; Boghosian, S.; Kaszkar, Z.; Sobczak, J.W.; Lisowski, W.; Venezia, A.M.; Tabakova, T. Gold catalysts

- supported on Y-modified ceria for CO-free hydrogen production *via* PROX. *Appl. Catal. B Environ.* **2016**, *188*, 154–168. doi: 10.1016/j.apcatb.2016.02.004
95. Mamontov, E.; Egami, T.; Brezny, R.; Koranne, M.; Tyagi, S. Lattice Defects and Oxygen Storage Capacity of Nanocrystalline Ceria and Ceria-Zirconia. *J. Phys. Chem. B* **2000**, *104*, 11110–11116. doi: 10.1021/jp0023011
96. Lykaki, M.; Pachatouridou, E.; Carabineiro, S.A.C.; Iliopoulou, E.; Andriopoulou, C.; Kallithrakas-Kontos, N.; Boghosian, S.; Konsolakis, M. Ceria nanoparticles shape effects on the structural defects and surface chemistry: Implications in CO oxidation by Cu/CeO₂ catalysts. *Appl. Catal. B Environ.* **2018**, *230*, 18–28. doi: 10.1016/j.apcatb.2018.02.035
97. Stefa, S. Rational Design and Development of Nanostructured Non-Precious Metal Oxide Catalysts for Energy and Environmental Applications. PhD Thesis, *in progress*.
98. Zhu, P.; Liu, M.; Zhou, R. Effect of interaction between CuO and CeO₂ on the performance of CuO-CeO₂ catalysts for selective oxidation of CO in H₂-rich streams. *Indian J. Chem.* **2012**, *51A*, 1529–1537.
99. Jampa, S.; Wangkawe, K.; Tantisriyanurak, S.; Changpradit, J.; Jamieson, A.M.; Chaisuwan, T.; Luengnaruemitchai, A.; Wongkasemjit, S. High performance and stability of copper loading on mesoporous ceria catalyst for preferential oxidation of CO in presence of excess of hydrogen. *Int. J. Hydrogen Energy* **2017**, *42*, 5537–5548. doi: 10.1016/j.ijhydene.2016.08.078
100. Aboukaïs, A.; Skaf, M.; Hany, S.; Cousin, R.; Aouad, S.; Labaki, M.; Abi-Aad, E. A comparative study of Cu, Ag and Au doped CeO₂ in the total oxidation of volatile organic compounds (VOCs). *Mater. Chem. Phys.* **2016**, *177*, 570–576. doi: 10.1016/j.matchemphys.2016.04.072
101. Zhu, P.; Li, J.; Huang, Q.; Yan, S.; Liu, M.; Zhou, R. High performance CuO-CeO₂ catalysts for selective oxidation of CO in excess hydrogen: Effect of hydrothermal preparation conditions. *J. Nat. Gas Chem.* **2009**, *18*, 346–353. doi: 10.1016/S1003-9953(08)60119-X
102. Guo, X.; Zhou, R. A new insight into the morphology effect of ceria on CuO/CeO₂ catalysts for CO selective oxidation in hydrogen-rich gas. *Catal. Sci. Technol.* **2016**, *6*, 3862–3871. doi: 10.1039/c5cy01816a
103. Sundar, R.S.; Deevi, S. CO oxidation activity of Cu-CeO₂ nano-composite catalysts prepared by laser vaporization and controlled condensation. *J. Nanoparticle Res.* **2006**, *8*, 497–509. doi: 10.1007/s11051-005-9030-0

104. Acerbi, N.; Tsang, S.C.; Golunski, S.; Collier, P. A practical demonstration of electronic promotion in the reduction of ceria coated PGM catalysts. *Chem. Commun.* **2008**, 1578–1580. doi: 10.1039/b718956g
105. Wang, C.; Cheng, Q.; Wang, X.; Ma, K.; Bai, X.; Tan, S.; Tian, Y.; Ding, T.; Zheng, L.; Zhang, J.; Li, X. Enhanced catalytic performance for CO preferential oxidation over CuO catalysts supported on highly defective CeO₂ nanocrystals. *Appl. Surf. Sci.* **2017**, 422, 932–943. doi: 10.1016/j.apsusc.2017.06.017
106. Wang, J.; Zhong, L.; Lu, J.; Chen, R.; Lei, Y.; Chen, K.; Han, C.; He, S.; Wan, G.; Luo, Y. A solvent-free method to rapidly synthesize CuO-CeO₂ catalysts to enhance their CO preferential oxidation: Effects of Cu loading and calcination temperature. *Mol. Catal.* **2017**, 443, 241–252. doi: 10.1016/j.mcat.2017.10.012
107. Konsolakis, M.; Carabineiro, S.A.C.; Marnellos, G.E.; Asad, M.F.; Soares, O.S.G.P.; Pereira, M.F.R.; Órfão, J.J.M.; Figueiredo, J.L. Effect of cobalt loading on the solid state properties and ethyl acetate oxidation performance of cobalt-cerium mixed oxides. *J. Colloid Interface Sci.* **2017**, 496, 141–149. doi: 10.1016/j.jcis.2017.02.014
108. Carabineiro, S.A.C.; Bastos, S.S.T.; Órfão, J.J.M.; Pereira, M.F.R.; Delgado, J.J.; Figueiredo, J.L. Exotemplated ceria catalysts with gold for CO oxidation. *Appl. Catal. A Gen.* **2010**, 381, 150–160. doi: 10.1016/j.apcata.2010.04.001
109. Carabineiro, S.A.C.; Silva, A.M.T.; Dražić, G.; Tavares, P.B.; Figueiredo, J.L. Gold nanoparticles on ceria supports for the oxidation of carbon monoxide. *Catal. Today* **2010**, 154, 21–30. doi: 10.1016/j.cattod.2010.01.036
110. Konsolakis, M.; Carabineiro, S.A.C.; Marnellos, G.E.; Asad, M.F.; Soares, O.S.G.P.; Pereira, M.F.R.; Órfão, J.J.M.; Figueiredo, J.L. Volatile organic compounds abatement over copper-based catalysts: Effect of support. *Inorganica Chim. Acta* **2017**, 455, 473–482. doi: 10.1016/j.ica.2016.07.059
111. Solsona, B.; Sanchis, R.; Dejoz, A.M.; García, T.; Ruiz-Rodríguez, L.; López Nieto, J.M.; Cecilia, J.A.; Rodríguez-Castellón, E. Total Oxidation of Propane Using CeO₂ and CuO-CeO₂ Catalysts Prepared Using Templates of Different Nature. *Catalysts* **2017**, 7, 96. doi: 10.3390/catal7040096
112. Zhang, F.; Wang, P.; Koberstein, J.; Khalid, S.; Chan, S.-W. Cerium oxidation state in ceria nanoparticles studied with X-ray photoelectron spectroscopy and absorption near edge spectroscopy. *Surf. Sci.* **2004**, 563, 74–82. doi: 10.1016/j.susc.2004.05.138
113. Giménez-Mañogil, J.; Bueno-López, A.; García-García, A. Preparation, characterisation and testing of CuO/Ce_{0.8}Zr_{0.2}O₂ catalysts for NO oxidation to NO₂ and mild

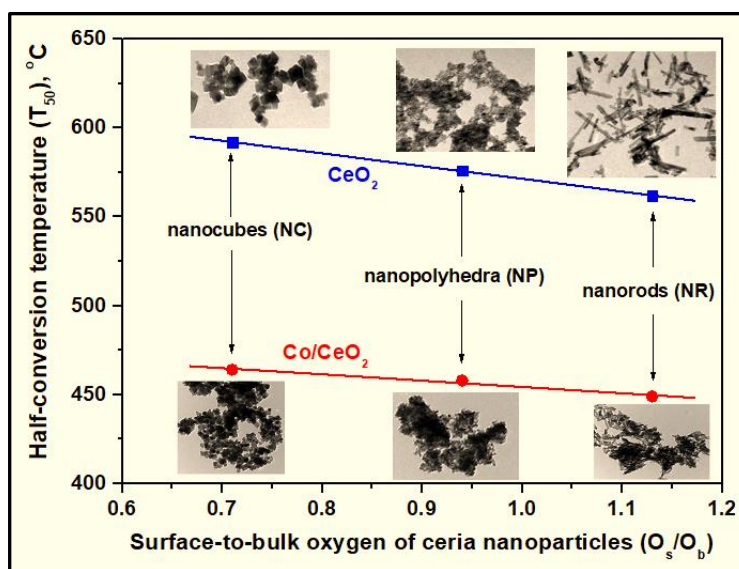
- temperature diesel soot combustion. *Appl. Catal. B Environ.* **2014**, *152–153*, 99–107. doi: 10.1016/j.apcatb.2014.01.018
114. Espinós, J.P.; Morales, J.; Barranco, A.; Caballero, A.; Holgado, J.P.; González-Elipe, A.R. Interface Effects for Cu, CuO, and Cu₂O Deposited on SiO₂ and ZrO₂. XPS Determination of the Valence State of Copper in Cu/SiO₂ and Cu/ZrO₂ Catalysts. *J. Phys. Chem. B* **2002**, *106*, 6921–6929. doi: 10.1021/jp014618m
115. Biesinger, M.C.; Lau, L.W.M.; Gerson, A.R.; Smart, R.St.C. Resolving surface chemical states in XPS analysis of first row transition metals, oxides and hydroxides: Sc, Ti, V, Cu and Zn. *Appl. Surf. Sci.* **2010**, *257*, 887–898. doi: 10.1016/j.apsusc.2010.07.086
116. Biesinger, M.C.; Hart, B.R.; Polack, R.; Kobe, B.A.; Smart, R.St.C. Analysis of mineral surface chemistry in flotation separation using imaging XPS. *Miner. Eng.* **2007**, *20*, 152–162. doi: 10.1016/j.mineng.2006.08.006
117. Wang, H.; Jin, B.; Wang, H.; Ma, N.; Liu, W.; Weng, D.; Wu, X.; Liu, S. Study of Ag promoted Fe₂O₃@CeO₂ as superior soot oxidation catalysts: The role of Fe₂O₃ crystal plane and tandem oxygen delivery. *Appl. Catal. B Environ.* **2018**, *237*, 251–262. doi: 10.1016/j.apcatb.2018.05.093
118. Nolan, M.; Parker, S.C.; Watson, G.W. The electronic structure of oxygen vacancy defects at the low index surfaces of ceria. *Surf. Sci.* **2005**, *595*, 223–232. doi: 10.1016/j.susc.2005.08.015
119. Nolan, M.; Fearon, J.E.; Watson, G.W. Oxygen vacancy formation and migration in ceria. *Solid State Ionics* **2006**, *177*, 3069–3074. doi: 10.1016/j.ssi.2006.07.045
120. Mullins, D.R.; Zhang, K.Z. Metal-support interactions between Pt and thin film cerium oxide. *Surf. Sci.* **2002**, *513*, 163–173. doi: 10.1016/S0039-6028(02)01704-1
121. Konsolakis, M.; Lykaki, M. Recent Advances on the Rational Design of Non-Precious Metal Oxide Catalysts Exemplified by CuO_x/CeO₂ Binary System: Implications of Size, Shape and Electronic Effects on Intrinsic Reactivity and Metal-Support Interactions. *Catalysts* **2020**, *10*, 160. doi: 10.3390/catal10020160
122. Sun, J.; Zhang, L.; Ge, C.; Tang, C.; Dong, L. Comparative study on the catalytic CO oxidation properties of CuO/CeO₂ catalysts prepared by solid state and wet impregnation. *Chinese J. Catal.* **2014**, *35*, 1347–1358. doi: 10.1016/S1872-2067(14)60138-8
123. Yao, S.; Mudiyansele, K.; Xu, W.; Johnston-Peck, A.C.; Hanson, J.C.; Wu, T.; Stacchiola, D.; Rodriguez, J.A.; Zhao, H.; Beyer, K.A.; Chapman, K.W.; Chupas, P.J.; Martínez-Arias, A.; Si, R.; Bolin, T.B.; Liu, W.; Senanayake, S.D. Unraveling the

- Dynamic Nature of a CuO/CeO₂ Catalyst for CO Oxidation in *Operando*: A Combined Study of XANES (Fluorescence) and DRIFTS. *ACS Catal.* **2014**, *4*, 1650–1661. doi: 10.1021/cs500148e
124. QQi, L.; Yu, Q.; Dai, Y.; Tang, C.; Liu, L.; Zhang, H.; Gao, F.; Dong, L.; Chen, Y. Influence of cerium precursors on the structure and reducibility of mesoporous CuO-CeO₂ catalysts for CO oxidation. *Appl. Catal. B Environ.* **2012**, *119–120*, 308–320. doi: 10.1016/j.apcatb.2012.02.029
125. Jia, A.-P.; Jiang, S.-Y.; Lu, J.-Q.; Luo, M.-F. Study of Catalytic Activity at the CuO-CeO₂ Interface for CO Oxidation. *J. Phys. Chem. C* **2010**, *114*, 21605–21610. doi: 10.1021/jp108556u
126. Shang, H.; Zhang, X.; Xu, J.; Han, Y. Effects of preparation methods on the activity of CuO/CeO₂ catalysts for CO oxidation. *Front. Chem. Sci. Eng.* **2017**, *11*, 603–612. doi: 10.1007/s11705-017-1661-z
127. Lykaki, M.; Stefa, S.; Carabineiro, S.A.C.; Pandis, P.K.; Stathopoulos, V.N.; Konsolakis, M. Facet-Dependent Reactivity of Fe₂O₃/CeO₂ Nanocomposites: Effect of Ceria Morphology on CO Oxidation. *Catalysts* **2019**, *9*, 371. doi: 10.3390/catal9040371
128. Piumetti, M.; Bensaid, S.; Andana, T.; Dosa, M.; Novara, C.; Giorgis, F.; Russo, N.; Fino, D. Nanostructured Ceria-Based Materials: Effect of the Hydrothermal Synthesis Conditions on the Structural Properties and Catalytic Activity. *Catalysts* **2017**, *7*, 174. doi: 10.3390/catal7060174
129. Konsolakis, M.; Lykaki, M. Facet-Dependent Reactivity of Ceria Nanoparticles Exemplified by CeO₂-Based Transition Metal Catalysts: A Critical Review. *Catalysts* **2021**, *11*, 452. doi: 10.3390/catal11040452

CHAPTER 4

Effects of Ceria's Morphology or Surface Promotion (Cs) on the Physicochemical Properties of Ceria-Based Transition Metal Catalysts M/CeO₂ (M: Co or Cu): Implications in N₂O Decomposition

Chapter 4 deals with the effect of ceria's morphology on the solid state properties and on the decomposition of N₂O (deN₂O) of ceria-based cobalt oxide catalysts is examined. In specific, three different ceria nanostructures (rods, polyhedra, cubes) were



hydrothermally synthesized and employed as supports for the cobalt oxide phase.

This chapter also focuses on the optimization of the deN₂O performance through the fine-tuning of the local surface chemistry of copper-ceria binary oxides by means of synthesis procedure and surface promotion. In brief, the effect of alkali promotion (Cs) on the deN₂O activity of Cu/CeO₂ mixed oxides, pre-optimized through the preparation method (co-precipitation among different synthesis routes), is investigated.

INTRODUCTION

Nitrous oxide (N₂O) is one of the most significant greenhouse gases contributing to the depletion of the ozone layer. N₂O has a much higher global warming potential (GWP) as compared to CO₂ (310 times higher) and a long atmospheric lifetime (114 years). The emissions of N₂O are derived by both natural and anthropogenic sources. The main anthropogenic sources for N₂O emissions involve agriculture (use of fertilizers), chemical industry (adipic and nitric acid production), the combustion of fossil fuels, as well as biomass burning, *etc.* [1–4].

In light of the above, the abatement of N₂O emissions is of paramount importance and the direct catalytic decomposition of nitrous oxide to molecular nitrogen and oxygen (deN₂O process) is considered to be a highly efficient remediation method. Moreover, since the deN₂O process follows a cationic redox mechanism involving the N₂O activation through electron transfer ($\text{N}_2\text{O} + \text{e}^- \rightarrow \text{N}_2 + \text{O}^-$) and the subsequent recombination of surface oxygen species into dioxygen ($2\text{O}^- \rightarrow \text{O}_2 + 2\text{e}^-$), it can be considered as a probe reaction for evaluating the electronic and redox properties of the catalyst surface [5–9]. Thus far, several catalytic systems, such as supported noble metals [10–12], perovskites [13–15], hexaaluminates [16–19], spinels [20–23], zeolites [24–27], mixed oxides [28–32], have been used for N₂O decomposition. Although noble metals (NMs) exhibit satisfactory activity for deN₂O process, their high cost and the deterioration of their catalytic efficiency from gases present in the exhaust gas stream (*e.g.*, O₂) act as inhibiting factors for practical applications [1,33]. Hence, research efforts have focused on the development of NMs-free mixed oxides of high activity, stability and low cost. The latest advances in the field of N₂O decomposition over NMs-free oxide catalysts, *i.e.*, single/mixed oxides, hexaaluminates, hydrotalcites, spinels and perovskites, have been lately reviewed by Konsolakis [1]. It was revealed that, by appropriately adjusting the synthesis parameters and/or by employing surface/structural promoters, very active composites can be obtained. For instance, Inoue and co-workers [34] examined the impact of different synthesis methods (precipitation, impregnation, combustion, hydrothermal) on the deN₂O performance of K-doped Co₃O₄. Impregnation of CoCO₃ with an aqueous solution of KOH led to optimum results due to the improved textural and redox properties.

Among the different transition metal oxides, cobalt spinel shows unique physicochemical characteristics, such as thermal stability, high reducibility, making it an excellent candidate for the deN₂O process [21,29,35,36]. However, the high cost of cobalt renders mandatory its dispersion to high surface area supports like ceria, magnesia *etc.* [37,38]. Among the various

supports investigated, ceria exhibits unique redox properties associated with its high oxygen storage capacity (OSC), rendering this material highly effective in many catalytic processes [29,39–41]. Furthermore, the synergistic effects induced by strong metal-ceria interactions, in nanoscale, can modify the surface chemistry of the materials through geometric or/and electronic perturbations, leading to improved redox properties and catalytic activity [42–46]. However, the catalytic efficiency of transition metal oxides, involving ceria-based mixed oxides, can be considerably affected by the different counterpart characteristics, such as particle size and morphology. In this regard, engineering the particle size and shape (*e.g.*, nanorods, nanocubes) through the employment of advanced nano-synthesis paths has lately received particular attention [41,47–49]. Interestingly, the support morphology greatly affects the redox properties, oxygen mobility and, subsequently, the catalytic activity of the mixed oxides. For instance, Lin *et al.* [50] prepared Co₃O₄/CeO₂ catalysts with three different support morphologies, namely polyhedra, nanorods and hexagonal shapes, with polyhedra exhibiting the highest catalytic activity for ammonia synthesis. In a similar manner, by tailoring the support morphology, CuO/CeO₂ nanoshaped materials of enhanced reducibility and deN₂O performance can be obtained [51]. Andrade-Martínez *et al.* [52] investigated the catalytic reduction of N₂O over CuO/SiO₂ catalysts, revealing the key role of the spherical ordered mesoporous support, along with its functionalization through copper addition, on the improved catalytic activity and stability, making this material comparable to noble metal-reported systems. Different support morphologies (rods, plates, cubes) have also been employed for the low-temperature CH₂Br₂ oxidation revealing the superiority of cobalt-ceria nanorods in the catalytic performance [53]. Moreover, cobalt oxide supported on ceria of different morphology (nanoparticles, nanorods and nanocubes) has been investigated for the catalytic oxidation of toluene with the nanoparticles exhibiting the highest catalytic activity due to the synergism at the interface between the two oxide phases which leads to improved reducibility [54].

In sub-chapter 4.2, ceria structures of various morphologies (nanopolyhedra, nanorods and nanocubes) were hydrothermally prepared and then cobalt was impregnated into the above ceria supports in order to explore the impact of support morphology on the surface chemistry and the deN₂O performance of Co/CeO₂ mixed oxides. The results clearly revealed that support morphology can exert a profound influence on the N₂O decomposition, paving the way toward the rational design of highly efficient deN₂O catalysts.

Besides the employment of advanced synthesis methods, the deN₂O performance of mixed oxides can be adjusted by means of electronic promotion, mainly through alkali modifiers.

The impact of alkali promotion on the deN₂O activity of various spinel-type catalysts has been thoroughly explored by Kotarba and co-workers [22,55–59].

The pronounced impact of alkali was clearly revealed, ascribed mainly to the facilitation of N₂O activation/dissociation through electron donation from the catalyst surface as well as to the facilitation of oxygen desorption. Similarly, alkali-induced, promotional effects were addressed for hydrotalcite-like compounds [60–63] and Co₃O₄-Ce₂O₃ mixed oxides [28,64], among others. In almost all cases, the beneficial effect of alkali followed the sequence Li << Na < K < Rb < Cs, which matches well the work function (Φ) trend.

Amongst the different mixed oxides, the CuO-Ceria binary system has received considerable attention due to the peculiar properties that can be developed by the complex, either electronic or geometric, metal-support interactions [65,66]. The role of CuO-Ceria interactions in catalysis and their implications in various processes (*e.g.*, water-gas shift reaction, preferential oxidation of CO, steam reforming, *etc.*) has been lately reviewed [65]. On the basis of the latest experimental (*e.g.*, *operando* techniques) and theoretical (*e.g.*, DFT calculations) advances in the field, it was revealed that the superiority of CuO-Ceria system can be correlated with a synergistic effect between the different counterparts. Various interrelated phenomena were revealed to affect the interfacial interactions and, in turn, the catalytic activity, such as: (i) electronic perturbations between copper and ceria, (ii) facilitation of the interplay between Cu²⁺/Cu⁺ and Ce³⁺/Ce⁴⁺ redox couples, (iii) enhanced oxygen mobility and reducibility. In this regard, the fine-tuning of CuO-Ceria oxides by means of advanced synthetic procedures and/or electronic promotion is of major importance towards the rational design of highly active catalysts [65,67–71]. Moreover, despite the extensive work in the field, there is still a lack of understanding in relation to the underlying mechanism of the synergistic effect linked to CuO-Ceria interactions, especially in the presence of surface dopants.

In these perspectives, the impact of synthesis parameters on the deN₂O performance of CuO-Ceria catalysts was extensively investigated in a previous work [66]. Among the different preparation methods, *i.e.*, impregnation, exotemplating and co-precipitation, the latter method resulted in an optimum deN₂O performance, ascribed mainly to the facilitation of the redox interplay between Ce⁴⁺/Ce³⁺ and Cu²⁺/Cu⁺ couples [66].

Based on the above aspects, the present chapter aims at exploring the potential of further adjusting the local surface chemistry of the Cu/Ceria oxides prepared by the co-precipitation method, by means of alkali (Cs) promotion. In this regard, a series of Cs-doped Cu/Ceria samples was prepared by the wet impregnation method in order to obtain a wide range of

alkali surface coverages. The solid state properties of as-prepared samples were determined by means of various characterization techniques (BET, XRD, H₂-TPR, XPS) in order to gain insight into the structure-property relationships. The results revealed that highly active, noble metal-free, deN₂O catalysts can be developed by co-adjusting the synthesis parameters and the electronic state of catalyst's surface by alkali modifiers.

4.1. EXPERIMENTAL

4.1.1. Materials Synthesis

The chemicals used were of analytical reagent grade. Ce(NO₃)₃·6H₂O (Fluka, purity ≥99.0%) and Co(NO₃)₂·6H₂O (Sigma-Aldrich, ≥ 98%) were employed as precursor compounds for the preparation of bare ceria as well as of Co/CeO₂ mixed oxides. Also, NaOH (Sigma-Aldrich, purity ≥98%), ethanol (ACROS Organics, purity 99.8%) and deionized water were used during materials synthesis. Also, cesium nitrate (CsNO₃, Sigma-Aldrich) was used for the preparation of Cs-doped Cu/CeO₂ mixed oxides.

The catalysts developed in this chapter (CeO₂-NP, CeO₂-NR, CeO₂-NC, Co/CeO₂-NP, Co/CeO₂-NR, Co/CeO₂-NC, CsCuCe-0.0, CsCuCe-1.0, CsCuCe-2.0, CsCuCe-3.0, CsCuCe-4.0) were prepared by the methods described in Chapter 2 in section 2.1 (Materials Synthesis). Table 2.1 presents all the materials developed in this study.

4.1.2. Materials Characterization

The porosity of the materials was evaluated by the N₂-adsorption isotherms at -196 °C. Structural characterization was carried out by means of X-ray diffraction (XRD). The collected spectra were analyzed by Rietveld refinement, allowing the determination of crystallite sizes by means of the Williamson–Hall plot. The redox properties were assessed by Temperature Programmed Reduction (TPR) experiments, employing H₂ as a reducing agent. The surface composition and the chemical state of each element were determined by X-ray photoelectron spectroscopy (XPS) analyses. The cobalt-ceria samples were imaged by transmission electron microscopy (TEM). The characterization techniques are fully described in Chapter 2 in section 2.2 (Characterization Techniques).

4.2. CHARACTERIZATION STUDIES OF Co/CeO₂ MIXED OXIDES

4.2.1. Textural and Structural Characterization (BET and XRD)

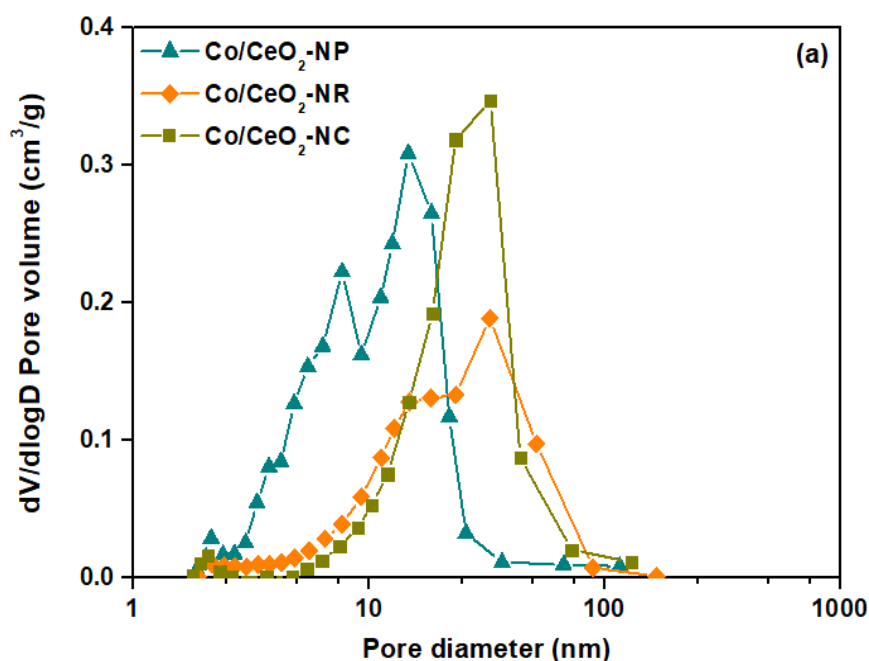
The main textural and structural characteristics of Co/CeO₂ mixed oxides are summarized in Table 4.1. The BET and XRD results of bare ceria samples have already been presented and analyzed in Chapter 3. According to the BET surface area of bare ceria samples (see Table 3.1), the addition of cobalt into CeO₂ decreases the surface area, resulting in the following order: Co/CeO₂-NR (72 m² g⁻¹) > Co/CeO₂-NP (71 m² g⁻¹) > Co/CeO₂-NC (28 m² g⁻¹).

Table 4.1. Textural and structural properties of Co/CeO₂ samples.

Sample	BET Analysis			XRD Analysis	
	BET Surface Area (m ² g ⁻¹)	Pore Volume (cm ³ g ⁻¹)	Average Pore Size (nm)	Crystallite size (nm), D _{XRD} ¹	
				CeO ₂	Co ₃ O ₄
Co/CeO ₂ -NC	28	0.15	22.6	24±1	19±1
Co/CeO ₂ -NR	72	0.31	17.4	14±1	16±1
Co/CeO ₂ -NP	71	0.17	9.8	11±1	15±1

¹ Calculated applying the Williamson–Hall plot after Rietveld refinement of diffractograms.

Figure 4.1a shows the BJH desorption pore size distributions (PSD) of Co/CeO₂ catalysts. According to the pore size distribution, all the samples have their maxima at a pore diameter more than 3 nm designating the presence of mesopores [72]. As it can be observed in Figure 4.1b which shows the adsorption–desorption isotherms, cobalt-ceria samples demonstrate type IV isotherms with a hysteresis loop at a relative pressure > 0.5, further corroborating the mesoporous structure of the materials [73,74].



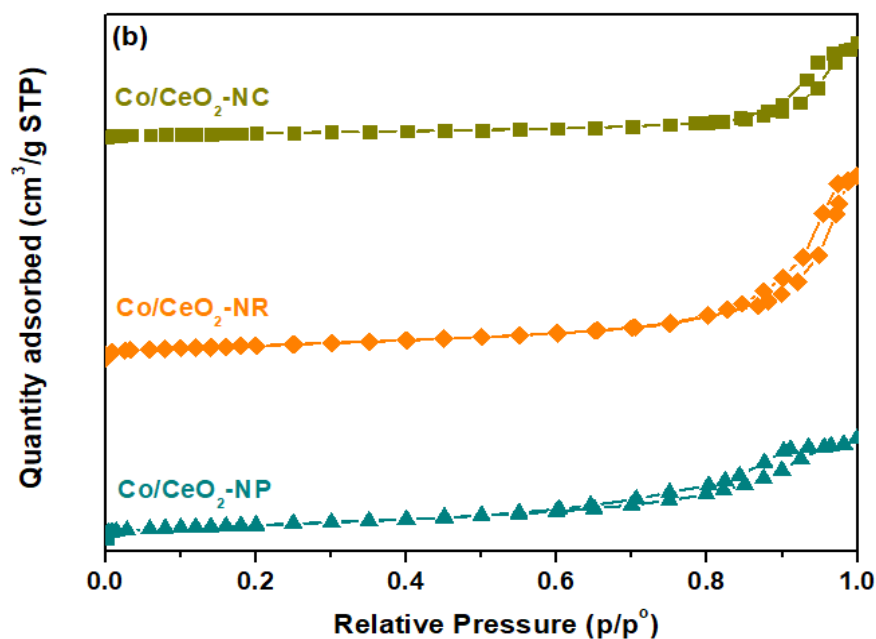


Figure 4.1. (a) The BJH (Barrett–Joyner–Halenda) desorption pore size distribution (PSD) and (b) the adsorption–desorption isotherms of Co/CeO₂ samples. Adapted with permission from Reference [75]. Copyright© 2019, MDPI.

The XRD patterns of the samples are shown in Figure 4.2. The main peaks can be indexed to (111), (200), (220), (311), (222), (400), (331), (420), (422), (511) and (440) planes which are attributed to ceria face-centred cubic fluorite structure (Fm3m symmetry, no. 225) [76,77]. There are three small peaks at 2 θ values of approximately 36°, 44° and 64° which are typical of Co₃O₄ [41]. These three diffraction peaks correspond to the (311), (400) and (440) planes of Co₃O₄, respectively. The average crystallite diameter of the oxide phases (CeO₂ and Co₃O₄) was assessed by an XRD analysis by means of the Williamson-Hall plot (Table 4.1). The CeO₂ crystallite size measurements showed 24, 14 and 11 nm for Co/CeO₂-NC, Co/CeO₂-NR and Co/CeO₂-NP, respectively. As it is obvious from Table 4.1, there is a small decrease in the ceria crystallite size for nanocubes and nanorods, whereas no changes are observed for nanopolyhedra, indicating that the structural characteristics of ceria supports do not get significantly affected upon cobalt addition, as it will be further corroborated by TEM analysis (see below). In a similar manner, the BET analysis (Table 4.1) indicates no significant modifications on the porous characteristics of ceria nanopolyhedra upon cobalt addition, which could be ascribed to their irregular morphology. It should be also noted that the samples with nanocubic morphology exhibit the smallest BET surface area and the largest CeO₂ and Co₃O₄ crystallite sizes in comparison to nanorods and nanopolyhedra. As for the crystallite size of cobalt oxide phase, the following sequence was obtained: Co/CeO₂-NC (19

nm) > Co/CeO₂-NR (16 nm) > Co/CeO₂-NP (15 nm), which perfectly matches the order obtained for CeO₂.

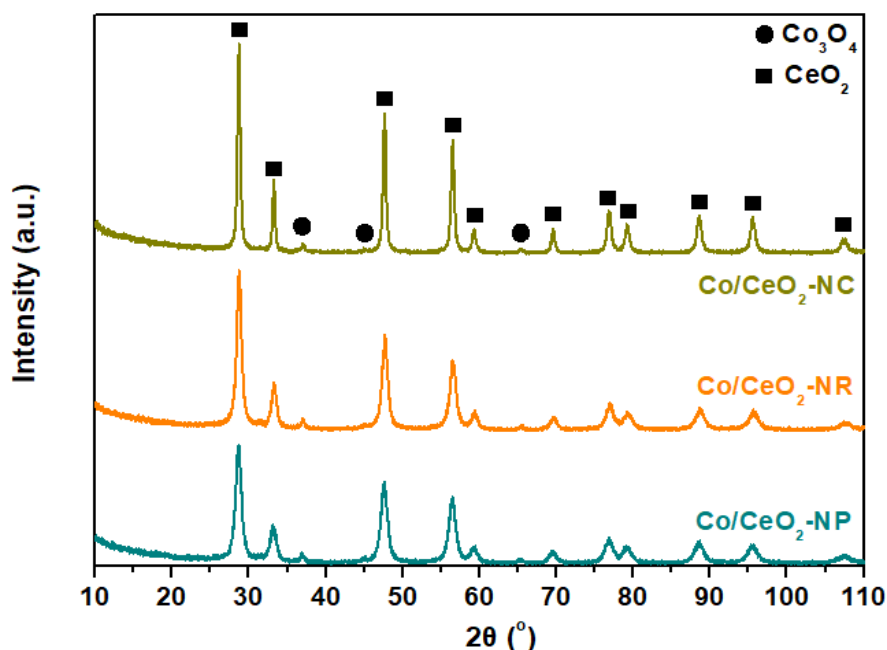


Figure 4.2. The XRD patterns of Co/CeO₂ samples. Adapted with permission from Reference [75]. Copyright© 2019, MDPI.

4.2.2. Morphological Characterization (TEM)

Transmission electron microscopy was performed in order to examine the morphological differences among the samples. Figures 4.3 (a-c) and (d-f) show the TEM images of bare ceria and cobalt-ceria samples. The rod-like morphology of CeO₂-NR is evident in Figure 4.3a which exhibits rods of length varying between 25 and 200 nm. Figures 4.3b and c show mainly irregular-shaped nanopolyhedra and cubes, respectively. As it is obvious from Figure 4.3(d-f), cobalt addition does not affect the morphology of ceria supports, as it has been also observed in Cu/CeO₂ and Fe/CeO₂ catalysts (see Chapter 3).

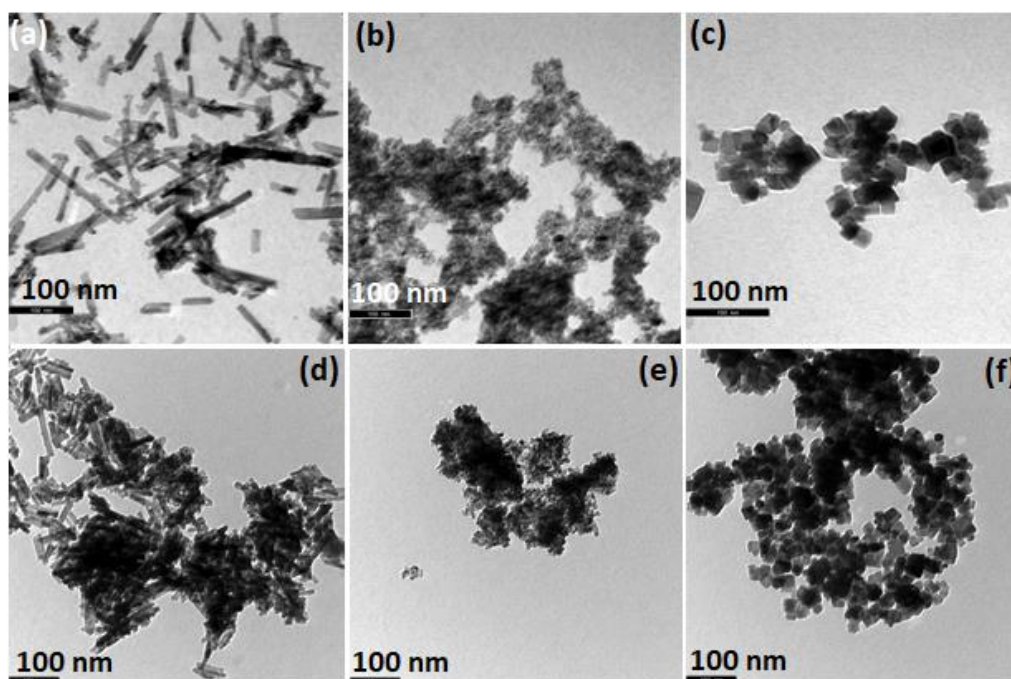


Figure 4.3. TEM images of the samples: (a) CeO₂-NR, (b) CeO₂-NP, (c) CeO₂-NC, (d) Co/CeO₂-NR, (e) Co/CeO₂-NP and (f) Co/CeO₂-NC.

4.2.3. Redox Properties (H₂-TPR)

H₂-TPR experiments took place to investigate the ceria shape effect on the redox properties of as-prepared samples. The assignment of the TPR peaks of bare ceria samples has already been performed in Chapter 3. However, in this context, it should be mentioned again that based on the surface-to-bulk oxygen ratio (O_s/O_b), the following order is acquired for bare ceria samples: CeO₂-NR (1.13) > CeO₂-NP (0.94) > CeO₂-NC (0.71), indicating the superior reducibility of the rod-shaped sample as it exhibits the highest amount of loosely bound oxygen species. The latter is expected to notably affect the deN₂O process, in which the desorption of adsorbed oxygen species mainly determines the reaction rate (*vide infra*).

The reduction profiles of Co/CeO₂ samples as well as that of a Co₃O₄ reference sample are shown in Figure 4.4. Pure Co₃O₄ shows two reduction peaks (a and b) in much lower temperatures than those of bare ceria samples (see Figure 3.5 in Chapter 3), namely 305 °C and 415 °C. They are ascribed to the stepwise reduction of Co₃O₄ → CoO → Co, respectively [50,78–80]. On the other hand, Co/CeO₂ samples exhibit two main peaks at the temperature range of 318–335 °C (peak a) and 388–405 °C (peak b), ascribed to the reduction of Co³⁺ to Co²⁺ and Co²⁺ to Co⁰, respectively [41,81,82]. They also exhibit a broad peak above 800 °C, attributed to ceria sub-surface oxygen reduction, while the capping oxygen reduction overlaps with the reduction of CoO [41,78,83]. Apparently, the reduction of the mixed

oxides takes place at lower temperatures as compared to bare ceria samples, demonstrating the beneficial effect of cobalt on the surface oxygen reduction of ceria. In fact, the interaction between the two oxide phases could be considered responsible for the improved reducibility and oxygen mobility, as thoroughly discussed in previous studies [54,65].

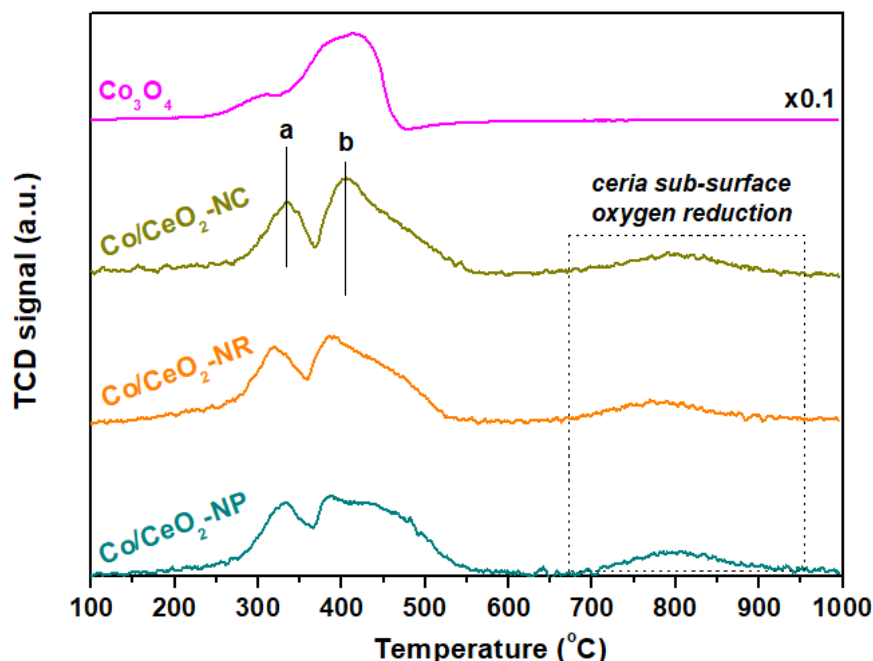


Figure 4.4. H₂-TPR profiles of pure Co₃O₄ and Co/CeO₂ samples. Adapted with permission from Reference [75]. Copyright© 2019, MDPI.

Table 4.2 summarizes the main TPR peaks along with the hydrogen consumption (mmol H₂ g⁻¹) for the Co/CeO₂ samples. According to the consumption of hydrogen in the low-temperature range, which could be related to the cobalt species reduction along with the ceria surface oxygen reduction, the Co/CeO₂-NP and Co/CeO₂-NR samples exhibit a similar H₂ uptake of about 2.40 mmol H₂ g⁻¹ while the sample of nanocubic morphology exhibits a much lower value (2.05 mmol H₂ g⁻¹). This trend matches well with the catalytic results (*vide infra*), revealing the key role of redox ability in the deN₂O process.

Table 4.2. Redox properties of Co/CeO₂ samples.

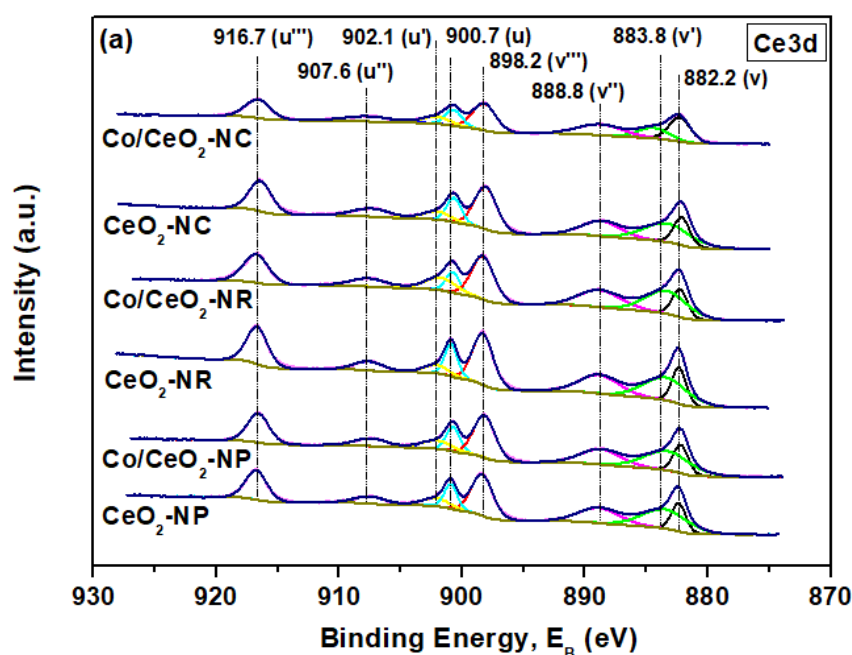
Sample	H ₂ consumption (mmol H ₂ g ⁻¹)			Peak Temperature (°C)	
	Peaks a+b	CeO ₂ peak	Total	Peak a	Peak b
Co/CeO ₂ -NP	2.40	0.61	3.01	333	388
Co/CeO ₂ -NR	2.37	0.62	2.99	318	388
Co/CeO ₂ -NC	2.05	0.32	2.37	335	405

Moreover, the Co/CeO₂-NR sample exhibits the lowest reduction temperature (peak at 318 °C) in comparison with the other samples (peak *ca.* 335 °C), indicating the facilitation of Co³⁺ species reduction over ceria nanorods. Noteworthy, the theoretical amount of hydrogen for the complete reduction of Co₃O₄ to Co (~1.76 mmol H₂ g⁻¹, based on a 7.8 wt.% nominal loading of Co) is always surpassed by the hydrogen amount required for the reduction of the Co/CeO₂ samples (Table 4.2). The latter reveals the facilitation of ceria capping oxygen reduction in the presence of cobalt, further corroborating the above findings.

4.2.4. Surface Analysis (XPS)

XPS analysis was performed in order to investigate the effect of ceria morphology on the elemental chemical states and surface composition of Co/CeO₂ mixed oxides. Figure 4.5a shows the Ce3d XPS spectra of bare ceria and Co/CeO₂ samples, which can be deconvoluted into eight components [84–86]. In brief, the three pairs of peaks labelled as (u, v; u'', v''; u''', v''') are ascribed to Ce⁴⁺, whereas the residual u' and v' peaks to Ce³⁺ species. The complete assignment of the peaks has been already discussed in Chapter 3 (section 3.2.4).

The corresponding O 1s spectra of bare ceria and Co/CeO₂ samples are depicted in Figure 4.5b. The low binding energy peak at 529.3 eV is attributed to the lattice oxygen (O_l) of Co₃O₄ and CeO₂ phases and the high binding energy peak at 531.3 eV corresponds to chemisorbed oxygen (O_{II}) such as adsorbed oxygen (O⁻/O₂²⁻) and water, carbonate as well as hydroxyl species [29,78].



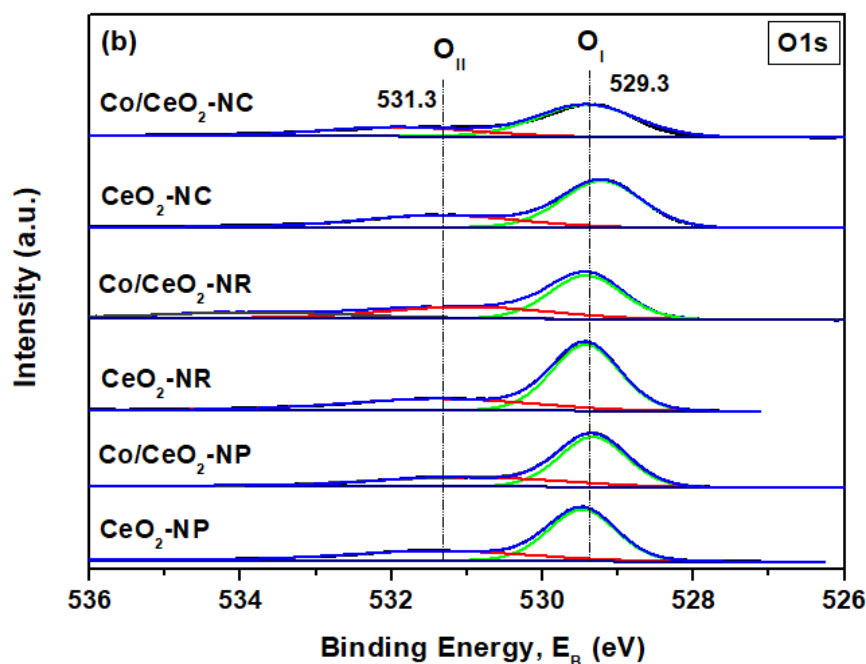


Figure 4.5. XPS spectra of (a) Ce 3d and (b) O 1s of bare CeO₂ and Co/CeO₂ samples. Adapted with permission from Reference [75]. Copyright© 2019, MDPI.

The proportion of Ce³⁺ (%) as well as the O_{II}/O_I ratio for all samples is summarized in Table 4.3. Bare ceria supports exhibit a similar amount of Ce³⁺ ranging from 23.3 to 25.3%. Regarding the Co/CeO₂ samples, the population of Ce³⁺ species is slightly higher, varying between 26.1 and 28.5%. In particular, the Co/CeO₂-NR sample exhibits the highest amount (28.5%) followed by Co/CeO₂-NP (26.7%) and Co/CeO₂-NC (26.1%), indicating its abundance in oxygen vacancies. Interestingly, the relative ratio of adsorbed to lattice oxygen (O_{II}/O_I) and the Ce³⁺ (%) follow the same order, namely, Co/CeO₂-NR (0.60) > Co/CeO₂-NP (0.53) > Co/CeO₂-NC (0.51), perfectly matched to the order obtained for the catalytic performance, as it will be discussed in the sequence. It should be also noted that Co addition to CeO₂-NR enhances both the population of reduced Ce³⁺ species and the O_{II}/O_I ratio, revealing the synergistic interactions between cerium and cobalt oxides towards the formation of highly reducible composites, in agreement with the TPR results.

Table 4.3. XPS results of bare CeO₂ and Co/CeO₂ samples.

Sample	Co ²⁺ /Co ³⁺	Ce ³⁺ (%)	O _{II} /O _I
CeO ₂ -NC	-	23.3	0.50
CeO ₂ -NR	-	24.3	0.47
CeO ₂ -NP	-	25.3	0.49
Co/CeO ₂ -NC	1.06	26.1	0.51
Co/CeO ₂ -NR	1.32	28.5	0.60
Co/CeO ₂ -NP	0.94	26.7	0.53

Figure 4.6a depicts the Co 2p XPS spectra of Co/CeO₂ samples along with the spectrum obtained for the Co₃O₄ reference sample for comparison purposes. The samples exhibit two major peaks of Co2p_{3/2} (780 eV) and Co2p_{1/2} (795 eV). According to peaks' position and shape, the structure of cobalt spinel is formed [29,87,88]. The Co²⁺/Co³⁺ ratio of Co/CeO₂ samples derived by the deconvolution of the Co2p_{1/2} and Co2p_{3/2} peaks is included in Table 4.3. The nanorod sample, which offers the best deN₂O performance (*vide infra*), exhibits the highest Co²⁺/Co³⁺ ratio (1.32), followed by nanocubes (1.06) and nanopolyhedra (0.94). In view of this fact, it has been reported that samples with high Co²⁺/Co³⁺ ratio exhibit better deN₂O performance [3,24,26,47,81], further corroborating the present findings. Also, Figure 4.6b shows the Co2p_{1/2} peak at higher magnification in order to make it more discernible.

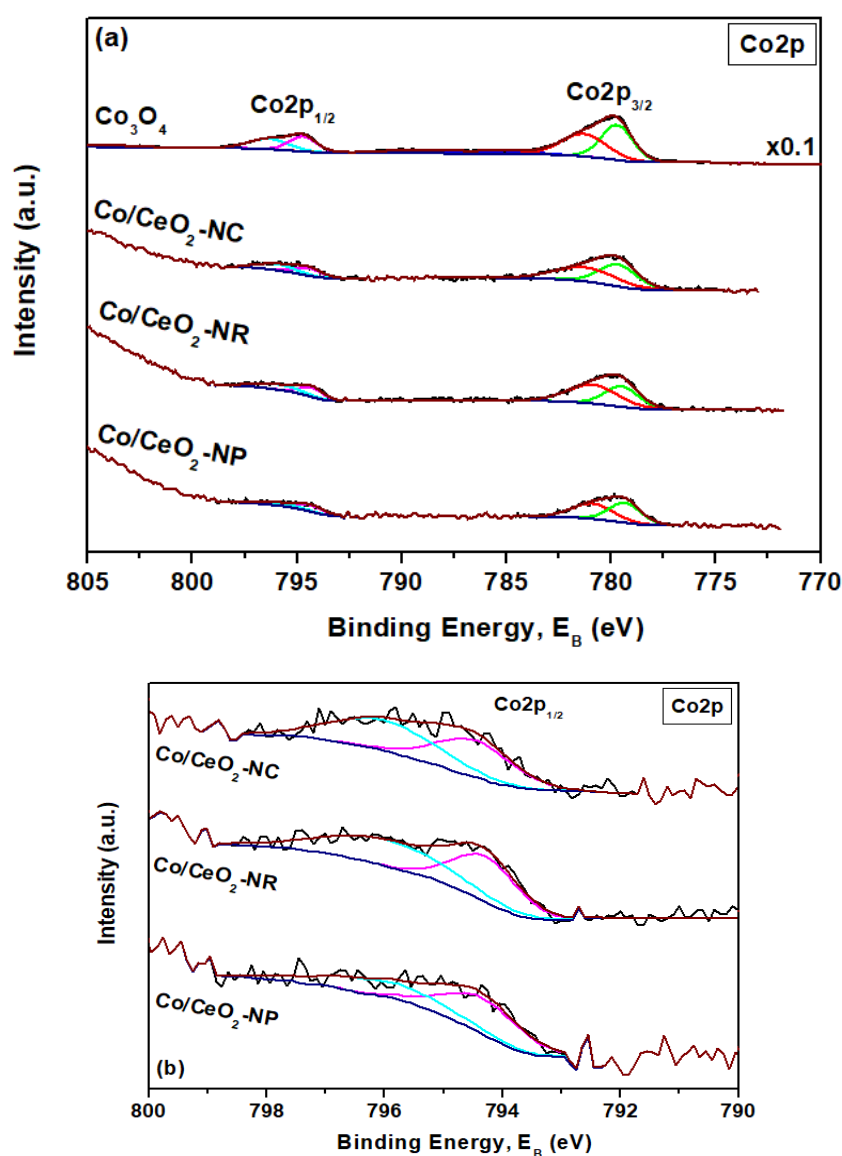


Figure 4.6. (a) Co 2p XPS spectra of Co₃O₄ and Co₃O₄/CeO₂ samples, (b) Magnification of the Co 2p_{1/2} peak in the Co/CeO₂-NX (NX: NP, NR, NC) samples. Adapted with permission from Reference [75]. Copyright© 2019, MDPI.

4.3. CHARACTERIZATION STUDIES OF Cs-PROMOTED Cu/CeO₂ MIXED OXIDES

4.3.1. Textural and Structural Characterization (BET and XRD)

The main textural properties of ceria-based materials are presented in Table 4.4. The un-doped sample shows the highest surface area ($57 \text{ m}^2 \text{ g}^{-1}$) and pore volume ($0.16 \text{ cm}^3 \text{ g}^{-1}$). Addition of Cs results in a progressive deterioration of textural properties, which is almost proportional to Cs content. In particular, the following order, in terms of BET surface area, is obtained: CsCuCe-0.0 ($57 \text{ m}^2 \text{ g}^{-1}$) > CsCuCe-1.0 ($31 \text{ m}^2 \text{ g}^{-1}$) > CsCuCe-2.0 ($24 \text{ m}^2 \text{ g}^{-1}$) > CsCuCe-3.0 ($12 \text{ m}^2 \text{ g}^{-1}$) > CsCuCe-4.0 ($5 \text{ m}^2 \text{ g}^{-1}$). This trend in BET surface area can be corroborated by considering the impact of Cs addition on the textural (pore volume and pore size distribution) and structural (crystallite size) characteristics of Cs-doped Cu/CeO₂ samples. The differential pore size distribution (PSD) curves of un-doped and Cs-doped samples (Figure 4.7) reveal a significant shift of the mean pore size to higher values combined with a moderate decrease of the total pore volume (Table 4.4) upon increasing Cs content. On the other hand, the crystallite size of both ceria and CuO generally increases upon increasing Cs content, without however following the same trend to the BET area (Table 4.4). Hence, the alkali-induced modifications on the pore size distribution could be mainly accounted for the decrease of BET area, in agreement with relevant literature studies [89,90].

Table 4.4. Textural and structural characteristics of Cs-doped Cu/CeO₂ mixed oxides.

Sample	BET Analysis			XRD Analysis			
	Nominal Cs content (wt.%)	BET surface area ($\text{m}^2 \text{ g}^{-1}$)	Pore volume ($\text{cm}^3 \text{ g}^{-1}$)	Average pore diameter (nm)	Average crystallite diameter, D_{XRD} (nm) ¹		Lattice parameter (Å)
					CeO ₂	CuO	
CsCuCe-0.0	0.0	57	0.16	11.05	13.3±0.2	28.6±0.5	5.415±0.001
CsCuCe-1.0	1.2	31	0.15	19.07	13.5±0.2	24.3±0.5	5.417±0.001
CsCuCe-2.0	2.4	24	0.14	22.94	14.2±0.2	38.7±1	5.415±0.001
CsCuCe-3.0	3.6	12	0.14	46.12	18.1±0.2	31.4±1	5.415±0.001
CsCuCe-4.0	4.8	5	0.09	70.53	19.8±0.2	31.2±1	5.414±0.001

¹ Calculated applying Williamson-Hall plot after Rietveld refinement of diffractograms.

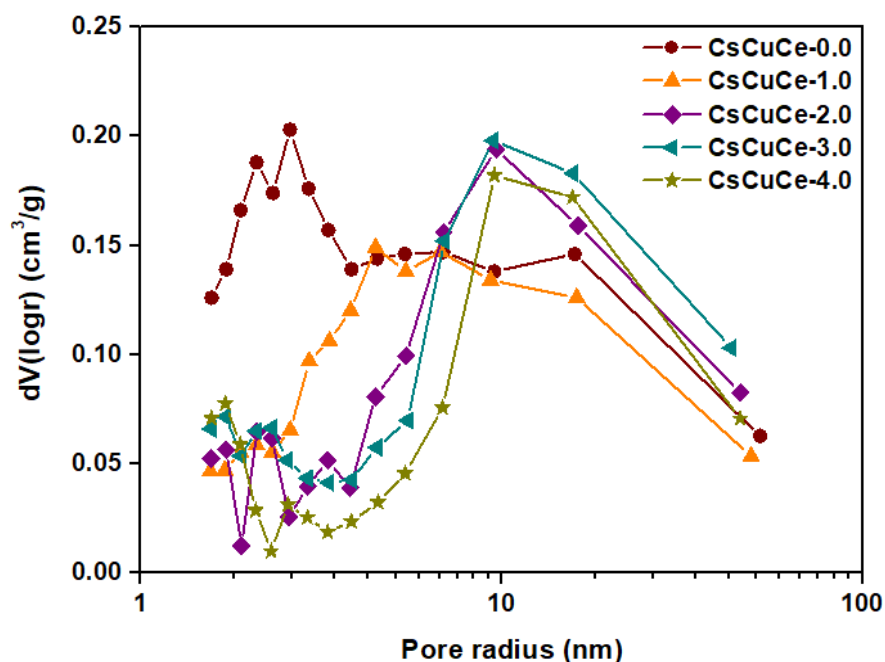


Figure 4.7. Differential pore size distribution (PSD) curves of Cs-doped Cu/CeO₂ mixed oxides. Adapted with permission from Reference [91]. Copyright© 2018, The Royal Society of Chemistry.

Figure 4.8 shows the XRD patterns of Cs-doped Cu/CeO₂ mixed oxides. The phases detected were CeO₂ cerianite (~82 wt.%) and CuO tenorite (~18 wt.%), for all samples, in agreement with the nominal composition of Cu/CeO₂ oxides. No visible diffraction lines corresponding to cesium oxides were detected by XRD, most likely due to its low content and the presence of small crystallites at the detection limit of XRD [90,92–94]. Moreover, no significant differences in CeO₂ lattice parameters were detected between the un-doped and Cs-doped samples, implying that cesium addition did not change the cerianite structure and lattice.

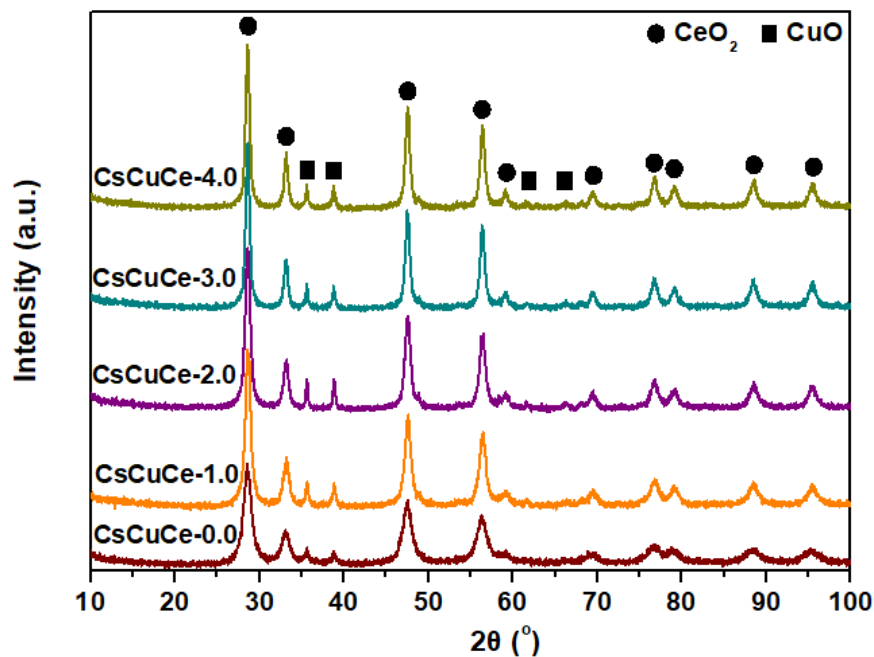


Figure 4.8. XRD patterns of Cs-doped Cu/CeO₂ mixed oxides. Adapted with permission from Reference [91]. Copyright© 2018, The Royal Society of Chemistry.

4.3.2. Redox Properties (H₂-TPR)

The influence of Cs promoter on the redox properties of Cu/CeO₂ catalysts was assessed by means of H₂-TPR. Figure 4.9 depicts the reduction profiles of un-doped and Cs-doped Cu/CeO₂ samples. In this point, it should be mentioned that the assignment of the reduction peaks of bare ceria and pure CuO has been already performed in Chapter 3. Briefly, bare CeO₂ reduction takes place in two steps, resulting in low (~500 °C) and high (> 700 °C) temperature peaks. The former is related to the reduction of surface oxygen, whereas the latter to the bulk oxygen reduction [95–102]. Bare CuO usually shows two overlapped peaks (one main accompanied by a shoulder) in the range of 150–300 °C, ascribed to the stepwise reduction of CuO to Cu₂O and metallic Cu [100,103,104]. However, Cu incorporation into the ceria lattice facilitates the surface shell reduction through synergistic interactions, favouring the reduction of both copper and ceria oxides [105,106].

Although there is a great discrepancy in relation to the precise assignment of H₂-TPR peaks in Cu–Ceria composites, it is generally accepted that there are three different CuO_x species: (i) highly dispersed CuO species on the ceria surface (low temperature (LT) peak), (ii) Cu²⁺ ions incorporated into CeO₂ lattice and/or CuO_x small clusters (intermediate temperature peak), (iii) bulk CuO_x phase (high temperature (HT) peak) [107–110]. Sundar *et al.* [109]

observed two reduction peaks for the Cu/CeO₂ catalysts. The LT peak was ascribed to finely dispersed CuO species whereas the HT peak to Cu₂O phase.

In view of the above discussion, the peaks at 212 °C (peak α) and 257 °C (peak β) observed in Cu/CeO₂ sample (Figure 4.9) can be ascribed to the reduction of well dispersed CuO and CuO_x clusters, respectively, along with the reduction of ceria surface oxygen. The latter is further supported by the fact that the amount of H₂ consumed over Cu/CeO₂ sample surpasses the one theoretically required for the complete reduction of CuO to Cu, as will be discussed in the sequence.

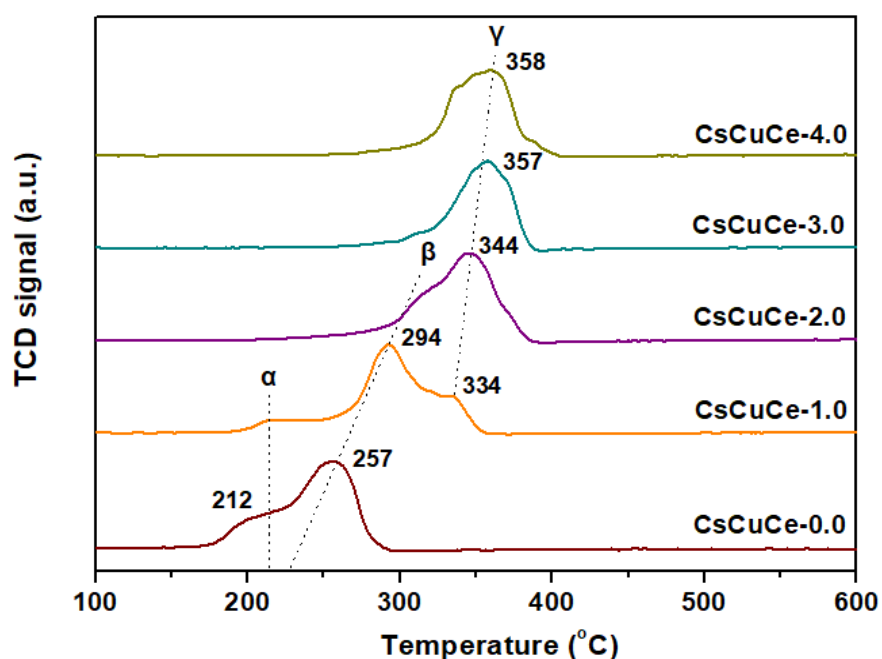


Figure 4.9. H₂-TPR profiles of Cs-doped Cu/CeO₂ mixed oxides. Adapted with permission from Reference [91]. Copyright© 2018, The Royal Society of Chemistry.

Upon increasing Cs content, the peak α at 212 °C (well dispersed CuO species) is progressively decreased in intensity and is almost absent for the Cs-1.0 sample. For higher loadings, the peak α is no longer visible. The latter is in agreement with the significant increase of Cu crystallite size for Cs loadings higher than 1.0 at/nm² (Table 4.4). On the other hand, a systematic upward shift is obtained for β peak at 257 °C; it is shifted to 294 °C for 1.0 at Cs/nm². Moreover, a peak at 334 °C (peak γ) is clearly resolved for 1.0 at Cs/nm², which gains in intensity at the expense of peak β and shifts to higher temperatures upon increasing Cs content. In light of the above discussion, the peak γ could be tentatively assigned to the reduction of partially oxidized Cu₂O phase. These findings point to the stabilization of lower oxidation state Cu species (Cu⁺) with increasing Cs content, implying the electronic nature of

Cs promotion, as will be further discussed in the sequence. It is worth pointing out that the present results are in agreement with those reported over Cs-doped CuO sample [111]; upon increasing Cs loading the high temperature peak related to the reduction of Cu^+ to Cu^0 is progressively shifted to higher temperatures. Similar upward shifts have been observed for alkali-doped Co/SiO_2 [112] and Pt/Ceria [105] catalysts. Hence, the upward shift of thermo-reduction profiles upon increasing Cs should be mainly ascribed to the electronic effect of electropositive modifier (Cs) towards the stabilization of lower valence Cu^+ species. The effect of Cs promoter on the redox properties of as-prepared samples is further explored by estimating the H_2 consumption in the low-temperature region (100–400 °C, Figure 4.9), where both the reduction of ceria surface oxygen and copper oxide (CuO_x) species is taking place (Table 4.5). It is evident that the real H_2 uptake in both un-doped and Cs-doped samples always surpasses the theoretical one ($2.5 \text{ mmol g}_{\text{cat}}^{-1}$ or $12.5 \text{ mmol g}_{\text{CuO}}^{-1}$ on the basis of a nominal Cu loading of 20 wt.%), implying the participation of ceria on the reduction process. In particular, the H_2 excess amount is about 1.5 mmol g^{-1} for intermediate Cs loadings ($1.0\text{--}2.0 \text{ Cs atoms/nm}^2$), corresponding to a theoretical ceria reduction degree (x in CeO_{2-x}) of about 0.3 ($\text{CeO}_{1.7}$). For high Cs-loaded samples ($3.0\text{--}4.0 \text{ Cs atoms/nm}^2$) the H_2 excess is slightly lower ($\sim 1.0 \text{ mmol g}^{-1}$), resulting in $\text{CeO}_{1.8}$ stoichiometry.

Table 4.5. Redox characteristics of the Cs-doped Cu/CeO₂ samples.

Sample	H_2 consumption ($\text{mmol H}_2 \text{ g}^{-1}$) ¹	H_2 excess ($\text{mmol H}_2 \text{ g}^{-1}$) ²	Ceria reduction degree (x in CeO_{2-x})
CsCuCe-0.0	3.5	1.0	0.21
CsCuCe-1.0	3.9	1.4	0.30
CsCuCe-2.0	3.8	1.3	0.28
CsCuCe-3.0	3.4	0.9	0.19
CsCuCe-4.0	3.6	1.1	0.25

¹ Estimated using the quantification of H_2 uptake in the low temperature range (100–400 °C) of the TPR profiles; ² Estimated by the subtraction of H_2 required for CuO reduction in 20 wt.% Cu/CeO₂ samples ($\sim 2.5 \text{ mmol g}^{-1}$) from the total H_2 consumption.

These findings can be corroborated by taking into account the strong interaction between ceria and copper, which facilitates the reduction of CeO_2 , as it has been thoroughly described in the literature [65]. More specifically, the redox equilibrium $\text{Cu}^{2+} + \text{Ce}^{3+} \leftrightarrow \text{Cu}^+ + \text{Ce}^{4+}$ can be considered for the enhanced reducibility of Cu/CeO₂ samples.

In particular, two apparently alternative explanations can be provided: i) dissociation of molecular H_2 to atomic H on Cu surface and its subsequent spillover to ceria, ii) strong electronic metal-support interactions (EMSI), perturbing the electronic band structure of metal oxide [65]. In this regard, a relationship between the electronic properties of the

metal (*e.g.*, work function) and ceria reduction temperature has been revealed [113,114]. Hence, the work function changes induced by Cs doping could be considered responsible for the different extent of ceria reduction. The latter can be well-rationalized by taking into account the classic Topping model, interpreting the local surface changes induced by alkali promotion [115]. Surface ionization of alkali promoters resulted in the formation of surface dipoles (*e.g.*, Cs⁺-Cs⁺), lowering catalyst surface work function. However, at high alkali coverage, the distance between dipoles is decreased, resulting in a depolarization of surface dipoles followed by an increase of work function. This is in accordance with the volcano-type dependence of deN₂O activity by alkali coverage, implying optimum promoter coverage [1,58]. In view of the above, the electronic modifications induced by electropositive (alkali) promotion could be accounted for the reduction of ceria and the stabilization of Cu⁺ species in Cs-doped Cu/CeO₂ samples. The underlying mechanism of alkali promotion will be further discussed below on the basis of surface characterization and catalytic evaluation studies.

4.3.3. Surface Analysis (XPS)

XPS analysis was also carried out in order to obtain information about the elemental chemical states and the surface composition. Figure 4.10a shows the Ce 3d XPS spectra for all samples. The complex spectra can be resolved into eight components by deconvolution with the assignment of each component defined in the figure (*v* represents the Ce 3d_{5/2} contributions and *u* represents the Ce 3d_{3/2} contributions) [66,116]. For 3d_{5/2} of Ce⁴⁺, a mixing of the Ce 3d⁹4f²Lⁿ⁻² and Ce 3d⁹4f¹Lⁿ⁻¹ states produces the peaks labelled *v* and *v''*, and the Ce 3d⁹4f¹Lⁿ final state forms the peak *v'''*. For 3d_{5/2} of Ce³⁺, the Ce 3d⁹4f²Lⁿ⁻¹ and Ce 3d⁹4f¹Lⁿ states correspond to peaks *v* and *v'*. For the Ce 3d_{3/2} level with the *u* structure, the same assignment can be reserved.

Figure 4.10b shows the O 1s XPS spectra of the mixed oxide samples. Two peaks (labelled as O_I and O_{II}) can be clearly observed. The low binding energy peak (O_I), at 529–530 eV, can be attributed to O²⁻ ions in the lattice, whereas the high energy peak (O_{II}), at 531–532 eV, could be assigned to low coordination surface oxygen species, surface oxygen defects, as well as to hydroxyl or carbonate species [66,117]. As it can be observed from Figure 4.10b, there is a shift of the O_I peak to lower binding energy for the promoted samples, an indication of the ionic character of Ce–O/Cu–O bonds. A similar shift to lower BE upon alkali addition has been observed for Co/CeO₂ catalysts [90].

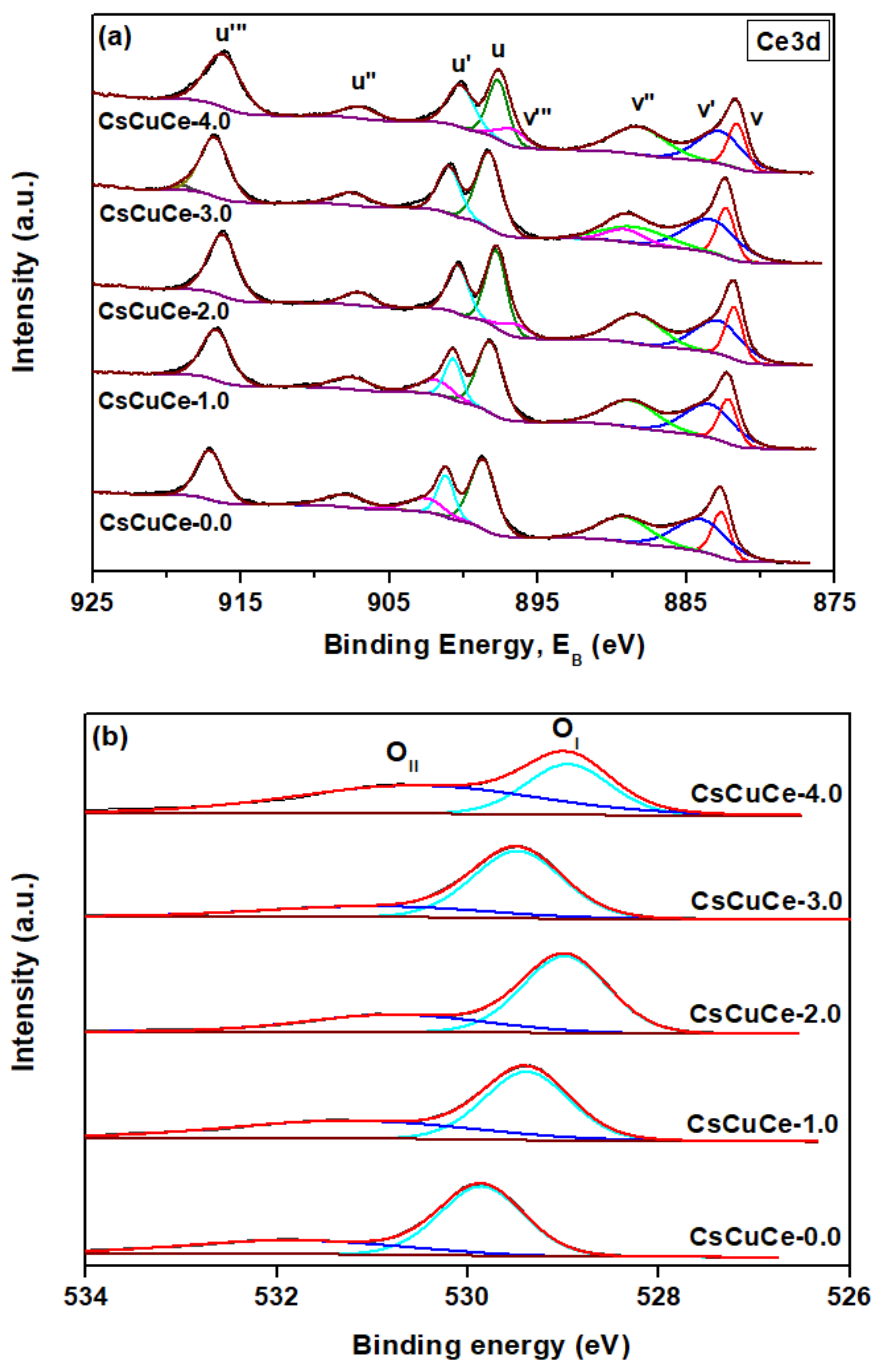


Figure 4.10. XPS spectra of (a) Ce 3d and (b) O 1s of Cs-doped Cu/CeO₂ samples. Adapted with permission from Reference [91]. Copyright© 2018, The Royal Society of Chemistry.

A relationship between the area of CeO₂ in the Ce 3d spectra and the percentage of u''' peak (which arises from a transition of the 4f'' final state) was established by Shyu *et al.* [116] from which the percentage of CeO₂ (Ce⁴⁺) was calculated using the following equation: % CeO₂ = % u'''/0.144. The concentration of Ce³⁺ can also be determined from the ratio: Ce³⁺/(Ce⁴⁺+Ce³⁺), where Ce⁴⁺ and Ce³⁺ represent the sums of the integrated XPS peak areas related to Ce⁴⁺ (v, v'', v''', u, u'' and u''') and Ce³⁺ (v', u') signals, respectively [63]. In Table 4.6

the obtained values for Ce³⁺ (%) are depicted, estimated using the equation: % Ce (III) = 100 - % u'''/0.144.

Table 4.6. Surface characteristics of the Cs-doped Cu/CeO₂ samples.

Sample	Relative concentration (%)		XPS atomic ratios	
	Cu ⁺	Ce ³⁺	Cu/Ce	Cs/Ce
CsCuCe-0.0	23.2	25.9	0.35	–
CsCuCe-1.0	25.3	24.5	0.28	0.08
CsCuCe-2.0	*	28.8	0.23	0.20
CsCuCe-3.0	*	30.3	0.20	0.25
CsCuCe-4.0	*	28.3	0.21	0.35

* Not calculated due to the overlapping of Cu 2p_{3/2} and Cs MNN peaks.

Surprisingly, the CsCuCe-1.0 sample shows the lowest amount of Ce³⁺ (24.5%) and the highest amount of Cu⁺ (25.3%) possibly due to the synergistic interaction between copper ↔ cesium ↔ cerium, which facilitates the redox equilibrium Cu²⁺ + Ce³⁺ ↔ Cu⁺ + Ce⁴⁺, as previously discussed. It should be noted however that the trend obtained for Ce³⁺ (%) in relation to Cs content is not monotonic. The latter could be possibly ascribed to the fact that the relative abundance of Ce³⁺ species is determined by various parameters, such as the extent of Cu-Ceria interactions, the concentration of surface defects, *etc.* [118]. Lee *et al.* [90] have reported that alkali addition to Co/CeO₂ catalysts does not clearly affect the concentration of Ce³⁺.

The Cu 2p XPS spectra (Figure 4.11) show two main peaks of Cu 2p_{1/2} (~953 eV) and Cu 2p_{3/2} (~933 eV) and shake-up satellite peaks centred at ~942 eV. The Cu 2p_{3/2} peak at ~933 eV and the presence of shake-up peaks are typical of CuO species, while lower energies *ca.* 932 eV and the absence of shake-up peaks are characteristic of further reduced Cu species, usually Cu₂O [66,119–123]. The addition of Cs causes a progressive slight shift of the Cu 2p_{3/2} peak to lower binding energy values (by *ca.* 0.6 eV), which is ascribed to the electron charge donation from the alkali metal [111,124]. The latter is in agreement with the TPR results, presented above. Upon increasing Cs content, the peak of Cs MNN *ca.* 927 eV starts to be visible and it superimposes with the Cu 2p_{3/2} peak (Figure 4.11).

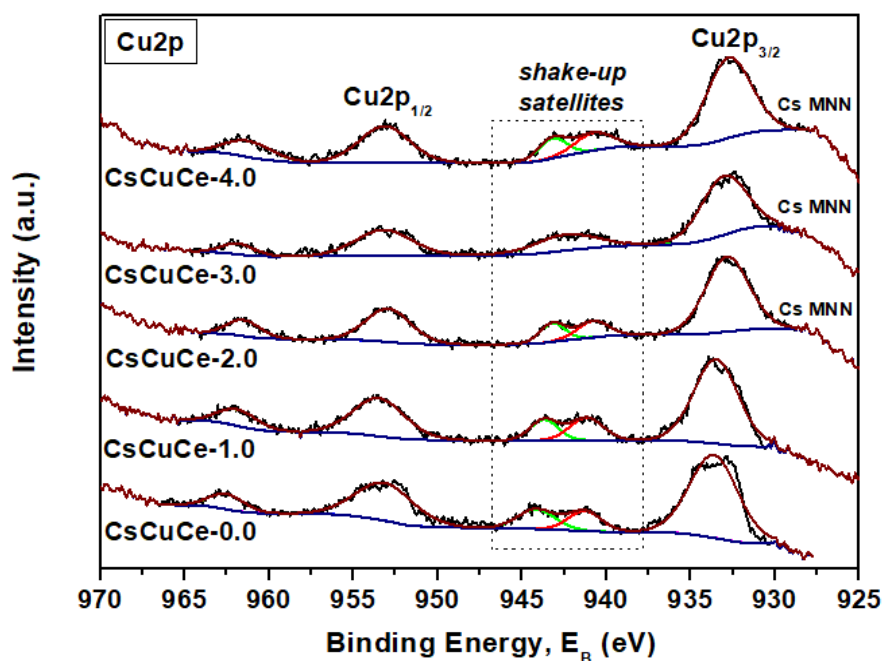


Figure 4.11. XPS Cu 2p spectra of Cs-doped Cu/CeO₂ samples. Adapted with permission from Reference [91]. Copyright© 2018, The Royal Society of Chemistry.

The discrimination of Cu oxidation states (Cu⁺ and Cu²⁺) is next carried out by comparing the Cu 2p spectra of as-prepared samples with the spectra of 100% pure reference CuO (Cu²⁺) sample, following a well-established procedure, described in detail in previous studies [66,125,126]. In particular, the relative concentration of Cu⁺ and Cu²⁺ species on the catalyst surface can be obtained by the following equations:

$$\text{Cu}^+(\%) = \frac{A - \left(\frac{A_{1s}}{B_s}\right) \cdot B}{A + B} \cdot 100 \quad (1)$$

$$\text{Cu}^{2+}(\%) = \frac{B \cdot \left[1 + \left(\frac{A_{1s}}{B_s}\right) \cdot B\right]}{A + B} \cdot 100 \quad (2)$$

where A is the area of the main Cu 2p_{3/2} peak, B is the area of the shake-up peak of investigated samples, whereas A_{1s}/B_s is the ratio of main/shake-up peaks for the reference CuO sample (1.89).

The relative content of Cu⁺ species is listed in Table 4.7 for samples with Cs content up to 1 at Cs/nm²; above that value the Cu 2p_{3/2} peak is superimposed with the Cs MNN peak. The CsCuCe-1.0 sample possesses the largest amount of Cu⁺ (25.3%), followed by CsCuCe-0.0

(23.2%). This order matches well with the deN₂O performance (see below), demonstrating the key role of Cu⁺ species, as will be further discussed in the sequence.

Figure 4.12 shows the Cs 3d spectra of Cs containing samples. The Cs 3d spectra show well-separated peaks at 724 eV and 739 eV, in agreement with the literature [127]. These features generally increase in intensity with increasing Cs content. In particular, the Cs/Ce surface ratio (Table 4.6) is increased almost proportionally to the nominal loading, implying that the alkali ions do not tend to diffuse into the bulk, in compliance with the XRD results (Table 4.4). On the other hand, the Cu/Ce XPS ratio follows the reverse trend indicating the progressive blockage of Cu upon increasing Cs content. The latter can be ascribed to the later addition of cesium promoter to the pre-synthesized Cu/CeO₂ oxides and to the large cationic radius of Cs⁺ ions, which hinders its migration to the bulk. Similar results were obtained for alkali-doped spinels [22,56,58] or hydrotalcite [62] catalysts, implying the preferential localization of alkali ions on the catalyst's surface.

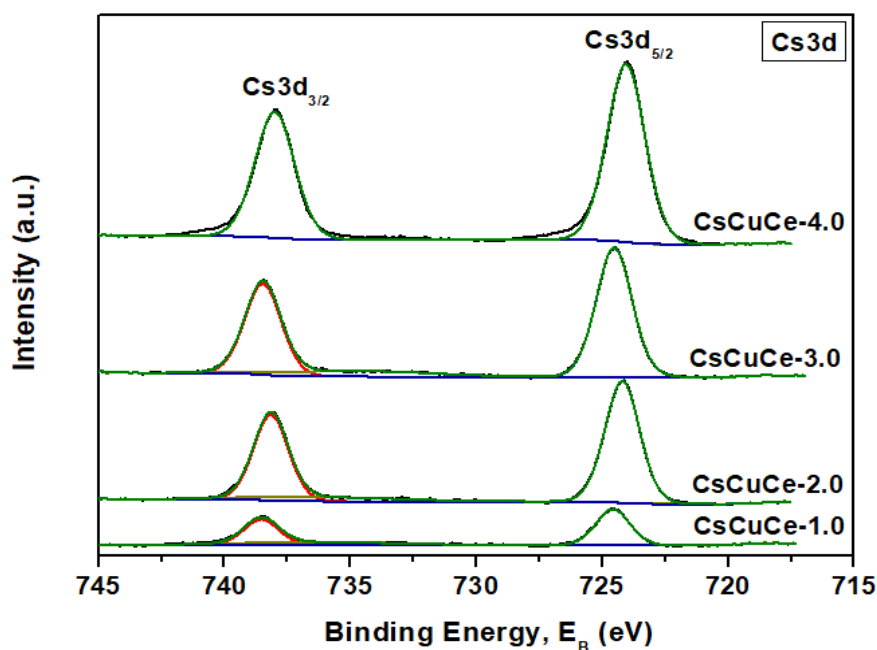
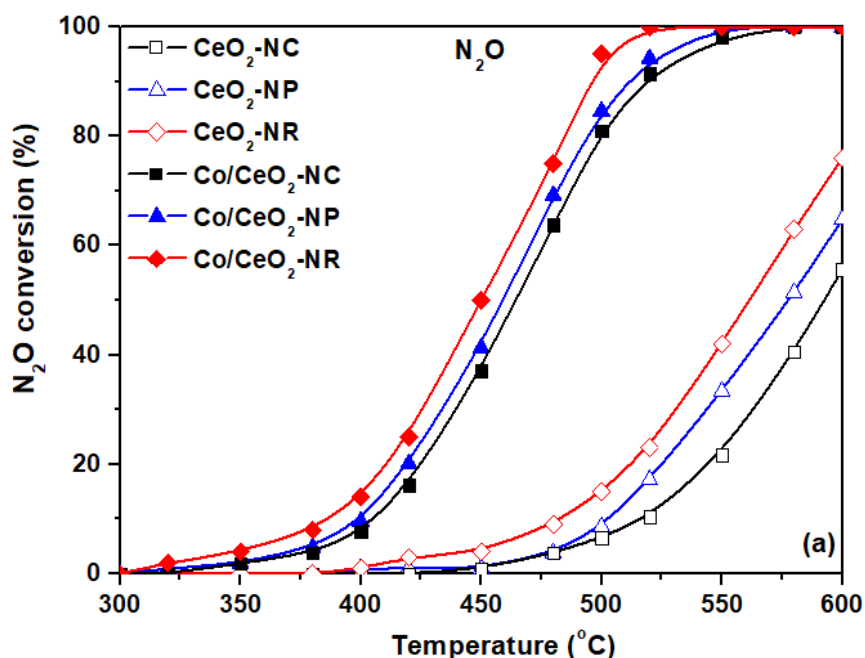


Figure 4.12. XPS Cs 3d spectra of Cs-doped Cu/CeO₂ samples. Adapted with permission from Reference [91]. Copyright© 2018, The Royal Society of Chemistry.

4.4. IMPLICATIONS IN N₂O DECOMPOSITION REACTION

4.4.1. N₂O Decomposition Performance of Co/CeO₂ Mixed Oxides

The impact of ceria's morphology on the catalytic decomposition of N₂O under oxygen deficient and oxygen excess conditions was next examined. Figures 4.13 a and b show the N₂O conversion profiles as a temperature function for bare ceria as well as of Co/CeO₂ samples in the absence and presence of oxygen, respectively. The Co/CeO₂-NR sample exhibits the best catalytic performance, both in the absence and presence of oxygen in the gas stream. Apparently, the addition of cobalt into ceria enormously enhances the catalytic efficiency without however, affecting the catalytic order of bare ceria samples, suggesting the pivotal role of ceria morphology on the deN₂O performance. In terms of half-conversion temperature (T_{50}), the following order is obtained for the mixed oxides in the absence of oxygen: Co/CeO₂-NR (449 °C) > Co/CeO₂-NP (458 °C) > Co/CeO₂-NC (464 °C). The same trend is observed in the presence of oxygen as well, although in slightly higher temperatures, due to its competitive sorption on the catalyst surface. In this point, it should be noted that the un-catalyzed reaction shows nearly zero N₂O conversion in the temperature range investigated, as previously reported [35,52,128].



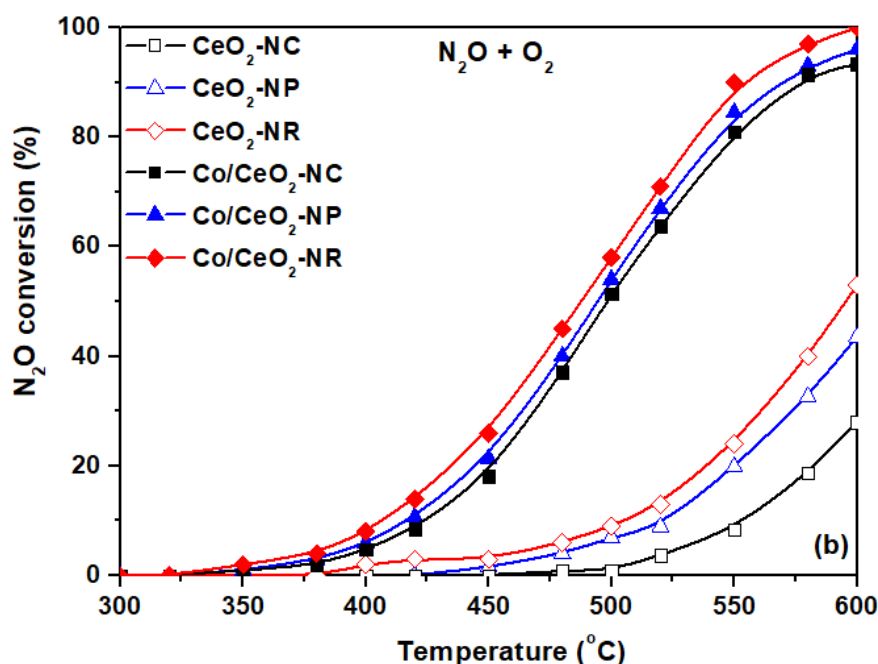
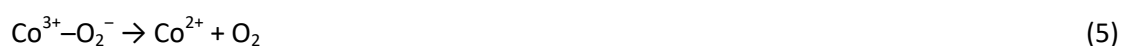


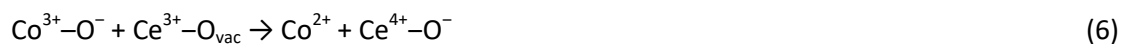
Figure 4.13. N₂O conversion as a function of temperature for bare CeO₂ and Co/CeO₂ samples of different morphology (a) in the absence and (b) in the presence of oxygen. Reaction conditions: 1000 ppm N₂O, 0 or 2 vol.% O₂, GHSV = 40,000 h⁻¹. Adapted with permission from Reference [75]. Copyright© 2019, MDPI.

The above findings can be well-interpreted by taking into account a redox-type mechanism for the decomposition of N₂O over cobalt spinel oxides [4,6,29,30,36,58,81,129–131]:



In this mechanistic sequence, N₂O is initially chemisorbed on the Co²⁺ sites (Eq. 3), which are considered as the active centres for initiating the N₂O dissociative adsorption. Then the regeneration of the active sites is taking place through the Co³⁺/Co²⁺ redox cycle, involving the combination of O⁻ into O₂⁻ (Eq. 4) and the desorption of molecular oxygen (Eq. 5), which finally leads to the regeneration of those sites [129].

However, in the case of Co₃O₄/CeO₂ mixed oxides, the excellent redox characteristics of ceria, such as oxygen storage capacity and oxygen mobility, can be further accounted for the regeneration of active sites through the following steps [129]:



Based on the above mechanistic scheme, the superiority of the Co/CeO₂ sample with the rod-like morphology can receive a consistent explanation. More specifically, nanorod-shaped ceria with {110} and {100} reactive planes exhibits enhanced oxygen kinetics and reducibility as it has the highest population of loosely bound oxygen species, which is a decisive factor in terms of deN₂O activity. In other words, the high amount of weakly bound oxygen species present in the Co/CeO₂ samples of rod-like morphology, linked directly to oxygen vacancy formation and oxygen mobility, could be considered responsible for the formation and the consequent regeneration of active sites. In this regard, a perfect interrelation between the catalytic performance (in terms of half-conversion temperature, T₅₀) and the redox properties (in terms of the ratio of surface oxygen to bulk oxygen, O_s/O_b) is disclosed, as illustrated in Figure 4.14. This clearly justifies the key role of redox properties on the deN₂O process. In a similar manner, Liu *et al.* [33] have pointed out that the synergistic interaction between the two oxide phases in CuO–CeO₂ mixed oxide, enhances the reducibility and consequently the deN₂O efficiency as the surface-adsorbed oxygen species are easily desorbed and the active sites' regeneration is enabled.

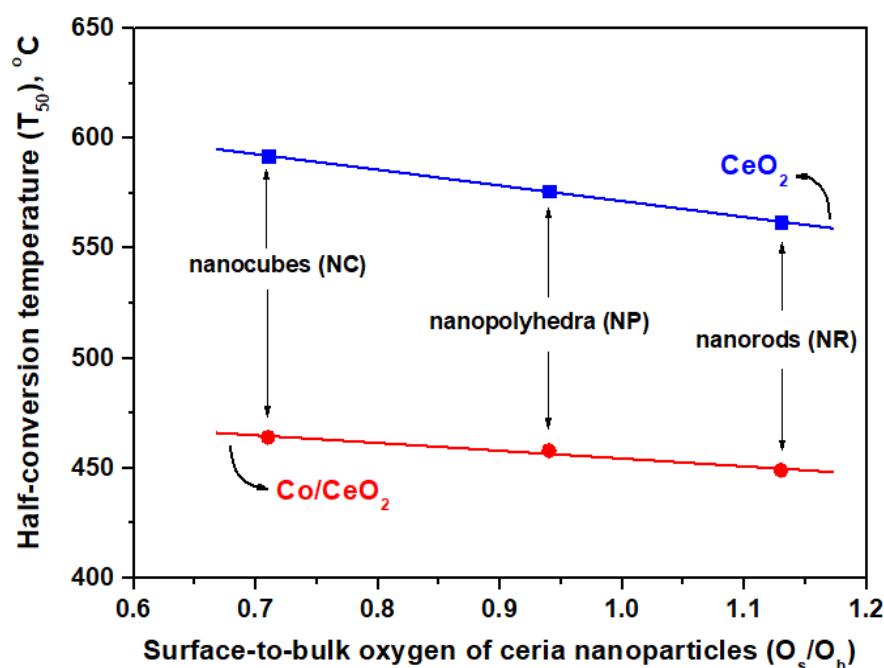


Figure 4.14. Half-conversion temperature (T₅₀) as a function of the TPR surface-to-bulk oxygen ratio (O_s/O_b). Adapted with permission from Reference [75]. Copyright© 2019, MDPI.

More interestingly, the deN₂O performance of CeO₂ as well as of Co/CeO₂ samples totally coincides, indicating the significance of ceria carrier. However, the superiority of the mixed oxides in comparison to bare ceria samples is evident, reflecting the synergistic interactions between cobalt and cerium oxides. The latter is manifested by the improved redox properties (in terms of H₂ consumption and TPR onset temperature) of Co/CeO₂ mixed oxides as compared to bare ceria (Table 4.2). In a similar manner, the addition of cobalt into ceria increases both the amount of the adsorbed oxygen species (O⁻/O₂²⁻) and Ce³⁺ (Table 4.3), related with the surface oxygen reduction and the abundance in oxygen vacancies (O_{vac}).

Moreover, ceria nanorods facilitate the reduction of Co³⁺ to Co²⁺ active sites (Table 4.3), further contributing to the superior catalytic performance of the Co/CeO₂-NR sample. Similarly, it has been recently reported that ceria nanorods stabilize the partial oxidation state of Co in CoO_x/CeO₂ catalysts *via* the facilitation of oxygen transfer at metal-support interface [132].

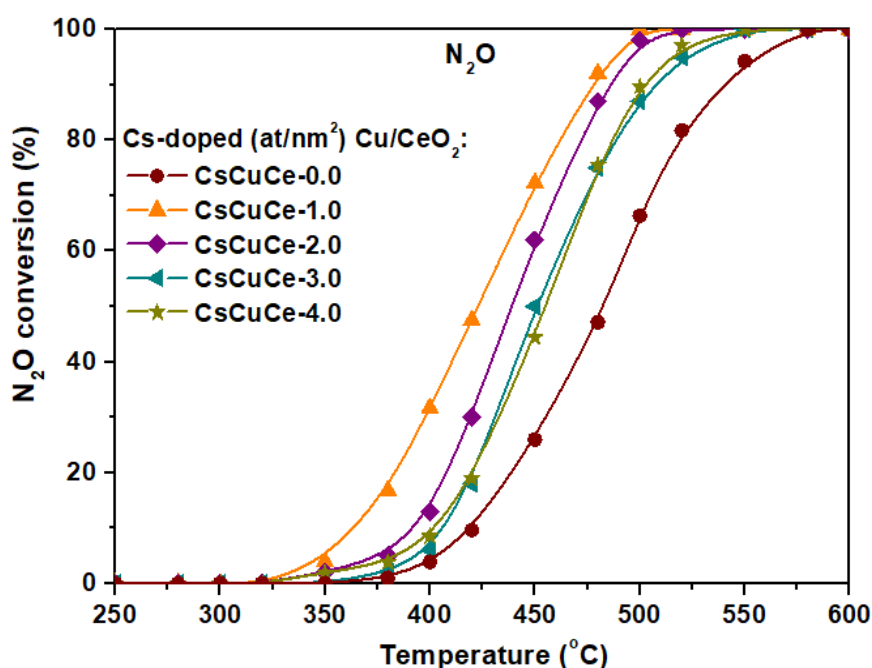
In this point, the enhanced textural characteristics (BET area and pore volume) of Co/CeO₂-NR as compared to Co/CeO₂-NC should be also mentioned, which could be further accounted for their enhanced deN₂O performance. Thus, by taking into account the specific activity normalized per unit of surface area (nmol m⁻² s⁻¹) instead of mass unit (nmol g⁻¹ s⁻¹), an inferior performance is observed for Co/CeO₂-NR as compared to Co/CeO₂-NC (Table 4.7). On the other hand, Co/CeO₂-NR exhibits superior deN₂O performance (both in terms of conversion and specific activity) as compared to Co/CeO₂-NP, despite their similar structural (crystallite size) and textural (surface area) properties (Table 4.1). The latter clearly reveals the importance of exposed facets and redox properties on the deN₂O process, as it has been similarly reported by Zabilskiy *et al.* [51] for CuO/CeO₂ nanostructures of different morphology. Therefore, on the basis of the present findings, it can be deduced that the enhanced N₂O conversion performance of Co/CeO₂-NR mixed oxides could be attributed to a compromise between redox and textural characteristics.

Table 4.7. N₂O conversion and specific activity of Co/CeO₂ samples at 420 °C; Reaction conditions: 1000 ppm N₂O, 0 or 2 vol.% O₂, GHSV = 40,000 h⁻¹.

Sample	N ₂ O conversion (%)		Specific activity			
	O ₂ absence	O ₂ presence	O ₂ absence		O ₂ presence	
			r (nmol g ⁻¹ s ⁻¹)	r (nmol m ⁻² s ⁻¹)	r (nmol g ⁻¹ s ⁻¹)	r (nmol m ⁻² s ⁻¹)
Co/CeO ₂ -NC	16.2	8.6	166	5.9	88	3.1
Co/CeO ₂ -NP	20.2	10.7	207	2.9	109	1.5
Co/CeO ₂ -NR	25	14	256	3.6	143	2.0

4.4.2. N₂O Decomposition Performance of Cs-promoted Cu/CeO₂ Mixed Oxides

Figure 4.15a depicts the deN₂O performance of Cs-doped (0–4.0 at Cs/nm²) Cu/CeO₂ mixed oxides in the absence of oxygen. The un-doped sample (CsCuCe-0.0) refers to the Cu/CeO₂ mixed oxide prepared by the precipitation method, *i.e.*, the optimum synthesis method as revealed in a previous work [66]. Herein, the potential to further enhance the deN₂O performance by means of alkali promotion is explored. The pronounced effect of Cs-doping is evident in Figure 4.15a. The optimum performance is obtained for a Cs-doping of 1.0 at Cs/nm² (CsCuCe-1.0), whereas a further increase of Cs content results in a progressive degradation. In particular, the following deN₂O performance, in terms of half-conversion temperature (T₅₀), is recorded: CsCuCe-0.0 (480 °C) < CsCuCe-4.0 (455 °C) < CsCuCe-3.0 (450 °C) < CsCuCe-2.0 (440 °C) < CsCuCe-1.0 (420 °C). Hence, the N₂O conversion profile of Cu/CeO₂ sample can be shifted by about 60 °C to lower temperatures by alkali promotion, implying its beneficial effect on deN₂O process. The corresponding catalytic results under oxygen excess conditions (2.0 v/v% O₂) are shown in Figure 4.15b.



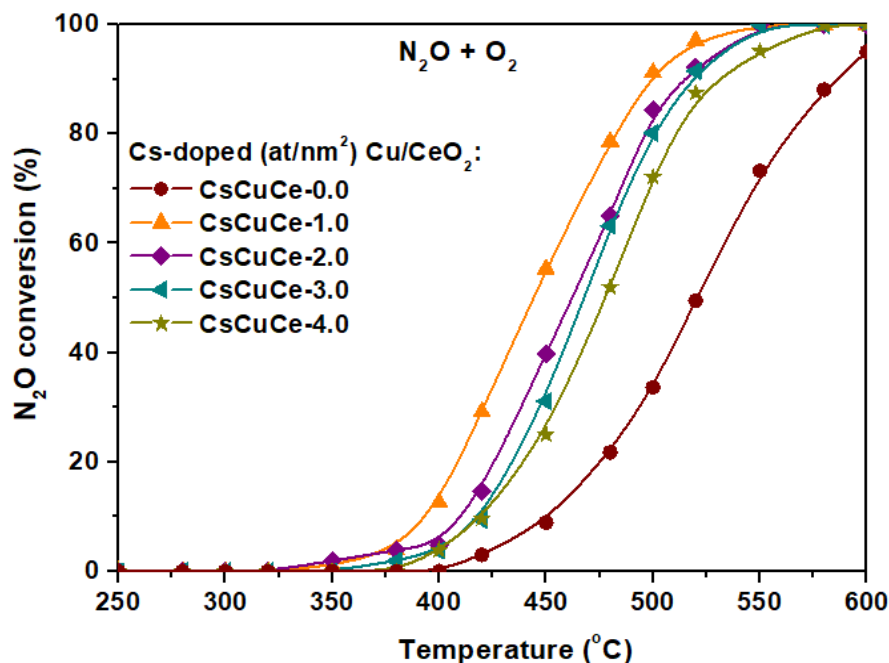


Figure 4.15. N₂O conversion profiles of Cs-doped Cu/CeO₂ samples (a) in the absence and (b) in the presence of oxygen. Reaction conditions: 1000 ppmv N₂O, 0 or 2.0 v/v% O₂ balanced with He; GHSV = 40,000 h⁻¹. Adapted with permission from Reference [91]. Copyright© 2018, The Royal Society of Chemistry.

Taking into account the co-existence of oxygen excess in real exhaust conditions [133], the enhanced deN₂O performance under oxidizing conditions is a prerequisite. In view of this fact, the inhibiting role of oxygen on N₂O decomposition, due to its competitive adsorption, has been well documented [1,106,134]. By comparing the deN₂O performance in the absence (Fig. 4.15a) and in the presence (Fig. 4.15b) of oxygen the following remarks can be drawn:

- (i) The same conversion sequence amongst the different samples is observed both in the absence and presence of oxygen.
- (ii) The deN₂O performance is hindered by oxygen excess, but to a different extent depending on Cs doping; the N₂O conversion profile of un-doped sample is up-shifted by 45 °C compared to 20 °C for the optimum promoted catalyst (CsCuCe-1.0). The latter is of major importance, demonstrating the potential of Cs-doped samples to satisfactorily abate N₂O under oxygen excess conditions.

Besides the resistance to excess oxygen, the enhanced deN₂O performance in a wide range of GHSV values and for a long time of stream (stability) is a prerequisite for practical applications. In this regard, the impact of GHSV and time-on-stream (TOS) on the N₂O conversion of the optimally promoted catalyst (CsCuCe-1.0) is next explored. Figure 4.16

depicts the effect of GHSV in the range of 10,000–40,000 h⁻¹, which usually exist in real exhaust systems [133]. It is obvious that the N₂O conversion profile is only slightly shifted to higher temperatures upon increasing the GHSV from 10,000 h⁻¹ to 40,000 h⁻¹, demonstrating the ability of the Cs-doped catalyst to abate N₂O in a wide range of GHSV values. More importantly, the N₂O conversion performance of Cs-doped samples remains stable *ca.* 90% for at least 12 h at 500 °C and under oxygen excess (Figure 4.17), indicating their potential for practical applications. However, the influence of other substances co-existing in real exhaust systems, such as H₂O and NO, on the activity and stability performance of Cs-doped Cu/CeO₂ samples, should be further explored to assess their applicability.

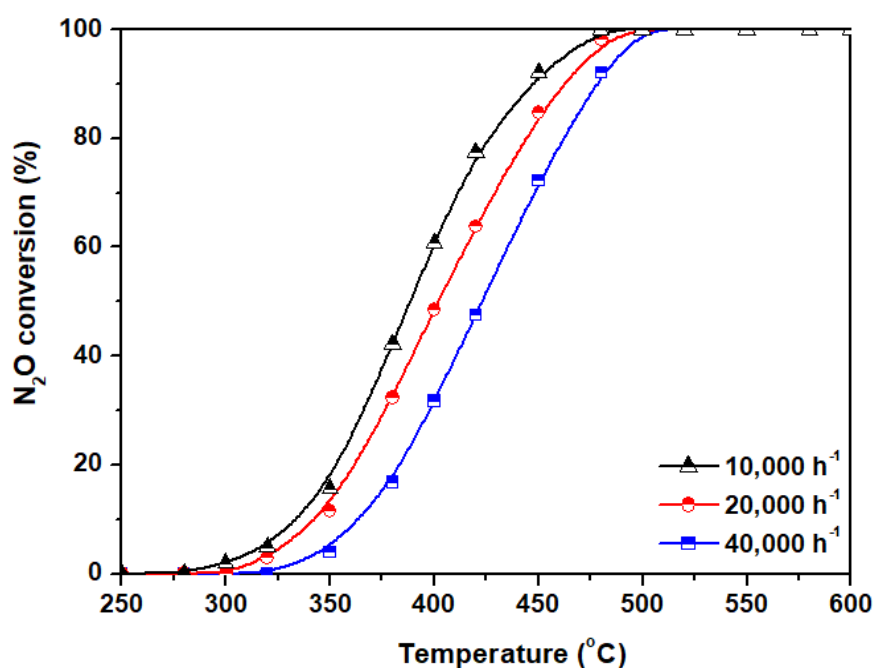


Figure 4.16. Effect of GHSV on the deN₂O performance of optimally promoted Cs-doped Cu/CeO₂ sample (CsCuCe-1.0). Reaction conditions: 1000 ppmv N₂O balanced with He; GHSV = 40,000 h⁻¹. Adapted with permission from Reference [91]. Copyright© 2018, The Royal Society of Chemistry.

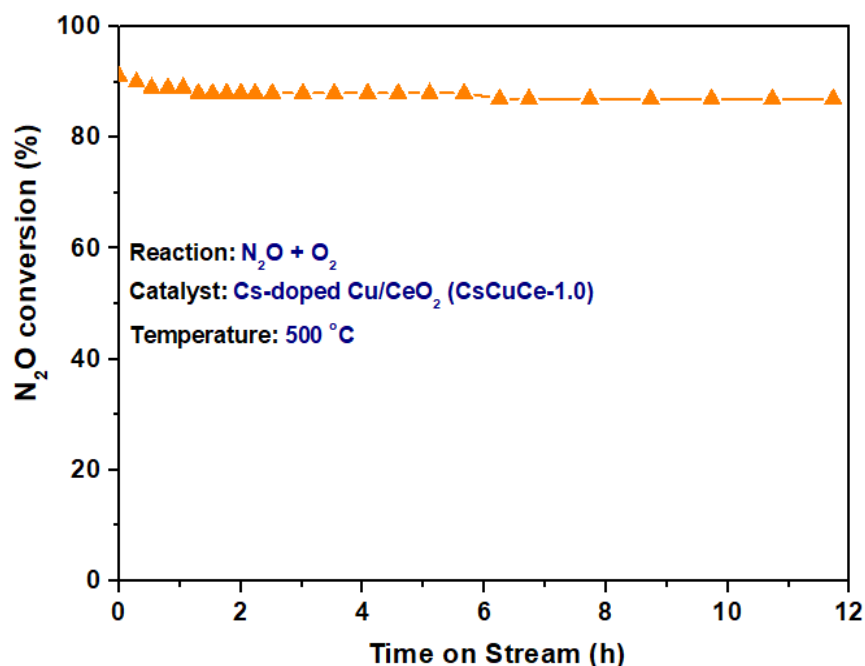


Figure 4.17. Effect of time-on-stream (TOS) on the deN₂O performance of optimally promoted Cs-doped Cu/CeO₂ sample (CsCuCe-1.0) in the presence of oxygen. Reaction conditions: 1000 ppmv N₂O, 2.0 v/v% O₂ balanced with He; GHSV = 40,000 h⁻¹. Adapted with permission from Reference [91]. Copyright© 2018, The Royal Society of Chemistry.

Figure 4.18 schematically illustrates the optimization approach followed in order to maximize the deN₂O performance of Cu/CeO₂ mixed oxides. The figure depicts the N₂O conversion profiles of the following three samples: (i) the Cu/CeO₂ sample prepared by the impregnation method, employing a commercial CeO₂ sample (Fluka) as supporting carrier (reference sample) [66], (ii) the Cu/CeO₂ sample optimized through synthesis procedure, *i.e.*, co-precipitation [66], (iii) the Cu/CeO₂ sample optimized by simultaneously applying the most favourable preparation method in addition to alkali promotion. The results clearly revealed the effectiveness of the proposed approach. The fine-tuning of Cu/CeO₂ mixed oxides by means of synthesis procedure and alkali promotion (Cs) can boost the catalytic performance, offering a half-conversion temperature (T₅₀) of *ca.* 200 °C lower as compared to reference Cu/CeO₂ sample. It should be noted here that an additional improvement is expected by engineering the size and shape of both CuO and CeO₂ particles at nanometer scale [65,135–137].

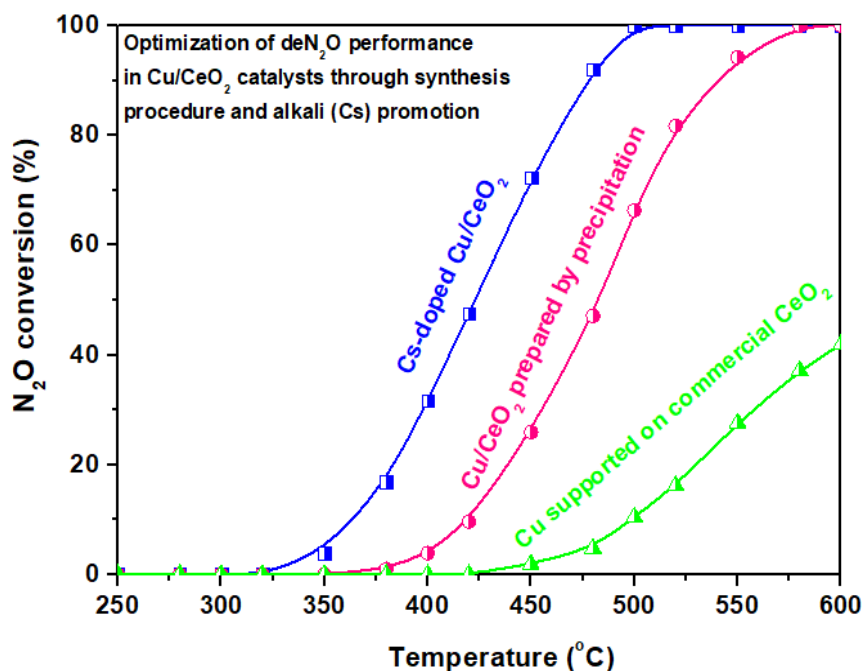


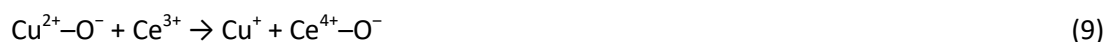
Figure 4.18. Effect of synthesis procedure and alkali promotion on the deN₂O performance of Cu/CeO₂ mixed oxides. Reaction conditions: 1000 ppmv N₂O balanced with He; GHSV = 40,000 h⁻¹. Adapted with permission from Reference [91]. Copyright© 2018, The Royal Society of Chemistry.

In Table 4.8, the deN₂O performance (in terms of T₅₀) of the most effective Cs-doped Cu/CeO₂ sample (1.0 at/nm²) is presented, in comparison with those reported in the literature for Cu/CeO₂ mixed oxides as well as with those of highly active noble metal-based catalysts. It is obvious that the deN₂O performance of the present samples is superior as compared to that of most Cu/CeO₂ samples with similar Cu content and noble-metal based catalysts under similar reaction conditions, being however inferior to that of Rh-based catalysts.

In light of the above results, it can be certainly inferred that the preparation method in conjunction with alkali promotion can exert significant modifications on the redox/surface properties of Cu/CeO₂ mixed oxides, which can be then reflected on the catalytic performance. In particular, the Cu/CeO₂ samples prepared by precipitation and subsequently promoted by cesium demonstrated the optimum deN₂O performance.

These findings can be well-rationalized on the basis of a redox-type mechanism, thoroughly described in previous studies [66,138], involving N₂O activation/decomposition on active sites through electron transfer, followed by the regeneration of the catalyst surface by the desorption of adsorbed oxygen species. In this particular scheme, the oxygen recombination steps are necessary to occur, in order for the active sites to be regenerated. On the basis of

this mechanistic sequence, the regeneration of active sites could be considered to take place between Cu²⁺/Cu⁺ and Ce³⁺/Ce⁴⁺ redox pairs:



The optimum deN₂O performance of the CsCuCe-1.0 sample could be mainly interpreted by taking into account the TPR and XPS findings, which reveal the electronic/redox changes induced by cesium promotion. According to the results, the CsCuCe-1.0 sample demonstrates the lowest amount of Ce³⁺ and the highest amount of Cu⁺, a fact that could be ascribed to the Cs-aided synergetic interaction between copper and cerium which in turn facilitates the redox pairs Cu²⁺/Cu⁺ and Ce³⁺/Ce⁴⁺. The latter can be considered responsible for the enhanced performance of CsCuCe-1.0 sample on the basis of the above-described reaction scheme.

Table 4.8. N₂O conversion performance of as-prepared samples in comparison to those reported in the literature.

Catalyst	Preparation method	Reaction conditions	T ₅₀ (°C)	Reference
Cs promoted 20 wt.% Cu/CeO ₂	Precipitation/Cs-doping by impregnation	0.1% N ₂ O; GHSV = 40,000 h ⁻¹ ; WHSV = 90,000 cm ³ h ⁻¹ g ⁻¹	420	[91]
20 wt.% Cu/CeO ₂	Precipitation	0.1% N ₂ O; GHSV = 40,000 h ⁻¹ ; WHSV = 90,000 cm ³ h ⁻¹ g ⁻¹	480	[91]
20 wt.% Cu/CeO ₂	Exotemplating	0.1% N ₂ O; GHSV = 40,000 h ⁻¹ ; WHSV = 90,000 cm ³ h ⁻¹ g ⁻¹	~485	[66]
20 wt.% Cu/CeO ₂	Mechanical mixing	0.1% N ₂ O; GHSV = 40,000 h ⁻¹ ; WHSV = 90,000 cm ³ h ⁻¹ g ⁻¹	>600	[66]
10 wt.% Cu/CeO ₂	Wet impregnation	0.25% N ₂ O; WHSV = 60,000 cm ³ h ⁻¹ g ⁻¹	380	[138]
4 wt.% Cu/CeO ₂	Deposition	0.25% N ₂ O; WHSV = 120,000 cm ³ h ⁻¹ g ⁻¹	460	[51]
Cu/CeO ₂ (Molar ratio Cu/Ce 1:1)	Hydrothermal	0.2% N ₂ O; GHSV=70,000 h ⁻¹ ; WHSV = 60,000 cm ³ h ⁻¹ g ⁻¹	380	[33]
67 mol.% Cu/CeO ₂	Citrate acid	0.26% N ₂ O; GHSV = 19,000 h ⁻¹	370	[139]
35.5 (40) mol.% Cu/CeO ₂	Hard template replication	0.25% N ₂ O; GHSV = 45,000 h ⁻¹	440	[32]
5 mol.% Cu/CeO ₂	Impregnation	5.0% N ₂ O; WHSV = 5,100 cm ³ h ⁻¹ g ⁻¹	430	[140]
0.5 wt.% Rh/Al ₂ O ₃	Impregnation	0.1% N ₂ O; GHSV = 10,000 h ⁻¹	340	[141]
0.5 wt.% Pt/Al ₂ O ₃	Impregnation	0.1% N ₂ O; GHSV = 10,000 h ⁻¹	500	[141]
0.5 wt.% Pd/Al ₂ O ₃	Impregnation	0.1% N ₂ O; GHSV = 10,000 h ⁻¹	>500	[141]

4.5. CONCLUDING REMARKS

Three different ceria nanoshaped materials (nanorods, nanocubes, nanopolyhedra) were hydrothermally synthesized and used as supports for the cobalt oxide phase. Both single CeO_2 and Co/CeO_2 mixed oxides were catalytically assessed during the decomposition of N_2O in the presence and absence of oxygen. For bare ceria samples, the following deN_2O order was obtained: $\text{CeO}_2\text{-NR}$ (nanorods) > $\text{CeO}_2\text{-NP}$ (nanopolyhedra) > $\text{CeO}_2\text{-NC}$ (nanocubes). Most importantly, cobalt addition to CeO_2 carriers greatly enhances the N_2O decomposition, without affecting the order obtained for bare ceria supports, clearly reflecting the key role of support. The present results clearly reveal the key role of support morphology on the textural, structural and redox properties, reflected then on the catalytic performance of Co/CeO_2 mixed oxides. Among the investigated samples, cobalt-ceria nanorods ($\text{Co/CeO}_2\text{-NR}$), exposing {100} and {110} facets, showed the best deN_2O performance, ascribed mainly to their abundance in Co^{2+} active sites in conjunction to their enhanced redox and textural properties.

Furthermore, the potential to adjust the surface chemistry of Cu/CeO_2 mixed oxides by means of synthesis procedure and alkali promotion is explored, by employing the N_2O decomposition as a probe reaction. The results revealed that the Cu/CeO_2 samples, pre-optimized by the co-precipitation method, can be further enhanced by Cs doping, offering highly active and oxygen-tolerant composites. The sample with 1.0 at Cs/nm² can offer a half-conversion temperature *ca.* 200 °C lower as compared to the reference Cu/CeO_2 sample. The superiority of this sample is mainly interpreted on the basis of the characterization results, which revealed that alkali addition can induce significant alterations on the electronic and redox properties. The enhanced reducibility and the abundance of partially reduced Cu^+ species, stabilized through alkali-aided metal-support interactions, could be considered responsible for the enhanced deN_2O performance of Cs-doped Cu/CeO_2 samples. The present findings corroborate that the fine-tuning of metal oxides' surface chemistry by synthesis procedures and alkali promotion can lead to highly active and stable noble metal-free catalytic composites.

REFERENCES

1. Konsolakis, M. Recent Advances on Nitrous Oxide (N₂O) Decomposition over Non-Noble-Metal Oxide Catalysts: Catalytic Performance, Mechanistic Considerations, and Surface Chemistry Aspects. *ACS Catal.* **2015**, *5*, 6397–6421. doi: 10.1021/acscatal.5b01605
2. Liu, Z.; He, F.; Ma, L.; Peng, S. Recent Advances in Catalytic Decomposition of N₂O on Noble Metal and Metal Oxide Catalysts. *Catal. Surv. Asia* **2016**, *20*, 121–132. doi: 10.1007/s10563-016-9213-y
3. Kim, M.-J.; Lee, S.-J.; Ryu, I.-S.; Jeon, M.-W.; Moon, S.-H.; Roh, H.-S.; Jeon, S.G. Catalytic decomposition of N₂O over cobalt based spinel oxides: The role of additives. *Mol. Catal.* **2017**, *442*, 202–207. doi: 10.1016/j.mcat.2017.05.029
4. Rutkowska, M. Catalytic decomposition of N₂O using a new generation of functionalized microporous and mesoporous inorganic materials. *Wiadomości Chem.* **2015**, *69*, 3–4.
5. Pietrzyk, P.; Zasada, F.; Piskorz, W.; Kotarba, A.; Sojka, Z. Computational spectroscopy and DFT investigations into nitrogen and oxygen bond breaking and bond making processes in model *de*NO_x and *de*N₂O reactions. *Catal. Today* **2007**, *119*, 219–227. doi: 10.1016/j.cattod.2006.08.054
6. Piskorz, W.; Zasada, F.; Stelmachowski, P.; Kotarba, A.; Sojka, Z. Decomposition of N₂O over the surface of cobalt spinel: A DFT account of reactivity experiments. *Catal. Today* **2008**, *137*, 418–422. doi: 10.1016/j.cattod.2008.02.027
7. Stelmachowski, P.; Zasada, F.; Piskorz, W.; Kotarba, A.; Paul, J.-F.; Sojka, Z. Experimental and DFT studies of N₂O decomposition over bare and Co-doped magnesium oxide—insights into the role of active sites topology in dry and wet conditions. *Catal. Today* **2008**, *137*, 423–428. doi: 10.1016/j.cattod.2007.11.028
8. Piskorz, W.; Zasada, F.; Stelmachowski, P.; Kotarba, A.; Sojka, Z. DFT Modeling of Reaction Mechanism and Ab Initio Microkinetics of Catalytic N₂O Decomposition over Alkaline Earth Oxides: From Molecular Orbital Picture Account to Simulation of Transient and Stationary Rate Profiles. *J. Phys. Chem. C* **2013**, *117*, 18488–18501. doi: 10.1021/jp405459g
9. Piskorz, W.; Zasada, F.; Stelmachowski, P.; Diwald, O.; Kotarba, A.; Sojka, Z. Computational and Experimental Investigations into N₂O Decomposition over MgO Nanocrystals from Thorough Molecular Mechanism to ab initio Microkinetics. *J. Phys. Chem. C* **2011**, *115*, 22451–22460. doi: 10.1021/jp2070826

10. Piumetti, M.; Hussain, M.; Fino, D.; Russo, N. Mesoporous silica supported Rh catalysts for high concentration N₂O decomposition. *Appl. Catal. B Environ.* **2015**, *165*, 158–168. doi: 10.1016/j.apcatb.2014.10.008
11. Kim, S.S.; Lee, S.J.; Hong, S.C. Effect of CeO₂ addition to Rh/Al₂O₃ catalyst on N₂O decomposition. *Chem. Eng. J.* **2011**, *169*, 173–179. doi: 10.1016/j.cej.2011.03.001
12. Hussain, M.; Fino, D.; Russo, N. Development of modified KIT-6 and SBA-15-spherical supported Rh catalysts for N₂O abatement: From powder to monolith supported catalysts. *Chem. Eng. J.* **2014**, *238*, 198–205. doi: 10.1016/j.cej.2013.06.032
13. Wu, Y.; Cordier, C.; Berrier, E.; Nuns, N.; Dujardin, C.; Granger, P. Surface reconstructions of LaCo_{1-x}Fe_xO₃ at high temperature during N₂O decomposition in realistic exhaust gas composition: Impact on the catalytic properties. *Appl. Catal. B Environ.* **2013**, *140–141*, 151–163. doi: 10.1016/j.apcatb.2013.04.002
14. Ivanov, D.V.; Pinaeva, L.G.; Isupova, L.A.; Sadovskaya, E.M.; Prosvirin, I.P.; Gerasimov, E.Yu.; Yakovleva, I.S. Effect of surface decoration with LaSrFeO₄ on oxygen mobility and catalytic activity of La_{0.4}Sr_{0.6}FeO_{3-δ} in high-temperature N₂O decomposition, methane combustion and ammonia oxidation. *Appl. Catal. A Gen.* **2013**, *457*, 42–51. doi: 10.1016/j.apcata.2013.03.007
15. Kumar, S.; Vinu, A.; Subrt, J.; Bakardjieva, S.; Rayalu, S.; Teraoka, Y.; Labhsetwar, N. Catalytic N₂O decomposition on Pr_{0.8}Ba_{0.2}MnO₃ type perovskite catalyst for industrial emission control. *Catal. Today* **2012**, *198*, 125–132. doi: 10.1016/j.cattod.2012.06.015
16. Pérez-Ramírez, J.; Santiago, M. Metal-substituted hexaaluminates for high-temperature N₂O abatement. *Chem. Commun.* **2007**, 619–621. doi: 10.1039/b613602h
17. Zhang, Y.; Wang, X.; Zhu, Y.; Zhang, T. Stabilization mechanism and crystallographic sites of Ru in Fe-promoted barium hexaaluminate under high-temperature condition for N₂O decomposition. *Appl. Catal. B Environ.* **2013**, *129*, 382–393. doi: 10.1016/j.apcatb.2012.10.001
18. Zhang, Y.; Wang, X.; Zhu, Y.; Hou, B.; Yang, X.; Liu, X.; Wang, J.; Li, J.; Zhang, T. Characterization of Fe Substitution into La-Hexaaluminate Systems and the Effect on N₂O Catalytic Decomposition. *J. Phys. Chem. C* **2014**, *118*, 1999–2010. doi: 10.1021/jp410207d
20. Amrousse, R.; Chang, P.-J.; Choklati, A.; Friche, A.; Rai, M.; Bachar, A.; Follet-Houttemane, C.; Hori, K. Catalytic decomposition of N₂O over Ni and Mg-magnetite

- catalysts. *Catal. Sci. Technol.* **2013**, *3*, 2288–2294. doi: 10.1039/c3cy00208j
21. Stelmachowski, P.; Maniak, G.; Kaczmarczyk, J.; Zasada, F.; Piskorz, W.; Kotarba, A.; Sojka, Z. Mg and Al substituted cobalt spinels as catalysts for low temperature deN₂O-Evidence for octahedral cobalt active sites. *Appl. Catal. B Environ.* **2014**, *146*, 105–111. doi: 10.1016/j.apcatb.2013.05.027
22. Grzybek, G.; Stelmachowski, P.; Gudyka, S.; Duch, J.; Ćmil, K.; Kotarba, A.; Sojka, Z. Insights into the twofold role of Cs doping on deN₂O activity of cobalt spinel catalyst-towards rational optimization of the precursor and loading. *Appl. Catal. B Environ.* **2015**, *168–169*, 509–514. doi: 10.1016/j.apcatb.2015.01.005
23. Zasada, F.; Piskorz, W.; Janas, J.; Gryboś, J.; Indyka, P.; Sojka, Z. Reactive Oxygen Species on the (100) Facet of Cobalt Spinel Nanocatalyst and their Relevance in ¹⁶O₂/¹⁸O₂ Isotopic Exchange, deN₂O, and deCH₄ Processes-A Theoretical and Experimental Account. *ACS Catal.* **2015**, *5*, 6879–6892. doi: 10.1021/acscatal.5b01900
24. Xie, P.; Luo, Y.; Ma, Z.; Wang, L.; Huang, C.; Yue, Y.; Hua, W.; Gao, Z. CoZSM-11 catalysts for N₂O decomposition: Effect of preparation methods and nature of active sites. *Appl. Catal. B Environ.* **2015**, *170–171*, 34–42. doi: 10.1016/j.apcatb.2015.01.027
25. Zou, W.; Xie, P.; Hua, W.; Wang, Y.; Kong, D.; Yue, Y.; Ma, Z.; Yang, W.; Gao, Z. Catalytic decomposition of N₂O over Cu-ZSM-5 nanosheets. *J. Mol. Catal. A Chem.* **2014**, *394*, 83–88. doi: 10.1016/j.molcata.2014.07.004
26. Zhang, X.; Shen, Q.; He, C.; Ma, C.; Cheng, J.; Liu, Z.; Hao, Z. Decomposition of nitrous oxide over Co-zeolite catalysts: role of zeolite structure and active site. *Catal. Sci. Technol.* **2012**, *2*, 1249–1258. doi: 10.1039/c2cy00465h
27. Rutkowska, M.; Piwowarska, Z.; Micek, E.; Chmielarz, L. Hierarchical Fe-, Cu- and Co-Beta zeolites obtained by mesotemplate-free method. Part I: Synthesis and catalytic activity in N₂O decomposition. *Microporous Mesoporous Mater.* **2015**, *209*, 54–65. doi: 10.1016/j.micromeso.2014.10.011
28. Xue, L.; He, H.; Liu, C.; Zhang, C.; Zhang, B. Promotion Effects and Mechanism of Alkali Metals and Alkaline Earth Metals on Cobalt-Cerium Composite Oxide Catalysts for N₂O Decomposition. *Environ. Sci. Technol.* **2009**, *43*, 890–895. doi: 10.1021/es801867y
29. Grzybek, G.; Stelmachowski, P.; Gudyka, S.; Indyka, P.; Sojka, Z.; Guillén-Hurtado, N.; Rico-Pérez, V.; Bueno-López, A.; Kotarba, A. Strong dispersion effect of cobalt spinel active phase spread over ceria for catalytic N₂O decomposition: The role of the

- interface periphery. *Appl. Catal. B Environ.* **2016**, *180*, 622–629. doi: 10.1016/j.apcatb.2015.07.027
30. Chromčáková, Ž.; Obalová, L.; Kovanda, F.; Legut, D.; Titov, A.; Ritz, M.; Fridrichová, D.; Michalik, S.; Kušrowski, P.; Jirátová, K. Effect of precursor synthesis on catalytic activity of Co_3O_4 in N_2O decomposition. *Catal. Today* **2015**, *257*, 18–25. doi: 10.1016/j.cattod.2015.03.030
31. Franken, T.; Palkovits, R. Investigation of potassium doped mixed spinels $\text{Cu}_x\text{Co}_{3-x}\text{O}_4$ as catalysts for an efficient N_2O decomposition in real reaction conditions. *Appl. Catal. B Environ.* **2015**, *176–177*, 298–305. doi: 10.1016/j.apcatb.2015.04.002
32. Zabilskiy, M.; Erjavec, B.; Djinović, P.; Pintar, A. Ordered mesoporous CuO-CeO_2 mixed oxides as an effective catalyst for N_2O decomposition. *Chem. Eng. J.* **2014**, *254*, 153–162. doi: 10.1016/j.cej.2014.05.127
33. Liu, Z.; He, C.; Chen, B.; Liu, H. CuO-CeO_2 mixed oxide catalyst for the catalytic decomposition of N_2O in the presence of oxygen. *Catal. Today* **2017**, *297*, 78–83. doi: 10.1016/j.cattod.2017.05.074
34. Yoshino, H.; Ohnishi, C.H.; Hosokawa, S.; Wada, K.; Inoue, M. Optimized synthesis method for $\text{K/Co}_3\text{O}_4$ catalyst towards direct decomposition of N_2O . *J. Mater. Sci.* **2011**, *46*, 797–805. doi: 10.1007/s10853-010-4818-4
35. Russo, N.; Fino, D.; Saracco, G.; Specchia, V. N_2O catalytic decomposition over various spinel-type oxides. *Catal. Today* **2007**, *119*, 228–232. doi: 10.1016/j.cattod.2006.08.012
36. Xue, L.; Zhang, C.; He, H.; Teraoka, Y. Catalytic decomposition of N_2O over CeO_2 promoted Co_3O_4 spinel catalyst. *Appl. Catal. B Environ.* **2007**, *75*, 167–174. doi: 10.1016/j.apcatb.2007.04.013
37. Shen, Q.; Li, L.; Li, J.; Tian, H.; Hao, Z. A study on N_2O catalytic decomposition over Co/MgO catalysts. *J. Hazard. Mater.* **2009**, *163*, 1332–1337. doi: 10.1016/j.jhazmat.2008.07.104
38. Yang, J.; Lukashuk, L.; Akbarzadeh, J.; Stöger-Pollach, M.; Peterlik, H.; Föttinger, K.; Rupprechter, G.; Schubert, U. Different Synthesis Protocols for $\text{Co}_3\text{O}_4\text{-CeO}_2$ Catalysts—Part 1: Influence on the Morphology on the Nanoscale. *Chem. Eur. J.* **2015**, *21*, 885–892. doi: 10.1002/chem.201403636
39. Wang, H.; Ye, J.L.; Liu, Y.; Li, Y.D.; Qin, Y.N. Steam reforming of ethanol over $\text{Co}_3\text{O}_4/\text{CeO}_2$ catalysts prepared by different methods. *Catal. Today* **2007**, *129*, 305–312. doi: 10.1016/j.cattod.2006.10.012

40. Qiu, N.; Zhang, J.; Wu, Z. Peculiar surface-interface properties of nanocrystalline ceria-cobalt oxides with enhanced oxygen storage capacity. *Phys. Chem. Chem. Phys.* **2014**, *16*, 22659–22664. doi: 10.1039/c4cp03390f
41. Luo, J.-Y.; Meng, M.; Li, X.; Li, X.-G.; Zha, Y.-Q.; Hu, T.-D.; Xie, Y.-N.; Zhang, J. Mesoporous Co₃O₄-CeO₂ and Pd/Co₃O₄-CeO₂ catalysts: Synthesis, characterization and mechanistic study of their catalytic properties for low-temperature CO oxidation. *J. Catal.* **2008**, *254*, 310–324. doi: 10.1016/j.jcat.2008.01.007
42. Elias, J.S.; Risch, M.; Giordano, L.; Mansour, A.N.; Shao-Horn, Y. Structure, Bonding, and Catalytic Activity of Monodisperse, Transition-Metal-Substituted CeO₂ Nanoparticles. *J. Am. Chem. Soc.* **2014**, *136*, 17193–17200. doi: 10.1021/ja509214d
43. Díez-Ramírez, J.; Sánchez, P.; Kyriakou, V.; Zafeiratos, S.; Marnellos, G.E.; Konsolakis, M.; Dorado, F. Effect of support nature on the cobalt-catalyzed CO₂ hydrogenation. *J. CO₂ Util.* **2017**, *21*, 562–571. doi: 10.1016/j.jcou.2017.08.019
44. Vinod, C.P. Surface science as a tool for probing nanocatalysis phenomena. *Catal. Today* **2010**, *154*, 113–117. doi: 10.1016/j.cattod.2010.03.018
45. Hu, P.; Huang, Z.; Amghouz, Z.; Makkee, M.; Xu, F.; Kapteijn, F.; Dikhtiarenko, A.; Chen, Y.; Gu, X.; Tang, X. Electronic Metal-Support Interactions in Single-Atom Catalysts. *Angew. Chem.* **2014**, *126*, 3486–3489. doi: 10.1002/ange.201309248
46. Cargnello, M.; Fornasiero, P.; Gorte, R.J. Opportunities for Tailoring Catalytic Properties Through Metal-Support Interactions. *Catal. Lett.* **2012**, *142*, 1043–1048. doi: 10.1007/s10562-012-0883-4
47. Mahammadunnisa, S.K.; Akanksha, T.; Krushnamurty, K.; Subrahmanyam, C. Catalytic decomposition of N₂O over CeO₂ supported Co₃O₄ catalysts. *J. Chem. Sci.* **2016**, *128*, 1795–1804. doi: 10.1007/s12039-016-1180-3
48. Cargnello, M.; Doan-Nguyen, V.V.T.; Gordon, T.R.; Diaz, R.E.; Stach, E. A.; Gorte, R.J.; Fornasiero, P.; Murray, C.B. Control of Metal Nanocrystal Size Reveals Metal-Support Interface Role for Ceria Catalysts. *Science* **2013**, *341*, 771–773. doi: 10.1126/science.1240148
49. Vayssilov, G.N.; Lykhach, Y.; Migani, A.; Staudt, T.; Petrova, G.P.; Tsud, N.; Skála, T.; Bruix, A.; Illas, F.; Prince, K.C.; Matolín, V.; Neyman, K.M.; Libuda, J. Support nanostructure boosts oxygen transfer to catalytically active platinum nanoparticles. *Nat. Mater.* **2011**, *10*, 310–315. doi: 10.1038/nmat2976
50. Lin, B.; Liu, Y.; Heng, L.; Ni, J.; Lin, J.; Jiang, L. Effect of ceria morphology on the catalytic activity of Co/CeO₂ catalyst for ammonia synthesis. *Catal. Commun.* **2017**,

- 101, 15–19. doi: 10.1016/j.catcom.2017.07.015
51. Zabilskiy, M.; Djinović, P.; Tchernychova, E.; Tkachenko, O.P.; Kustov, L.M.; Pintar, A. Nanoshaped CuO/CeO₂ Materials: Effect of the Exposed Ceria Surfaces on Catalytic Activity in N₂O Decomposition Reaction. *ACS Catal.* **2015**, *5*, 5357–5365. doi: 10.1021/acscatal.5b01044
52. Andrade-Martínez, J.; Ortega-Zarzosa, G.; Gómez-Cortés, A.; Rodríguez-González, V. N₂O catalytic reduction over different porous SiO₂ materials functionalized with copper. *Powder Technol.* **2015**, *274*, 305–312. doi: 10.1016/j.powtec.2015.01.048
53. Mei, J.; Ke, Y.; Yu, Z.; Hu, X.; Qu, Z.; Yan, N. Morphology-dependent properties of Co₃O₄/CeO₂ catalysts for low temperature dibromomethane (CH₂Br₂) oxidation. *Chem. Eng. J.* **2017**, *320*, 124–134. doi: 10.1016/j.cej.2017.03.038
54. Hu, F.; Peng, Y.; Chen, J.; Liu, S.; Song, H.; Li, J. Low content of CoO_x supported on nanocrystalline CeO₂ for toluene combustion: The importance of interfaces between active sites and supports. *Appl. Catal. B Environ.* **2019**, *240*, 329–336. doi: 10.1016/j.apcatb.2018.06.024
55. Zasada, F.; Stelmachowski, P.; Maniak, G.; Paul, J.-F.; Kotarba, A.; Sojka, Z. Potassium Promotion of Cobalt Spinel Catalyst for N₂O Decomposition—Accounted by Work Function Measurements and DFT Modelling. *Catal. Lett.* **2009**, *127*, 126–131. doi: 10.1007/s10562-008-9655-6
56. Maniak, G.; Stelmachowski, P.; Kotarba, A.; Sojka, Z.; Rico-Pérez, V.; Bueno-López, A. Rationales for the selection of the best precursor for potassium doping of cobalt spinel based deN₂O catalyst. *Appl. Catal. B Environ.* **2013**, *136–137*, 302–307. doi: 10.1016/j.apcatb.2013.01.068
57. Maniak, G.; Stelmachowski, P.; Zasada, F.; Piskorz, W.; Kotarba, A.; Sojka, Z. Guidelines for optimization of catalytic activity of 3d transition metal oxide catalysts in N₂O decomposition by potassium promotion. *Catal. Today* **2011**, *176*, 369–372. doi: 10.1016/j.cattod.2010.11.043
58. Stelmachowski, P.; Maniak, G.; Kotarba, A.; Sojka, Z. Strong electronic promotion of Co₃O₄ towards N₂O decomposition by surface alkali dopants. *Catal. Commun.* **2009**, *10*, 1062–1065. doi: 10.1016/j.catcom.2008.12.057
59. Inger, M.; Kowalik, P.; Saramok, M.; Wilk, M.; Stelmachowski, P.; Maniak, G.; Granger, P.; Kotarba, A.; Sojka, Z. Laboratory and pilot scale synthesis, characterization and reactivity of multicomponent cobalt spinel catalyst for low temperature removal of N₂O from nitric acid plant tail gases. *Catal. Today* **2011**, *176*, 365–368. doi:

- 10.1016/j.cattod.2010.11.044
60. Obalová, L.; Maniak, G.; Karásková, K.; Kovanda, F.; Kotarba, A. Electronic nature of potassium promotion effect in Co-Mn-Al mixed oxide on the catalytic decomposition of N₂O. *Catal. Commun.* **2011**, *12*, 1055–1058. doi: 10.1016/j.catcom.2011.03.017
61. Obalová, L.; Karásková, K.; Wach, A.; Kustrowski, P.; Mamulová-Kutláková, K.; Michalik, S.; Jirátová, K. Alkali metals as promoters in Co-Mn-Al mixed oxide for N₂O decomposition. *Appl. Catal. A Gen.* **2013**, *462–463*, 227–235. doi: 10.1016/j.apcata.2013.05.011
62. Obalová, L.; Karásková, K.; Jirátová, K.; Kovanda, F. Effect of potassium in calcined Co-Mn-Al layered double hydroxide on the catalytic decomposition of N₂O. *Appl. Catal. B Environ.* **2009**, *90*, 132–140. doi: 10.1016/j.apcatb.2009.03.002
63. Karásková, K.; Obalová, L.; Jirátová, K.; Kovanda, F. Effect of promoters in Co-Mn-Al mixed oxide catalyst on N₂O decomposition. *Chem. Eng. J.* **2010**, *160*, 480–487. doi: 10.1016/j.cej.2010.03.058
64. Xue, L.; Zhang, C.; He, H.; Teraoka, Y. Promotion effect of residual K on the decomposition of N₂O over cobalt-cerium mixed oxide catalyst. *Catal. Today* **2007**, *126*, 449–455. doi: 10.1016/j.cattod.2007.06.021
65. Konsolakis, M. The role of Copper–Ceria interactions in catalysis science: Recent theoretical and experimental advances. *Appl. Catal. B Environ.* **2016**, *198*, 49–66. doi: 10.1016/j.apcatb.2016.05.037
66. Konsolakis, M.; Carabineiro, S.A.C.; Papista, E.; Marnellos, G.E.; Tavares, P.B.; Agostinho Moreira, J.; Romaguera-Barcelay, Y.; Figueiredo, J.L. Effect of preparation method on the solid state properties and the deN₂O performance of CuO-CeO₂ oxides. *Catal. Sci. Technol.* **2015**, *5*, 3714–3727. doi: 10.1039/c5cy00343a
67. Yang, Z.; Xie, L.; Ma, D.; Wang, G. Origin of the High Activity of the Ceria-Supported Copper Catalyst for H₂O Dissociation. *J. Phys. Chem. C* **2011**, *115*, 6730–6740. doi: 10.1021/jp200005r
68. Qiao, Z.-A.; Wu, Z.; Dai, S. Shape-Controlled Ceria-based Nanostructures for Catalysis Applications. *ChemSusChem* **2013**, *6*, 1821–1833. doi: 10.1002/cssc.201300428
69. Dong, L.; Yao, X.; Chen, Y. Interactions among supported copper-based catalyst components and their effects on performance: A review. *Chinese J. Catal.* **2013**, *34*, 851–864. doi: 10.1016/S1872-2067(12)60592-0
70. Szabová, L.; Camellone, M.F.; Huang, M.; Matolín, V.; Fabris, S. Thermodynamic, electronic and structural properties of Cu/CeO₂ surfaces and interfaces from first-

- principles DFT+U calculations. *J. Chem. Phys.* **2010**, *133*, 234705. doi: 10.1063/1.3515424
71. Szabová, L.; Skála, T.; Matolínová, I.; Fabris, S.; Farnesi Camellone, M.; Matolín, V. Copper-ceria interaction: A combined photoemission and DFT study. *Appl. Surf. Sci.* **2013**, *267*, 12–16. doi: 10.1016/j.apsusc.2012.04.098
72. Allwar, A.; Md Noor, A.; Nawi, M. Textural Characteristics of Activated Carbons Prepared from Oil Palm Shells Activated with ZnCl₂ and Pyrolysis Under Nitrogen and Carbon Dioxide. *J. Phys. Sci.* **2008**, *19*, 93–104.
73. Anushree; Kumar, S.; Sharma, C. Synthesis, characterization and catalytic wet air oxidation property of mesoporous Ce_{1-x}Fe_xO₂ mixed oxides. *Mater. Chem. Phys.* **2015**, *155*, 223–231. doi: 10.1016/j.matchemphys.2015.02.034
74. Tan, L.; Tao, Q.; Gao, H.; Li, J.; Jia, D.; Yang, M. Preparation and catalytic performance of mesoporous ceria-base composites CuO/CeO₂, Fe₂O₃/CeO₂ and La₂O₃/CeO₂. *J. Porous Mater.* **2017**, *24*, 795–803. doi: 10.1007/s10934-016-0318-5
75. Lykaki, M.; Papista, E.; Kaklidis, N.; Carabineiro, S.A.C.; Konsolakis, M. Ceria nanoparticles' morphological effects on the N₂O decomposition performance of Co₃O₄/CeO₂ mixed oxides. *Catalysts* **2019**, *9*, 233. doi: 10.3390/catal9030233
76. Sharma, V.; Eberhardt, K.M.; Sharma, R.; Adams, J.B.; Crozier, P.A. A spray drying system for synthesis of rare-earth doped cerium oxide nanoparticles. *Chem. Phys. Lett.* **2010**, *495*, 280–286. doi: 10.1016/j.cplett.2010.06.060
77. Farahmandjou, M.; Zarinkamar, M. Synthesis of nano-sized ceria (CeO₂) particles via a cerium hydroxy carbonate precursor and the effect of reaction temperature on particle morphology. *J. Ultrafine Grained Nanostructured Mater.* **2015**, *48*, 5–10. doi: 10.7508/JUFGNSM.2015.01.002
78. Yu, S.-W.; Huang, H.-H.; Tang, C.-W.; Wang, C.-B. The effect of accessible oxygen over Co₃O₄-CeO₂ catalysts on the steam reforming of ethanol. *Int. J. Hydrogen Energy* **2014**, *39*, 20700–20711. doi: 10.1016/j.ijhydene.2014.07.139
79. Konsolakis, M.; Carabineiro, S.A.C.; Marnellos, G.E.; Asad, M.F.; Soares, O.S.G.P.; Pereira, M.F.R.; Órfão, J.J.M.; Figueiredo, J.L. Effect of cobalt loading on the solid state properties and ethyl acetate oxidation performance of cobalt-cerium mixed oxides. *J. Colloid Interface Sci.* **2017**, *496*, 141–149. doi: 10.1016/j.jcis.2017.02.014
80. Mock, S.A.; Sharp, S.E.; Stoner, T.R.; Radetic, M.J.; Zell, E.T.; Wang, R. CeO₂ nanorods-supported transition metal catalysts for CO oxidation. *J. Colloid Interface Sci.* **2016**, *466*, 261–267. doi: 10.1016/j.jcis.2015.12.026

81. Wang, Y.; Hu, X.; Zheng, K.; Zhang, H.; Zhao, Y. Effect of precipitants on the catalytic activity of Co–Ce composite oxide for N₂O catalytic decomposition. *Reac. Kinet. Mech. Cat.* **2018**, *123*, 707–721. doi: 10.1007/s11144-017-1293-9
82. Wang, L.; Liu, H. Mesoporous Co-CeO₂ catalyst prepared by colloidal solution combustion method for reverse water-gas shift reaction. *Catal. Today* **2018**, *316*, 155–161. doi: 10.1016/j.cattod.2018.04.015
83. Kumar Megarajan, S.; Rayalu, S.; Teraoka, Y.; Labhsetwar, N. High NO oxidation catalytic activity on non-noble metal based cobalt-ceria catalyst for diesel soot oxidation. *J. Mol. Catal. A Chem.* **2014**, *385*, 112–118. doi: 10.1016/j.molcata.2014.01.026
84. Cui, Y.; Dai, W.-L. Support morphology and crystal plane effect of Cu/CeO₂ nanomaterial on the physicochemical and catalytic properties for carbonate hydrogenation. *Catal. Sci. Technol.* **2016**, *6*, 7752–7762. doi: 10.1039/c6cy01575a
85. Guo, X.; Zhou, R. A new insight into the morphology effect of ceria on CuO/CeO₂ catalysts for CO selective oxidation in hydrogen-rich gas. *Catal. Sci. Technol.* **2016**, *6*, 3862–3871. doi: 10.1039/c5cy01816a
86. Wang, C.; Cheng, Q.; Wang, X.; Ma, K.; Bai, X.; Tan, S.; Tian, Y.; Ding, T.; Zheng, L.; Zhang, J.; Li, X. Enhanced catalytic performance for CO preferential oxidation over CuO catalysts supported on highly defective CeO₂ nanocrystals. *Appl. Surf. Sci.* **2017**, *422*, 932–943. doi: 10.1016/j.apsusc.2017.06.017
87. Dou, J.; Tang, Y.; Nie, L.; Andolina, C.M.; Zhang, X.; House, S.; Li, Y.; Yang, J.; Tao, F. Complete Oxidation of Methane on Co₃O₄/CeO₂ Nanocomposite: A Synergic Effect. *Catal. Today* **2018**, *311*, 48–55. doi: 10.1016/j.cattod.2017.12.027
88. Konsolakis, M.; Sgourakis, M.; Carabineiro, S.A.C. Surface and redox properties of cobalt-ceria binary oxides: On the effect of Co content and pretreatment conditions. *Appl. Surf. Sci.* **2015**, *341*, 48–54. doi: 10.1016/j.apsusc.2015.02.188
89. Ang, M.L.; Oemar, U.; Kathiraser, Y.; Saw, E.T.; Lew, C.H.K.; Du, Y.; Borgna, A.; Kawi, S. High-temperature water-gas shift reaction over Ni/xK/CeO₂ catalysts: Suppression of methanation via formation of bridging carbonyls. *J. Catal.* **2015**, *329*, 130–143. doi: 10.1016/j.jcat.2015.04.031
90. Lee, Y.-L.; Jha, A.; Jang, W.-J.; Shim, J.-O.; Rode, C.V.; Jeon, B.-H.; Bae, J.W.; Roh, H.-S. Effect of alkali and alkaline earth metal on Co/CeO₂ catalyst for the water-gas shift reaction of waste derived synthesis gas. *Appl. Catal. A Gen.* **2018**, *551*, 63–70. doi: 10.1016/j.apcata.2017.12.009

91. Lykaki, M.; Papista, E.; Carabineiro, S.A.C.; Tavares, P.B.; Konsolakis, M. Optimization of N₂O decomposition activity of CuO-CeO₂ mixed oxides by means of synthesis procedure and alkali (Cs) promotion. *Catal. Sci. Technol.* **2018**, *8*, 2312–2322. doi: 10.1039/c8cy00316e
92. Shi, Z.; Yang, H.; Gao, P.; Li, X.; Zhong, L.; Wang, H.; Liu, H.; Wei, W.; Sun, Y. Direct conversion of CO₂ to long-chain hydrocarbon fuels over K-promoted CoCu/TiO₂ catalysts. *Catal. Today* **2018**, *311*, 65–73. doi: 10.1016/j.cattod.2017.09.053
93. Cao, S.; Monnier, J.R.; Regalbuto, J.R. Alkali promotion of alumina-supported ruthenium catalysts for hydrogenation of levulinic acid to γ -valerolactone. *J. Catal.* **2017**, *347*, 72–78. doi: 10.1016/j.jcat.2017.01.009
94. Srifá, A.; Okura, K.; Okanishi, T.; Muroyama, H.; Matsui, T.; Eguchi, K. Hydrogen production by ammonia decomposition over Cs-modified Co₃Mo₃N catalysts. *Appl. Catal. B Environ.* **2017**, *218*, 1–8. doi: 10.1016/j.apcatb.2017.06.034
95. Piumetti, M.; Bensaid, S.; Andana, T.; Russo, N.; Pirone, R.; Fino, D. Cerium-copper oxides prepared by solution combustion synthesis for total oxidation reactions: From powder catalysts to structured reactors. *Appl. Catal. B Environ.* **2017**, *205*, 455–468. doi: 10.1016/j.apcatb.2016.12.054
96. Caputo, T.; Lisi, L.; Pirone, R.; Russo, G. On the role of redox properties of CuO/CeO₂ catalysts in the preferential oxidation of CO in H₂-rich gases. *Appl. Catal. A Gen.* **2008**, *348*, 42–53. doi: 10.1016/j.apcata.2008.06.025
97. Qin, J.; Lu, J.; Cao, M.; Hu, C. Synthesis of porous CuO-CeO₂ nanospheres with an enhanced low-temperature CO oxidation activity. *Nanoscale* **2010**, *2*, 2739–2743. doi: 10.1039/c0nr00446d
98. Carabineiro, S.A.C.; Bastos, S.S.T.; Órfão, J.J.M.; Pereira, M.F.R.; Delgado, J.J.; Figueiredo, J.L. Exotemplated ceria catalysts with gold for CO oxidation. *Appl. Catal. A Gen.* **2010**, *381*, 150–160. doi: 10.1016/j.apcata.2010.04.001
99. Carabineiro, S.A.C.; Silva, A.M.T.; Dražić, G.; Tavares, P.B.; Figueiredo, J.L. Gold nanoparticles on ceria supports for the oxidation of carbon monoxide. *Catal. Today* **2010**, *154*, 21–30. doi: 10.1016/j.cattod.2010.01.036
100. Chen, X.; Carabineiro, S.A.C.; Bastos, S.S.T.; Tavares, P.B.; Órfão, J.J.M.; Pereira, M.F.R.; Figueiredo, J.L. Catalytic oxidation of ethyl acetate on cerium-containing mixed oxides. *Appl. Catal. A Gen.* **2014**, *472*, 101–112. doi: 10.1016/j.apcata.2013.11.043
101. Carabineiro, S.A.C.; Chen, X.; Konsolakis, M.; Psarras, A.C.; Tavares, P.B.; Órfão, J.J.M.;

- Pereira, M.F.R.; Figueiredo, J.L. Catalytic oxidation of toluene on Ce-Co and La-Co mixed oxides synthesized by exotemplating and evaporation methods. *Catal. Today* **2015**, *244*, 161–171. doi: 10.1016/j.cattod.2014.06.018
102. Piumetti, M.; Bensaid, S.; Russo, N.; Fino, D. Nanostructured ceria-based catalysts for soot combustion: Investigations on the surface sensitivity. *Appl. Catal. B Environ.* **2015**, *165*, 742–751. doi: 10.1016/j.apcatb.2014.10.062
103. Konsolakis, M.; Ioakeimidis, Z. Surface/structure functionalization of copper-based catalysts by metal-support and/or metal-metal interactions. *Appl. Surf. Sci.* **2014**, *320*, 244–255. doi: 10.1016/j.apsusc.2014.08.114
104. Mai, H.; Zhang, D.; Shi, L.; Yan, T.; Li, H. Highly active Ce_{1-x}Cu_xO₂ nanocomposite catalysts for the low temperature oxidation of CO. *Appl. Surf. Sci.* **2011**, *257*, 7551–7559. doi: 10.1016/j.apsusc.2011.03.124
105. Evin, H.N.; Jacobs, G.; Ruiz-Martinez, J.; Thomas, G.A.; Davis, B.H. Low Temperature Water–Gas Shift: Alkali Doping to Facilitate Formate C–H Bond Cleaving over Pt/Ceria Catalysts—An Optimization Problem. *Catal. Lett.* **2008**, *120*, 166–178. doi: 10.1007/s10562-007-9297-0
106. Carabineiro, S.A.C.; Papista, E.; Marnellos, G.E.; Tavares, P.B.; Maldonado-Hódar, F.J.; Konsolakis, M. Catalytic decomposition of N₂O on inorganic oxides: Effect of doping with Au nanoparticles. *Mol. Catal.* **2017**, *436*, 78–89. doi: 10.1016/j.mcat.2017.04.009
107. Arango-Díaz, A.; Moretti, E.; Talon, A.; Storaro, L.; Lenarda, M.; Núñez, P.; Marrero-Jerez, J.; Jiménez-Jiménez, J.; Jiménez-López, A.; Rodríguez-Castellón, E. Preferential CO oxidation (CO-PROX) catalyzed by CuO supported on nanocrystalline CeO₂ prepared by a freeze-drying method. *Appl. Catal. A Gen.* **2014**, *477*, 54–63. doi: 10.1016/j.apcata.2014.02.033
108. Luo, M.-F.; Song, Y.-P.; Lu, J.-Q.; Wang, X.-Y.; Pu, Z.-Y. Identification of CuO Species in High Surface Area CuO-CeO₂ Catalysts and Their Catalytic Activities for CO Oxidation. *J. Phys. Chem. C* **2007**, *111*, 12686–12692. doi: 10.1021/jp0733217
109. Sundar, R.S.; Deevi, S. CO oxidation activity of Cu-CeO₂ nano-composite catalysts prepared by laser vaporization and controlled condensation. *J. Nanoparticle Res.* **2006**, *8*, 497–509. doi: 10.1007/s11051-005-9030-0
110. Cecilia, J.A.; Arango-Díaz, A.; Marrero-Jerez, J.; Núñez, P.; Moretti, E.; Storaro, L.; Rodríguez-Castellón, E. Catalytic Behaviour of CuO-CeO₂ Systems Prepared by Different Synthetic Methodologies in the CO-PROX Reaction under CO₂-H₂O Feed Stream. *Catalysts* **2017**, *7*, 160. doi: 10.3390/catal7050160

111. Pasha, N.; Lingaiah, N.; Reddy, P.S.S.; Prasad, P.S.S. Direct Decomposition of N₂O over Cesium-doped CuO Catalysts. *Catal. Lett.* **2009**, *127*, 101–106. doi: 10.1007/s10562-008-9641-z
112. Jacobs, G.; Das, T.K.; Zhang, Y.; Li, J.; Racoillet, G.; Davis, B.H. Fischer-Tropsch synthesis: support, loading, and promoter effects on the reducibility of cobalt catalysts. *Appl. Catal. A Gen.* **2002**, *233*, 263–281. doi: 10.1016/S0926-860X(02)00195-3
113. Acerbi, N.; Tsang, S.C.; Golunski, S.; Collier, P. A practical demonstration of electronic promotion in the reduction of ceria coated PGM catalysts. *Chem. Commun.* **2008**, 1578–1580. doi: 10.1039/b718956g
114. Frost, J.C. Junction effect interactions in methanol synthesis catalysts. *Nature* **1988**, *334*, 577–580. doi: 10.1038/334577a0
115. Topping, J. On the mutual potential energy of a plane network of doublets. *Proc. R. Soc. Lond. A* **1927**, *114*, 67–72. doi: 10.1098/rspa.1927.0025
116. Shyu, J.Z.; Otto, K.; Watkins, W.L.H.; Graham, G.W.; Belitz, R.K.; Gandhi, H.S. Characterization of Pd/ γ -alumina catalysts containing ceria. *J. Catal.* **1988**, *114*, 23–33. doi: 10.1016/0021-9517(88)90005-X
117. Aranda, A.; Agouram, S.; López, J.M.; Mastral, A.M.; Sellick, D.R.; Solsona, B.; Taylor, S.H.; García, T. Oxygen defects: The key parameter controlling the activity and selectivity of mesoporous copper-doped ceria for the total oxidation of naphthalene. *Appl. Catal. B Environ.* **2012**, *127*, 77–88. doi: 10.1016/j.apcatb.2012.07.033
118. Yao, X.; Gao, F.; Yu, Q.; Qi, L.; Tang, C.; Dong, L.; Chen, Y. NO reduction by CO over CuO-CeO₂ catalysts: effect of preparation methods. *Catal. Sci. Technol.* **2013**, *3*, 1355–1366. doi: 10.1039/c3cy20805b
119. Konsolakis, M.; Carabineiro, S.A.C.; Tavares, P.B.; Figueiredo, J.L. Redox properties and VOC oxidation activity of Cu catalysts supported on Ce_{1-x}Sm_xO₈ mixed oxides. *J. Hazard. Mater.* **2013**, *261*, 512–521. doi: 10.1016/j.jhazmat.2013.08.016
120. Lamonier, C.; Bennani, A.; Huysseer, A.D.; Aboukaïs, A. Evidence for different copper species in precursors of copper-cerium oxide catalysts for hydrogenation reactions. An X-ray diffraction, EPR and X-ray photoelectron spectroscopy study. *J. Chem. Soc., Faraday Trans.* **1996**, *92*, 131–136. doi: 10.1039/FT9969200131
121. Kundakovic, Lj.; Flytzani-Stephanopoulos, M. Reduction characteristics of copper oxide in cerium and zirconium oxide systems. *Appl. Catal. A Gen.* **1998**, *171*, 13–29. doi: 10.1016/S0926-860X(98)00056-8

122. Liu, W.; Flytzani-Stephanopoulos, M. Total Oxidation of Carbon-Monoxide and Methane over Transition Metal Fluorite Oxide Composite Catalysts: II. Catalyst Characterization and Reaction-Kinetics. *J. Catal.* **1995**, *153*, 317–332. doi: 10.1006/jcat.1995.1133
123. Ayastuy, J.L.; Gurbani, A.; González-Marcos, M.P.; Gutiérrez-Ortiz, M.A. Selective CO oxidation in H₂ streams on CuO/Ce_xZr_{1-x}O₂ catalysts: Correlation between activity and low temperature reducibility. *Int. J. Hydrogen Energy* **2012**, *37*, 1993–2006. doi: 10.1016/j.ijhydene.2011.04.178
124. Chaturvedi, S.; Rodriguez, J.A.; Hrbek, J. Cs promoted oxidation of Zn and Cu-Zn surfaces: a combined experimental and theoretical study. *Surf. Sci.* **1997**, *384*, 260–275. doi: 10.1016/S0039-6028(97)00232-X
125. Biesinger, M.C.; Hart, B.R.; Polack, R.; Kobe, B.A.; Smart, R.St.C. Analysis of mineral surface chemistry in flotation separation using imaging XPS. *Miner. Eng.* **2007**, *20*, 152–162. doi: 10.1016/j.mineng.2006.08.006
126. Biesinger, M.C.; Lau, L.W.M.; Gerson, A.R.; Smart, R.St.C. Resolving surface chemical states in XPS analysis of first row transition metals, oxides and hydroxides: Sc, Ti, V, Cu and Zn. *Appl. Surf. Sci.* **2010**, *257*, 887–898. doi: 10.1016/j.apsusc.2010.07.086
127. Moulder, J.F.; Stickle, W.F.; Sobol, P.E.; Bomben, K.D. Handbook of X-ray Photoelectron Spectroscopy: A Reference Book of Standard Spectra for Identification and Interpretation of XPS Data. Physical Electronics Division, Perkin-Elmer Corporation, 1992, pp. 136–137.
128. Ma, J.; Rodriguez, N.M.; Vannice, M.A.; Baker, R.T.K. Nitrous oxide decomposition and reduction over copper catalysts supported on various types of carbonaceous materials. *Top. Catal.* **2000**, *10*, 27–38. doi: 10.1023/A:1019199614339
129. You, Y.; Chang, H.; Ma, L.; Guo, L.; Qin, X.; Li, J.; Li, J. Enhancement of N₂O decomposition performance by N₂O pretreatment over Ce-Co-O catalyst. *Chem. Eng. J.* **2018**, *347*, 184–192. doi: 10.1016/j.cej.2018.04.081
130. Iwanek, E.; Krawczyk, K.; Petryk, J.; Sobczak, J.W.; Kaszukur, Z. Direct nitrous oxide decomposition with CoO_x-CeO₂ catalysts. *Appl. Catal. B Environ.* **2011**, *106*, 416–422. doi: 10.1016/j.apcatb.2011.05.049
131. Abu-Zied, B.M.; Soliman, S.A.; Abdellah, S.E. Pure and Ni-substituted Co₃O₄ spinel catalysts for direct N₂O decomposition. *Chinese J. Catal.* **2014**, *35*, 1105–1112. doi: 10.1016/S1872-2067(14)60058-9
132. Savereide, L.; Nauert, S.L.; Roberts, C.A.; Notestein, J.M. The effect of support

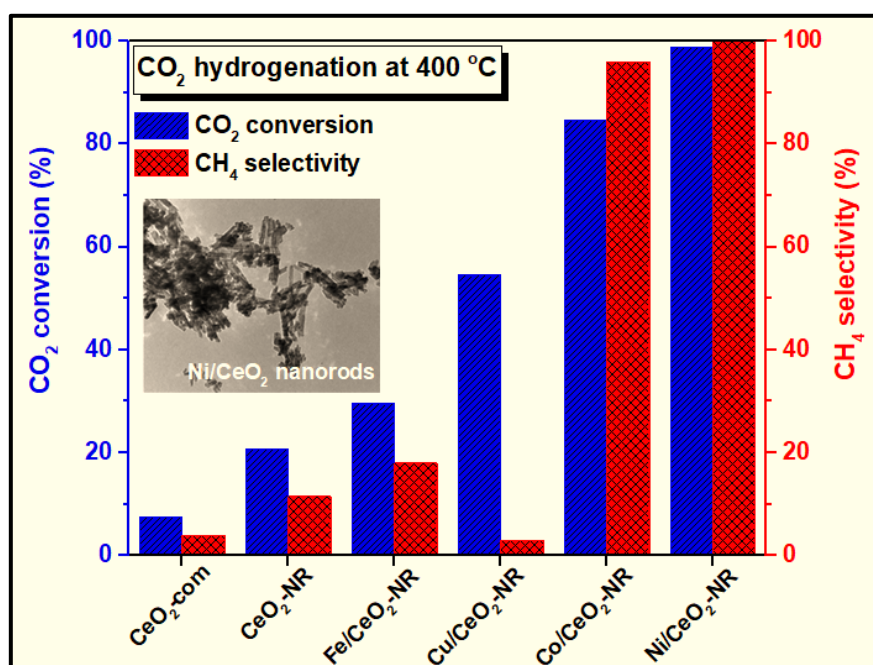
- morphology on $\text{CoO}_x/\text{CeO}_2$ catalysts for the reduction of NO by CO. *J. Catal.* **2018**, *366*, 150–158. doi: 10.1016/j.jcat.2018.08.005
133. Ruiz-Martínez, E.; Sánchez-Hervás, J.M.; Otero-Ruiz, J. Effect of operating conditions on the reduction of nitrous oxide by propane over a Fe-zeolite monolith. *Appl. Catal. B Environ.* **2005**, *61*, 306–315. doi: 10.1016/j.apcatb.2005.06.005
134. Konsolakis, M.; Aligizou, F.; Goula, G.; Yentekakis, I.V. N_2O decomposition over doubly-promoted $\text{Pt(K)}/\text{Al}_2\text{O}_3\text{-(CeO}_2\text{-La}_2\text{O}_3)$ structured catalysts: On the combined effects of promotion and feed composition. *Chem. Eng. J.* **2013**, *230*, 286–295. doi: 10.1016/j.cej.2013.06.083
135. Trovarelli, A.; Llorca, J. Ceria Catalysts at Nanoscale: How Do Crystal Shapes Shape Catalysis? *ACS Catal.* **2017**, *7*, 4716–4735. doi: 10.1021/acscatal.7b01246
136. Lykaki, M.; Pachatouridou, E.; Iliopoulou, E.; Carabineiro, S.A.C.; Konsolakis, M. Impact of the synthesis parameters on the solid state properties and the CO oxidation performance of ceria nanoparticles. *RSC Adv.* **2017**, *7*, 6160–6169. doi: 10.1039/c6ra26712b
137. Lykaki, M.; Pachatouridou, E.; Carabineiro, S.A.C.; Iliopoulou, E.; Andriopoulou, C.; Kallithrakas-Kontos, N.; Boghosian, S.; Konsolakis, M. Ceria nanoparticles shape effects on the structural defects and surface chemistry: Implications in CO oxidation by Cu/CeO_2 catalysts. *Appl. Catal. B Environ.* **2018**, *230*, 18–28. doi: 10.1016/j.apcatb.2018.02.035
138. Zabilskiy, M.; Djinović, P.; Erjavec, B.; Dražić, G.; Pintar, A. Small CuO clusters on CeO_2 nanospheres as active species for catalytic N_2O decomposition. *Appl. Catal. B Environ.* **2015**, *163*, 113–122. doi: 10.1016/j.apcatb.2014.07.057
139. Zhou, H.; Huang, Z.; Sun, C.; Qin, F.; Xiong, D.; Shen, W.; Xu, H. Catalytic decomposition of N_2O over $\text{Cu}_x\text{Ce}_{1-x}\text{O}_y$ mixed oxides. *Appl. Catal. B Environ.* **2012**, *125*, 492–498. doi: 10.1016/j.apcatb.2012.06.021
140. Adamski, A.; Zajac, W.; Zasada, F.; Sojka, Z. Copper ionic pairs as possible active sites in N_2O decomposition on $\text{CuO}_x/\text{CeO}_2$ catalysts. *Catal. Today* **2012**, *191*, 129–133. doi: 10.1016/j.cattod.2012.01.022
141. Parres-Esclapez, S.; Illán-Gómez, M.J.; De Lecea, C.S.M.; Bueno-López, A. On the importance of the catalyst redox properties in the N_2O decomposition over alumina and ceria supported Rh, Pd and Pt. *Appl. Catal. B Environ.* **2010**, *96*, 370–378. doi: 10.1016/j.apcatb.2010.02.034

CHAPTER 5

Effects of Ceria's Morphology and Active Phase Nature over Ceria-Based Transition Metal Catalysts M/CeO₂ (M: Fe, Co, Cu, Ni): Implications in CO₂ Hydrogenation

Chapter 5

deals with the combined effect of ceria's morphology and active phase nature on the physicochemical properties and the CO₂ hydrogenation performance at atmospheric



pressure over ceria-based transition metal catalysts is investigated. In particular, the hydrothermally synthesized ceria nanorods (NR) and nanocubes (NC) were used as supports for the various transition metals, *i.e.*, Fe, Co, Cu, Ni. It was found that the conversion of CO₂ followed the order: Ni/CeO₂ > Co/CeO₂ > Cu/CeO₂ > Fe/CeO₂ > CeO₂, independently of the support morphology. Also, it ought to be mentioned that bare ceria, Cu/CeO₂ and Fe/CeO₂ samples were very selective for CO production, whereas Co/CeO₂ and Ni/CeO₂ catalysts were selective towards methane (CH₄) demonstrating the key role of metal-support combination.

INTRODUCTION

It is widely accepted that CO₂ emissions are the main contributors to the observed temperature rise in the atmosphere [1]. Therefore, research efforts concerning the mitigation of CO₂ emissions focus, generally, on the following approaches: i) complete and/or partial replacement of carbon-based fuels with Renewable Energy Sources (RESs), ii) carbon dioxide capture and storage (CCS) technology and iii) chemical conversion/utilization of CO₂ toward value-added chemicals and fuels [2].

The last approach has attracted intense interest over the past decades, with CO₂ hydrogenation being one of the most investigated methods, due to the vast variety of products [3,4]. This route can also provide an effective way to the valorization of CO₂ emissions and the efficient storage of surplus power from non-intermittent RESs (*e.g.*, solar, wind) in the form of "green" hydrogen, providing either CO through the mildly endothermic reverse water-gas shift (rWGS) reaction (Eq. 1) or CH₄ through the highly exothermic methanation reaction, often referred to as the "Sabatier reaction" (Eq. 2) [5].



Other possible products of potential value from CO₂ hydrogenation include methanol [6–9], dimethyl ether [10], formic acid [11] and hydrocarbons [12]. Among the different CO₂ hydrogenation products, carbon monoxide is a valuable feedstock for the C1 chemical industry, since various liquid synthetic hydrocarbons and chemicals can be produced by its subsequent upgrading, through the well-established Fischer-Tropsch synthesis [13,14]. Moreover, carbon dioxide methanation can effectively convert a less manageable energy vector, such as gaseous hydrogen into a high-energy source such as methane, since CH₄ possesses three times the volumetric energy density of hydrogen [15].

Regarding the overall sustainability of the proposed process, it should be pointed out that the general scheme of the CO₂ hydrogenation concept is associated to the use of "green" H₂, originated by the excess energy provided by RESs and the concentrated amounts of CO₂ emissions as feedstock. In this regard, the CO₂ hydrogenation process could be implemented near a source of highly concentrated CO₂ emissions, such as effluent streams of steel industry or a CO₂ capture plant. By employing highly active and inexpensive catalysts, large amounts of CO₂ can be potentially mitigated with the concurrent production of value-added products, such as CH₄ or CO, which can be used as fuels or feedstock in the chemical industry. Regarding the use of renewable hydrogen, it can be exploited entirely in the

hydrogenation process or it can be partially converted to the electricity required for the reaction process. Also, excess hydrogen can be directly injected into the gas grid or used in fuel cell powered vehicles. Various comprehensive studies have been devoted to the sustainability of the CO₂ hydrogenation process, to which the reader can refer [16–20].

Although the hydrogenation of CO₂ can be a promising way to reduce the environmental carbon print, several limitations arise for the implementation of a technology based on either Eq. 1 or Eq. 2. The first is associated with the activation of carbon dioxide itself, a fully oxidized and thermodynamically stable compound whose reduction is not energetically favourable [21], and thus requires strong reductants (*i.e.*, H₂) or electrochemical-assisted reduction processes [22,23]. Secondly, CO₂ hydrogenation is subjected to kinetic and equilibrium limitations, thus reaction rates need to be promoted [24]. Numerous catalytic systems have been employed in order to overcome these limitations and several reviews in the literature summarize the catalysts explored for either rWGS [25–27] or CO₂ methanation [28–31] reactions. The most studied catalytic systems are composites with metals supported on a reducible metal oxide (*e.g.*, CeO₂, ZrO₂) or a combination of them. These systems have been employed as bi-functional catalysts, with oxide supports mainly providing oxygen vacancies to activate CO₂, and metal active sites dissociating molecular hydrogen, the so-called hydrogen spillover process [26,32].

Among the oxides investigated, CeO₂ has attracted considerable attention as a supporting carrier, due to its high oxygen mobility and unique redox properties, as cerium can rapidly change between its two oxidation states (Ce³⁺ and Ce⁴⁺) [33,34]. Moreover, ceria is a basic oxide promoting a strong interaction with CO₂, facilitating its adsorption [35]. Apart from bare ceria's excellent redox properties, many studies have focused on the development of highly efficient and low-cost ceria-based catalytic composites, since the combination of various non-noble transition metals (TMs) (*e.g.*, Cu, Co, Ni, Fe) with ceria, can further enhance the catalytic activity and/or selectivity due to the peculiar metal-support synergistic interactions [36–38]. Despite their adequate catalytic activity, the use of precious metals like Ru [39], Rh [40] and Pd [41] as active phases is generally not preferable, since their high cost and scarcity might render the process financially non-viable. Thus, from a techno-economical point of view, the use of TMs-based catalysts may be favourable, since these metals can achieve comparable activity to that of the most active noble metal catalysts, though at a substantially lower cost [42,43]. In this regard, our efforts were recently focused on developing inexpensive TMs-based catalytic composites, with particular emphasis on middle-late 3d metals, *i.e.*, Cu, Co, Ni, Fe, which were found to adsorb and consequently

activate CO₂ through a charge transfer from metal phase to CO₂ moiety [44]. In particular, density functional theory (DFT) calculations have revealed spontaneous chemisorption of CO₂ and favourable thermodynamic properties for the aforementioned metals, with Cu, however, exhibiting a weaker interaction with CO₂ [44].

In order to develop highly efficient ceria-based catalysts, research efforts have been devoted to the rational design of catalytic materials by means of advanced synthetic and/or promotional routes [45–50]. The ultimate goal would be to obtain catalytic systems with adequate stability, CO₂ conversion activity and high product selectivity, in order to exclusively generate CO or CH₄ in a real large-scale process. Towards the fine-tuning of CeO₂-based materials, the development of catalytic materials in the nanoscale is of great importance. Nanomaterials exhibit abundance in surface atoms and defect sites such as oxygen vacancies, whereas the electronic perturbations between the metal and support nanoparticles greatly affect the catalytic performance [36,37,51,52]. Moreover, by tailoring the shape of nanoparticles by means of advanced synthetic routes (*e.g.*, hydrothermal method), different crystal facets can be exposed leading to different oxygen storage capacity (OSC) and oxygen mobility [45,46,53,54]. For example, Ouyang *et al.* [55] have investigated ceria morphological effects during methanol synthesis from CO₂ hydrogenation over CuO/CeO₂ mixed oxides; copper-ceria nanorods exhibited the highest CO₂ conversion and methanol yield due to the strongest metal-support interaction, as compared to nanocubes and nanospheres. Similarly, Au/CeO₂ nanorods were found to exhibit a stronger gold-ceria interaction and higher activity in the forward WGS reaction than cubic and polyhedral CeO₂ [56]. Also, Liu *et al.* [57] reported a better activity for ceria nanocubes in the rWGS reaction than nanorods and nanopolyhedra, with the nanocubic samples prepared preferentially exposing (100) planes, a potentially more active surface than (110) and (111) planes.

Although there are several studies regarding the hydrogenation of CO₂ over ceria-based composites, it should be noted that CO₂ hydrogenation proceeds through a complex reaction pathway, being affected to a different extent by various factors, such as the metal-oxide interactions, the formation of oxygen vacancies, the reducibility, *etc.* [49,58–62]. Furthermore, selectivity towards CO, CH₄ or other possible compounds can vary remarkably when using catalytic composites with various active metal phases supported onto ceria, depending thus on the metal entity employed [63–65].

In light of the above, the aim of the present study is to investigate the effect of non-noble metal phase nature (Co, Cu, Fe, Ni) and support morphology (nanorods, nanocubes) on the

physicochemical properties and, consequently, on the CO₂ hydrogenation performance of ceria-based nanocatalysts.

5.1. EXPERIMENTAL

5.1.1. Materials Synthesis

The chemicals used were of analytical reagent grade. Ce(NO₃)₃·6H₂O (purity ≥ 99.0%, Fluka), Co(NO₃)₂·6H₂O (≥ 98%, Sigma-Aldrich), Cu(NO₃)₂·2.5H₂O (Fluka), Fe(NO₃)₃·9H₂O (≥ 98%, Sigma-Aldrich) and Ni(NO₃)₂·6H₂O (purity ≥ 98%, Sigma-Aldrich) were employed as precursor compounds for the preparation of bare ceria as well as of ceria-based transition metal catalysts (M/CeO₂, M: Co, Cu, Fe, Ni). Also, NaOH (≥98%, Honeywell Fluka), ethanol (purity 99.8%, ACROS Organics) and double deionized water were used during materials synthesis. The catalysts developed in this chapter (CeO₂-NR, CeO₂-NC, Co/CeO₂-NP, Co/CeO₂-NR, Co/CeO₂-NC) were prepared by the methods described in Chapter 2 in section 2.1 (Materials Synthesis). Also, Table 2.1 in Chapter 2 presents all the materials developed in this study.

5.1.2. Materials Characterization

Structural characterization was carried out by means of X-ray diffraction (XRD) The collected spectra were analyzed by Rietveld refinement, allowing the determination of crystallite sizes by means of the Williamson-Hall plot. The redox properties were assessed by Temperature Programmed Reduction (TPR) experiments, employing H₂ as a reducing agent. The surface composition and the chemical state of each element were determined by X-ray photoelectron spectroscopy (XPS) analyses. The samples were imaged by transmission electron microscopy (TEM). The characterization techniques are fully described in Chapter 2 in section 2.2 (Characterization Techniques).

5.2. CHARACTERIZATION STUDIES OF M/CeO₂ MIXED OXIDES (M: Fe, Co, Cu, Ni)

5.2.1. Textural and Structural Characterization (BET and XRD)

The textural, structural and redox properties of bare ceria as well as of M/CeO₂ catalysts of nanorod-like and nanocubic morphology are presented in Table 5.1. Bare ceria supports (CeO₂-NR and CeO₂-NC) exhibit a BET surface area of 92 and 40 m² g⁻¹, respectively. In all cases, the addition of the transition metals to the ceria carriers leads to a slight decrease of the surface area. However, the order obtained for bare supports remained unaffected, with the rod-shaped samples exhibiting higher surface area than the corresponding nanocubic ones, regardless of the nature of the metal phase added into the ceria carrier.

Regarding the XRD analysis, the average crystallite diameter of CeO₂ phase was calculated by applying Scherrer's equation on the XRD diffractions (Table 5.1). In particular, ceria's mean particle size is larger in the CeO₂-NC sample (19 nm) than that of CeO₂-NR (13 nm). In general, the crystallite size of ceria with regard to the M/CeO₂ samples follows the reverse order as compared to the BET area, namely, the lower the surface area the larger the ceria crystallite size. On the basis of the present textural characteristics, it could be stated that the surface area and ceria crystallite size is not significantly affected by the transition metal's nature. The textural/structural properties of ceria-supported transition metal catalysts are mainly determined by the support characteristics, as further corroborated by TEM analysis (*vide infra*).

Table 5.1. Textural, structural and redox properties of as-prepared samples.

Sample	BET Analysis		XRD Analysis		TPR Analysis
	BET Surface Area (m ² g ⁻¹)	Pore volume (cm ³ g ⁻¹)	Average crystallite diameter D _{XRD} (nm)		OSC (mmol O ₂ g ⁻¹) ¹
			CeO ₂	M _x O _y	
CeO ₂ -NC	40	0.12	19	-	0.21
CeO ₂ -NR	92	0.71	13	-	0.29
Fe/CeO ₂ -NC ²	32	0.19	17	52	0.67
Fe/CeO ₂ -NR ²	69	0.19	10	7	0.75
Co/CeO ₂ -NC	28	0.15	24	19	1.03
Co/CeO ₂ -NR	72	0.31	14	16	1.19
Cu/CeO ₂ -NC	34	0.29	19	52	0.75
Cu/CeO ₂ -NR	75	0.40	12	43	0.90
Ni/CeO ₂ -NC ³	32	0.21	22	17	0.78
Ni/CeO ₂ -NR ³	72	0.38	14	23	0.92

¹ Calculated by integration of the TPR peaks in the low-temperature range (surface oxygen reduction); ² Data taken from [66]; ³ Data taken from [67].

The XRD diffraction patterns of M/CeO₂ samples are presented in Figure 5.1 with the main peaks for all samples at 28.5°, 33.1°, 47.5°, 56.3°, 59.1°, 69.4°, 76.7°, and 79.1° corresponding to the (111), (200), (220), (311), (222), (400), (331) and (420) planes of a face-centred cubic (FCC) fluorite structure of ceria (Fm3m symmetry, no. 225) [68] with (111), (220) and (311) planes mostly prevailing in the samples structure. Powder XRD analysis demonstrated the existence of CuO, Co₃O₄, NiO and Fe₂O₃ for M/CeO₂-NX (M: Cu, Co, Ni, Fe, NX: NR-nanorods, NC-nanocubes), respectively, with no peaks associated to other crystal phases, except ceria. The primary crystallite sizes of ceria and corresponding metal oxide phases were estimated and these are also presented in Table 5.1. It is worth mentioning that the ceria crystallite size of all nanocubic samples is higher than that of the rod-shaped ones. Moreover, no significant changes were observed on ceria particle sizes upon metal incorporation, implying that the structural features of ceria remain unaffected by metal addition, as further verified by TEM analysis (see below).

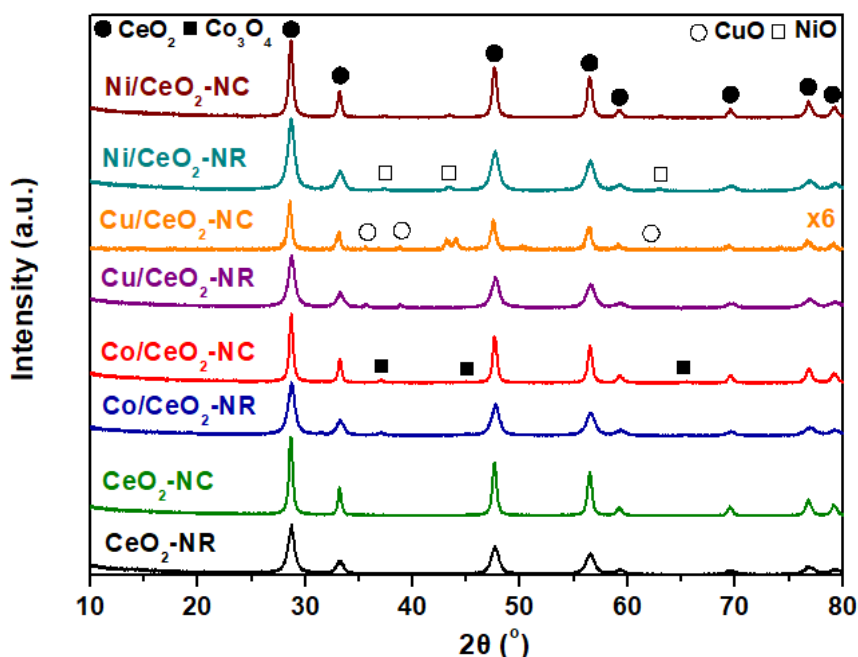


Figure 5.1. XRD patterns of as-prepared samples of nanorod-like (NR) and nanocubic (NC) morphology.

5.2.2. Morphological Characterization (TEM)

The TEM images of as-prepared samples of rod-like and cubic morphology are depicted in Figure 5.2. The NR samples (Figure 5.2 a, c, e, g, i) display ceria in a uniform rod-like morphology, while the existence of nanocubic morphology is evident in the samples

denoted as NC (Figure 5.2 b, d, f, h, j). Apparently, the addition of the active metal phase to ceria carrier has no effect on the support morphology, since distinctive rod-like and cubic particles are still clearly observed after the introduction of the metal phase in the well-defined support structure.

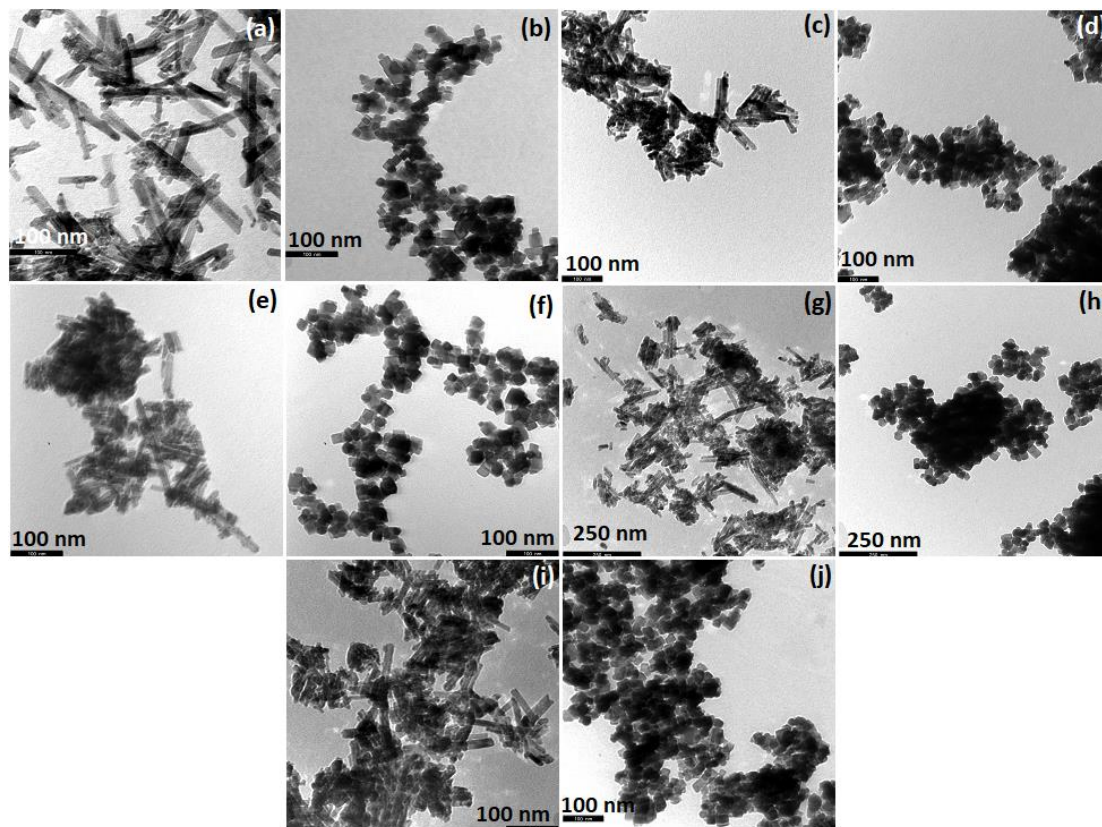


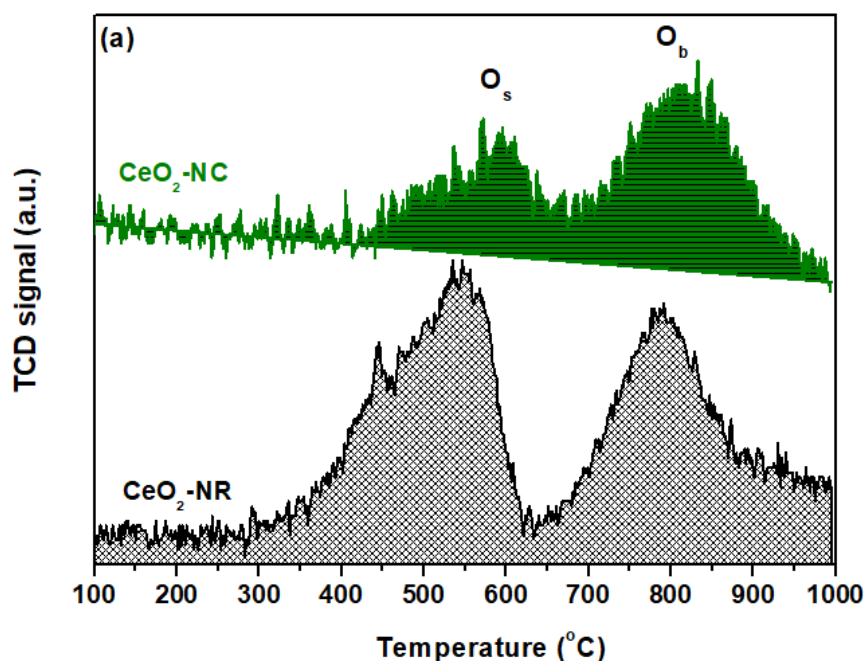
Figure 5.2. TEM images of as-prepared samples of nanorod-like (NR) and nanocubic (NC) morphology: (a) CeO₂-NR, (b) CeO₂-NC, (c) Co/CeO₂-NR, (d) Co/CeO₂-NC, (e) Cu/CeO₂-NR, (f) Cu/CeO₂-NC, (g) Fe/CeO₂-NR, (h) Fe/CeO₂-NC, (i) Ni/CeO₂-NR, (j) Ni/CeO₂-NC.

5.2.3. Redox Properties (H₂-TPR)

The H₂-TPR profiles of bare ceria and ceria-supported transition metal (Co, Cu, Ni) samples of nanorod-like (NR) and nanocubic (NC) morphology are shown in Figure 5.3. The main TPR peaks at 545–590 °C and 790–810 °C are attributed to ceria's surface oxygen (O_s) and bulk oxygen (O_b) reduction, respectively (Figure 5.3a) [69,70]. Interestingly, significant quantitative and qualitative differences between the reduction profiles are observed, implying the pivotal role of morphology on the redox features of ceria nanoparticles. In particular, ceria nanorods exhibit higher oxygen storage capacity (OSC) than ceria nanocubes, *i.e.*, 0.29 mmol g⁻¹ for CeO₂-NR as compared to 0.21 mmol g⁻¹ for CeO₂-NC.

These results clearly show that the rod-shaped ceria nanoparticles possess the highest population of weakly bound labile oxygen species.

Nevertheless, in complete contrast to textural/structural properties, the metal incorporation to ceria carrier greatly affects the redox properties of ceria-supported transition metal composites. In all cases, metal addition facilitates the surface oxygen reduction shifting the O_s peak (Figure 5.3b) to lower temperatures. In other words, the reduction of TMs/Ceria composites is taking place at considerably lower temperatures in comparison to single metal and ceria oxides, indicating the beneficial impact of metal incorporation on surface oxygen reduction. In view of this fact, the metal-support interactions could be accounted for the enhanced reducibility and oxygen exchange kinetics of mixed oxides, as extensively discussed in previous studies [36,69,70,73–76]. The latter is further demonstrated by the estimation of OSC of ceria-based transition metal catalysts (TMs/CeO₂) in the low temperature region, in which the reduction of both the metal oxide (M_xO_y) and CeO₂ surface oxygen is taking place. More importantly, regardless of the metal entity (Cu, Co, Fe, Ni), the OSC is always higher in the rod-shaped samples as compared to the nanocubic ones (Table 5.1), clearly demonstrating the crucial role of ceria nanostructure towards determining the redox properties of TMs/CeO₂ catalysts.



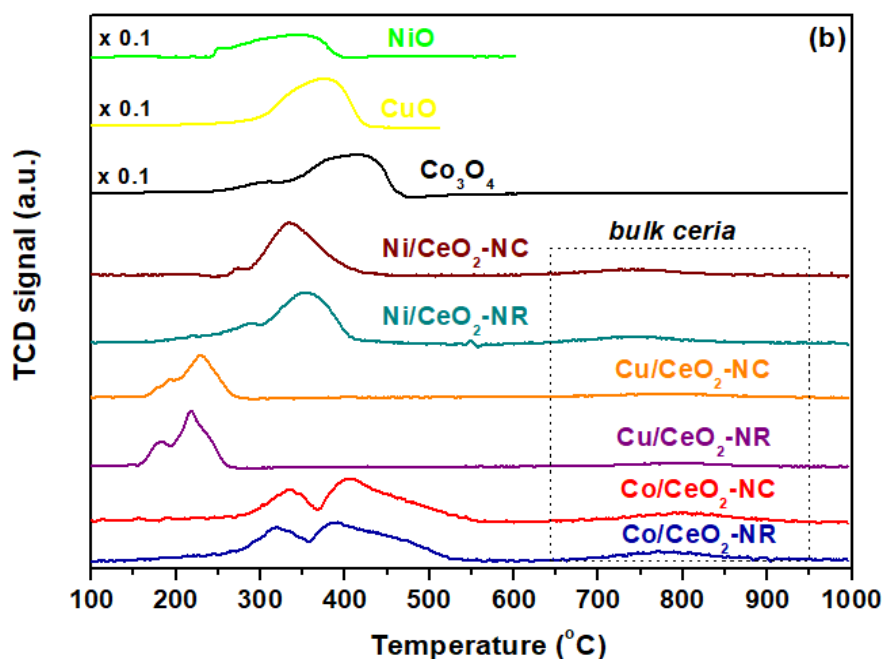


Figure 5.3. H₂-TPR profiles of (a) bare ceria and (b) ceria-supported transition metal (Co, Cu, Ni) samples of nanorod-like (NR) and nanocubic (NC) morphology.

5.2.4. Surface Analysis (XPS)

In this point, it should be mentioned that the rod-shaped as-prepared and reduced samples (denoted as M/CeO₂-NR(R)) were further characterized by XPS analysis, as they exhibit the optimum redox properties. Analysis of the Ce 3d XPS spectra (Figure 5.4) of rod-shaped as-prepared and reduced M/CeO₂ samples indicated that the reduced samples exhibit higher values of Ce³⁺ species (Table 5.2), implying ceria's facile reduction under reducing conditions (H₂-pretreatment), as that prevailing under reaction conditions. Moreover, the reduced Ni/CeO₂-NR(R) sample exhibits the highest concentration of Ce³⁺ species (30.4%) as compared to the corresponding Co/CeO₂-NR(R) (29.9%), Fe/CeO₂-NR(R) (26.9%), and Cu/CeO₂-NR(R) sample (25.5%), implying the facile reduction of ceria nanorods in the presence of nickel. Similar results have been previously obtained over Ni/CeO₂ catalysts attributed to the hydrogen spillover effect; dissociation of molecular hydrogen on the metal surface resulting in highly mobile atomic hydrogen species which reduces Ce⁴⁺ species adjacent to the metal [77]. Recently, it was shown by means of *in situ* studies that Ce³⁺ species play a key role on the CO₂ methanation reaction mechanism, as they promote the activation of CO₂ [64].

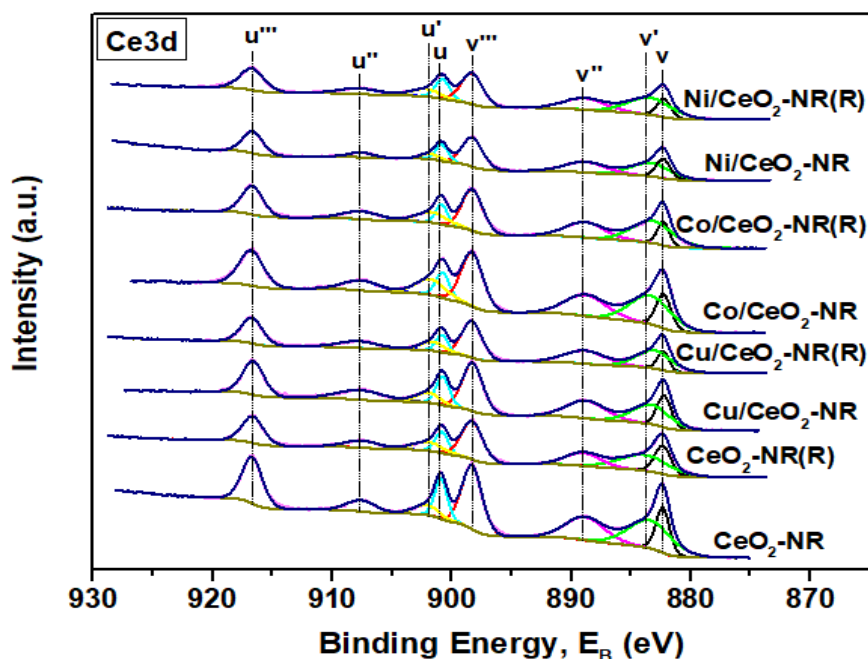


Figure 5.4. XPS Ce 3d spectra of as-prepared and reduced bare CeO_2 and M/CeO_2 samples of rod-like morphology.

5.3. IMPLICATIONS IN CO_2 HYDROGENATION REACTION

The catalytic performance of the as-prepared samples in the CO_2 hydrogenation reaction was investigated in the temperature range of 200–500 °C. A commercial CeO_2 sample (Fluka, $S_{\text{BET}} = 15 \text{ m}^2 \text{ g}^{-1}$), denoted as $\text{CeO}_2\text{-com}$, was also tested as a reference sample. Figure 5.5 depicts CO_2 conversion of all samples in the temperature range investigated, as compared to the thermodynamic equilibrium CO_2 conversion profiles for methanation and rWGS reactions. It is obvious that there are significant differences between the samples, mostly depending on metal's nature. Regarding CO_2 conversion, the following order is obtained: $\text{CeO}_2 < \text{Fe}/\text{CeO}_2 < \text{Cu}/\text{CeO}_2 < \text{Co}/\text{CeO}_2 < \text{Ni}/\text{CeO}_2$, signifying the pivotal role of metal-support combination [67]. $\text{Ni}/\text{CeO}_2\text{-NR}$ exhibits by far the optimum performance, offering *ca.* 98% conversion at 300 °C. In other words, by combining Ni with ceria nanorods extremely active CO_2 methanation catalysts can be obtained, which practically reach the equilibrium at very low temperatures of *ca.* 300 °C [67]. The beneficial effect of the synthesis method on the catalytic activity is obvious, as all nanoceria samples exhibit far better CO_2 conversion values than $\text{CeO}_2\text{-com}$.

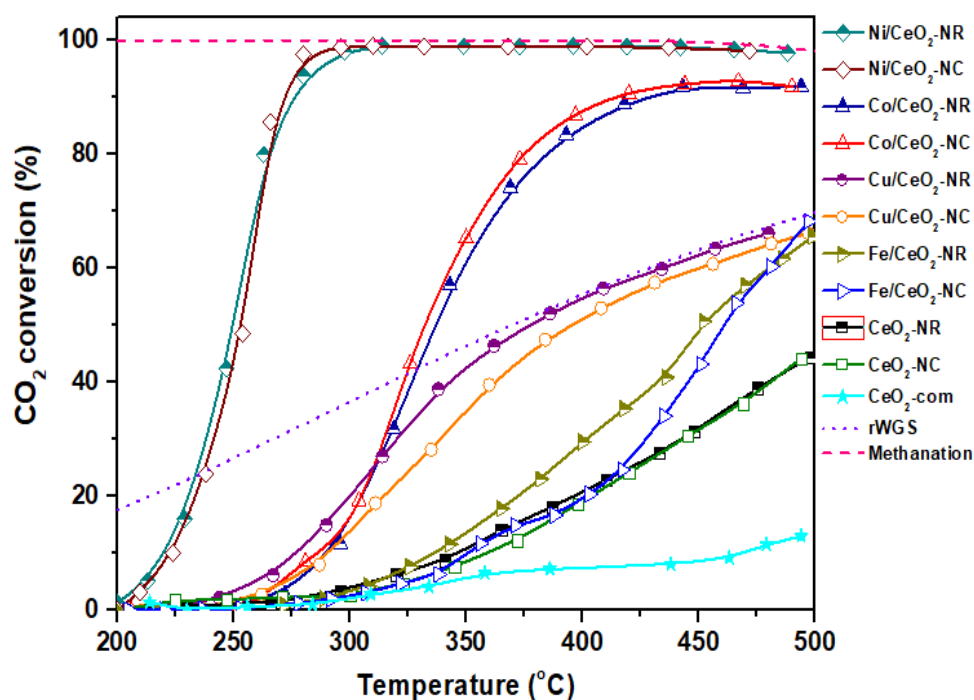


Figure 5.5. Experimental (solid lines) and theoretical (dotted and dashed lines) CO₂ conversion profiles for commercial CeO₂, bare ceria-NX and M/CeO₂-NX samples in CO₂ hydrogenation reaction. The dotted and dashed lines correspond to rWGS and methanation reactions' equilibrium, respectively. Reaction conditions: F = 100 cm³/min, GHSV = 20,000 h⁻¹, H₂:CO₂ = 9:1, P = 1 atm [67].

The impact of the nature of the metal phase (Cu, Fe, Co, Ni) on the CO₂ hydrogenation performance is further evaluated on the basis of the selectivity towards CO and CH₄, as depicted in Figure 5.6a and b, respectively. Apparently, commercial ceria, nano-ceria, Fe/CeO₂-NX and Cu/CeO₂-NX samples are all highly selective to CO (> 90%). Thus, maximum CO₂ conversion values for these samples are expected to be closer to those for the rWGS reaction equilibrium, a much less favourable reaction than CO₂ methanation, as indeed shown by the corresponding equilibrium curve (dotted line) in Figure 5.5 [67]. Similar results for CO production over CeO₂ [57,78] and Cu-based catalysts are reported in the literature [14,58,79–83]. The increase in temperature obviously increases the CO₂ conversion, but to a different extent for each sample. As expected, CO₂ conversion initially increases and reaches a plateau for the highly selective towards methane Ni/ CeO₂-NX and Co/CeO₂-NX catalysts, favouring the exothermic CO₂ methanation (Eq. 2) below 500 °C, in agreement with the thermodynamic calculations [67]. A different trend is shown for bare ceria, Fe/CeO₂-NX and Cu/CeO₂-NX samples, as CO₂ conversion increases steadily, but to a lesser extent, as compared to Ni/ CeO₂-NX and Co/CeO₂-NX samples, approaching in the case of Cu-based

catalysts the equilibrium for rWGS reaction [67]. Bare ceria carriers, although clearly favouring the rWGS reaction, demonstrated CO_2 conversion values that are much below the corresponding values predicted by thermodynamics [67]. In light of the above results, it should be highlighted that the as-prepared cobalt catalysts are highly efficient in methane production at temperatures as low as 400 °C, under the reaction conditions employed. On the other hand, the as-prepared copper catalysts are highly selective to CO, reaching rWGS equilibrium values at *ca.* 380 °C. In a similar manner, Dai *et al.* [79] reported 100% selectivity to CO for Cu/CeO₂, attributed to the presence of Cu⁰ active sites, whereas selectivity to CH₄ for Co/CeO₂ increased markedly between 350–400 °C.

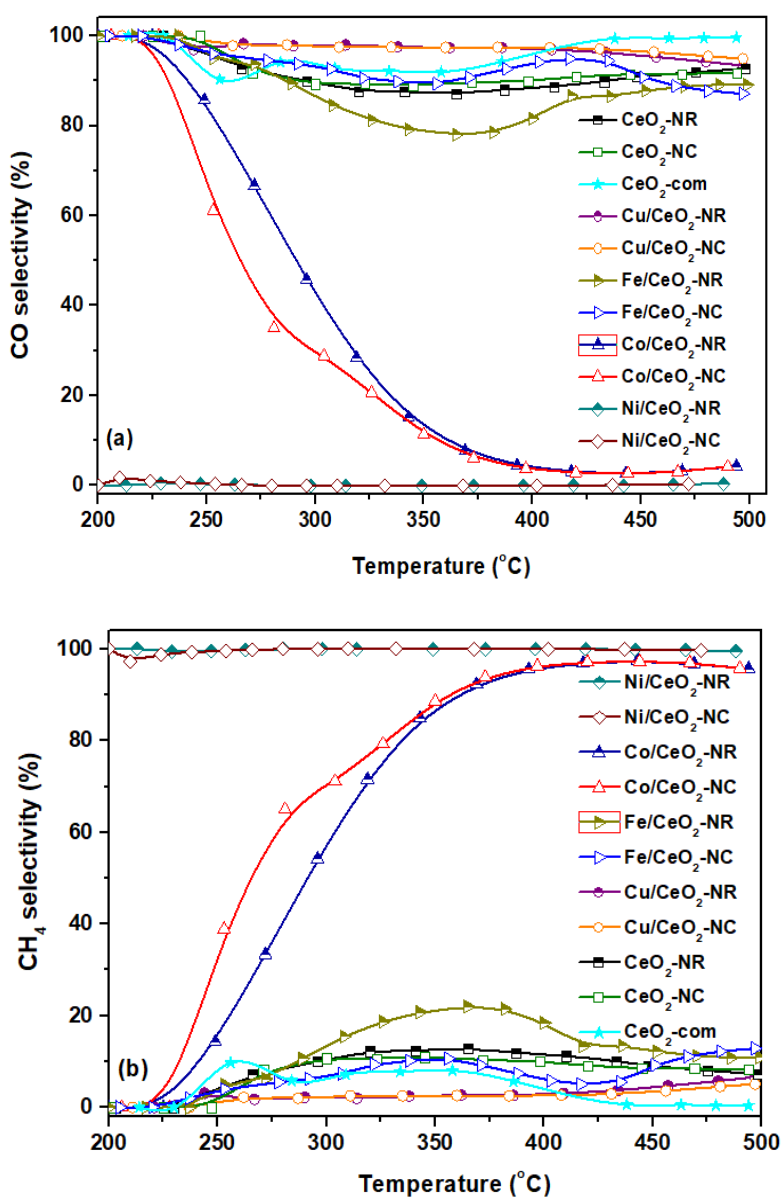


Figure 5.6. Selectivity to (a) CO and (b) CH₄ as a function of temperature for all samples in the CO₂ hydrogenation reaction. Reaction conditions: F = 100 cm³/min, GHSV = 20,000 h⁻¹, H₂:CO₂ = 9:1, P = 1 atm [67].

Also, it is worth mentioning that the high conversion performance of Ni catalysts is followed by 100% selectivity to CH₄ (Figure 5.6b) in the entire temperature range studied. Interestingly, the Cu/CeO₂-NR catalyst is totally selective to CO (rWGS reaction), reaching the equilibrium at temperatures higher than 400 °C. Hence, the combination of Ni with CeO₂-NR favours the CO₂ methanation reaction, whereas the rWGS reaction is favoured over Cu/CeO₂-NR. Moreover, stability experiments performed over the optimum catalytic materials (rod-shaped samples), revealed a stable performance without any deterioration of activity/selectivity [84,85].

The obtained differences in activity/selectivity among the metal-based catalysts can be corroborated by taking into account the underlying mechanism of the metal-catalyzed CO₂ hydrogenation reaction, in conjunction to the present characterization results. In particular, the dissociation of adsorbed CO, considered as the rate-determining step of the CO₂ methanation process [86,87], has been proposed to proceed by two main pathways: direct CO_{ads} dissociation and H-assisted CO_{ads} dissociation. The first mechanism is proposed to occur over group VIII metal-based catalysts, such as Co [88,89]. In view of this fact, Liu *et al.* [44] demonstrated that Co showed more favourable thermodynamics and low CO₂ decomposition barriers for CO₂ reduction compared to Cu. In a similar manner, a close relationship between the CO₂ and H₂ adsorption capacity of Co/KIT-6 catalysts and their CO₂ conversion/selectivity performance has been revealed [90]. In particular, high H₂ adsorption capacity can provide a large number of active H species for the further hydrogenation of intermediate species (such as HCOO⁻) to methane, whereas the low H₂ adsorption and activation capacity is favourable to CO formation.

On the contrary, a redox mechanism has been proposed in the literature for rWGS over Cu-based catalysts [23,91]. Specifically, Cu⁰ atoms can act as active sites for the dissociation of CO₂ and the Cu₂O formed is subsequently reduced by hydrogen to regenerate metallic Cu species. Hydrogen was proposed to be only a reducing agent without direct participation in the formation of intermediate species in the rWGS reaction [92]. The facile reduction of Cu/CeO₂-NX catalysts towards reduced copper species at temperatures lower than *ca.* 300 °C, corroborated by the H₂-TPR results (Figure 5.3), can possibly favour this redox mechanism, thus being the reason for the high selectivity towards CO even at low temperatures.

The superior performance of Ni/CeO₂-NR could be attributed to the improved reducibility and oxygen mobility offered mainly by ceria nanorods, as it has been previously reported [93]. This is in accordance with the abundance of reduced Ce³⁺ species, as shown by XPS and

H₂-TPR analyses (see above). In particular, nickel can easily dissociate molecular hydrogen into H ad-atoms onto the catalytic surface [94]. These H_(ad) species can then migrate to ceria *via* an activated surface diffusion process, hydrogenating the species formed upon CO₂ adsorption, mainly at the Ni-ceria interface, towards methane formation [95]. In view of these mechanistic aspects, it was very recently shown by means of isotopic and *in situ* DRIFTS studies [96] that the higher methanation activity of Ni/CeO₂ compared to Ni/Al₂O₃ catalysts can be mainly assigned to the nickel-ceria interactions as well as to the high oxygen mobility of ceria, which hinders the accumulation of water and carbon-containing species on the catalyst surface. In a similar manner, the increased methanation activity of CeO₂-based samples has been ascribed to the high concentration of Ce³⁺ species, which promotes CO₂ adsorption leading to higher coverage in formate active species [64,77,95]. Also, the Ni/CeO₂ catalyst was found to be the most active for CO₂ methanation in comparison to other lanthanide-supported nickel catalysts, due to the strong interaction between nickel and ceria in conjunction to the high H₂ dissociation ability of reduced Ni sites [97]. Therefore, on the basis of the present studies, the superiority of Ni/CeO₂-NR can be attributed to the synergistic interactions between nickel particles and ceria nanorods towards enhancing the reducibility, *i.e.*, high population of Ce³⁺ species under reaction conditions, and in turn the CO₂ methanation performance.

Regarding the impact of support morphology, it can be concluded that the CO₂ conversion and selectivity of the samples are not significantly affected by the support morphology (NR vs. NC), as shown in Figures 5.5 and 5.6. In particular, a slightly better conversion performance is obtained for Cu/CeO₂-NR and Fe/CeO₂-NR samples as compared to Cu/CeO₂-NC and Fe/CeO₂-NC, whereas for bare CeO₂, Co/CeO₂ and Ni/CeO₂ samples, minor differences in conversion performance between NC and NR were observed.

5.4. CONCLUDING REMARKS

The present results revealed the strong effect of metal phase and reaction conditions on the CO₂ hydrogenation performance of nanoceria-based M/CeO₂ catalysts of different morphology (nanorods or nanocubes). It was shown that hydrothermally synthesized nanoceria carriers exhibited better catalytic activity in the hydrogenation of CO₂ than commercial ceria. More importantly, metal addition into the nanostructured ceria support led to a significant increase in the catalytic activity, with CO₂ conversion following the order Ni/CeO₂ > Co/CeO₂ > Cu/CeO₂ > Fe/CeO₂ > CeO₂. The main product of the reaction was determined by the nature of the metal entity incorporated into cerium oxide, with the Co/CeO₂ and

Ni/CeO₂ catalysts exhibiting high selectivity towards CH₄ and CO₂ conversion values close to equilibrium, whereas bare ceria, Cu/CeO₂ and Fe/CeO₂ samples were selective towards CO. The Cu/CeO₂ catalysts exhibited remarkable CO selectivity even under hydrogen excess conditions and very close to equilibrium CO₂ conversion values for rWGS reaction. From a practical point of view, the Ni/CeO₂ catalyst demonstrated an excellent conversion and selectivity performance, offering 98.8% CO₂ conversion and 100% selectivity to methane at 300 °C. On the other hand, Cu/CeO₂ samples were highly selective for CO production, exhibiting 57% CO₂ conversion and ~97% CO selectivity at 400 °C. These results are considered very promising in the sense of employing these catalysts in real scale processes with variable H₂:CO₂ ratios, where renewable hydrogen from excess RES power can be used to efficiently and selectively converting CO₂ to CO or CH₄.

REFERENCES

1. Olah, G.A.; Prakash, G.K.S.; Goepfert, A. Anthropogenic Chemical Carbon Cycle for a Sustainable Future. *J. Am. Chem. Soc.* **2011**, *133*, 12881–12898. doi: 10.1021/ja202642y
2. Xiaoding, X.; Moulijn, J.A. Mitigation of CO₂ by Chemical Conversion: Plausible Chemical Reactions and Promising Products. *Energy Fuels* **1996**, *10*, 305–325. doi: 10.1021/ef9501511
3. Vu, T.T.N.; Desgagnés, A.; Iliuta, M.C. Efficient approaches to overcome challenges in material development for conventional and intensified CO₂ catalytic hydrogenation to CO, methanol, and DME. *Appl. Catal. A Gen.* **2021**, *617*, 118119. doi: 10.1016/j.apcata.2021.118119
4. Centi, G.; Perathoner, S. Opportunities and prospects in the chemical recycling of carbon dioxide to fuels. *Catal. Today* **2009**, *148*, 191–205. doi: 10.1016/j.cattod.2009.07.075
5. Sabatier, P.; Senderens, J.B. New Synthesis of Methane. *Comptes Rendus Hebd. Seances Acad. Sciences* **1902**, *134*, 514–516.
6. Bahruji, H.; Bowker, M.; Hutchings, G.; Dimitratos, N.; Wells, P.; Gibson, E.; Jones, W.; Brookes, C.; Morgan, D.; Lalev, G. Pd/ZnO catalysts for direct CO₂ hydrogenation to methanol. *J. Catal.* **2016**, *343*, 133–146. doi: 10.1016/j.jcat.2016.03.017
7. Li, M.M.-J.; Zeng, Z.; Liao, F.; Hong, X.; Tsang, S.C.E. Enhanced CO₂ hydrogenation to methanol over CuZn nanoalloy in Ga modified Cu/ZnO catalysts. *J. Catal.* **2016**, *343*, 157–167. doi: 10.1016/j.jcat.2016.03.020
8. Senanayake, S.D.; Ramírez, P.J.; Waluyo, I.; Kundu, S.; Mudiyansele, K.; Liu, Z.; Liu, Z.; Axnanda, S.; Stacchiola, D.J.; Evans, J.; Rodriguez, J.A. Hydrogenation of CO₂ to Methanol on CeO_x/Cu(111) and ZnO/Cu(111) Catalysts: Role of the Metal-Oxide Interface and Importance of Ce³⁺ Sites. *J. Phys. Chem. C* **2016**, *120*, 1778–1784. doi: 10.1021/acs.jpcc.5b12012
9. Vourros, A.; Garagounis, I.; Kyriakou, V.; Carabineiro, S.A.C.; Maldonado-Hódar, F.J.; Marnellos, G.E.; Konsolakis, M. Carbon dioxide hydrogenation over supported Au nanoparticles: Effect of the support. *J. CO₂ Util.* **2017**, *19*, 247–256. doi: 10.1016/j.jcou.2017.04.005
10. Aguayo, A.T.; Ereña, J.; Sierra, I.; Olazar, M.; Bilbao, J. Deactivation and regeneration of hybrid catalysts in the single-step synthesis of dimethyl ether from syngas and CO₂. *Catal. Today* **2005**, *106*, 265–270. doi: 10.1016/j.cattod.2005.07.144

11. Zhang, Y.; Fei, J.; Yu, Y.; Zheng, X. Silica immobilized ruthenium catalyst used for carbon dioxide hydrogenation to formic acid (I): the effect of functionalizing group and additive on the catalyst performance. *Catal. Commun.* **2004**, *5*, 643–646. doi: 10.1016/j.catcom.2004.08.001
12. Saeidi, S.; Amin, N.A.S.; Rahimpour, M.R. Hydrogenation of CO₂ to value-added products - A review and potential future developments. *J. CO₂ Util.* **2014**, *5*, 66–81. doi: 10.1016/j.jcou.2013.12.005
13. Kaiser, P.; Unde, R.B.; Kern, C.; Jess, A. Production of Liquid Hydrocarbons with CO₂ as Carbon Source based on Reverse Water-Gas Shift and Fischer-Tropsch Synthesis. *Chemie Ingenieur Technik* **2013**, *85*, 489–499. doi: 10.1002/cite.201200179
14. Pastor-Pérez, L.; Baibars, F.; Le Sache, E.; Arellano-García, H.; Gu, S.; Reina, T.R. CO₂ valorisation via Reverse Water-Gas Shift reaction using advanced Cs doped Fe-Cu/Al₂O₃ catalysts. *J. CO₂ Util.* **2017**, *21*, 423–428. doi: 10.1016/j.jcou.2017.08.009
15. Tada, S.; Ochieng, O.J.; Kikuchi, R.; Haneda, T.; Kameyama, H. Promotion of CO₂ methanation activity and CH₄ selectivity at low temperatures over Ru/CeO₂/Al₂O₃ catalysts. *Int. J. Hydrogen Energy* **2014**, *39*, 10090–10100. doi: 10.1016/j.ijhydene.2014.04.133
16. Mazza, A.; Bompard, E.; Chicco, G. Applications of power to gas technologies in emerging electrical systems. *Renew. Sustain. Energy Rev.* **2018**, *92*, 794–806. doi: 10.1016/j.rser.2018.04.072
17. Lewandowska-Bernat, A.; Desideri, U. Opportunities of Power-to-Gas technology. *Energy Procedia* **2017**, *105*, 4569–4574. doi: 10.1016/j.egypro.2017.03.982
18. Van Leeuwen, C.; Mulder, M. Power-to-gas in electricity markets dominated by renewables. *Appl. Energy* **2018**, *232*, 258–272. doi: 10.1016/j.apenergy.2018.09.217
19. Götz, M.; Lefebvre, J.; Mörs, F.; McDaniel Koch, A.; Graf, F.; Bajohr, S.; Reimert, R.; Kolb, T. Renewable Power-to-Gas: A technological and economic review. *Renew. Energy* **2016**, *85*, 1371–1390. doi: 10.1016/j.renene.2015.07.066
20. Ghaib, K.; Ben-Fares, F.-Z. Power-to-Methane: A state-of-the-art review. *Renew. Sustain. Energy Rev.* **2018**, *81*, 433–446. doi: 10.1016/j.rser.2017.08.004
21. Zangeneh, F.T.; Sahebdehfar, S.; Ravanchi, M.T. Conversion of carbon dioxide to valuable petrochemicals: An approach to clean development mechanism. *J. Nat. Gas Chem.* **2011**, *20*, 219–231. doi: 10.1016/S1003-9953(10)60191-0
22. Ma, J.; Sun, N.; Zhang, X.; Zhao, N.; Xiao, F.; Wei, W.; Sun, Y. A short review of catalysis for CO₂ conversion. *Catal. Today* **2009**, *148*, 221–231. doi:

- 10.1016/j.cattod.2009.08.015
23. Saeidi, S.; Najari, S.; Fazlollahi, F.; Nikoo, M.K.; Sefidkon, F.; Klemeš, J.J.; Baxter, L.L. Mechanisms and kinetics of CO₂ hydrogenation to value-added products: A detailed review on current status and future trends. *Renew. Sustain. Energy Rev.* **2017**, *80*, 1292–1311. doi: 10.1016/j.rser.2017.05.204
 24. Centi, G.; Perathoner, S. Heterogeneous catalytic reactions with CO₂: Status and perspectives. *Stud. Surf. Sci. Catal.* **2004**, *153*, 1–8. doi: 10.1016/S0167-2991(04)80212-X
 25. Wang, W.; Wang, S.; Ma, X.; Gong, J. Recent advances in catalytic hydrogenation of carbon dioxide. *Chem. Soc. Rev.* **2011**, *40*, 3703–3727. doi: 10.1039/c1cs15008a
 26. Boaro, M.; Colussi, S.; Trovarelli, A. Ceria-Based Materials in Hydrogenation and Reforming Reactions for CO₂ Valorization. *Front. Chem.* **2019**, *7*, 28. doi: 10.3389/fchem.2019.00028
 27. Porosoff, M.D.; Yan, B.; Chen, J.G. Catalytic reduction of CO₂ by H₂ for synthesis of CO, methanol and hydrocarbons: challenges and opportunities. *Energy Environ. Sci.* **2016**, *9*, 62–73. doi: 10.1039/c5ee02657a
 28. Scibioh, M.A.; Viswanathan, B. Chapter 5–Heterogeneous Hydrogenation of CO₂. *Carbon Dioxide Chem. Fuels* **2018**, 191–253. doi: 10.1016/B978-0-444-63996-7.00005-5
 29. Ghaib, K.; Nitz, K.; Ben-Fares, F.-Z. Chemical Methanation of CO₂: A Review. *ChemBioEng Rev.* **2016**, *3*, 266–275. doi: 10.1002/cite.201600066
 30. Frontera, P.; Macario, A.; Ferraro, M.; Antonucci, P. Supported Catalysts for CO₂ Methanation: A Review. *Catalysts* **2017**, *7*, 59. doi: 10.3390/catal7020059
 31. Gao, J.; Liu, Q.; Gu, F.; Liu, B.; Zhong, Z.; Su, F. Recent advances in methanation catalysts for the production of synthetic natural gas. *RSC Adv.* **2015**, *5*, 22759–22776. doi: 10.1039/c4ra16114a
 32. Winter, L.R.; Chen, R.; Chen, X.; Chang, K.; Liu, Z.; Senanayake, S.D.; Ebrahim, A.M.; Chen, J.G. Elucidating the roles of metallic Ni and oxygen vacancies in CO₂ hydrogenation over Ni/CeO₂ using isotope exchange and in situ measurements. *Appl. Catal. B Environ.* **2019**, *245*, 360–366. doi: 10.1016/j.apcatb.2018.12.069
 33. Melchionna, M.; Fornasiero, P. The role of ceria-based nanostructured materials in energy applications. *Mater. Today* **2014**, *17*, 349–357. doi: 10.1016/j.mattod.2014.05.005
 34. Montini, T.; Melchionna, M.; Monai, M.; Fornasiero, P. Fundamentals and Catalytic

- Applications of CeO₂-Based Materials. *Chem. Rev.* **2016**, *116*, 5987–6041. doi: 10.1021/acs.chemrev.5b00603
35. Hemalatha, P.; Bhagiyalakshmi, M.; Ganesh, M.; Palanichamy, M.; Murugesan, V.; Jang, H.T. Role of ceria in CO₂ adsorption on NaZSM-5 synthesized using rice husk ash. *J. Ind. Eng. Chem.* **2012**, *18*, 260–265. doi: 10.1016/j.jiec.2011.11.046
36. Konsolakis, M. The role of Copper–Ceria interactions in catalysis science: Recent theoretical and experimental advances. *Appl. Catal. B Environ.* **2016**, *198*, 49–66. doi: 10.1016/j.apcatb.2016.05.037
37. Cargnello, M.; Doan-Nguyen, V.V.T.; Gordon, T.R.; Diaz, R.E.; Stach, E.A.; Gorte, R.J.; Fornasiero, P.; Murray, C.B. Control of Metal Nanocrystal Size Reveals Metal-Support Interface Role for Ceria Catalysts. *Science* **2013**, *341*, 771–773. doi: 10.1126/science.1240148
38. Cargnello, M.; Fornasiero, P.; Gorte, R.J. Opportunities for Tailoring Catalytic Properties Through Metal-Support Interactions. *Catal. Lett.* **2012**, *142*, 1043–1048. doi: 10.1007/s10562-012-0883-4
39. Sharma, S.; Hu, Z.; Zhang, P.; McFarland, E.W.; Metiu, H. CO₂ methanation on Ru-doped ceria. *J. Catal.* **2011**, *278*, 297–309. doi: 10.1016/j.jcat.2010.12.015
40. Beuls, A.; Swalus, C.; Jacquemin, M.; Heyen, G.; Karelavic, A.; Ruiz, P. Methanation of CO₂: Further insight into the mechanism over Rh/γ-Al₂O₃ catalyst. *Appl. Catal. B Environ.* **2012**, *113–114*, 2–10. doi: 10.1016/j.apcatb.2011.02.033
41. Díez-Ramírez, J.; Valverde, J.L.; Sánchez, P.; Dorado, F. CO₂ Hydrogenation to Methanol at Atmospheric Pressure: Influence of the Preparation Method of Pd/ZnO Catalysts. *Catal. Lett.* **2016**, *146*, 373–382. doi: 10.1007/s10562-015-1627-z
42. Klankermayer, J.; Wesselbaum, S.; Beydoun, K.; Leitner, W. Selective Catalytic Synthesis Using the Combination of Carbon Dioxide and Hydrogen: Catalytic Chess at the Interface of Energy and Chemistry. *Angew. Chem. Int. Ed.* **2016**, *55*, 7296–7343. doi: 10.1002/anie.201507458
43. Spezzati, G.; Benavidez, A.D.; DeLaRiva, A.T.; Su, Y.; Hofmann, J.P.; Asahina, S.; Olivier, E.J.; Neethling, J.H.; Miller, J.T.; Datye, A.K.; Hensen, E.J.M. CO oxidation by Pd supported on CeO₂(100) and CeO₂(111) facets. *Appl. Catal. B Environ.* **2019**, *243*, 36–46. doi: 10.1016/j.apcatb.2018.10.015
44. Liu, C.; Cundari, T.R.; Wilson, A.K. CO₂ Reduction on Transition Metal (Fe, Co, Ni, and Cu) Surfaces: In Comparison with Homogeneous Catalysis. *J. Phys. Chem. C* **2012**, *116*, 5681–5688. doi: 10.1021/jp210480c

45. Konsolakis, M.; Lykaki, M. Recent Advances on the Rational Design of Non-Precious Metal Oxide Catalysts Exemplified by CuO_x/CeO₂ Binary System: Implications of Size, Shape and Electronic Effects on Intrinsic Reactivity and Metal-Support Interactions. *Catalysts* **2020**, *10*, 160. doi: 10.3390/catal10020160
46. Konsolakis, M.; Lykaki, M. Facet-Dependent Reactivity of Ceria Nanoparticles Exemplified by CeO₂-Based Transition Metal Catalysts: A Critical Review. *Catalysts* **2021**, *11*, 452. doi: 10.3390/catal11040452
47. Konsolakis, M.; Ioakeimidis, Z. Surface/structure functionalization of copper-based catalysts by metal-support and/or metal-metal interactions. *Appl. Surf. Sci.* **2014**, *320*, 244–255. doi: 10.1016/j.apsusc.2014.08.114
48. Park, J.B.; Graciani, J.; Evans, J.; Stacchiola, D.; Senanayake, S.D.; Barrio, L.; Liu, P.; Sanz, J.F.; Hrbek, J.; Rodriguez, J.A. Gold, Copper, and Platinum Nanoparticles Dispersed on CeO_x/TiO₂(110) Surfaces: High Water-Gas Shift Activity and the Nature of the Mixed-Metal Oxide at the Nanometer Level. *J. Am. Chem. Soc.* **2010**, *132*, 356–363. doi: 10.1021/ja9087677
49. Kattel, S.; Liu, P.; Chen, J.G. Tuning Selectivity of CO₂ Hydrogenation Reactions at the Metal/Oxide Interface. *J. Am. Chem. Soc.* **2017**, *139*, 9739–9754. doi: 10.1021/jacs.7b05362
50. Owen, R.E.; Plucinski, P.; Mattia, D.; Torrente-Murciano, L.; Ting, V.P.; Jones, M.D. Effect of support of Co-Na-Mo catalysts on the direct conversion of CO₂ to hydrocarbons. *J. CO₂ Util.* **2016**, *16*, 97–103. doi: 10.1016/j.jcou.2016.06.009
51. Le, T.A.; Kim, T.W.; Lee, S.H.; Park, E.D. Effects of Na content in Na/Ni/SiO₂ and Na/Ni/CeO₂ catalysts for CO and CO₂ methanation. *Catal. Today* **2018**, *303*, 159–167. doi: 10.1016/j.cattod.2017.09.031
52. Sun, C.; Li, H.; Chen, L. Nanostructured ceria-based materials: synthesis, properties, and applications. *Energy Environ. Sci.* **2012**, *5*, 8475–8505. doi: 10.1039/c2ee22310d
53. Yao, X.; Tang, C.; Gao, F.; Dong, L. Research progress on the catalytic elimination of atmospheric molecular contaminants over supported metal-oxide catalysts. *Catal. Sci. Technol.* **2014**, *4*, 2814–2829. doi: 10.1039/c4cy00397g
54. Ganduglia-Pirovano, M.V.; Hofmann, A.; Sauer, J. Oxygen vacancies in transition metal and rare earth oxides: Current state of understanding and remaining challenges. *Surf. Sci. Rep.* **2007**, *62*, 219–270. doi: 10.1016/j.surfrep.2007.03.002
55. Ouyang, B.; Tan, W.; Liu, B. Morphology effect of nanostructure ceria on the Cu/CeO₂ catalysts for synthesis of methanol from CO₂ hydrogenation. *Catal. Commun.* **2017**,

- 95, 36–39. doi: 10.1016/j.catcom.2017.03.005
56. Si, R.; Flytzani-Stephanopoulos, M. Shape and Crystal-Plane Effects of Nanoscale Ceria on the Activity of Au-CeO₂ Catalysts for the Water–Gas Shift Reaction. *Angew. Chem. Int. Ed.* **2008**, *47*, 2884–2887. doi: 10.1002/anie.200705828
57. Liu, Y.; Li, Z.; Xu, H.; Han, Y. Reverse water-gas shift reaction over ceria nanocube synthesized by hydrothermal method. *Catal. Commun.* **2016**, *76*, 1–6. doi: 10.1016/j.catcom.2015.12.011
58. Yang, S.-C.; Pang, S.H.; Sulmonetti, T.P.; Su, W.-N.; Lee, J.-F.; Hwang, B.-J.; Jones, C.W. Synergy between Ceria Oxygen Vacancies and Cu Nanoparticles Facilitates the Catalytic Conversion of CO₂ to CO under Mild Conditions. *ACS Catal.* **2018**, *8*, 12056–12066. doi: 10.1021/acscatal.8b04219
59. Muroyama, H.; Tsuda, Y.; Asakoshi, T.; Masitah, H.; Okanishi, T.; Matsui, T.; Eguchi, K. Carbon dioxide methanation over Ni catalysts supported on various metal oxides. *J. Catal.* **2016**, *343*, 178–184. doi: 10.1016/j.jcat.2016.07.018
60. Pan, Q.; Peng, J.; Sun, T.; Wang, S.; Wang, S. Insight into the reaction route of CO₂ methanation: Promotion effect of medium basic sites. *Catal. Commun.* **2014**, *45*, 74–78. doi: 10.1016/j.catcom.2013.10.034
61. Le, T.A.; Kim, M.S.; Lee, S.H.; Kim, T.W.; Park, E.D. CO and CO₂ methanation over supported Ni catalysts. *Catal. Today* **2017**, *293–294*, 89–96. doi: 10.1016/j.cattod.2016.12.036
62. Ussa Aldana, P.A.; Ocampo, F.; Kobl, K.; Louis, B.; Thibault-Starzyk, F.; Daturi, M.; Bazin, P.; Thomas, S.; Roger, A.C. Catalytic CO₂ valorization into CH₄ on Ni-based ceria-zirconia. Reaction mechanism by *operando* IR spectroscopy. *Catal. Today* **2013**, *215*, 201–207. doi: 10.1016/j.cattod.2013.02.019
63. Martin, N.M.; Velin, P.; Skoglundh, M.; Bauer, M.; Carlsson, P.-A. Catalytic hydrogenation of CO₂ to methane over supported Pd, Rh and Ni catalysts. *Catal. Sci. Technol.* **2017**, *7*, 1086–1094. doi: 10.1039/c6cy02536f
64. Martin, N.M.; Hemmingsson, F.; Schaefer, A.; Ek, M.; Merte, L.R.; Hejral, U.; Gustafson, J.; Skoglundh, M.; Dippel, A.-C.; Gutowski, O.; Bauer, M.; Carlsson, P.-A. Structure-function relationship for CO₂ methanation over ceria supported Rh and Ni catalysts under atmospheric pressure conditions. *Catal. Sci. Technol.* **2019**, *9*, 1644–1653. doi: 10.1039/c8cy02097c
65. Guo, C.; Wei, S.; Zhou, S.; Zhang, T.; Wang, Z.; Ng, S.-P.; Lu, X.; Wu, C.-M.L.; Guo, W. Initial Reduction of CO₂ on Pd-, Ru-, and Cu-Doped CeO₂(111) Surfaces: Effects of

- Surface Modification on Catalytic Activity and Selectivity. *ACS Appl. Mater. Interfaces* **2017**, *9*, 26107–26117. doi: 10.1021/acsami.7b07945
66. Stefa, S. Rational Design and Development of Nanostructured Non-Precious Metal Oxide Catalysts for Energy and Environmental Applications. PhD Thesis, *in progress*.
67. Varvoutis, G. Design and Evaluation of Advanced CeO₂-Based Transition Metal Catalytic Composites for CO₂ Activation by Renewable H₂ toward Chemicals and Fuels. PhD Thesis, *in progress*.
68. Sharma, V.; Eberhardt, K.M.; Sharma, R.; Adams, J.B.; Crozier, P.A. A spray drying system for synthesis of rare-earth doped cerium oxide nanoparticles. *Chem. Phys. Lett.* **2010**, *495*, 280–286. doi: 10.1016/j.cplett.2010.06.060
69. Uzunoglu, A.; Zhang, H.; Andreescu, S.; Stanciu, L.A. CeO₂-MO_x (M: Zr, Ti, Cu) mixed metal oxides with enhanced oxygen storage capacity. *J. Mater. Sci.* **2015**, *50*, 3750–3762. doi: 10.1007/s10853-015-8939-7
70. Hermes, E.D.; Jenness, G.R.; Schmidt, J.R. Decoupling the electronic, geometric and interfacial contributions to support effects in heterogeneous catalysis. *Mol. Simul.* **2015**, *41*, 123–133. doi: 10.1080/08927022.2014.926549
71. Lykaki, M.; Pachatouridou, E.; Iliopoulou, E.; Carabineiro, S.A.C.; Konsolakis, M. Impact of the synthesis parameters on the solid state properties and the CO oxidation performance of ceria nanoparticles. *RSC Adv.* **2017**, *7*, 6160–6169. doi: 10.1039/c6ra26712b
72. Yu, S.-W.; Huang, H.-H.; Tang, C.-W.; Wang, C.-B. The effect of accessible oxygen over Co₃O₄-CeO₂ catalysts on the steam reforming of ethanol. *Int. J. Hydrogen Energy* **2014**, *39*, 20700–20711. doi: 10.1016/j.ijhydene.2014.07.139
73. Van Deelen, T.W.; Hernández Mejía, C.; De Jong, K.P. Control of metal-support interactions in heterogeneous catalysts to enhance activity and selectivity. *Nat. Catal.* **2019**, *2*, 955–970. doi: 10.1038/s41929-019-0364-x
74. Mitchell, S.; Qin, R.; Zheng, N.; Pérez-Ramírez, J. Nanoscale engineering of catalytic materials for sustainable technologies. *Nat. Nanotechnol.* **2021**, *16*, 129–139. doi: 10.1038/s41565-020-00799-8
75. Dong, L.; Yao, X.; Chen, Y. Interactions among supported copper-based catalyst components and their effects on performance: A review. *Chinese J. Catal.* **2013**, *34*, 851–864. doi: 10.1016/S1872-2067(12)60592-0
76. Puigdollers, A.R.; Schlexer, P.; Tosoni, S.; Pacchioni, G. Increasing Oxide Reducibility: The Role of Metal/Oxide Interfaces in the Formation of Oxygen Vacancies. *ACS Catal.*

- 2017**, 7, 6493–6513. doi: 10.1021/acscatal.7b01913
77. Bian, Z.; Chan, Y.M.; Yu, Y.; Kawi, S. Morphology dependence of catalytic properties of Ni/CeO₂ for CO₂ methanation: A kinetic and mechanism study. *Catal. Today* **2020**, 347, 31–38. doi: 10.1016/j.cattod.2018.04.067
78. Kovacevic, M.; Mojet, B.L.; Van Ommen, J.G.; Lefferts, L. Effects of Morphology of Cerium Oxide Catalysts for Reverse Water Gas Shift Reaction. *Catal. Lett.* **2016**, 146, 770–777. doi: 10.1007/s10562-016-1697-6
79. Dai, B.; Zhou, G.; Ge, S.; Xie, H.; Jiao, Z.; Zhang, G.; Xiong, K. CO₂ reverse water-gas shift reaction on mesoporous M-CeO₂ catalysts. *Can. J. Chem. Eng.* **2017**, 95, 634–642. doi: 10.1002/cjce.22730
80. Lin, L.; Yao, S.; Liu, Z.; Zhang, F.; Li, N.; Vovchok, D.; Martínez-Arias, A.; Castañeda, R.; Lin, J.; Senanayake, S.D.; Su, D.; Ma, D.; Rodriguez, J.A. In Situ Characterization of Cu/CeO₂ Nanocatalysts for CO₂ Hydrogenation: Morphological Effects of Nanostructured Ceria on the Catalytic Activity. *J. Phys. Chem. C* **2018**, 122, 12934–12943. doi: 10.1021/acs.jpcc.8b03596
81. Liu, Y.; Liu, D. Study of bimetallic Cu-Ni/γ-Al₂O₃ catalysts for carbon dioxide hydrogenation. *Int. J. Hydrogen Energy* **1999**, 24, 351–354. doi: 10.1016/S0360-3199(98)00038-X
82. Chen, C.-S.; Cheng, W.-H.; Lin, S.-S. Study of iron-promoted Cu/SiO₂ catalyst on high temperature reverse water gas shift reaction. *Appl. Catal. A Gen.* **2004**, 257, 97–106. doi: 10.1016/S0926-860X(03)00637-9
83. Zhang, X.; Zhu, X.; Lin, L.; Yao, S.; Zhang, M.; Liu, X.; Wang, X.; Li, Y.-W.; Shi, C.; Ma, D. Highly Dispersed Copper over β-Mo₂C as an Efficient and Stable Catalyst for the Reverse Water Gas Shift (RWGS) Reaction. *ACS Catal.* **2017**, 7, 912–918. doi: 10.1021/acscatal.6b02991
84. Konsolakis, M.; Lykaki, M.; Stefa, S.; Carabineiro, S.A.C.; Varvoutis, G.; Papista, E.; Marnellos, G.E. CO₂ Hydrogenation over Nanoceria-Supported Transition Metal Catalysts: Role of Ceria Morphology (Nanorods versus Nanocubes) and Active Phase Nature (Co versus Cu). *Nanomaterials* **2019**, 9, 1739. doi: 10.3390/nano9121739
85. Varvoutis, G.; Lykaki, M.; Stefa, S.; Papista, E.; Carabineiro, S.A.C.; Marnellos, G.E.; Konsolakis, M. Remarkable efficiency of Ni supported on hydrothermally synthesized CeO₂ nanorods for low-temperature CO₂ hydrogenation to methane. *Catal. Commun.* **2020**, 142, 106036. doi: 10.1016/j.catcom.2020.106036
86. Jwa, E.; Lee, S.B.; Lee, H.W.; Mok, Y.S. Plasma-assisted catalytic methanation of CO

- and CO₂ over Ni-zeolite catalysts. *Fuel Process. Technol.* **2013**, *108*, 89–93. doi: 10.1016/j.fuproc.2012.03.008
87. Miao, B.; Ma, S.S.K.; Wang, X.; Su, H.; Chan, S.H. Catalysis mechanisms of CO₂ and CO methanation. *Catal. Sci. Technol.* **2016**, *6*, 4048–4058. doi: 10.1039/c6cy00478d
88. Zhen, W.; Li, B.; Lu, G.; Ma, J. Enhancing catalytic activity and stability for CO₂ methanation on Ni@MOF-5 via control of active species dispersion. *Chem. Commun.* **2015**, *51*, 1728–1731. doi: 10.1039/c4cc08733j
89. Weatherbee, G.D.; Bartholomew, C.H. Hydrogenation of CO₂ on group VIII metals. II. Kinetics and mechanism of CO₂ hydrogenation on nickel. *J. Catal.* **1982**, *77*, 460–472. doi: 10.1016/0021-9517(82)90186-5
90. Zhou, G.; Liu, H.; Xing, Y.; Xu, S.; Xie, H.; Xiong, K. CO₂ hydrogenation to methane over mesoporous Co/SiO₂ catalysts: Effect of structure. *J. CO₂ Util.* **2018**, *26*, 221–229. doi: 10.1016/j.jcou.2018.04.023
91. Ginés, M.J.L.; Marchi, A.J.; Apesteguía, C.R. Kinetic study of the reverse water-gas shift reaction over CuO/ZnO/Al₂O₃ catalysts. *Appl. Catal. A Gen.* **1997**, *154*, 155–171. doi: 10.1016/S0926-860X(96)00369-9
92. Chen, C.-S.; Cheng, W.-H. Study on the mechanism of CO formation in reverse water gas shift reaction over Cu/SiO₂ catalyst by pulse reaction, TPD and TPR. *Catal. Lett.* **2002**, *83*, 121–126. doi: 10.1023/A:1021006718974
93. Lykaki, M.; Pachatouridou, E.; Carabineiro, S.A.C.; Iliopoulou, E.; Andriopoulou, C.; Kallithrakas-Kontos, N.; Boghosian, S.; Konsolakis, M. Ceria nanoparticles shape effects on the structural defects and surface chemistry: Implications in CO oxidation by Cu/CeO₂ catalysts. *Appl. Catal. B Environ.* **2018**, *230*, 18–28. doi: 10.1016/j.apcatb.2018.02.035
94. Quindimil, A.; De-La-Torre, U.; Pereda-Ayo, B.; Davó-Quiñonero, A.; Bailón-García, E.; Lozano-Castelló, D.; González-Marcos, J.A.; Bueno-López, A.; González-Velasco, J.R. Effect of metal loading on the CO₂ methanation: A comparison between alumina supported Ni and Ru catalysts. *Catal. Today* **2020**, *356*, 419–432. doi: 10.1016/j.cattod.2019.06.027
95. Lin, J.; Ma, C.; Wang, Q.; Xu, Y.; Ma, G.; Wang, J.; Wang, H.; Dong, C.; Zhang, C.; Ding, M. Enhanced low-temperature performance of CO₂ methanation over mesoporous Ni/Al₂O₃-ZrO₂ catalysts. *Appl. Catal. B Environ.* **2019**, *243*, 262–272. doi: 10.1016/j.apcatb.2018.10.059
96. Cárdenas-Arenas, A.; Quindimil, A.; Davó-Quiñonero, A.; Bailón-García, E.; Lozano-

- Castelló, D.; De-La-Torre, U.; Pereda-Ayo, B.; González-Marcos, J.A.; González-Velasco, J.R.; Bueno-López, A. Isotopic and *in situ* DRIFTS study of the CO₂ methanation mechanism using Ni/CeO₂ and Ni/Al₂O₃ catalysts. *Appl. Catal. B Environ.* **2020**, *265*, 118538. doi: 10.1016/j.apcatb.2019.118538
97. Alcalde-Santiago, V.; Davó-Quiñonero, A.; Lozano-Castelló, D.; Quindimil, A.; De-La-Torre, U.; Pereda-Ayo, B.; González-Marcos, J.A.; González-Velasco, J.R.; Bueno-López, A. Ni/LnO_x Catalysts (Ln = La, Ce or Pr) for CO₂ Methanation. *ChemCatChem* **2019**, *11*, 810–819. doi: 10.1002/cctc.201801585

CHAPTER 6

General Conclusions and Future Research Outlook

Chapter 6 provides the general conclusions drawn by the present thesis while some guidelines and perspectives for future research are being proposed.



GENERAL CONCLUSIONS

In the present thesis, a series of bare ceria and ceria-based transition metal catalysts (M_xO_y/CeO_2 , M: Cu, Co, Fe, Ni) were developed, thoroughly characterized by several *in situ* and *ex situ* techniques and evaluated in various catalytic reactions, including CO oxidation, N_2O decomposition and CO_2 hydrogenation to CO and CH_4 . As already mentioned in the Abstract, the present thesis has focused on the following research objectives towards the establishment of reliable structure-activity relationships:

- (i) Ceria shape effects on the structural defects and surface chemistry,
- (ii) Facet-dependent reactivity of ceria-based transition metal catalytic materials,
- (iii) Shape/electronic effects on the surface chemistry and the catalytic performance.
- (iv) Development of cost-efficient and highly-active ceria-based transition metal catalytic materials,
- (v) Rational design of metal oxide catalysts through advanced synthetic/promotional routes,
- (vi) Fine-tuning of the local surface chemistry towards the development of highly active/selective catalytic materials,

On the basis of the above objectives and the progress achieved in the framework of the present thesis, the following conclusions can be drawn:

- ✓ In the framework of rational design, different preparation methods were employed and it was revealed that the hydrothermal method results in the development of ceria nanoparticles of specific architecture, *i.e.*, nanorods, nanopolyhedra, nanocubes, exposing distinctive crystal facets of different coordination environments, leading to diverse catalytic reactivity. Ceria nanorods, exposing the {100} and {110} crystal planes, demonstrated the optimum redox properties and enhanced oxygen kinetics, linked to their abundance in structural defects and oxygen vacancies. On the basis of oxygen storage capacity (OSC), the following order was obtained: nanorods > nanopolyhedra > nanocubes, which is well-related to the anionic vacancies' formation energy, namely, {110} < {100} < {111}.
- ✓ In the context of developing cost-efficient and highly-active catalytic materials, various earth-abundant and of low cost transition metals (Cu, Co, Fe, Ni) were used as active phases in combination with ceria carriers of different

structure/morphology. The engineering of size/shape of the support in conjunction to metal's entity can strongly affect the interfacial reactivity through both geometric and electronic interactions, offering metal oxide systems with the desired properties. The addition of the transition metal phase to the different ceria supports significantly enhances the surface oxygen reduction and oxygen kinetics through metal-support interactions, following, however, the same trend with the bare ceria nanoparticles, revealing the crucial role of support morphology on the redox properties of the ceria-based catalysts. It was clearly revealed that extremely active ceria-based metal oxides can be obtained with a catalytic performance comparable or even superior to that of NMs-based catalysts.

- ✓ In the case of CO oxidation reaction, the copper-ceria catalyst of rod-like morphology exhibited a half-conversion temperature (T_{50}) of *ca.* 70 °C, which is much lower to that of a typical noble metal oxidation catalyst, such as Pt/Al₂O₃ (T_{50} = 230 °C). Perfect relationships were disclosed between the reaction rate (r_{CO} , mmol s⁻¹ g⁻¹) and the following activity descriptors: (a) the population of oxygen vacancies expressed by the I_D/I_{F2g} ratio and (b) the oxygen storage capacity (OSC).
- ✓ The pivotal role of support morphology was revealed as well in the case of the N₂O decomposition reaction as cobalt-ceria nanorods, exposing {100} and {110} facets, exhibited the best deN₂O performance in the presence and in the absence of oxygen, ascribed mainly to their enhanced redox, surface and textural properties. A perfect relationship was disclosed between the half-conversion temperature (T_{50}) and the surface-to-bulk oxygen ratio (O_s/O_b).
- ✓ Surface engineering (*e.g.*, by alkali promoters) can be used as an additional adjustment tool towards regulating the local surface structure and electronic environment. In this regard, Cu/CeO₂ catalysts pre-optimized through the preparation method (co-precipitation) and subsequently promoted by alkali (Cs), exhibited superior deN₂O performance, leading to oxygen-tolerant composites.
- ✓ In the case of CO₂ hydrogenation reaction, it was revealed that the metal's nature rather than the support morphology plays an important role in the CO₂ conversion, following the sequence: CeO₂ < Fe/CeO₂ < Cu/CeO₂ < Co/CeO₂ < Ni/CeO₂, indicating the pivotal role of metal-support combination. From a practical point of view, the Ni/CeO₂-NR catalyst demonstrated an excellent conversion and selectivity performance (*ca.* 98% yield to methane at 300 °C), being superior to the most of

state-of-the-art catalysts. On the other hand, Cu/CeO₂ samples were highly selective towards rWGS reaction, exhibiting *ca.* 60% yield to CO at 400 °C.

FUTURE RESEARCH OUTLOOK

The main objective of the present thesis was the development of cost-efficient noble metal-free ceria-based catalytic systems of high activity, stability, selectivity, of which their use could be extended to practical applications. As clearly demonstrated by the current thesis, the rational design through the fine-tuning of size, shape, chemical/electronic environment, can lead to materials of high catalytic efficiency. In particular, the above-mentioned factors can have a great impact on the reactivity of the metal sites, as well as on the interfacial activity through both geometric and electronic synergistic interactions towards the development of noble metal-free highly active and selective composites for several energy and environmental applications.

In this context, special pretreatment protocols or activation procedures can notably affect the metal dispersion and the population of oxygen defects, with great implications in the catalytic performance. Besides the modulation of local surface chemistry by means of size/shape engineering and electronic/chemical modification through alkali promotion, the addition of carbon-based materials, such as reduced graphene oxide (rGO) or graphitic carbon nitride (g-C₃N₄) or the employment of metal-organic frameworks (MOFs) can be adopted as additional functionalization tools towards the regulation of the electronic environment and the oxygen exchange kinetics of metal oxides. Another approach towards the fine-tuning of metal oxides could be the implementation of computational studies (*e.g.*, Density Functional Theory (DFT) calculations) prior to catalysts' synthesis, in order to obtain the required feedback that would lead to the appropriate functionalization of specific parameters. In addition, it should be mentioned that reducible oxides, such as ceria or titania, could be combined with bimetallic or carbide-based materials towards the development of multifunctional composites with enhanced properties and catalytic performance. Moreover, taking into account the pivotal role of support morphology, as clearly demonstrated in the present thesis, research efforts could be extended to the development of catalytic composites with predefined active phase's shape in combination with the distinct morphology of the support.

In the end, the deductions made from the current thesis could provide the design principles for the development of catalytic composites free of noble metals or of very low noble metal content, paving the way towards their replacement or their decrease in energy and

environmental applications in which their use is inevitable. In any case, the fundamental understanding of structure-property relationships is a prerequisite factor towards the rational design of efficient and inexpensive catalytic composites.

Curriculum Vitae

PERSONAL INFORMATION

Maria Lykaki

📍 Euripidou 8, Chrisopigi, Chania 73100, Crete, Greece

☎ +30 28210 37234 📠 +30 6976718257

✉ mlykaki@isc.tuc.gr

Sex Female | **Date of Birth** 05 January 1988 | **Nationality** Greek

WORK EXPERIENCE

01/03/2020 – 30/11/2021

Research project NANOCO2, Technical University of Crete.

01/03/2019 – 29/02/2020

Research project LIGBIO-GASOFC, Technical University of Crete.

17/06/2015 – 08/09/2015

HIOTAKIS SA (Production factory of dough products).

Supervision of the production process.

16/07/2013 – 30/06/2014

Agricultural Cooperation of Kofina.

Chemical and Microbiological analysis of milk and dairy products.

12/10/2009 – 31/12/2009

Internship in MILLS of Crete.

Analysis of flour and dough.

01/07/2008 – 30/09/2008

Internship in Mediterranean Agronomic Institute of Chania (M.A.I.CH.).

Analysis and control of antioxidant activity of natural products.

EDUCATION AND TRAINING

2016 – 2021

PhD "Synthesis and Characterization of Ceria-Based Nano-Structured Materials: Structure–Activity Relationships".

School of Production Engineering & Management, Technical University of Crete.

2010 – 2013

Master of Science in Energy and Environmental Chemical Technologies, Department of Science, Technical University of Crete.

2005 – 2010

Diploma in Chemistry, Department of Chemistry, University of Crete.

PERSONAL SKILLS

Mother tongue

Greek

English

C2 (Certificate of Proficiency in English, The University of Michigan)

French

DELFI B1 Junior. Learning in progress to B2 level.

Spanish

Learning in progress.

Digital competence

International Diploma in IT Skills Standard, University of Cambridge. Electronic Communication (Internet Explorer, Microsoft Outlook), Databases, (Microsoft Access), Spreadsheets (Microsoft Excel), Word Processing (Microsoft Word), Using the computer and managing files, Presentations (Microsoft Power point).

Driving license

B

ADDITIONAL INFORMATION

Publications

1. Maria Lykaki, Sofia Stefa, Sónia A.C. Carabineiro, Miguel A. Soria, Luís M. Madeira and Michalis Konsolakis, "Shape Effects of Ceria Nanoparticles on the Water–Gas Shift Performance of $\text{CuO}_x/\text{CeO}_2$ Catalysts", *Catalysts* 11 (2021) 753.
<https://doi.org/10.3390/catal11060753>
2. Georgios Varvoutis, Maria Lykaki, Sofia Stefa, Vassilios Binas, George E. Marnellos, Michalis Konsolakis, "Deciphering the role of Ni particle size and nickel-ceria interfacial perimeter in the low-temperature CO_2 methanation reaction over remarkably active Ni/ CeO_2 nanorods", *Applied Catalysis B: Environmental* 297 (2021) 120401.
<https://doi.org/10.1016/j.apcatb.2021.120401>
3. Michalis Konsolakis and Maria Lykaki, "Facet-Dependent Reactivity of Ceria Nanoparticles Exemplified by CeO_2 -Based Transition Metal Catalysts: A Critical Review", Review Article, *Catalysts* 11 (2021) 452.
<https://doi.org/10.3390/catal11040452>
4. Georgios Varvoutis, Maria Lykaki, Eleni Papista, Sónia A.C. Carabineiro, Antonios C. Psarras, Georgios E. Marnellos, Michalis Konsolakis, "Effect of alkali (Cs) doping on the surface chemistry and CO_2 hydrogenation performance of CuO/CeO_2 catalysts", *Journal of CO_2 Utilization* 44 (2021) 101408.
<https://doi.org/10.1016/j.jcou.2020.101408>
5. Sofia Stefa, Maria Lykaki, Vasillios Binas, Pavlos K. Pandis, Vassilis N. Stathopoulos and Michalis Konsolakis, "Hydrothermal Synthesis of ZnO–Doped Ceria Nanorods: Effect of ZnO Content on the Redox Properties and the CO Oxidation Performance", *Applied Sciences* 10 (2020) 7605.
<https://doi.org/10.3390/app10217605>
6. Sofia Stefa, Maria Lykaki, Dimitrios Fragkoulis, Vasileios Binas, Pavlos K. Pandis, Vassilis N. Stathopoulos and Michalis Konsolakis, "Effect of the Preparation Method on the Physicochemical Properties and the CO Oxidation Performance of Nanostructured $\text{CeO}_2/\text{TiO}_2$ Oxides", *Processes* 8 (2020) 847.
<https://doi.org/10.3390/pr8070847>
7. Georgios Varvoutis, Maria Lykaki, Sofia Stefa, Eleni Papista, Sónia A.C. Carabineiro, Georgios E. Marnellos, Michalis Konsolakis, "Remarkable efficiency of Ni supported on hydrothermally synthesized CeO_2 nanorods for low-temperature CO_2 hydrogenation to methane", *Catalysis Communications* 142 (2020) 106036.
<https://doi.org/10.1016/j.catcom.2020.106036>
8. Michalis Konsolakis and Maria Lykaki, "Recent Advances on the Rational Design of Non-Precious Metal Oxide Catalysts Exemplified by $\text{CuO}_x/\text{CeO}_2$ Binary System: Implications of Size, Shape and Electronic Effects on Intrinsic Reactivity and Metal-Support Interactions", Review Article, *Catalysts* 10 (2020) 160.
<https://doi.org/10.3390/catal10020160>
9. Michalis Konsolakis, Maria Lykaki, Sofia Stefa, Sónia A. C. Carabineiro, Georgios Varvoutis, Eleni Papista and Georgios E. Marnellos, " CO_2 Hydrogenation over Nanoceria-Supported Transition Metal Catalysts: Role of Ceria Morphology (Nanorods versus Nanocubes) and Active Phase Nature (Co versus Cu)", *Nanomaterials* 9 (2019) 1739.
<https://doi.org/10.3390/nano9121739>
10. Alireza Khataee, Dimitrios Kalderis, Peyman Gholami, Arezoo Fazli, Marilena Moschogiannaki, Vasileios Binas, Maria Lykaki, Michalis Konsolakis, " $\text{Cu}_2\text{O}-\text{CuO}@\text{biochar}$ composite: Synthesis,

- characterization and its efficient photocatalytic performance", *Applied Surface Science* 498 (2019) 143846.
<https://doi.org/10.1016/j.apsusc.2019.143846>
11. Maria Lykaki, Sofia Stefa, Sónia A. C. Carabineiro, Pavlos K. Pandis, Vassilis N. Stathopoulos and Michalis Konsolakis, "Facet-Dependent Reactivity of Fe₂O₃/CeO₂ Nanocomposites: Effect of Ceria Morphology on CO Oxidation", *Catalysts* 9 (2019) 371.
<https://doi.org/10.3390/catal9040371>
 12. Maria Lykaki, Eleni Papista, Nikolaos Kaklidis, Sónia A. C. Carabineiro and Michalis Konsolakis, "Ceria Nanoparticles' Morphological Effects on the N₂O Decomposition Performance of Co₃O₄/CeO₂ Mixed Oxides", *Catalysts* 9 (2019) 233.
<https://doi.org/10.3390/catal9030233>
 13. Maria Lykaki, Eleni Papista, Sónia A. C. Carabineiro, Pedro B. Tavares and Michalis Konsolakis, "Optimization of N₂O decomposition activity of CuO–CeO₂ mixed oxides by means of synthesis procedure and alkali (Cs) promotion", *Catalysis Science & Technology* 8 (2018) 2312–2322.
<https://doi.org/10.1039/C8CY00316E>
 14. Maria Lykaki, Eleni Pachatouridou, Sónia A.C. Carabineiro, Eleni Iliopoulou, Chrysanthi Andriopoulou, N. Kallithrakas-Kontos, Soghomon Boghosian, Michalis Konsolakis, "Ceria nanoparticles shape effects on the structural defects and surface chemistry: Implications in CO oxidation by Cu/CeO₂ catalysts", *Applied Catalysis B: Environmental* 230 (2018) 18–28.
<https://doi.org/10.1016/j.apcatb.2018.02.035>
 15. Maria Lykaki, Eleni Pachatouridou, Eleni Iliopoulou, Sónia A. C. Carabineiro and Michalis Konsolakis, "Impact of the synthesis parameters on the solid state properties and the CO oxidation performance of ceria nanoparticles", *RSC Advances* 7 (2017) 6160–6169.
<https://doi.org/10.1039/C6RA26712B>

Citations: 351

h-index: 9

Conferences

1. Μ. Λυκάκη, Γ. Βαρβούτης, S.A.C. Carabineiro, Γ. Μαρνέλλος, Μ. Κονσολάκης, "Επίδραση της μορφολογίας νανο-σωματιδίων CeO₂ κατά την αντίδραση μετατόπισης του υδραερίου σε καταλύτες CuO/CeO₂", 1^ο Διαδικτυακό Συμπόσιο Νέων Επιστημόνων «Ορυκτοί Πόροι-Περιβάλλον-Χημική Μηχανική», 26–28 Φεβρουαρίου 2021.
2. Γ. Βαρβούτης, Μ. Λυκάκη, Ε. Πάπιστα, Α. Ψαρράς, Γ.Ε. Μαρνέλλος, Μ. Κονσολάκης, "Επίδραση της προσθήκης Cs στην επιφανειακή χημεία και στην απόδοση της αντίδρασης αναγωγής CO₂ καταλυτών CuO/CeO₂", 1^ο Διαδικτυακό Συμπόσιο Νέων Επιστημόνων «Ορυκτοί Πόροι-Περιβάλλον-Χημική Μηχανική», 26–28 Φεβρουαρίου 2021.
3. Σ. Στέφα, Μ. Λυκάκη, Β. Μπίνας, Μ. Κονσολάκης, "Μελέτη των φυσικοχημικών ιδιοτήτων και της φωτοκαταλυτικής δραστηρότητας γραφιτικού νιτριδίου του άνθρακα (g-C₃N₄)", 1^ο Διαδικτυακό Συμπόσιο Νέων Επιστημόνων «Ορυκτοί Πόροι-Περιβάλλον-Χημική Μηχανική», 26–28 Φεβρουαρίου 2021.
4. Μ. Konsolakis, Μ. Lykaki, S. Stefa, S.A.C. Carabineiro, G. Varvoutis, E. Papista and G. Marnellos, "Catalytic hydrogenation of CO₂ to methane over transition metals (Ni, Co) supported on nano-ceria", 2nd Webinar on Material Science & Nanotechnology, 18–19 November 2020.
5. G. Varvoutis, Μ. Lykaki, S. Stefa, E. Mandela, G.E. Marnellos, Μ. Konsolakis, "CO₂ hydrogenation over alkali-promoted CuO/CeO₂

- catalysts", 2nd Webinar on Material Science & Nanotechnology, 18–19 November 2020.
6. M. Konsolakis, S. Papaefthimiou, D. Ipsakis, M. Lykaki, S. Stefa, G. Varvoutis, G.E. Marnellos, "Turning CO₂ emissions to CH₄ by means of green H₂ and novel catalytic materials", 5th HAAE Energy Transition Symposium, Athens, 30 September – 2 October 2020.
 7. M. Konsolakis, M. Lykaki, S. Stefa, S.A.C. Carabineiro, G. Varvoutis, E. Papista, G. Marnellos, "Rational design of ceria-based nanocatalysts for CO₂ hydrogenation to value-added products", International Conference on Materials and Nanomaterials, Paris, France 17–19 July 2019.
 8. Μ. Λυκάκη, Σ. Στέφα, Β. Μπίνας, S.A.C. Carabineiro, Π. Πανδής, Β. Σταθόπουλος, Μ. Κονσολάκης, "Επίδραση της μορφολογίας του φορέα (νανο-CeO₂) στα φυσικοχημικά και καταλυτικά χαρακτηριστικά υποστηριγμένων μετάλλων μετάπτωσης MO_x/CeO₂ (M: Ni, Co, Fe)", 12^ο Πανελλήνιο Επιστημονικό Συνέδριο Χημικής Μηχανικής, Αθήνα, 29–31 Μαΐου 2019.
 9. Γ. Βαρβούτης, Ε. Πάπιστα, Ν. Κακλίδης, Γ.Ε. Μαρνέλλος, S.A.C. Carabineiro, Μ. Λυκάκη, Σ. Στέφα, Μ. Κονσολάκης, "Επίδραση της μορφολογίας του φορέα κατά την αντίδραση υδρογόνωσης CO₂ σε καταλύτες μετάλλων μετάπτωσης υποστηριγμένων σε CeO₂", 12^ο Πανελλήνιο Επιστημονικό Συνέδριο Χημικής Μηχανικής, Αθήνα, 29–31 Μαΐου 2019.
 10. Σ. Στέφα, Μ. Λυκάκη, Β. Μπίνας, Π. Πανδής, Β. Σταθόπουλος, Μ. Κονσολάκης, "Επίδραση της μεθόδου σύνθεσης στα φυσικοχημικά χαρακτηριστικά νανοδομημένων οξειδίων CeO₂-TiO₂", 12^ο Πανελλήνιο Επιστημονικό Συνέδριο Χημικής Μηχανικής, Αθήνα, 29–31 Μαΐου 2019.
 11. Α. Λαμπρόπουλος, Ν. Κακλίδης, Ε. Πάπιστα, Β. Μπίνας, Μ. Λυκάκη, Μ. Κονσολάκης, Γ.Ε. Μαρνέλλος, "Επίδραση των συνθηκών πυρόλυσης ελληνικού λιγνίτη στις φυσικοχημικές ιδιότητες και στην ενεργότητα αεριοποίησης των παραγόμενων εξανθρακωμάτων", 12^ο Πανελλήνιο Επιστημονικό Συνέδριο Χημικής Μηχανικής, Αθήνα, 29–31 Μαΐου 2019.
 12. Μ. Λυκάκη, Ε. Παχατουρίδου, S.A.C. Carabineiro, Ε. Ηλιοπούλου, Χ. Ανδριοπούλου, Ν. Καλλίθρακας-Κόντος, Σ. Μπογοσιάν, Μ. Κονσολάκης, "Επίδραση της μορφολογίας του φορέα στις δομικές ατέλειες και την επιφανειακή χημεία υποστηριγμένων καταλυτών CuO/CeO₂", 15^ο Πανελλήνιο Συμπόσιο Κατάλυσης, Ιωάννινα, 18–20 Οκτωβρίου 2018.
 13. Μ. Λυκάκη, Ε. Πάπιστα, S.A.C. Carabineiro, P.B. Tavares, Μ. Κονσολάκης, "Βελτιστοποίηση της δραστηριότητας μικτών οξειδίων CuO/CeO₂ διαμέσου της μεθόδου σύνθεσης και της επιφανειακής προώθησης – Η περίπτωση της καταλυτικής διάσπασης του N₂O", 15^ο Πανελλήνιο Συμπόσιο Κατάλυσης, Ιωάννινα, 18–20 Οκτωβρίου 2018.
 14. Μ. Λυκάκη, Σ. Στέφα, S.A.C. Carabineiro, Π. Πανδής, Β. Σταθόπουλος, Μ. Κονσολάκης, "Επίδραση της νανοδομής του φορέα (CeO₂) στα φυσικοχημικά χαρακτηριστικά και στην καταλυτική δραστηριότητα μικτών οξειδίων Fe₂O₃/CeO₂", 15^ο Πανελλήνιο Συμπόσιο Κατάλυσης, Ιωάννινα, 18–20 Οκτωβρίου 2018.
 15. Ν. Κακλίδης, Μ. Λυκάκη, Μ. Κονσολάκης και Γ.Ε. Μαρνέλλος, "Αεριοποίηση εξανθρακωμάτων ελαιοπυρήνα προς παραγωγή αερίου σύνθεσης με χρήση CO₂ ή H₂O ως μέσων αεριοποίησης", 15^ο Πανελλήνιο Συμπόσιο Κατάλυσης, Ιωάννινα, 18–20 Οκτωβρίου 2018.
 16. Μ. Λυκάκη, Ε. Παχατουρίδου, Ε. Ηλιοπούλου, S.A.C. Carabineiro, Μ. Κονσολάκης, "Υδροθερμική σύνθεση νανοσωματιδίων CeO₂: Επίδραση στις φυσικοχημικές και καταλυτικές ιδιότητες μικτών οξειδίων

- CuO/CeO₂", 11^o Πανελλήνιο Επιστημονικό Συνέδριο Χημικής Μηχανικής, Θεσσαλονίκη, 25–27 Μαΐου 2017.
17. Μ. Λυκάκη, Ε. Πάπιστα, Ν. Κακλίδης, S. Carabineiro, Μ. Κονσολάκης, "Επίδραση των μορφολογικών χαρακτηριστικών νανοσωματιδίων CeO₂ στην καταλυτική διάσπαση N₂O σε μικτά οξειδία Co₃O₄/CeO₂", 11^o Πανελλήνιο Επιστημονικό Συνέδριο Χημικής Μηχανικής, Θεσσαλονίκη, 25–27 Μαΐου 2017.
 18. Μ. Lykaki, E. Pachatouridou, E.F. Iliopoulou, S.A.C. Carabineiro, M. Konsolakis, "Impact of synthesis parameters on the solid state properties and the CO oxidation performance of ceria nanoparticles", 13th European Congress on Catalysis, Florence, Italy, 27–31 August 2017.
 19. Μ. Λυκάκη και Μ. Κονσολάκης, "Τροποποίηση της επιφανειακής χημείας υποστηριγμένων καταλυτών χαλκού μέσω αλληλεπιδράσεων μετάλλου-φορέα", 14^o Πανελλήνιο Συμπόσιο Κατάλυσης, Πάτρα, 13–15 Οκτωβρίου 2016.
 20. Μ. Λυκάκη, Ε. Παχατουρίδου, Ε.Φ. Ηλιοπούλου, S.A.C. Carabineiro, Μ. Κονσολάκης, "Επίδραση της μεθόδου σύνθεσης στην επιφανειακή και καταλυτική συμπεριφορά νανο-δημητρίας", 14^o Πανελλήνιο Συμπόσιο Κατάλυσης, Πάτρα, 13–15 Οκτωβρίου 2016.
 21. Ε. Πάπιστα, Μ. Λυκάκη, S.A.C. Carabineiro, Γ.Ε. Μαρινέλλος, Μ. Κονσολάκης, "Τροποποίηση της επιφανειακής χημείας μικτών οξειδίων CuO-CeO₂ δια μέσω της επιφανειακής προώθησης με αλκάλια (Cs): η περίπτωση της καταλυτικής διάσπασης του N₂O", 14^o Πανελλήνιο Συμπόσιο Κατάλυσης, Πάτρα, 13–15 Οκτωβρίου 2016.

Seminars

20/05/2015 – 16/06/2015: Πρόγραμμα κατάρτισης «Επιταγή Διασύνδεσης με την Αγορά Εργασίας Άνεργων Αποφοίτων Πανεπιστημίων και ΤΕΙ» (Κέντρο Διά Βίου Μάθησης ΕΡΕΥΝΑ).

25/05/2013: Σεμινάριο (Association of Greek Chemists).
Θέμα: Αέρια Χρωματογραφία – Φασματομετρία Μάζας, Οργανολογία, εφαρμογές και πρακτικές συμβουλές για αποτελεσματική χρήση.

09/02/2013: Σεμινάριο (TrainMiC, Association of Greek Chemists).
Θέμα: Principles and Applications of Metrology in Chemistry.

15-16/10/2011: Επιμορφωτικό σεμινάριο (Association of Greek Chemists).
Θέμα: Υγρή Χρωματογραφία Συζευγμένη με Φασματομετρία Μάζας (LC-MS).

Honours and awards

04/08/2017–28/02/2019: PhD Fellowship grant by the Hellenic Foundation for Research and Innovation (HFRI) and the General Secretariat for Research and Technology (GSRT).

2010–2011: Scholarship from the Technical University of Crete for excellence during 1st year's postgraduate studies.

2005–2006: Scholarship from the State Scholarships Foundation for excellence during 1st year's undergraduate studies.

Memberships

Member of the Association of Greek Chemists.